ENERGY LABORATORY

MASSACHUSETTS INSTITUTE
OF TECHNOLOGY

RESEARCH ON THE EXTERNAL FLUID MECHANICS OF OCEAN THERMAL ENERGY CONVERSION PLANTS

Report Covering Experiments in a Current

by

David H. Coxe, David J. Fry, and E. Eric Adams

Energy Laboratory Report No. MIT-EL 81-049
September 1981

COO-4683-8

RESEARCH ON THE EXTERNAL FLUID MECHANICS OF OCEAN THERMAL ENERGY CONVERSION PLANTS

Report Covering Experiments in a Current

David H. Coxe
David J. Fry
E. Eric Adams

Energy Laboratory

and

Ralph M. Parsons Laboratory
for
Water Resources and Hydrodynamics

Department of Civil Engineering
Massachusetts Institute of Technology

Prepared under the support of

Division of Central Solar Technology
U.S. Department of Energy

Under Contract No. ET-78-S-02-4683

Energy Laboratory Report No. MIT-EL 81-049

September 1981

ABSTRACT

This report describes a set of experiments in a physical model study to explore plume transport and recirculation potential for a range of generic Ocean Thermal Energy Conversion (OTEC) plant designs and ambient conditions. Tests were conducted in a thermally-stratified 12 m x 18 m x 0.6 m basin, at an undistorted length scale ratio of 1:300, which allowed the upper 180 m of the ocean to be studied. Conditions which have been tested include a range of plant sizes (nominally 200 MWe - 600 MWe); a range of discharge configurations (mixed vs. non-mixed evaporator and condenser flows, multiple vs. radial slot discharge port(s), variation of discharge-intake separation and variation of discharge angle); and a range of ambient current speeds (0.15 - 1.0 m/s), and density profiles (surface mixed layers of 31 to 64 m). The tests described herein complement those reported previously (Adams et al., 1979) for a stagnant-ambient environment.

Measurements included temperature, dye concentration and visual observations from still and motion pictures. Results derived from these measurements are presented in tables and graphs in prototype dimensions for direct use by OTEC designers. Many of the results are also analyzed and presented in non-dimensional terms to extend their generality. No significant recirculation was observed for any tests with a discharge directed with a vertical (downward) component. For tests with a horizontal discharge, recirculation was observed to be a complex function of a number of parameters. For sufficiently shallow discharge submergence, low to moderate current speeds, and with plants employing a radial slot discharge, recirculation could result from dynamic pressures caused by the proximity of the free surface - despite the negative plume buoyancy. This mode was labelled "confinement-induced" recirculation and led to measurements of direct recirculation ranging from 25% to 40%. For certain combinations of ambient current speed and generally positive plume buoyancy (resulting from deeper discharge submergence), the plume was observed to billow upward resulting in "current-induced" recirculation. This was observed for both radial slot and multiple port discharge configurations although somewhat greater recirculation was observed with the former configuration. Measured recirculation for current-induced recirculation fell in the range 0 to 10% with a peak occurring at intermediate current speeds of about 0.5 m/s. Experiments with a mixed evaporator and condenser discharge showed less tendency for direct recirculation of either type than the separate (evaporator only) discharges, but the effects of recirculation, as measured by the drop in evaporator intake temperature (below the ambient temperature at the level of the intake) were not very different. A simple mathematical model, based on the governing length

scales, was successfully calibrated to the observed values of direct recirculation for the radial discharge case.

Various measures of plume transport were summarized to help designers predict the impact of OTEC operation on the environment and to establish guidelines for spacing of multiple plants. Minimum near field dilutions were observed in the range between 5 and 10 indicating that the peak concentration of any chemicals contained in the discharge would be between 10 and 20% of the discharge concentration. Near field horizontal and vertical dimensions of the plume wake were found to be correlated with a length scale derived from discharge kinematic momentum flux and ambient current speed. The rise and fall of the equilibrium plume elevation (above or below the discharge elevation) was found to be governed by a ratio of length scales based on the ambient density profile and the discharge kinematic momentum and buoyancy fluxes.

ACKNOWLEDGEMENT

This report represents part of a study being supported by the Ocean Systems Branch, Division of Central Solar Technology of the U.S. Department of Energy, under Contract No. ET-78-S-02-4683. Administration at M.I.T. has been performed by the Office of Sponsored Programs under account no. 88786. Technical program support is also being provided by Argonne National Laboratory. The cooperation and suggestions from Drs. Lloyd Lewis and Robert Cohen at DOE, and from Drs. John D. Ditmars and Robert A. Paddock at ANL are gratefully acknowledged.

The experiments were conducted at M.I.T.'s R.M. Parsons Laboratory by Mr. David H. Coxe and Dr. David J. Fry while they were Graduate Research Assistants. Research guidance and supervision was provided by Dr. E. Eric Adams, Research Engineer in the M.I.T. Energy Laboratory and project Principal Investigator. Valuable assistance in experimental design and construction was also provided by Messrs. Edward F. McCaffrey, Electronics Engineer, and Roy G. Milley and Arthur Rudolph, Machinists. The report was written largely by David Coxe and an earlier version was submitted by him to the Department of Civil Engineering in partial fulfillment of the degree of Master of Science. Portions of the dimensional analysis of Section 5.4 were contributed subsequently by David Fry. Computer work was performed on the Multics System at the M.I.T. Information Processing Center, and the report was skillfully typed by Mrs. Liza Drake and Mrs. Zigrida Garnis.

TABLE OF CONTENTS

	Page
Abstract	2
Acknowledgements	4
Table of Contents	5
List of Figures	7
List of Tables	11
List of Symbols	12
Chapter I Introduction	15
1.1 Principles of OTEC Power Plant Operation	15
1.2 Current Prototype Designs and External Flow Considerations	18
1.3 Previous Modeling Efforts and Their Relationship to this Study	20
1.4 Summary	23
Chapter II Characterization of the Prototype and Model Schematization	25
2.1 Schematization of the Power Plant	25
2.2 Schematization of the Ambient Ocean	28
Chapter III Experimental Layout	34
3.1 The Model Basin	34
3.2 The OTEC Model	34
3.3 The Towing Apparatus	42
3.4 The Discharge and Intake Water Circuits	46
3.5 The Stratification System	48
3.6 The Temperature Measurement System	49
3.7 The Dye Measurement System	56
3.8 The Photographs	59
Chapter IV Procedures	64
4.1 Procedures Prior to and During an Experiment	64
4.2 Data Reduction	66
4.2.1 Fluorescent Dye Samples	66
4.2.2 Slide Photographs	67
4.2.3 Temperature Data	67

Page

4.2.3.1 Calibrations 67
4.2.3.2 Temperature Data Manipulations 69

Chapter V Experimental Results and Analysis 71

5.1 Run Conditions 71
5.2 Data Summary 82
5.3 Discussion of Results as Related to OTEC Plant and Site Parameters 88

5.3.1 OTEC Plant Recirculation as Influenced by OTEC Plant and Site Parameters 89
5.3.2 Dilution Analysis 107
5.3.3 Analysis of Plume Characteristics 115
5.3.4 Ambient Profile Perturbations 116

5.4 Further Data Interpretation through Dimensional Analysis 117

5.4.1 Governing Variables 117
5.4.2 Definition of Length Scales 118
5.4.3 Recirculation Analysis 128
5.4.4 Dilution Analysis 143
5.4.5 Analysis of Additional Plume Characteristics 148

Chapter VI Summary and Conclusions 159

6.1 Summary 159

6.2 Conclusions 160

References 164

Appendix I: Side View Photographic Tracings of the Discharge Plume 167

Appendix II: Overhead View Photographic Tracings of the Discharge Wake 194

Appendix III: Experimental (spatially averaged) Density Profiles 216

LIST OF FIGURES

Figure No.	Title	Page
1	OTEC Power Cycle	16
2	Examples of Vertical Temperature Profiles for the Tropical Ocean	17
3	Symmetrical and Asymmetrical OTEC Plant Designs	26
4	Experimental OTEC Schematizations (with experimental parameter ranges)	27
5	Ocean Density Profiles	29
6	Superimposed Experimental Profile (Scale 1:300) for Comparison of Density Variation	30
7	Schematic Diagram of the Experimental Setup	35
8	Cutaway View of M.I.T. OTEC Model	37
9	Details of Model Intake	38
10	Details of Model Discharge Port a) Radial Discharge Port b) Separate Discharge Port	39 39 40
11	Photograph of the OTEC Model	41
12(a)	Schematic of the Towing Apparatus	43
12(b)	Blow Up Schematic of the Towing Carriage	44
13(a)	Photograph of the Towing Apparatus	45
13(b)	Close up Photograph of the Towing Carriage	45
14(a)	Photograph of the Flow Apparatus Showing the Constant Head Tank, Pool Filter and Rotometers	47
14(b)	A Close up Photograph of the Flow Manifold, Flow Control Valves and Orifice Meters	47
15	Spatial Variability of Density Profile	50
16	Temporal Variation of Experimental Profiles	51
17	Typical Ambient Density Profiles	52
18	Field Probe Locations	54

Figure No.	Title	Page
19	Data Acquisition System	55
20	Flow Chart for the Temperature Data Acquisition System	57
21	Cross Sectional Schematic of the Side View Photographic Apparatus	60
22	Photograph of a Typical Cross Section	62
23	Overhead Photograph of a Photo-station Showing a Photo-sub and a Spotlight	63
24a	Influence of Power Plant Size on Direct Recirculation Over a Range of Current Speeds	90
24b	Influence of Power Plant Size on Intake Temperature Depression Over a Range of Current Speeds	91
25a	A Comparison Between Mixed and Evaporator Radial Discharges Over a Range of Discharge Areas as they Affect Direct Recirculation	95
25b	A Comparison Between Mixed and Evaporator Radial Discharges Over a Range of Discharge Areas as they Affect Intake Temperature Depression	96
26a	The Influence of Varying Mixed Layer Depth on Direct Recirculation Over a Range of Current Speeds for a 400 MWe Plant with a Radial Evaporator Discharge at a Medium Discharge Depth	98
26b	The Influence of Varying Mixed Layer Depth on Intake Temperature Depression Over a Range of Current Speeds for a 400 MWe Plant with a Radial Evaporator Discharge at a Medium Discharge Depth	99
27a	Effect of Varying Discharge Depth for Mixed and Non-Mixed Discharges on Direct Recirculation Over a Range of Current Speeds	101
27b	Effect of Varying Discharge Depth for Mixed and Non-Mixed Discharges on Intake Temperature Depression Over a Range of Current Speeds	102
28a	A Comparison of Radial Versus Separate Ports with Variations in Mixed Versus Non-Mixed Discharge Configurations and Port Size (Direct Recirculation Versus Current Speed)	105

Figure No.	Title	Page
28b	A Comparison of Radial Versus Separate Ports with Variations in Mixed Versus Non-Mixed Discharge Configurations and Port Size (Intake Temperature Depression Versus Current Speed)	106
29	Plot of Centerline Dilution (c_o/c_f) Versus Average Dilution ($\frac{W_{450} t_{450} V}{Q_o}$)	108
	a) Radial Discharge Configuration	108
	b) 4-Jet Discharge Configuration	109
30	Schematic Representation of Near Field Recirculation (flow rate, temperature, and dye concentration noted for each flow)	110
31	Upstream Penetration Distance of Experiments with "Swept Back" Conditions	125
32	Distance to Point of Maximum Jet Thickness for Stagnant Water Tests	127
33	Quantification of the Distribution between Stratification and Current Dominated Experiments	127
34	Modes of Recirculation Definition Sketches	129
	a) Confinement Induced Recirculation	129
	b) Current Induced Recirculation	129
35a	Integral Model Predictions and Experimental Data of h_d/ℓ'_B at Attachment (with Intake, k=1)	131
35b	Integral Model Predictions and Experimental Data of h_d/ℓ'_B at Detachment (with Intake, k=1)	132
36	Normalized Recirculation for Experiments with Fully Covered Intakes	134
37	"Swept Back" Plume Thickness at the Position of the OTEC Plant	134
38	"Swept Back" Plume Rise or Fall at the Position of the OTEC Plant	135
39	Normalized Recirculation for Fully "Swept Back" Plumes ($Q_{back}/Q_T = 1.0$)	135
40	Model Predictions of Recirculation (λ) for the Evaporator Discharge of a Base Case 400 MW OTEC Plant	140
41	Base Case 400 MW Evaporator Discharge Conditions	141
42a	Centerline (S) Dilution Versus Dimensionally Derived Dilution for (Radial Port) Stratification Dominated Experiments	144

Figure No.	Title	Page
42b	Average Dilution (S_{ave}) Versus Dimensionally Derived Dilution for (Radial Port) Stratification Dominated Experiments	145
43a	Centerline Dilution (S_c) Versus Dimensionally Derived Dilution for (Radial Port) Current Dominated Experiments	146
43b	Average Dilution (S_{ave}) Versus Dimensionally Derived Dilution for (Radial Port) Current Dominated Experiments	147
44	Normalized Plume Width versus Longitudinal Distance for Current Dominated Experiments	149
45	Maximum Near Field Plume Thickness versus ℓ_S for Stagnant Water Experiments	151
46	Distance to Maximum Near Field Plume Thickness for Stratification Dominated Experiments	152
47	Maximum Near Field Plume Thickness for Stratification Dominated Experiments	152
48a	Plume Thickness for Stagnant Water Tests	154
48b	Plume Thickness 450 m. Downstream of Plant (for Experiments with $Q_{back}/Q_T = 0$)	154
49	Stagnation Length for all Radial Horizontal Discharge Experiments	155
50	Normalized Plume Width versus Longitudinal Distance for Stratification Dominated Experiments	156
51	Observed Plume Rise or Fall for Ambient Current and Stangant Water Experiments	158

LIST OF TABLES

Table No.	Title	Page
1	Oceanograhpic Characteristics at Prospective OTEC Sites	32
2	Experimental Parameter Schematization	72
3	Experimental Parameters	77
4	Experimental Results	83
5	Analysis of Near Field Recirculation and Dilution for Discharge Ports Located Below the Mixed Layer Depth	112
6	Important Independent Variables and Length Scales	120
7	Measured and Predicted Values of Direct Recirculation	138

LIST OF SYMBOLS

A_o 1/8 of total discharge port area

B_o discharge kinematic buoyancy flux (local) = $Q_o[\rho_o - \rho_{amb}(z=h_d)]g/\rho$

B_o discharge kinematic buoyancy flux (relative to free surface) = $Q_o[\rho_o - \rho_{amb}(z=0)]g/\rho$

c_i intake concentration

c_N near field concentration (See Fig. 29)

c_o discharge concentration

F_o^* discharge densimetric Froude number = $h_o/\sqrt{g|\Delta\rho_o/\rho|A_o}^{1/2}$

H depth of mixed layer

h_b centerline plume thickness below discharge elevation (See Fig. 34)

h_d depth of discharge

h_t centerline plume thickness above discharge elevation (See Fig. 34)

h_{eq} equilibrium depth of plume centerline

h_i depth of intake

h_o half-height of discharge port

Δh_o $(\Delta\rho_o/\rho)g/N^2$

L_r length scale ratio between model and prototype

ℓ_B buoyancy length scale

ℓ_H a vertical length scale used in recirculation analysis

ℓ_Q discharge length scale

ℓ_{Q_i} intake length scale

ℓ_S stratification length scale

ℓ_V current length scale

M_o discharge kinematic momentum flux = Q_oU_o

N Brunt-Väisälä frequency = $[g\partial\rho/\rho\partial z]^{1/2}$

Q_{back} fraction of near field flow rate swept vertically back by current (variable used in recirculation analysis)

Q_i intake flow rate (evaporator)

Q_o discharge flow rate (evaporator in non-mixed; evaporator and condenser in mixed concept)

Q_r ratio of flow rates between model and prototype

Q_T total near field flow rate (variable used in recirculation analysis)

$\mathbb{R}_e$ Reynolds number of jet discharge

r radial coordinate

r_c plant radius (See Fig. 4)

r_h hydraulic radius used to define $\mathbb{R}_e$

r_i plant radius at intake (See Fig. 4)

r_o plant radius at discharge (See Fig. 4)

S salinity

S_{ave} $\frac{W_{450} t_{450} V}{Q_o}$ as derived from photographic measurements of W_{450} and t_{450}

S_c centerline plume dilution

S_N near field dilution (See Fig. 30)

t_{450} thickness of wake at x=450 m (prototype) as seen in the side view photographic tracings

T temperature

T_{amb} ambient temperature

T_{ai} average temperature of intake flow

T_{ao} average temperature of ambient water involved in near field mixing

T_i intake temperature

T_N near field temperature (See Fig. 29)

T_o discharge temperature

T' characteristic "trophical ocean" temperature derived from measured densities (See Section 5.1)

T'_{amb} ambient value of T'

T'_i value of T' at intake

$\Delta T'_i$ intake temperature rise (depression) = $[T'_i - T'_{amb}\ (z=h_i)]$

t_{450} plume thickness at x = -450 m (prototype) as seen in the side view photographs

t_r ratio of time scales between model and prototype

U_r ratio of velocity between model and prototype

u_o discharge velocity

V ambient current speed

W_{450} width of the wake at x = -450 m (prototype) as seen in the plan view photographic tracings

X_s distance to the stagnation point as seen in the plan view photographic tracings

x longitudinal coordinate

z vertical coordinate (positive downward)

α_H horizontal angle of distance

α_V vertical angle of discharge

λ direct recirculation fraction (ratio of dye concentrations at intake and discharge

λ_N near field recirculation fraction (ratio of dye concentrations at intake and near field (See Fig. 30)

ν kinematic viscosity

ρ density

ρ_{amb} density of ambient water

ρ_o density of discharge

$\Delta\rho_a$ characteristic density difference of ambient profile = $[\rho_{amb}(z=165) - \rho_{amb}(z=0)] = \Delta\rho'\ (z=0)$

$\Delta\rho_o$ discharge density difference = $[\rho_o - \rho_{amb}(z=z_o)]$

$\Delta\rho^*$ (small) density difference characterizing mixed layer (See Fig. 4)

$\Delta\rho'$ relative density difference used to plot profiles = $[\rho_{amb}(z=165) - \rho]$

σ_t density difference = $(\rho - 1.0) * 10^3 gm/cm^3$

I. INTRODUCTION

1.1 Principles of OTEC Power Plant Operation

Ocean Thermal Energy Conversion (OTEC) is a means of power generation which takes advantage of the temperature differences existing between the upper and lower thermal strata in a tropical ocean. The upper layer of the ocean gains its energy from solar radiation. The underlying water is colder due to the return flow from polar regions induced by global ocean circulation.

An OTEC power plant would produce power based on the same thermodynamic principles which are used in a conventional steam-electric power plant. Figure 1 is a simple illustration of a closed cycle OTEC power cycle. Heat from the warm upper water is used in an evaporator to vaporize a working fluid (e.g., ammonia) in a pressurized vessel. The vapor is expanded through a turbo-generator to produce electric power and is then condensed using the cold lower water. Using this type of a power cycle, the major difference between an OTEC plant and a conventional power plant is its low thermodynamic efficiency.

The thermal efficiency of an OTEC plant is limited by the low temperature difference which drives its power cycle. Figure 2 shows representative vertical temperature profiles for a tropical ocean, each exhibiting a characteristic mixed layer of warm water near the surface above a stably stratified density structure. Typical temperature differences between the surface and a depth of 500 to 1000 m vary from 18 to 24°C. Based on this temperature range, the net efficiency of an OTEC plant is estimated to be 0.02 to 0.03 as compared to 0.30 to 0.40 for a conventional power plant [Jirka, et al., 1977]. In order to produce

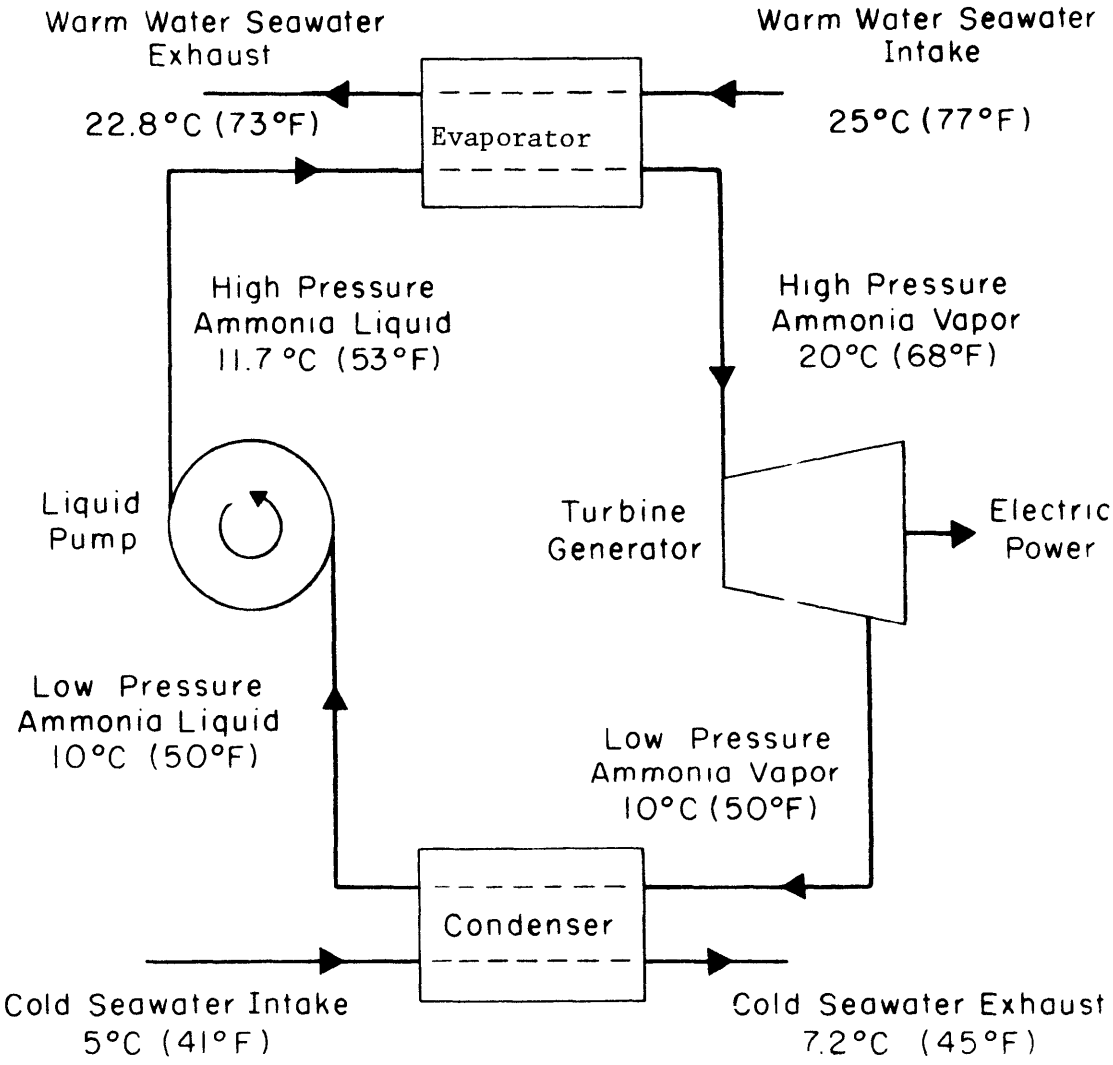

Figure 1: OTEC Power Cycle

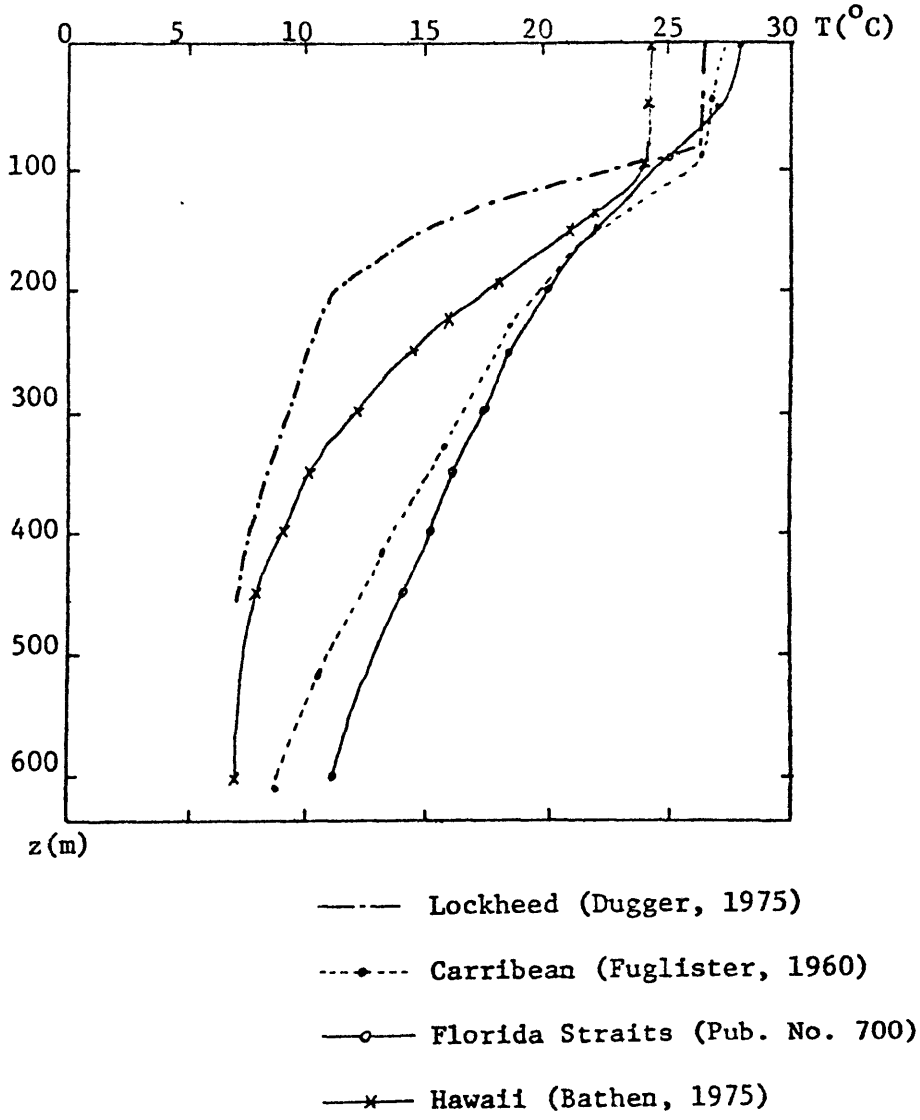

Figure 2: Examples of Vertical Temperature Profiles for the Tropical Ocean (From Jirka, et al, 1977).

quantities of power comparable to conventional power plants, an OTEC plant must utilize tremendous amounts of water to exploit the low grade energy resource. For example, for an OTEC plant to produce 200 MWe with the system depicted in Figure 1, the warm and cold water intake flows would each have to be about 1000 m^3/sec [Fry, 1976].

1.2 Current Prototype Designs and External Flow Considerations

OTEC power plant configurations currently (1980) under consideration vary from a free floating ship which "grazes" for the optimal thermal resource to a fixed design where the thermal resource is a function of the power plant site. In each case, the power plants rely upon the temperature difference between the warm sea water intake near the surface and the cold sea water intake 500 - 1500 m below the surface to drive a heat engine. Since the temperature of the deep cold water is expected to remain constant, the temperature differential will primarily depend upon the warm water intake temperature. With the available potential energy of the water utilized, the slightly cooled warm and slightly warmed cold water intake flows must be discharged. Because of the enormous flows involved, the warm water intake temperature is not only a function of ambient ocean variability, but of potential interactions between the flow fields generated by the evaporator intake, the plant discharges and the warm mixed layer [Ditmars, et al., 1979]. The extent of these interactions depends upon a number of factors, including the location and vertical separation distance between the intake and discharge ports relative to the mixed layer, the ambient ocean currents,

the angle of the discharge with respect to the horizontal, and the buoyancy of the discharge flow relative to the ambient density structure. The degradation of the thermal resource available to a plant due to near field flow interactions (generally interpreted in terms of a lowering of the average warm water intake temperature) is called recirculation. This condition may result from some fraction of the discharge volume flux entering the warm water intake ("direct" recirculation), recirculation of water entrained by the discharge jet ("indirect" recirculation), turbulent mixing of the upper stratified layers (induced by the discharge jets) accompanied by a lowering of the mixed layer temperature ("indirect" recirculation), or non-selective withdrawal of the upper stratified layers by the intake port.

Because of the adverse effects of recirculation on power output [Allender, et al., 1978], it is desirable to be able to identify those prototype plant designs which will minimize recirculation and thus provide optimal energy extraction for a given site environment.

Operation of an OTEC plant may not only influence the utilization of the thermal resource, but may also be the cause of seriously damaging ecological disruption. These environmental concerns include the effects of OTEC induced changes in water temperature and salinity distributions, the effects of nutrient redistribution within the water column, and the influences of working fluid leaks and biocide applications on the food chain [Ditmars, et al., 1979]. Clearly, the physical processes governing environmental problems are germane to the thermal resource problem.

1.3 Previous Modeling Efforts and Their Relationship to this Study

The OTEC concept was introduced as early as 1881 by d'Arsonval. Nearly 50 years passed before Claude (1930) built the first operational OTEC system and proved its feasibility. However, the technology of the time was not sufficiently advanced, and the costs of coal and oil were too low to justify further system development. As technology has evolved and fuel costs have soared, OTEC has been looked upon with renewed interest. As a result, numerical and physical modeling studies have been undertaken to assess OTEC feasibility and to evaluate the behavior within the ocean environment of proposed power plant designs. In their baseline designs, TRW [1975] and Lockheed [1975] both acknowledged the need for an in depth analysis of the external flow fields induced by the operation of an OTEC plant. Studies relating to the external flow field as well as to the larger scale physical and biological environment have appeared consistently in the annual OTEC conferences.

Several investigators [Lockheed, 1975; Kirchoff, et al., 1975; Fry, 1976; Giannotti, 1977; Van Dusen, 1974; Ditmars, et al., 1979] have used integral techniques to analyze the behavior of individual buoyant jets representing evaporator and/or condenser flows discharging into a stratified stagnant environment. These analyses are useful for estimating discharge jet trajectories, dilutions and spreading characteristics for a plant operating in an ocean with little or no current and in which the discharge jets and intake flows do not interact. Bathen (1975), in studying the environmental impacts of 100 and 240 MWe OTEC plants offshore Keyhole, Hawaii, used the results of an integral jet analysis for a mixed discharge plume in a flowing, uniformly mixed, thermal environment

as input to a two-dimensional, numerical heat transport model.

Intake withdrawal characteristics (without consideration of discharge jet interaction) have been studied under various idealized schematizations relevant to OTEC by Craya [1949], Gabriel [1949], Mangarella [1975], Fry [1976], and Sundaram et al. [1977]. The purpose of these studies was to examine whether operation of an evaporator intake could selectively withdraw warm water from near the intake or whether intake temperatures would be reduced by withdrawing a portion of the intake flow from beneath the surface mixed layer.

The studies referenced above have focused on either the discharge or the intake dynamics separately. Recently studies have been performed to examine possible interaction between the two. Roberts et al. [1976] developed a two-dimensional (Cartesian coordinates) numerical model of the external flow fields as generated by a Lockheed [1975] baseline plant design operating in a density stratified, stagnant ambient ocean. The schematization and relevance (to three-dimensional prototypes) is questionable; however, their results indicate the general types of circulation which can occur.

Sundaram et al. [1977] examined, experimentally, highly schematic versions of OTEC plant intakes and discharges operating in a two-layered stagnant or a uniform, flowing ambient ocean. Their results indicated that direct recirculation varied with the magnitude of the current speed, and was dependent upon the vertical separation between the intake and discharge ports, the (negative) buoyancy of the discharge jet relative to the ambient, and the orientation of the discharge ports. Some of their results are comparable to the general trends which were found in this study.

OTEC modeling studies performed at MIT have included two major research efforts. In the first, Jirka et al. [1977] studied interaction between an evaporator intake and a mixed evaporator and condenser discharge located at the interface of a two-layer ocean. Radial slot and symmetrical 4-port discharge configurations, stagnant and mild ambient currents ($\leq$ 0.1 m/s) and plant sizes up to 200 MWe were considered. Although also somewhat schematic, the tests were designed to include all of the relevant features and physical processes which would characterize prototype OTEC operation. A mathematical model was calibrated to measurements of jet thickness and recirculation, and was used to extrapolate model results in order to estimate the likelihood of prototype recirculation.

A present research effort at MIT is designed to extend the work of Jirka et al. [1977] and involves several phases. Adams et al. [1979] examined flow field interactions for OTEC plants, with power output ranging from 200 - 600 MWe, operating in a continuous temperature-stratified stagnant ocean. Separate (evaporator only) and mixed evaporator and condenser radial slot and symmetric 4-port discharges were used with mixed layer depths ranging from 30 - 70 meters. Results from these stagnant water experiments indicated significant recirculation only for plants with upward directed discharge jets and for larger plant sizes (600 MWe) employing an evaporator discharge.

A second phase of the present program has examined in more detail various jet interactions which can occur in an OTEC environment. These can include the interaction between an evaporator discharge and intake beneath a free surface and the interaction between separate, but closely

spaced, evaporator and condenser discharges. These studies [Fry, 1980] show that the interaction between the two discharge jets may effect a mixed discharge configuration without the necessity of mixing the discharge effluents inside the plant; the mixed discharge mode reduces the probability of direct recirculation due to negative buoyancy.

The present study extends the stagnant water tests reported in Adams et al. [1979] to incorporate a realistic range of ocean current velocities. The purpose of both studies combined has been to examine a broad range of realistic prototype operating conditions in order to provide optimum design and operating constraints for a given ocean environment. To complement the stagnant water tests, this study examines the performance of various OTEC plant configurations operating in an ocean with continuous temperature stratification and uniform ambient currents ranging up to approximately 1 m/s. Discharge configurations include radial slot and 4-port separate with vertical and horizontal variations in port alignment. Sensitivity of plant performance to variations in ocean baseline parameters, discharge flow rates and velocities, and relative distances between discharge and intake ports are also examined within this framework.

1.4 Summary

The objective of this report is to present and analyze data taken from a series of physical modeling tests aimed at reproducing prototype OTEC plant flow field interactions under realistic ocean conditions. Chapter 2 describes the pertinent aspects of the ocean environment, the important features of current OTEC plant designs, and the manner in which these prototype characteristics were modeled experimentally.

Chapter 3 describes the experimental layout and operation. Chapter 4 lists the procedures used to obtain and reduce the experimental data. The experimental results and analysis are presented in Chapter 5. Summary and conclusions based on these results follow in Chapter 6.

II. CHARACTERIZATION OF THE PROTOTYPE AND MODEL SCHEMATIZATION

2.1 Schematization of the Power Plant

A number of OTEC plant designs have been advanced [See OTEC Conference Proceedings]. Some, such as the early designs from the University of Massachusetts [Heronemus, et al., 1975] are highly "asymetrical," relying on the ocean currents (e.g., the Gulf Stream) to supply a continuous stream of warm water for the evaporator intake. These plants are of limited versatility since each must be designed for site-specific conditions. The designs considered in this study are limited to those which can be modeled as "symmetrical" vertical columns such as the early designs of Lockheed [1975] and TRW [1975]. The column, or spar-buoy design does not rely on ambient ocean currents. Both "symmetrical" and "asymmetrical" designs are shown in Figure 3.

The parameters which are used to characterize the OTEC plant are shown in Figure 4, along with the ranges corresponding to the parameter variations in the model tests. These parameter ranges are an extension of the stagnant water tests [Adams, et al., 1979], allowing for realistic ocean currents and additional breadth in port size and discharge velocity ranges. The evaporator intake, with a flow Q_i, is located at a depth h_i below the surface. The condenser intake is not modeled. Two discharge modes have been considered. A design in which the evaporator and condenser flows are discharged separately is referred to as a "non-mixed" discharge mode ($Q_o = Q_i$). A design in which the evaporator and the condenser flows are combined within the plant prior to discharge is referred to as a "mixed" discharge mode ($Q_o = 2Q_i$). The latter concept

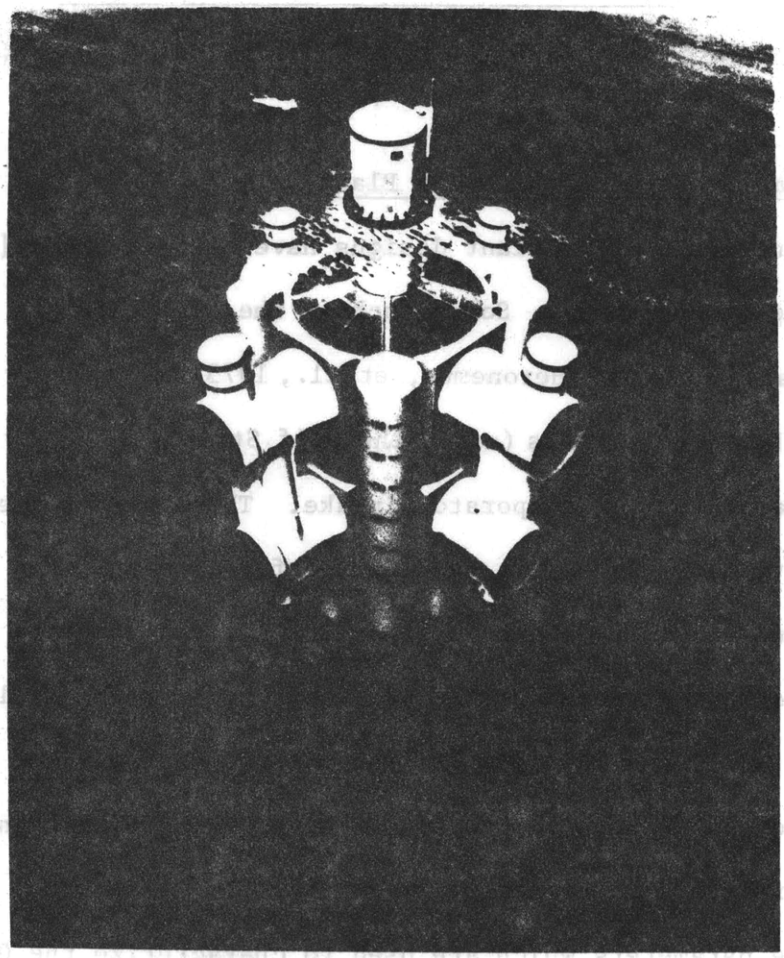

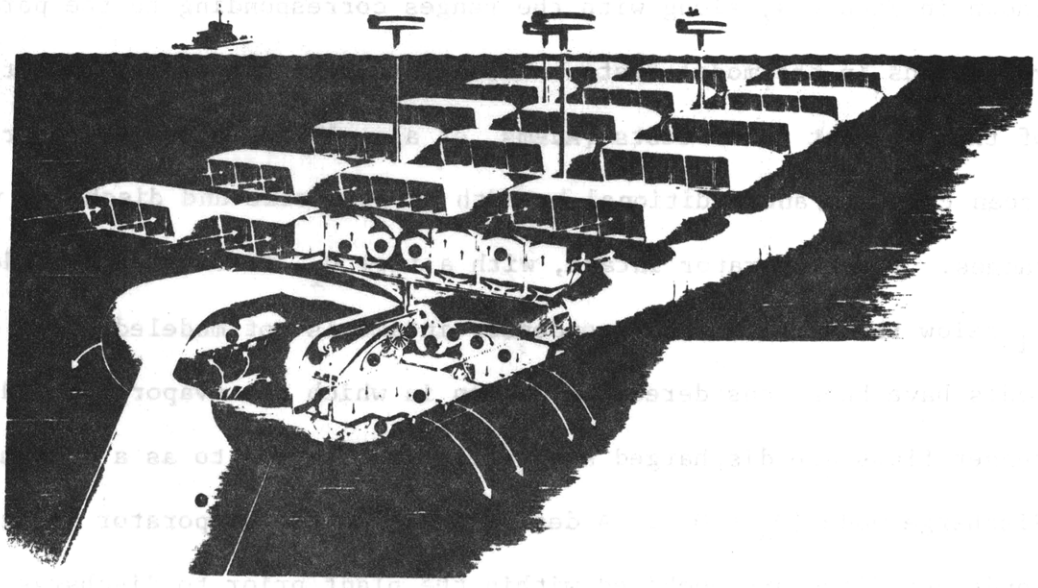

Figure 3: Symmetrical and Asymmetrical OTEC Plant Designs

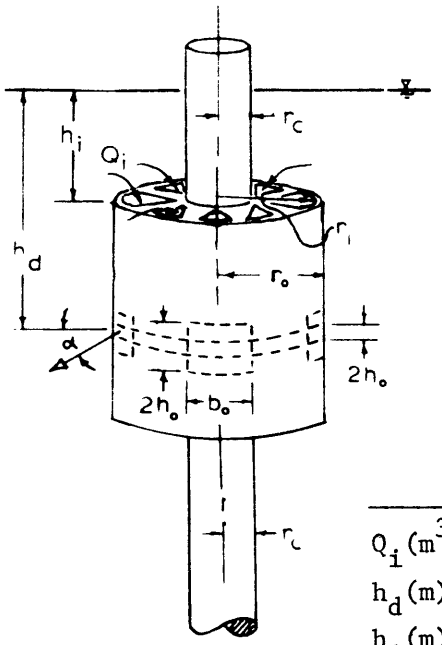

RADIAL OR SEPARATE JET DISCHARGE

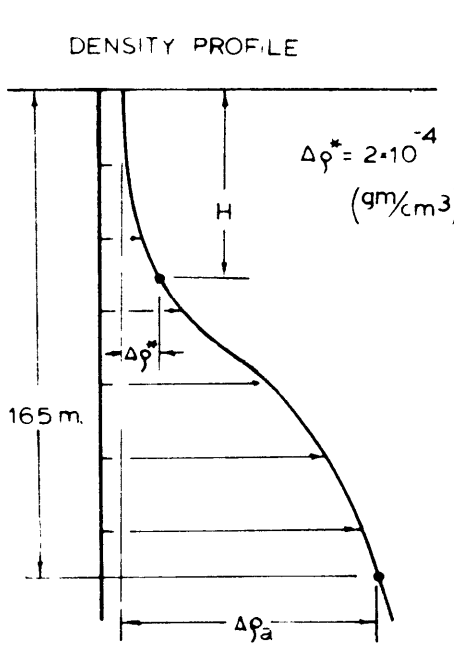

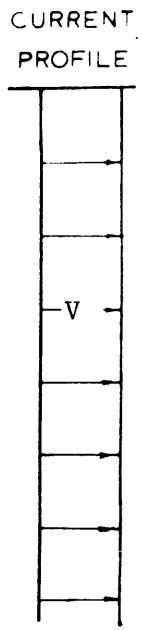

EXPERIMENTAL MODEL (1:300)

	capability	tests to date
$Q_i (m^3/s)$	500-3000	1000-3000
h_d (m)	23-170	38-99
h_i (m)	0-60	7-9
α	0°&45°	0°&45°
r_i (m)	20 m.	20 m.
r_o (m)	23 m.	23 m.
r_c (m)	11 m.	11 m.
h_o (m)	Depends on Q_i	1.0-4.4 (radial)
		6.0-12.2 (4-jet)
b_o (m)		10.7-10.9 (4-jet)
u_o (m/s)		1.6-7.1
V (m/s)	0-1.2	0-1.0

Figure 4: Experimental OTEC Schematizations (with experimental parameter ranges)

could potentially help to reduce recirculation between the discharge and the evaporator intake due to the negative buoyancy of the discharge. The possibility of effecting a mixed discharge situation by merging closely spaced evaporator and condenser discharge jets is being examined concurrently with this research [Fry, 1980]. For the "non-mixed" discharges, only the evaporator discharge is modeled, thus assuming no interaction between the evaporator and condenser discharges.

Two types of generic discharge configurations are evaluated in this study. In the "radial" discharge configuration, a radial slot of height $2h_o$ completely encircles the plant circumference. Although none of the presently proposed OTEC designs exhibit this geometry, it is a useful basis for evaluation and for comparison with previous OTEC modeling studies [Adams, et al., 1979; Jirka, et al., 1977]. It has an obvious advantage for analytical (cylindrically two-dimensional) and experimental modeling and it preserves many of the characteristics of more complicated three-dimensional designs so long as equality of mass, momentum and heat fluxes are maintained.

In a "separate" discharge configuration, four separate jets with rectangular cross-sections (height $2h_o$ and width b_o) are arranged around the plant circumference at angles of 90° to one another. This condition closely approximates probable round port designs with the mixed or non-mixed discharge concept.

2.2 Schematization of the Ambient Ocean

Figure 5 [Miller, 1977] shows ocean density profiles for several tropical locations. Near the surface, vertical momentum transfer from

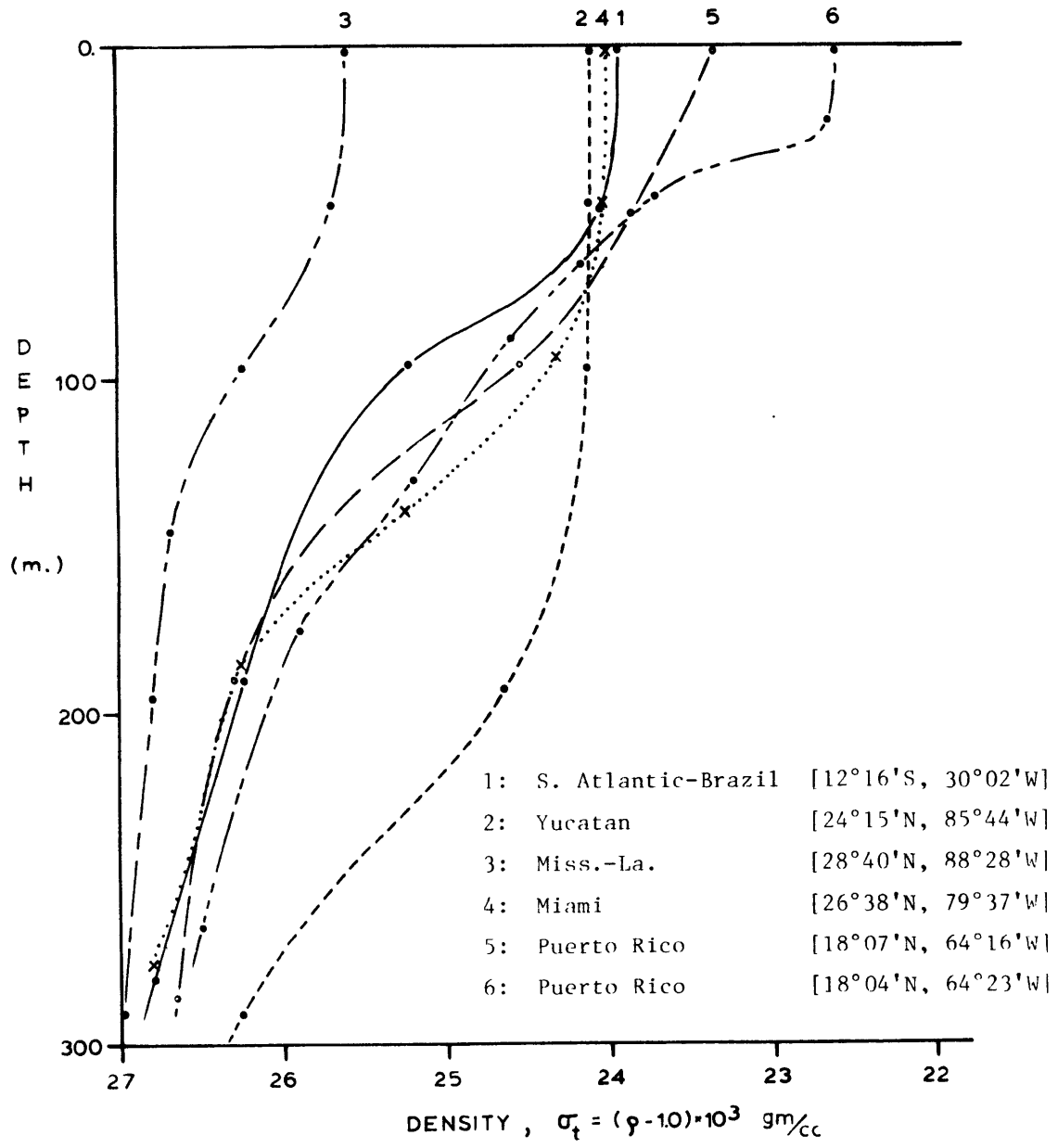

Figure 5: Ocean Density Profiles [Miller, 1977]

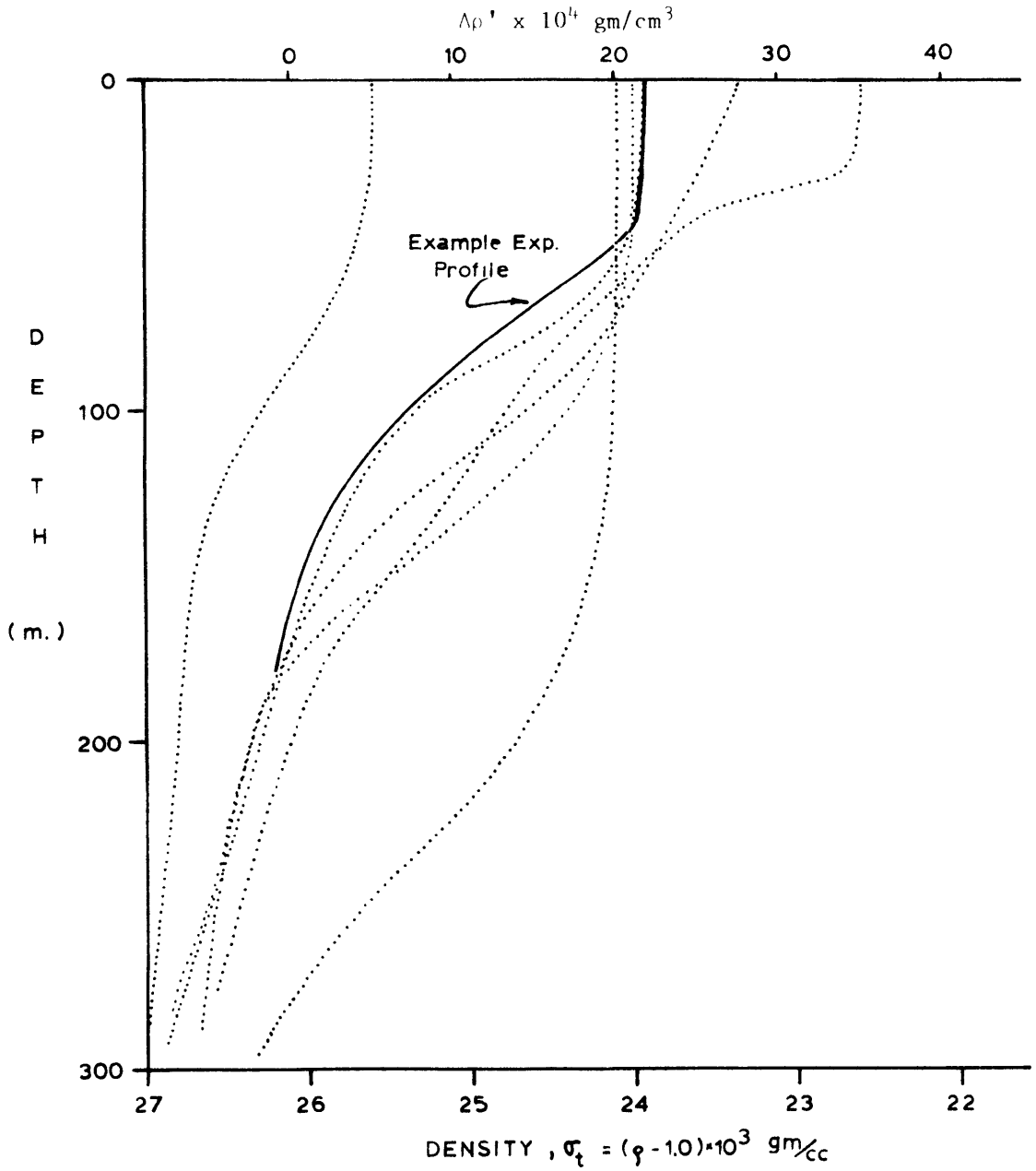

Figure 6: Superimposed Experimental Profile (Scale 1:300) for Comparison of Density Variation

wind and wave action and cooling maintains a well-mixed layer of warm water. Below this layer exists a thermocline, where temperature drops rapidly accounting for a strong density gradient. This gradient gradually decreases with depth until the water temperature becomes essentially constant. The stable density structure in the thermocline is an important inhibitor to vertical momentum and heat transfer, and therefore, is an important consideration in the study of OTEC external fluid mechanics.

As shown in Figure 6, this study considers realistic continuous density profiles which are comparable to actual ocean density profiles. Each density profile produced in the laboratory is different in detail, but can be categorized using the parameters H and $\Delta\rho_a$. H is the mixed layer depth, defined as the depth where the ambient density differs from the surface density by an arbitrary but small abount. $\Delta\rho_a$ is the density difference between the surface and 165 meters or $[\rho_{amb}(165) - \rho_{amb}(0)]$. A reference depth of 165 m is chosen because it is slightly above the model basin depth of 180 m and thus outside of any potential thermal boundary layer.

Although ocean water density is a function of both salinity and temperature, experimental density profiles were generated in fresh water using temperature differences to generate density differences. The distinction between temperature and density is important in modeling an OTEC power plant. A plant generates power by operating on the temperature difference between thermal layers, while the external fluid dynamics are governed by the difference in densities (buoyancy).

In addition to density structure, ocean currents are important in the consideration of whether the operation of an OTEC plant will influence

the thermal resource utilization. Currents of some magnitude are present throughout the ocean, although in most cases they vary in speed and direction. Table 1 lists some average current speeds, density differences and mixed layer depths at sites of interest.

Site	Monthly Mean* ΔT (°C)	Monthly Mean* Density Difference (10^{-4}g/cm^3)	Monthly Mean Mixed Layer Depth, H (m)	Monthly Mean Surface Currents V (m/sec)
Sri Lanka	21.0-21.9	35.5-38.6	30-80	.25-.62
Mombasa	18.2-21.2	29-5-38.5	30-90	.30-.62
Jakarta	22.1-23.4	35.1-40.1	55-80	.25-.52
Dampier Land	20.7-23.2	30.8-37.9	30-80	.25-.47
Manila	22.7-24.9	34.9-41.7	20-80	.30-.52
Guam	23.4-24.8	36.6-40.9	60-120	.30-.47
Baja California	18.1-23.5	23.2-37.4	10-30	.25-.31
Panama - Pacific Side	22.5-23.3	34.9-38.8	0-30	.30-.52
Panama - Caribbean Side	21.4-23.1	32.9-38.4	40-110	.30-.62
Ivory Coast	19.8-23.6	27.5-37.7	0-30	.25-.31
Gulf of Mexico - w. of Tampa. Fla.	19.5-22.6	25.5-33.5	20-120	.20-.60
Hawaii - Keahole Pt.	18.2-20.6	28.0-34.4	100-150	.10-.30
Puerto Rico - Punta Tuna	21.6-22.7	33.2-37.8	40-110	.30-.62

TABLE 1: Oceanographic Characteristics at Prospective OTEC Sites [Wolf, 1979; Bathen et al., 1975; Molinari et al., 1978]

* Between surface and 1000 m

As shown in Figure 4 this study examines a broad range of realistic prototype currents.

The currents are generated by towing a model OTEC plant through a temperature-stratified basin. Thus, prototype conditions are modeled with a uniform ambient current and a horizontally uniform, vertically stratified environment.

III. EXPERIMENTAL LAYOUT

3.1 The Model Basin

The experiments were conducted in a 12.2m x 18.3m x 0.60m (40' x 60' x 24") basin located on the first floor of the Ralph M. Parsons Laboratory for Water Resources and Hydrodynamics at M.I.T. There is a 4.6 m (15 ft) long plexiglass window in one wall of the basin which allows for visual observation of the model tests. The floor and sides of the basin are insulated to minimize heat losses to the surroundings. Figure 7 presents a general layout of the basin showing the experimental setup for the tests of the model in a current.

3.2 The OTEC Model

To retain dynamic similitude between the prototype and the scale model, densimetric Froude scaling was chosen, thereby preserving similarity of the buoyant mixing process. This process is the most important characteristic in determining the external flow and temperature fields [Jirka, et al., 1975]. An undistorted length scale of 1:300 was selected to provide a compromise between two competing objectives: obtaining large jet Reynolds numbers to insure turbulent flow and measurement resolution (both dictating large scale ratios) and modeling large ocean depths (dictating a small scale ratio). The 1:300 scale and the 0.60m basin depth allows the upper 180m of the ocean to be modeled. This was sufficient to prevent interaction of the discharge with the bottom for any horizontal dishcarge and for most discharges directed downward. (As shown in the photographic tracings of Appendix I,

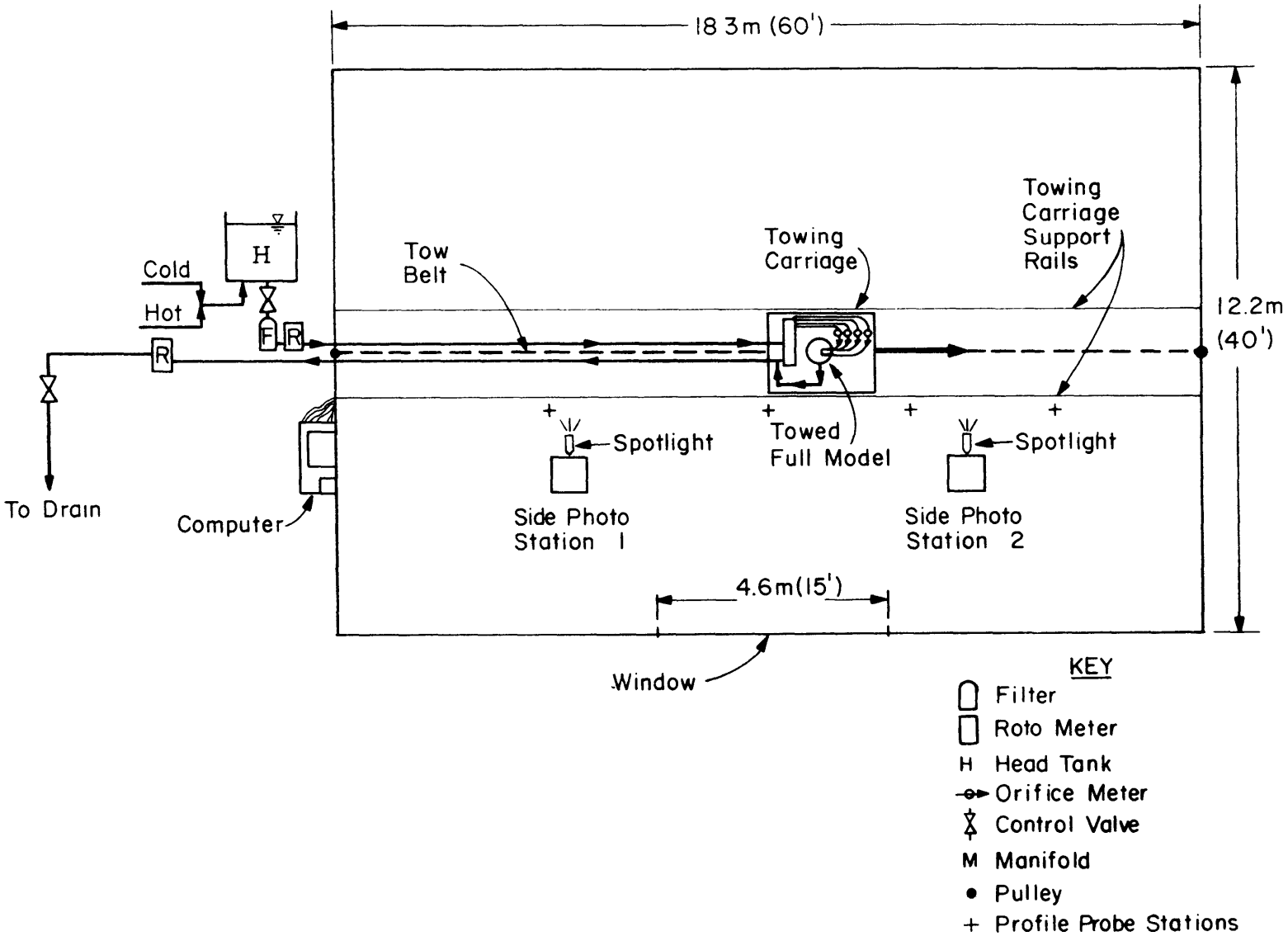

Figure 7: Schematic Diagram of the Experimental Setup

some bottom interaction was observed in the experiments where the discharge was directed downward . The basin was not deep enough to model either the condenser discharge in a non-mixed design or the (cold water) intake. With the 1:300 scale ratio, the minimum jet Reynolds number, based on the discharge hydraulic radius, was 2800, obtained for the case of a 200 MWe plant with non-mixed discharge. For Re > 1500, the discharge jet is expected to be fully turbulent. Under these conditions, the jet mixing zone characteristics can be taken as Reynolds number independent and thus similar [Jirka, et al., 1975]. Reynolds numbers for all of the experiments are listed in Table 3.

Using the same density differences in the model as are in the prototype, densimetric Froude scaling, and an undistorted length scale ratio, L_r, of 1/300, the scale ratios for velocity, time and flow rate between model and prototype are determined as follows:

$$U_r = L_r^{1/2} = \left(\frac{1}{300}\right)^{1/2} = 0.058$$

$$t_r = L_r^{1/2} = \left(\frac{1}{300}\right)^{1/2} = 0.058$$

$$Q_r = L_r^{5/2} = \left(\frac{1}{300}\right)^{5/2} = 6.4 \times 10^{-7}$$

A cutaway three-dimensional view of the plexiglass model in the 4-port (separate) discharge configuration is shown in Figure 8. Figures 9 and 10 show details of the intake and discharge ports. The stagnant water tests [Adams et al.] used one half of this model attached to the plexiglass window so that the wall was taken as a plane of symmetry. The full model, as shown in the photograph of Figure 11, was used for the

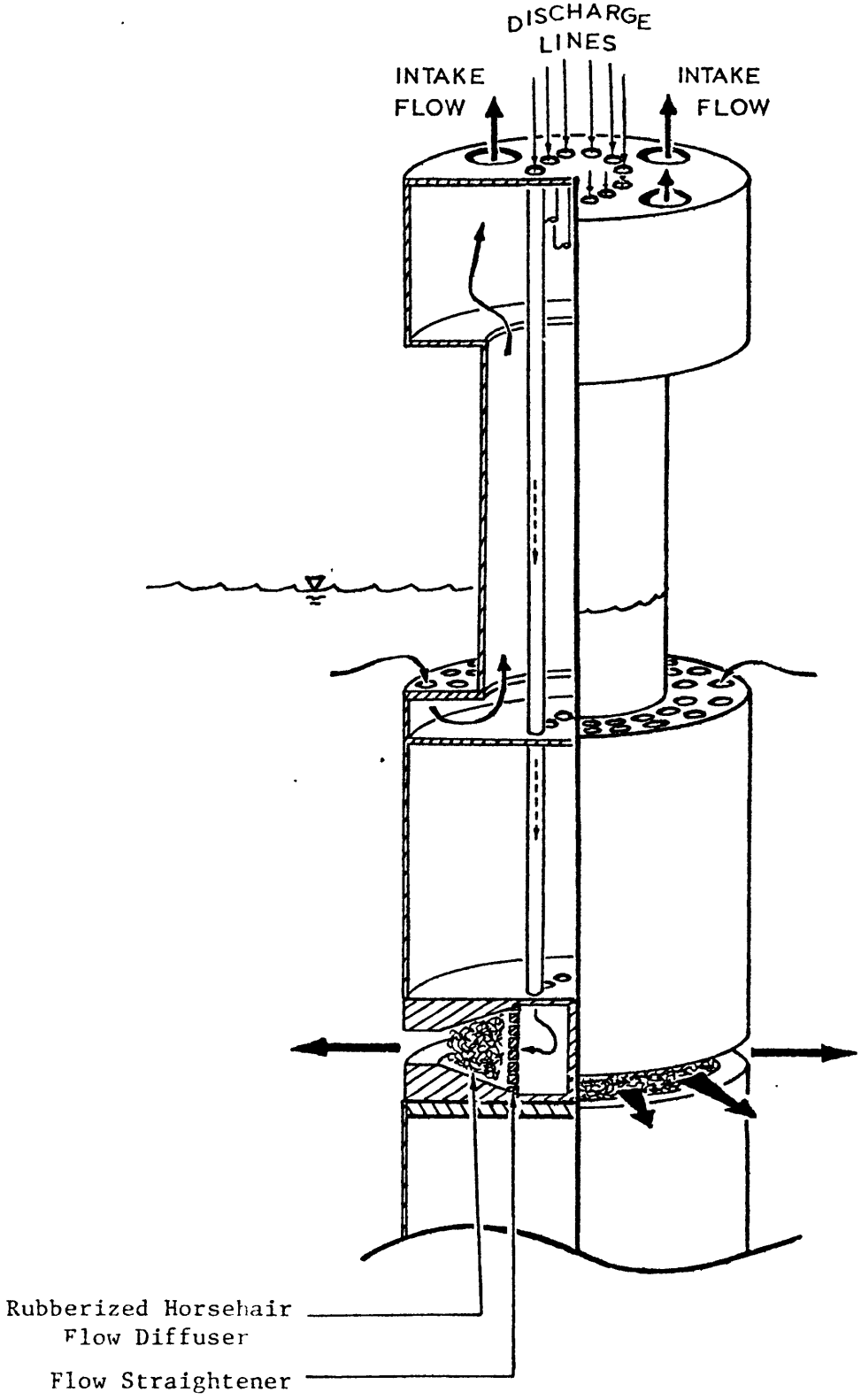

Figure 8: Cutaway View of M.I.T. OTEC Model

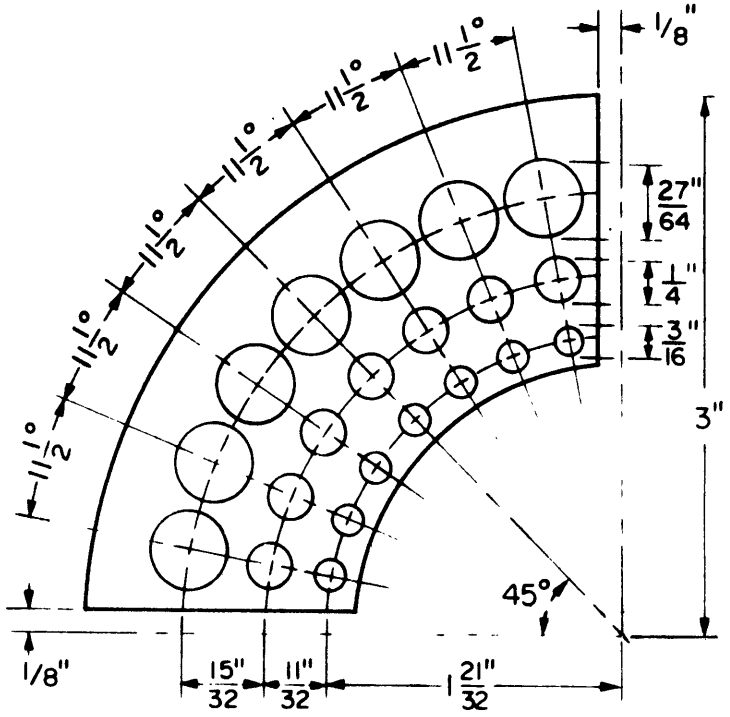

NOTE: All walls are 1/4" thick

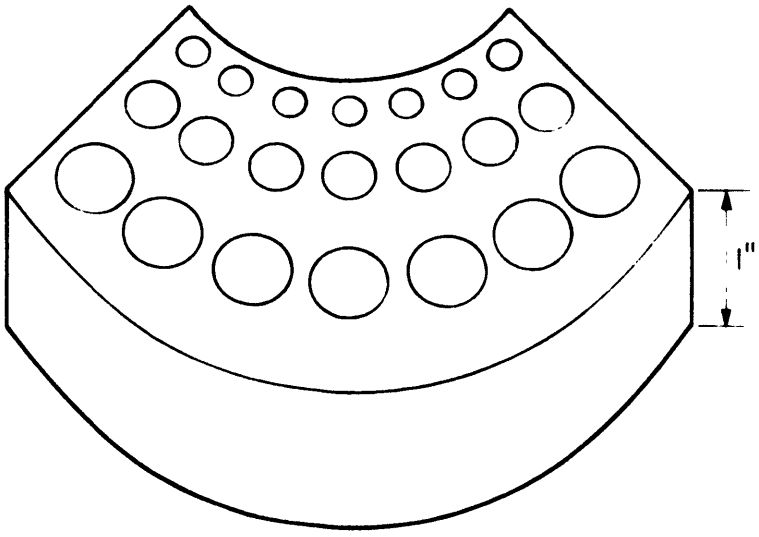

Figure 9: Details of Model Intake

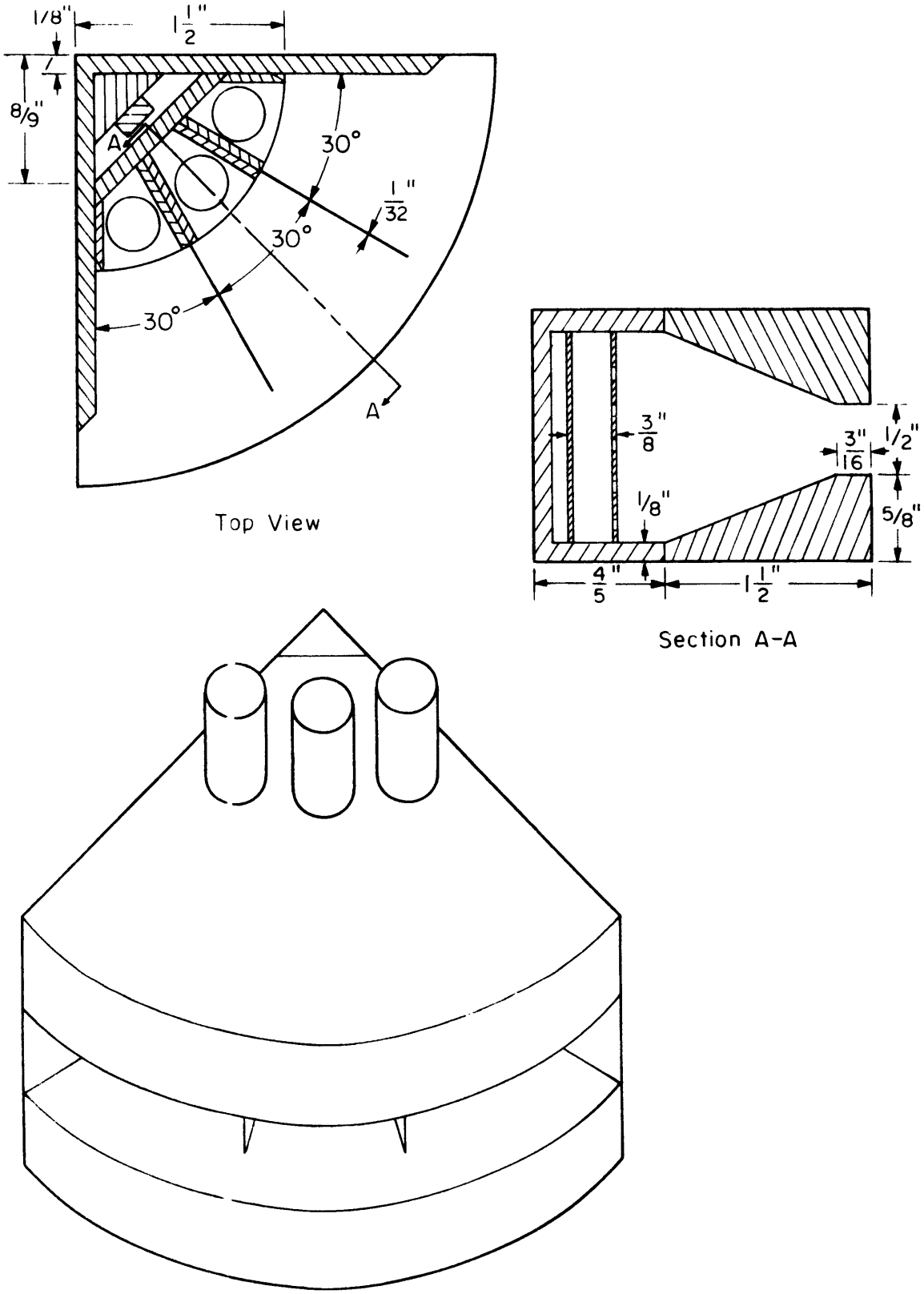

Figure 10: Details of Model Discharge Port
a) Radial Discharge Port

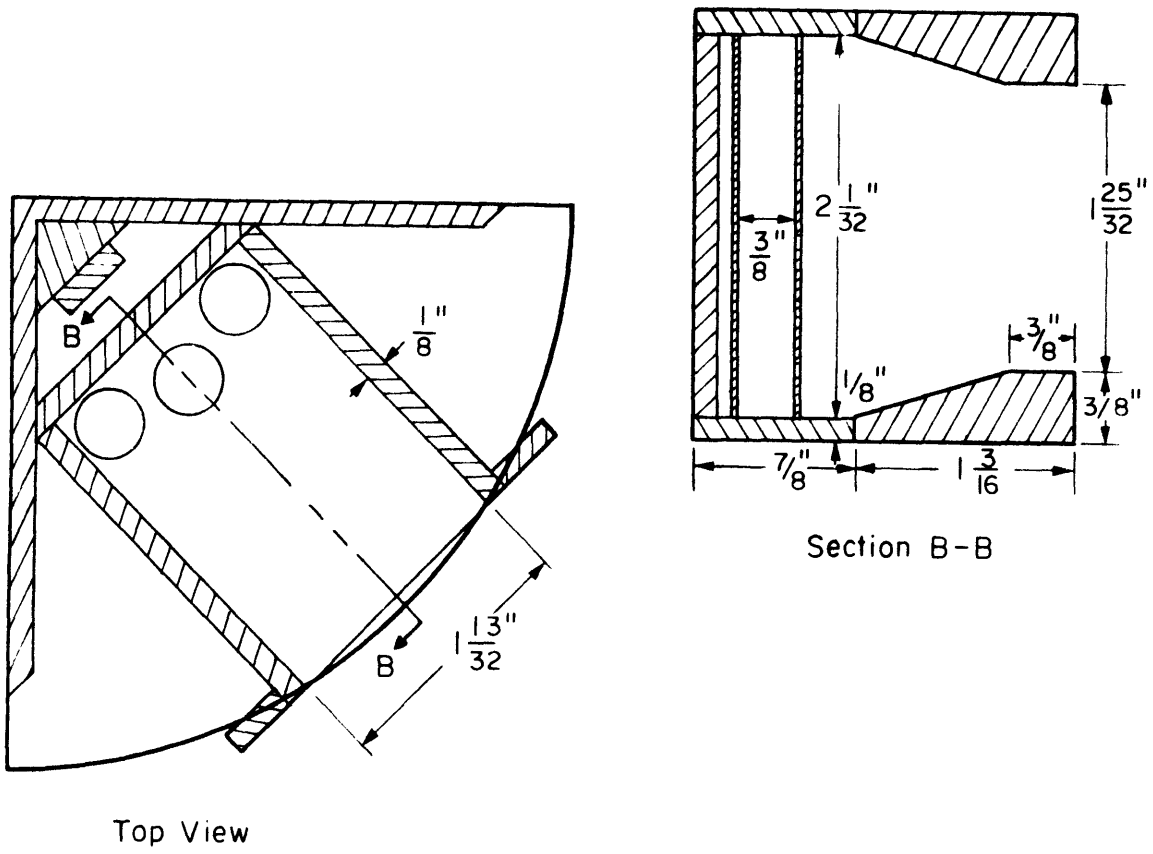

Figure 10 cont'd: Details of Model Discharge Port
b) Separate Discharge Port

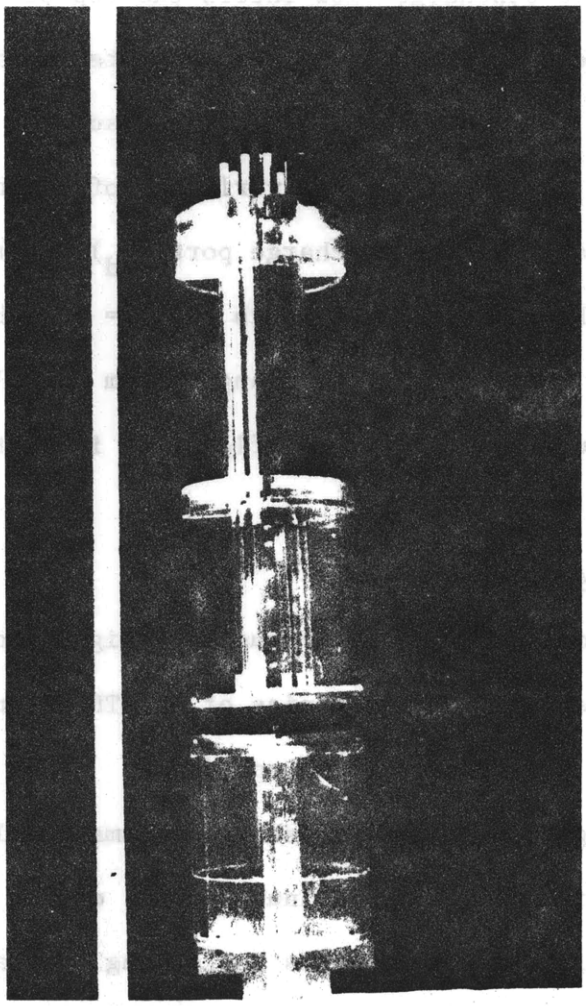

Figure 11: Photograph of the OTEC Model (note: some of the side walls are left out for closer viewing)

tests in a stratified current. The intake flow (warm surface water) enters the model through a radial configuration of circular port holes. It then travels through a large plexiglass tube where it is pumped out of the model. The discharge flow enters the top of the model through brass tubes. These brass tubes bypass the water inside the intake flow tube and deliver the discharge flow to the discharge ports.

The model design allows for variation of the depth of the intake port (h_i), the depth of the discharge port (h_d) and thus the distance between the intake and discharge ports ($h_{sep} = h_d - h_i$). The discharge ports are easily removed to allow changes from radial to separate discharge configurations or for modifications in port size.

3.3 The Towing Apparatus

The OTEC model towing apparatus is designed to provide the ability to study the external fluid mechanics of an OTEC plant as affected by a broad range of prototype current speeds.

The towing apparatus is presented schematically in Figure 12 and pictorially in Figure 13. A continuous belt, driven by a reversible 3 horsepower varispeed motor, pulls the towing carriage across the basin. An overhead support rail guides the belt, forming a closed loop with each side of the towing carriage. The model intake and discharge hoses, attached to trolley wheels in the overhead support rail, are pulled by the towing carriage as it crosses the basin. Figure 12b shows the OTEC model located in stage no. 1 of the towing carriage with data acquisition equipment located on stages 2 and 3.

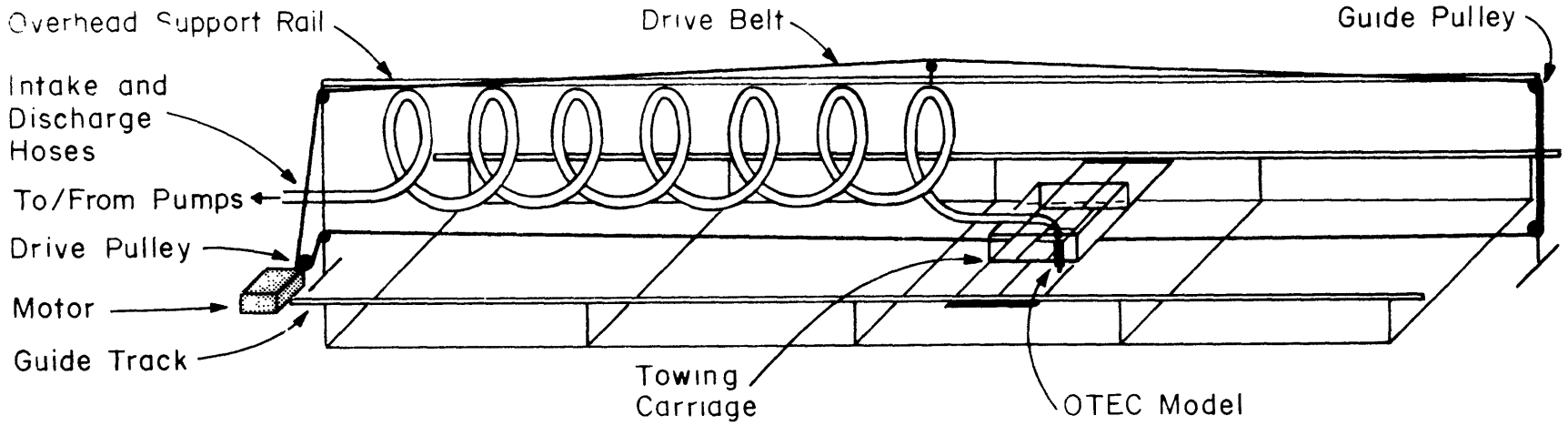

Figure 12(a): Schematic of the Towing Apparatus

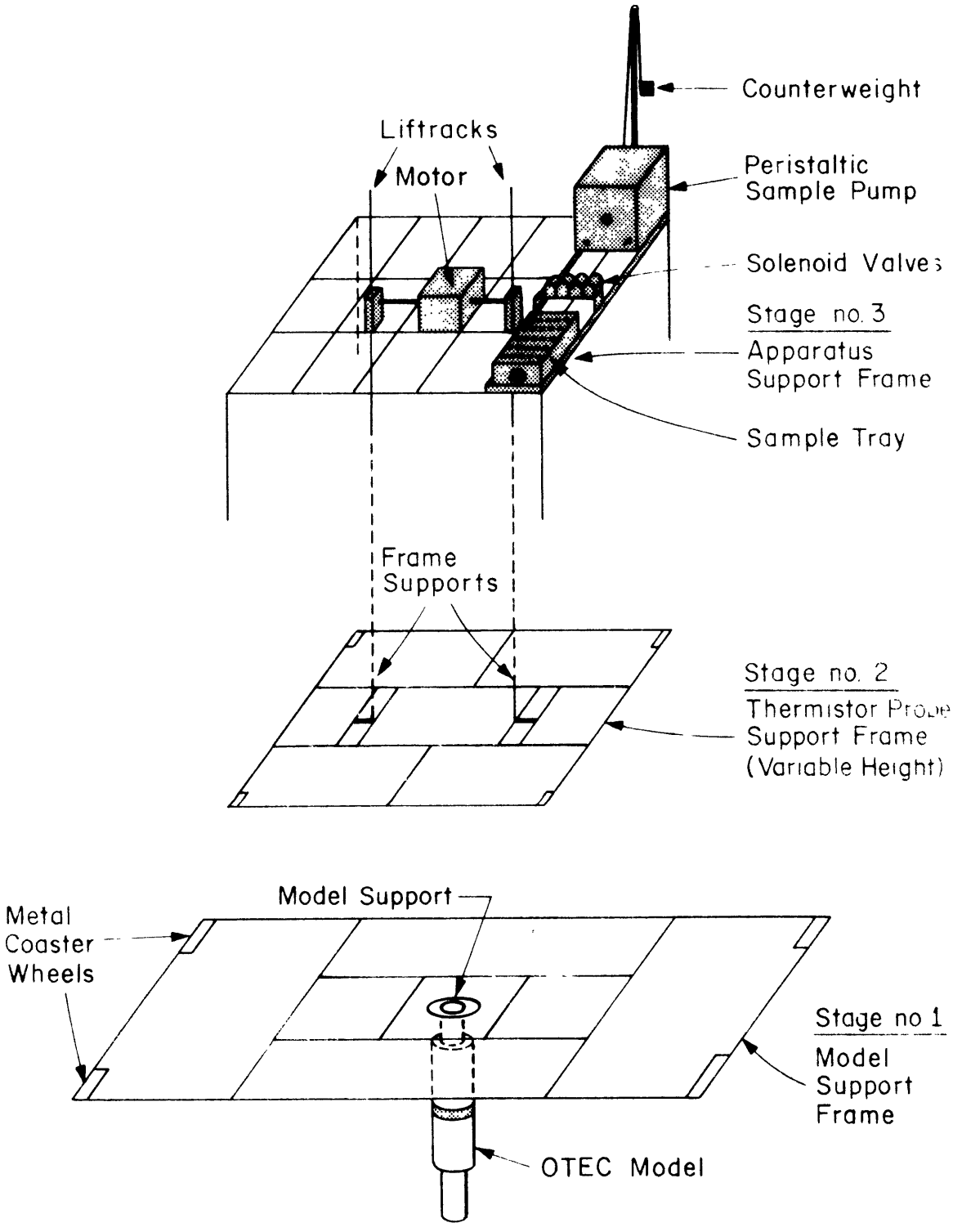

Figure 12(b): Blow Up Schematic of the Towing Carriage

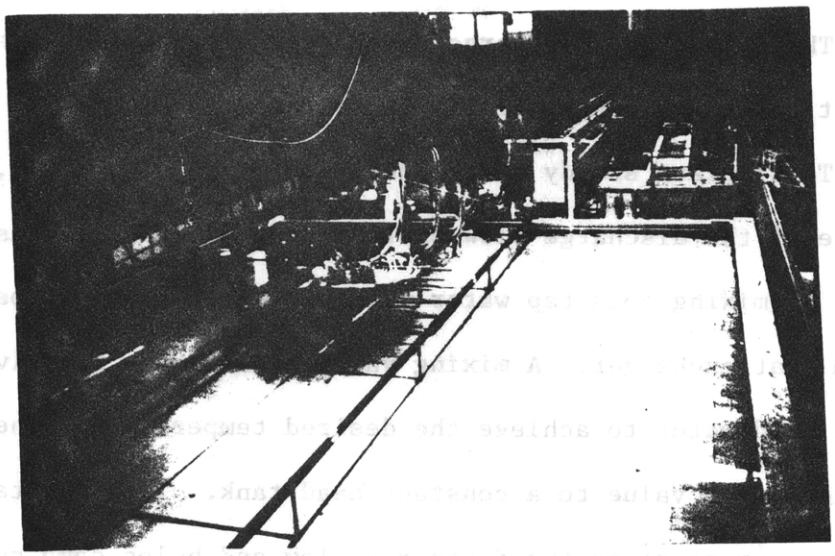

Figure 13(a): Photograph of the Towing Apparatus

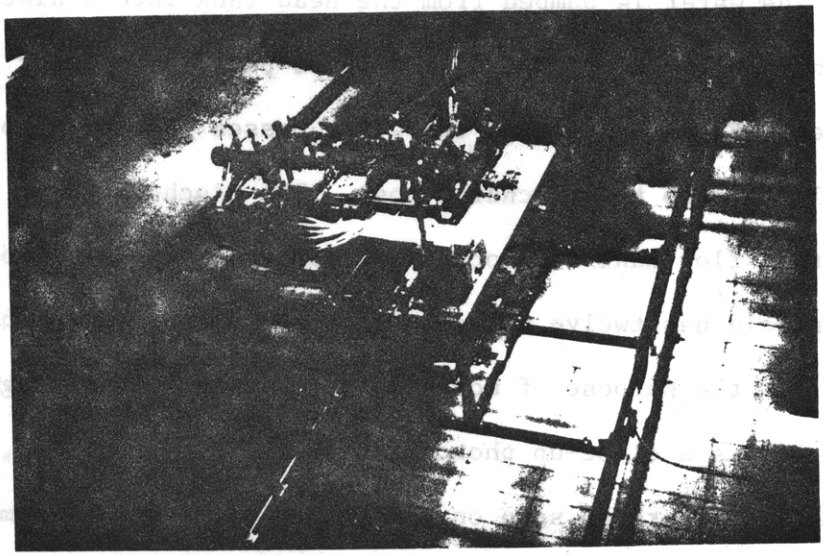

Figure 13(b): Close up Photograph of the Towing Carriage

3.4 The Discharge and Intake Water Circuits

The intake and discharge water flow circuits for the stratified current tests are schematically illustrated in Figure 7.

To simulate steady state operation of an OTEC plant, the temperature of the discharge flow must be kept constant. This is accomplished by mixing cold tap water with hot water that has passed through a steam heat exchanger. A mixing valve adjusts the relative flow of hot and cold water to achieve the desired temperature. The water flows from the mixing value to a constant head tank. The head tank provides a constant pressure to the discharge flow and helps damp out short term temperature fluctuations.

The water is pumped from the head tank into a diatomaceous earth swimming pool filter. The filter helps purify the water for photographic purposes. From the filter, the water passes through a rotometer and control valve to the discharge hose. The discharge hose carries the water to a flow manifold located on stage no. 3 of the towing carriage. The manifold has twelve valves with hoses connected to individual orifice meters for the purpose of monitoring the flow rate through each port. Figure 14b is a close-up photograph of the flow manifold, control valves and orifice meters as seen on the towing carriage. From the orifice meters, the flow passes through flexible plastic tubine to the brass tubes in the upper portion of the model and out to the discharge ports. The discharge temperature is monitored in the flow lines near the model and before it enters the discharge hose. Figure 14a is a photograph of the flow apparatus showing the constant head tank, pool filter and rotometers along with the intake and discharge hoses.

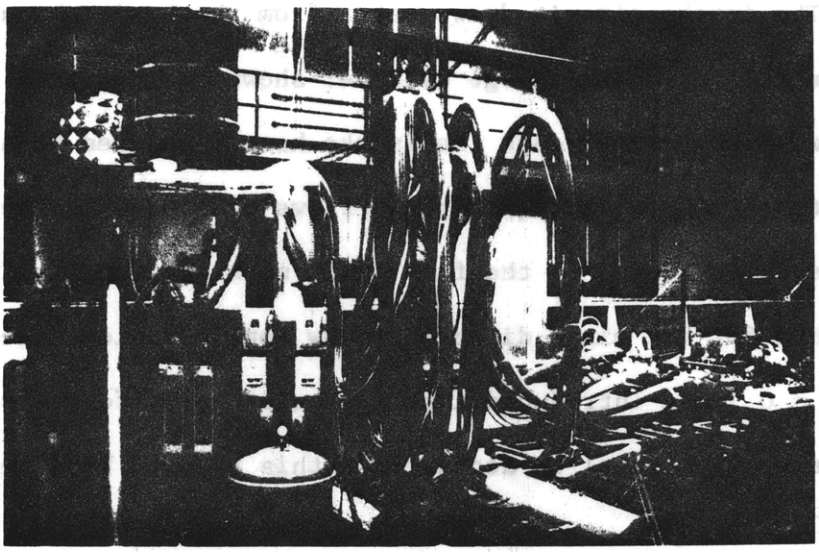

Figure 14(a): Photograph of the Flow Apparatus Showing the Constant Head Tank, Pool Filter and Rotometers

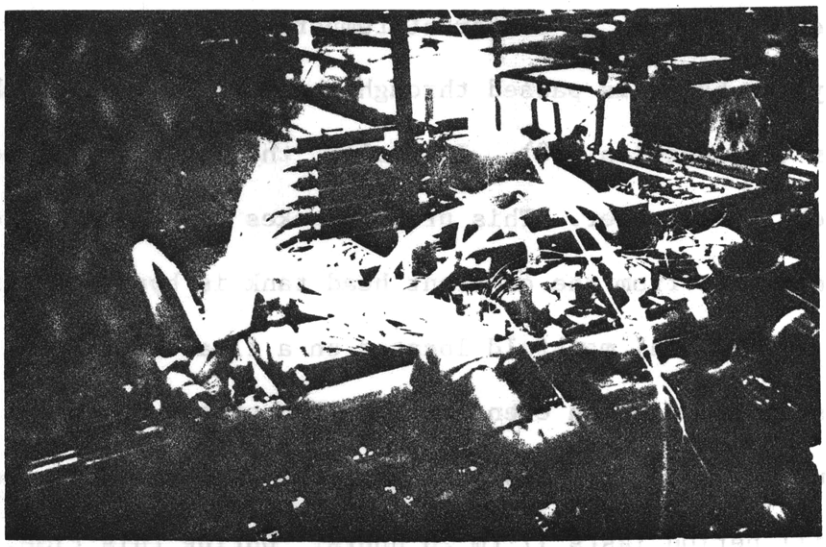

Figure 14(b): A Close up Photograph of the Flow Manifold, Flow Control Valves and Orifice Meters

The intake circuit draws water from the basin through the perforations in the top of the large cylinder shown in Figure 8. The water is withdrawn by a pump through the intake hose, measured by a rotometer, and controlled by a valve before it flows to a drain. The intake temperature is monitored in the flow lines near the model. It should be noted that for the mixed discharge flow configuration a net flow ($Q_o - Q_i = Q_i$) was introduced into the basin; no effort was made to adjust the water level to account for this effect, but the resulting effect was small.

3.5 The Stratification System

In order to simulate an actual ocean density profile, the basin is filled with water of different temperatures. All water used to stratify the basin is passed through the pool filter for photographic purposes (see section 3.8). Initially, the basin is filled partway with (cold) city water. This process takes approximately one hour. Then, hot water from the constant head tank is bypassed through a hose network to a radial manifold located on a float in the center of the basin. This system provides an even distribution of the hot water over the cold water surface and minimizes mixing of the cold and hot water. The warm water fill period lasts 17 to 20 hours. During this time, diffusion takes place between the warm and the cold water resulting in a smooth temperature profile. Once the filling has ceased, surface cooling mixes the upper layers thereby lowering the mixed layer temperature. The difference in density between the entering hot and cold water is designed to be greater than the desired density difference, $\Delta\rho_a$. This allows one to four hours from the time when the hot water is turned off to when the surface has cooled enough so that the desired density difference

between upper and lower layers has been achieved.

The spatial and temporal variability of typical temperature profiles obtained with this filling procedure are demonstrated in Figures 15 and 16. Figure 15 shows profiles of mean temperature (and density difference) ± one standard deviation as determined from ten probes mounted vertically at each of nine stations within the basin before the start of a typical experiment. The average standard deviation of temperature is about 0.1°C with a maximum of about 0.25°C occurring at the thermocline. The corresponding average and maximum standard deviations for density are about 3.0×10^{-5} and 7.5×10^{-5} gm/cm^3 respectively.

Figure 16 shows the temporal variation of the mean temperature (and density difference) profiles following basin fill-up. This indicates that for a typical experiment lasting 30 minutes, the maximum change in temperature occurred near the surface and was about 0.5°C.

Three types of ambient density profiles, each requiring a different fill-up procedure, were used to encompass a range of profiles which might occur at potential OTEC sites. Figure 17 shows typical basin temperature (density) profiles characterized by shallow, medium and deep mixed layer depths.

3.6 The Temperature Measurement System

Temperature measurements were made using approximately 100 Yellow Springs, Incorporated, series 700 thermilinear thermister probes (time constant = 1 sec, repeatability ≈ .05°C). Two probes were used to monitor the intake temperature and two probes were used to monitor the discharge temperature. Four sets of ten stationary probes, designated

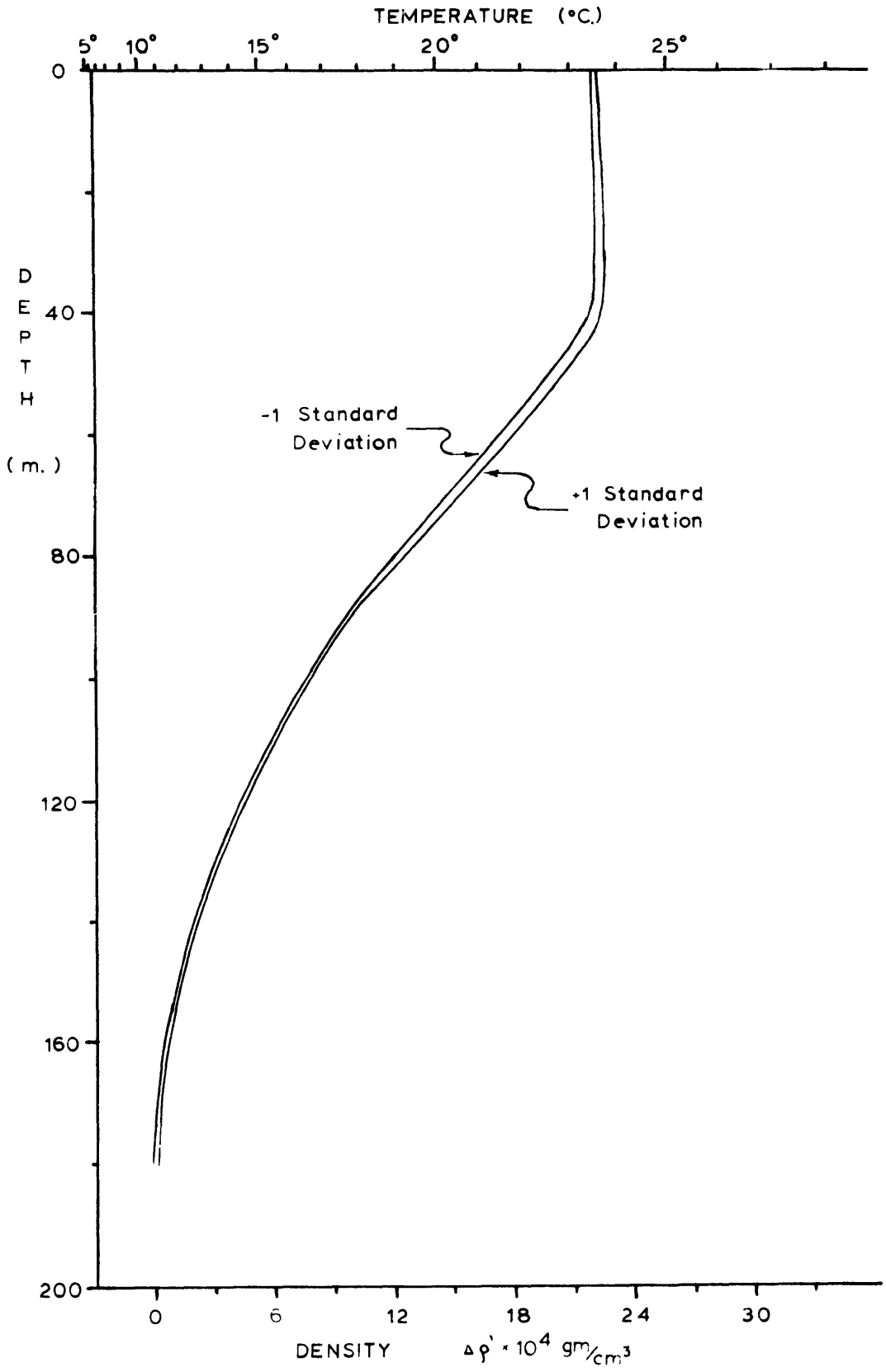

Figure 15: Spatial Variability of Density Profile

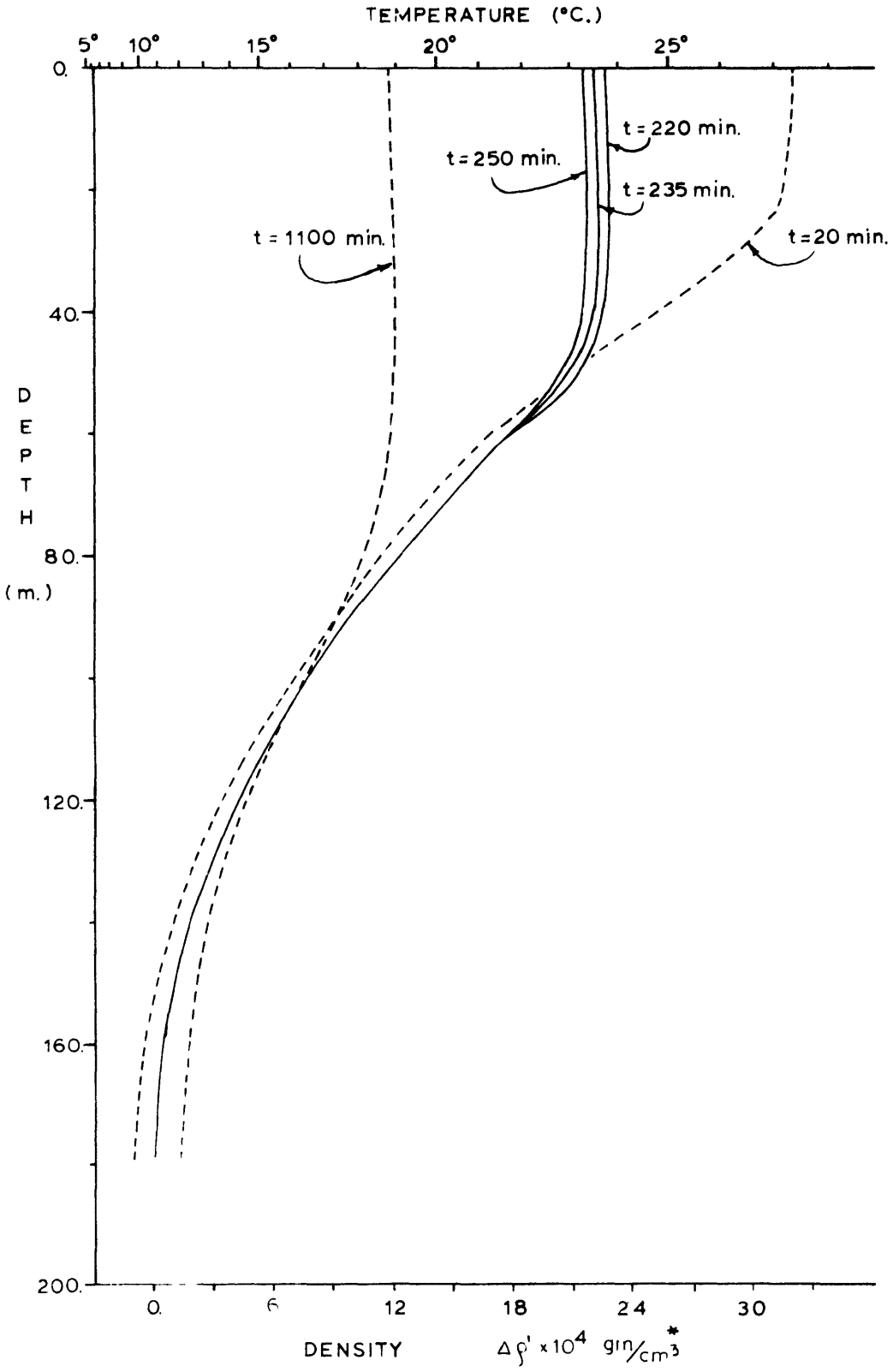

Figure 16: Temporal Variation of Experimental Profiles

*referenced to 0 at z=165m. and t=235 min.

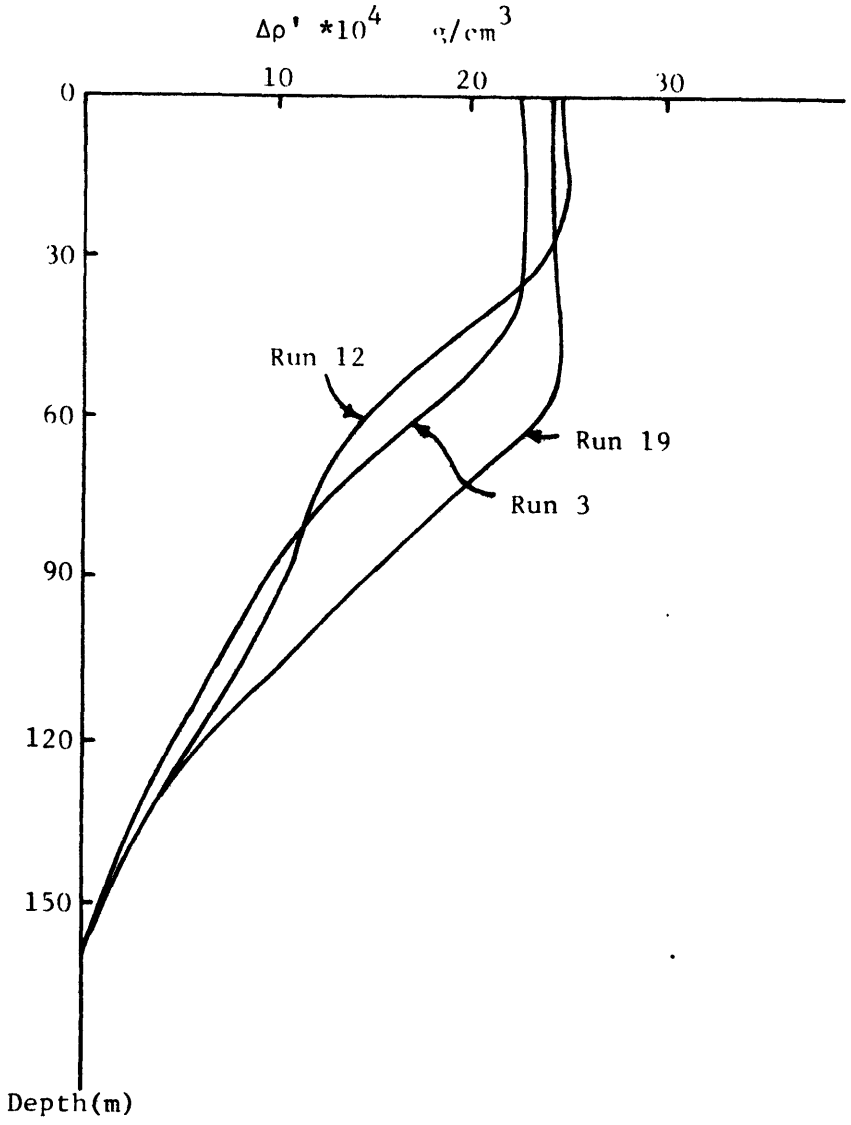

Figure 17: Typical Ambient Density Profiles

Run 12 - Shallow H
Run 3 - Medium H
Run 19 - Deep H

as profile probes, were located along the towing track (see Figure 7), and were aligned in vertical arrays to measure the ambient temperature profile at various times prior to the start of and during an experiment.

The remaining probes, designated as field probes, were fixed to stage no. 2 of the towing carriage as shown in Figure 18. Stage no. 2 was supported by two motorized vertically traversing lift racks (see Figure 12b) and was remotely controlled from outside of the basin. Two probes, vertically separated by about 15 cm were located at each horizontal position so that with a vertical travel of 45 cm the entire vertical column (60 cm) could be sampled. The horizontal spacing of the probes was selected so as to document the important features of the anticipated temperature field.

Figure 19 is a photograph of the data acquisition system specially designed for this study [McCaffrey, 1980]. This system consists of the following components:

A) General purpose computer; MITS, Altair 8800B with 48K bits of static RAM memory, 8K bits of PROM memory, 10 input and output ports, and an 8080 microprocessor clocked at 2.0 MHZ.

B) Disk storage unit; MITS, Altair 99DCDD, eight inch hard sectored floppy disk with a data capacity of 300K bits per diskette.

C) Hard copy unit; Centronics 703, 5x7 inch dot-matrix bidirectional intelligent printing terminal.

D) Display terminal; Lear Siegler ADM-3A, 12" rectangular screen, standard 64 ASCll character set displayed in 24 lines of 80 characters.

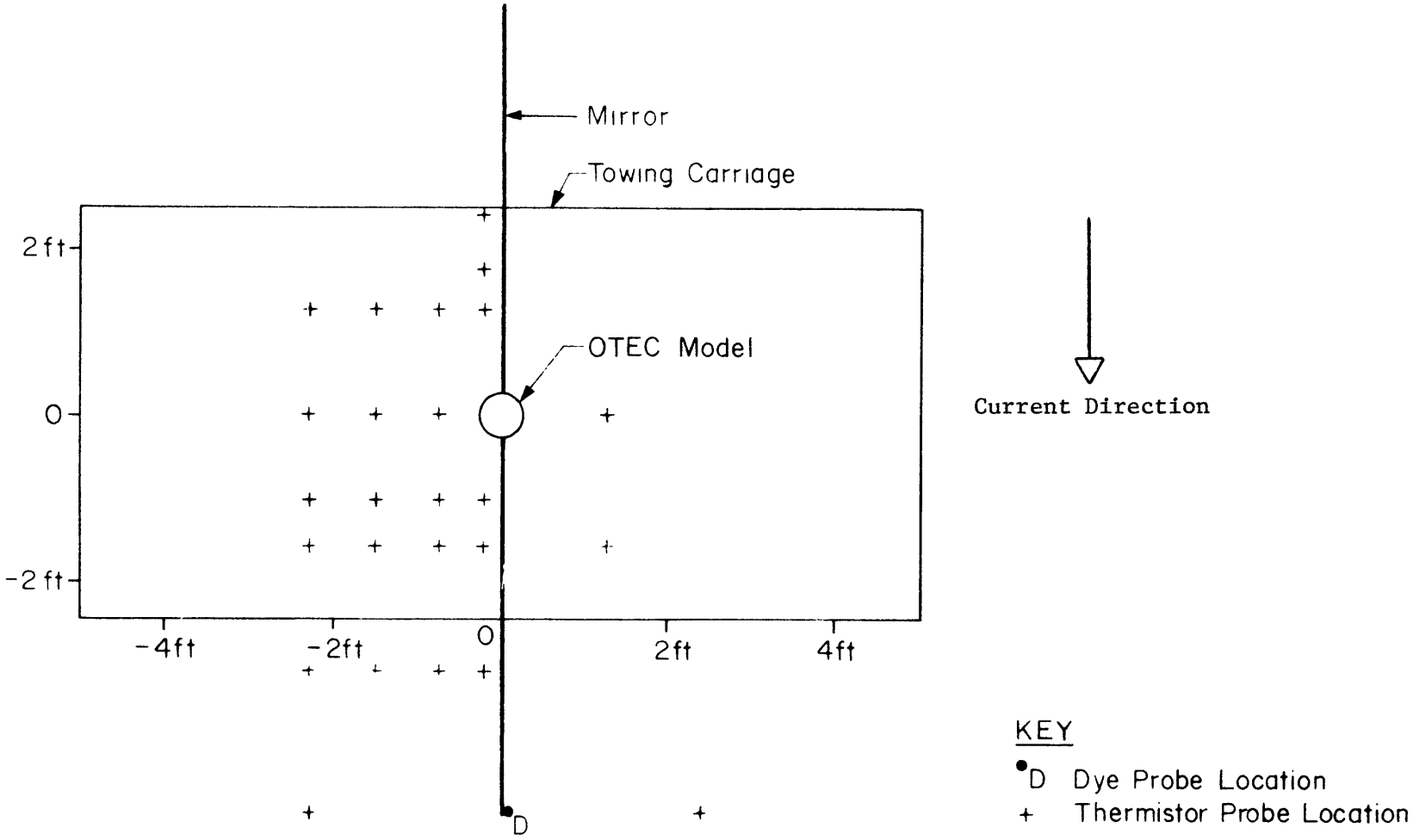

Figure 18: Field Probe Locations

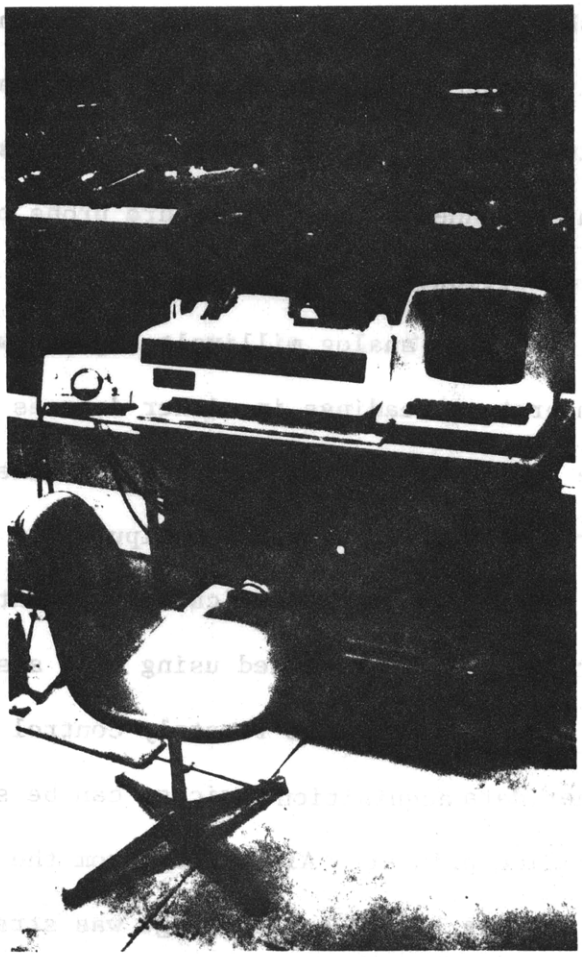

Figure 19: Data Acquisition System

E) Data scanner; ADDS Model 012130; scanning 100 channels of random access two pole reed relay switching.

F) Modem; RS232; 300 baud.

Figure 20 shows a flow chart for these components as integrated into a 300 channel per second thermal data acquisition system. Temperature information from the YSI 700 thermistors is scanned by the reed relay unit which connects the temperature probe output to a YSI thermivolt signal conditioner. The thermivolt signal conditioner is scaled to produce linear DC analog millivolt signals which are directly convertible to temperature readings in either degrees Celsius or Fahrenheit. These scaled analog voltages are digitized by a 12 bit converter and stored on disk for further manipulation and transfer to a larger computer system. During a typical experiment between 1800 and 2500 temperature readings were recorded using this system.

The switch panel, designed to remotely control the field probe elevations and other data acquisition devices, can be seen in Figure 19, to the left of the line printer. All wiring from the control box and computer terminal leading to the tow carriage was strapped to the intake and discharge hoses.

3.7 The Dye Measurement System

Fluorescent dye (Rhodamine B) measurements were used to complement temperature measurements in determining recirculation and far field dilution. Dye measurements are more useful than temperature measurements in determining the dilution of various constituents which may be released

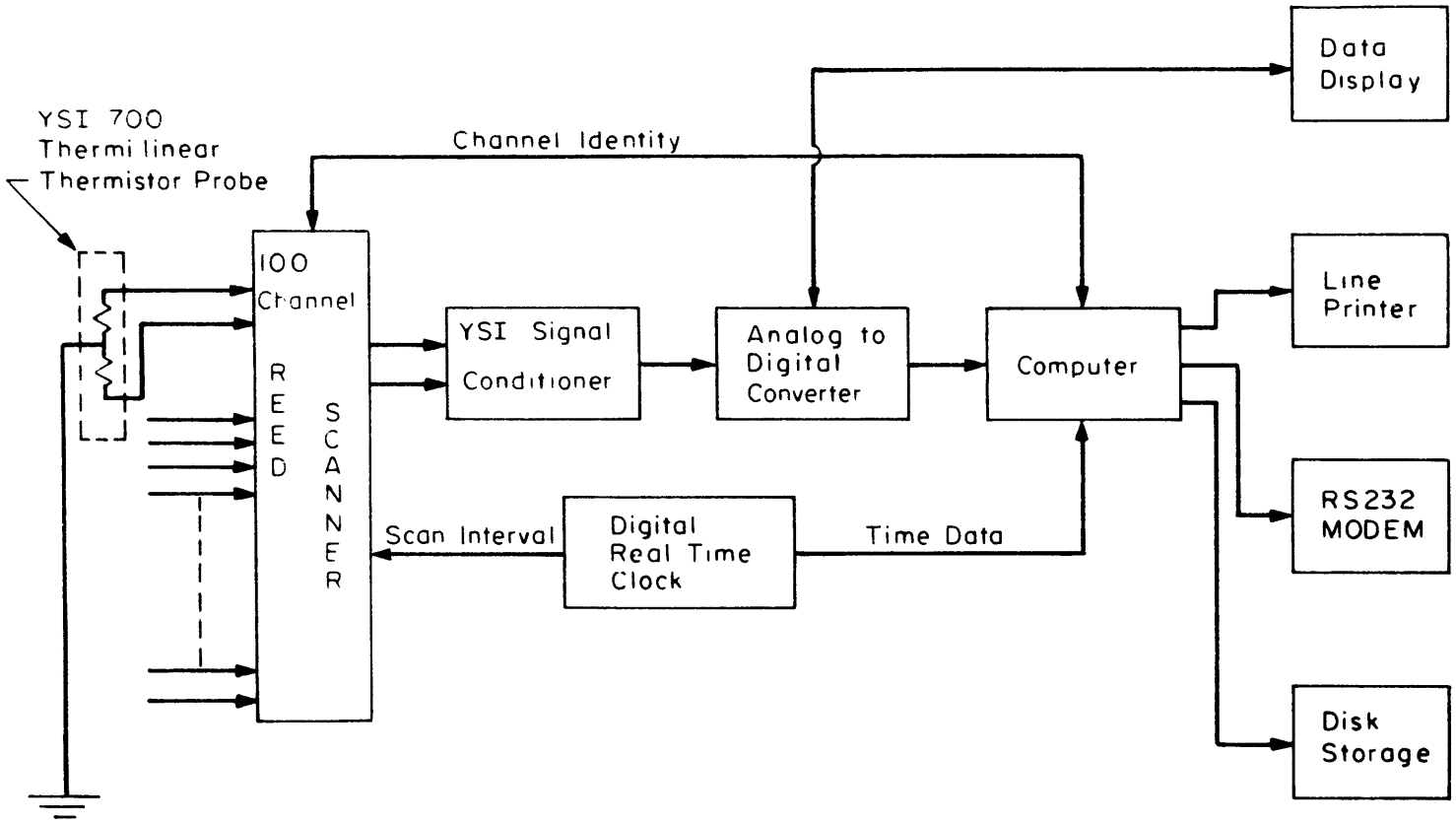

Figure 20: Flow Chart for the Temperature Data Acquisition System

with the discharge (e.g. products of corrosion, biocides, etc.) because the ambient concentration of these constituents, like the background dye concentration but unlike the ambient temperature, is nearly zero. Similarly, dye is useful for measuring direct recirculation of the discharge water into the intake. However, any overall decrease in the intake temperature must be assessed using temperature measurements since this may be due to disruption of the ambient profile (indirect recirculation) as well as direct recirculation. Finally, because the dye is used only as a tracer, the discharge concentration can be adjusted to any convenient level to allow more precise measurement than is possible with temperature.

Sample dye concentrations were measured with a Turner Model IV fluorometer allowing a threshold detection of 1 part per billion (ppb). Experiments could be run with discharge concentrations of as much as 50,000 ppb and basin background concentrations of less than 30 ppb. A dye concentration of 10 ppb above the background concentrations was distinguishable and it was estimated that measurement of direct recirculation down to 10 ppb/50,000 ppb = 0.0002 or 0.02% was possible.

Three types of dye samples were taken during an experiment using the homemade sampling apparatus shown schematically on stage no. 3 of the towing carriage in Figure 12b. A peristaltic pump delivered a continuous flow from four sample points at once to a bottle rack capable of holding 40 individual samples or ten sets of four samples each. Two sample probes attached to stage no. 2 of the towing carriage (see Figure 18) were located approximately 1.5 m (450 m in the prototype) behind the OTEC model to measure plume dilution. These probes were separated

by a vertical distance of about 15 cm so that dilution samples were taken with temperature scans as the probes traversed the water column. A third sample was taken from the intake flow line and the fourth sample was taken from the discharge flow line. These dye samples were used to measure direct recirculation of the discharge water into the intake.

The sample flows and bottle rack were controlled by the switch panel described in Section 3.6. Using this apparatus, ten sets of four samples could be taken at will during the course of an experiment.

3.8 The Photographs

Injection of the fluorescent dye into the flow stream also served to tag the discharge jet for photographic purposes. Both overhead photographs of the power plant wake and side view photographs of a cross sectional plane along the axis of the model were taken.

Figure 21 serves to illustrate the apparatus that was used to take the side view pictures. A 1000 watt spotlight equiped with a light shutter emits a horizontal slit of light above the water surface. A 300 cm long, 5 cm wide mirror attached to the towing carriage deflects the light slit downward to illuminate a vertical plane along the axis of the model, parallel to the direction of the current. This plane of light is approximately 50 cm long over the full depth of the water column. A water tight box, dubbed photo-sub, uses mirrors to reflect the field of vision of a 35 mm camera through a front glass window at the elevation of the submerged model. Thus, as the towing carriage moves past the photo station, pictures are taken of the 50 cm x 60 cm (longitudinal x vertical) planes illuminated by the spotlight. On

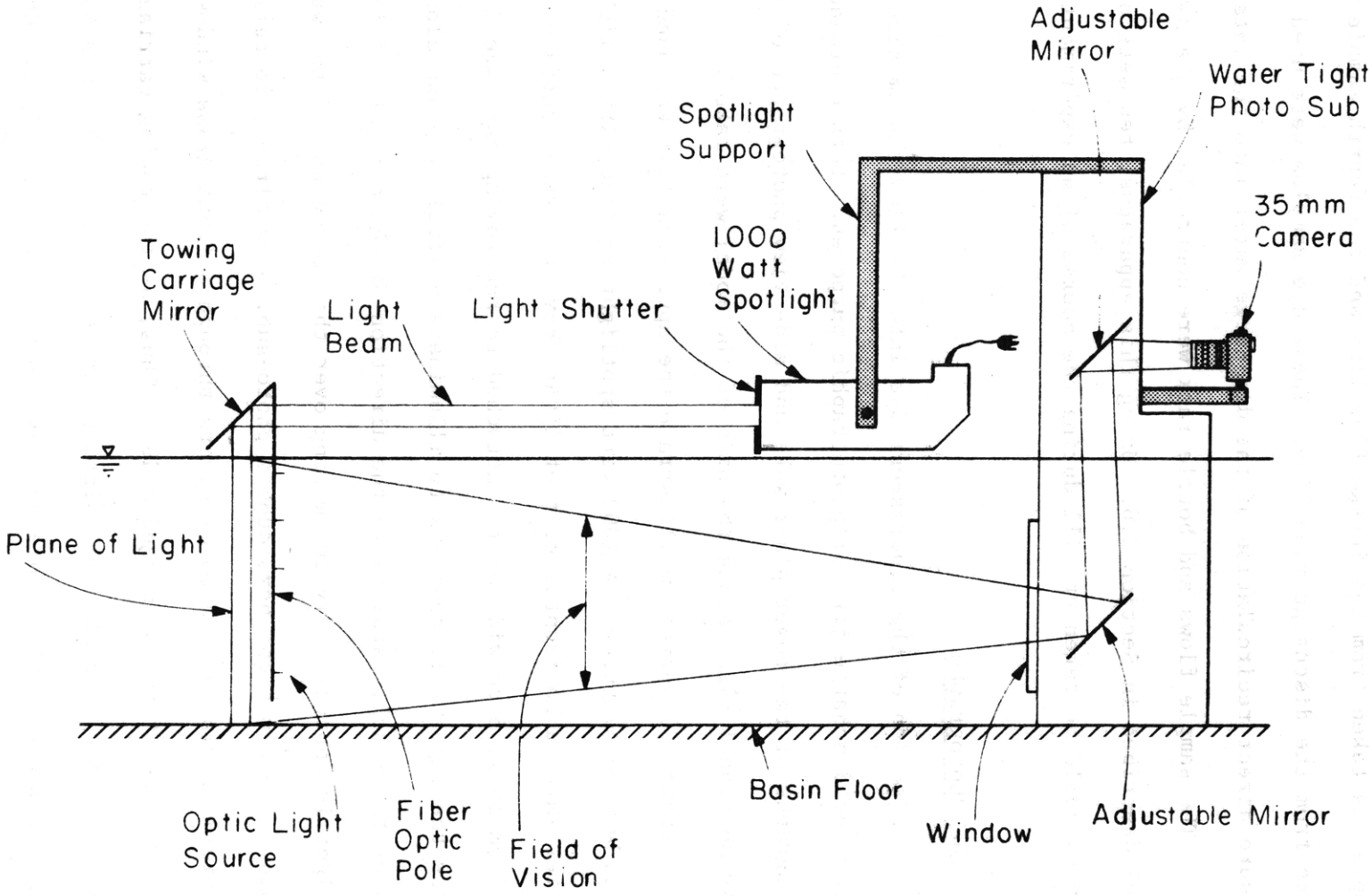

Figure 21: Cross Sectional Schematic of the Side View Photographic Apparatus

the average, ten such pictures were needed to capture the flow field perturbations extending up to 1.5 m (450 m prototype) to either side of the model. Figure 22 shows a cross section photographed as the model moved by the field of vision. Figure 23 is an overhead photograph of a photo-station.

Since the photographs were taken from a position perpendicular to the plane of interest, complications due to parallax error were avoided. However, water used to fill the basin had to be filtered (see Section 3.4) to improve clarity. In order to measure quantitatively the position and thickness of the spreading layer, eight marker poles containing fiber optic strands were mounted along the mirror attached to the towing carriage (see Figure 21). When illuminated with the light slit, these strands produced dots of light down the marker poles providing a reference grid. One marker pole is discernible in Figure 22, preceeding the model. The vertical dot spacing is 10 to 20 cm while the marker pole diameter is 0.3 cm.

Overhead pictures, used to record the effect of current speed on OTEC plants wakes, were taken from a second floor walkway using the overhead lighting in the laboratory for illumination. A grid of black crosses was painted on the basin floor for easy reference. Figure 13(a) is an overhead photograph taken during an experiment.

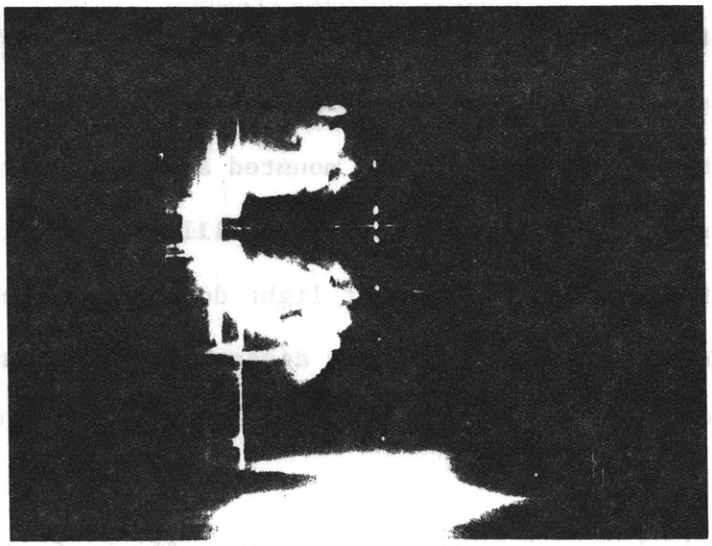

Figure 22: Photograph of a Typical Cross Section

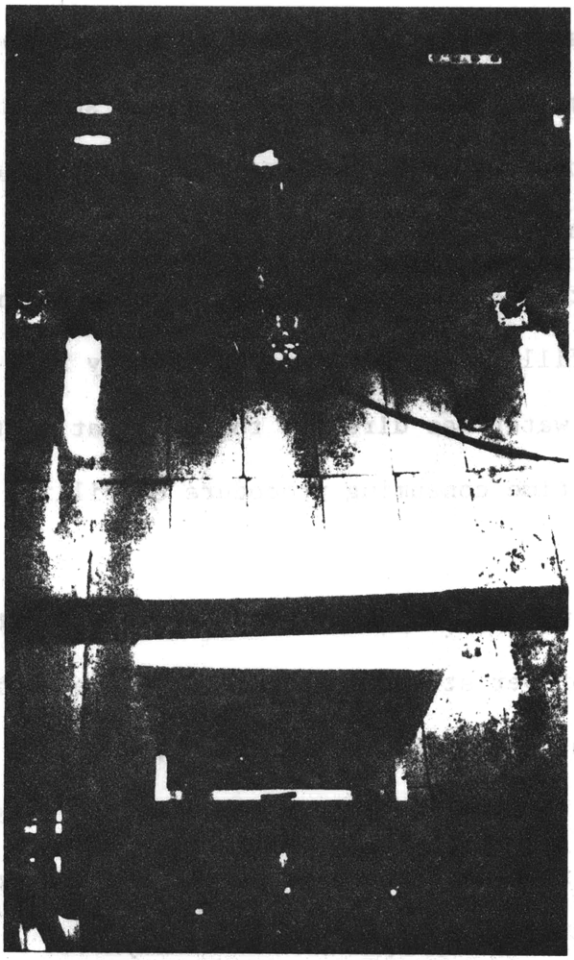

Figure 23: Overhead Photograph of a Photo-station Showing a Photo-sub (foreground) and a spotlight

IV. PROCEDURES

4.1 Procedures Prior to and During an Experiment

Standard procedures were developed for the stratified-current experiments to insure repeatability and to minimize operator error.

The experiments were scheduled to begin soon after dusk. The darkness of the room served to enhance the illumination of the dye for photographic purposes.

Stratification of the model basin usually began the night before an experiment by filling the basin approximately half way with cold water. Then, hot water was directed to the float in the center of the basin and the time consuming procedure of filling the basin with hot water began.

The following day, the fill temperature and water depth were monitored to insure proper stratification. Once the basin had been filled a computer program, DEMO (written in BASIC), was used to scan and print out the thermistor probe readings on the display terminal. This allowed for continuous monitoring of changes in the temperature profile and the density difference between upper and lower layers.

Just before the start of the experiment, the water for the discharge flow was turned on, injected with fluorescent dye, and run through a bypass to a drain. This allowed for fine adjustment and stabilization of the discharge temperature and dye concentration.

A computer program, SCANNER (written in BASIC), was used to scan and record the thermistor probe readings for each experiment. When the proper density difference, $\Delta\rho_a$, had been reached, SCANNER was used to

measure the ambient temperature profile and to obtain a probe calibration. Finally, the intake pump was used to suck all air from the intake and discharge circuits. The experiment began when the dyed discharge flow was routed through the model, the intake circuit was activated, and the varispeed towing motor was turned on and adjusted for the proper tow speed. Temperature scans began when the wake was judged to be in steady state.

Since one tow of the model across the basin disrupted the stratification significantly, an experiment usually investigated two different current speeds, in succession, over different portions of the basin, to maximize use of water and time. The first speed was designed to be slower than the second so as to minimize interference of the plant wakes and to insure that steady state operating conditions were established. Prototype current speeds greater than 0.75 m/sec were examined separately. Thus, each current speed investigated was given a run number, e.g., experiment no. 43 consists of runs 43a and 43b.

The procedure for taking the temperature measurements was basically the same for each current speed investigated. The scans usually began with the top probes near the surface. Upon completion of one level, the probe support frame (stage no. 2) was lowered to a new depth. Ten to fifteen seconds were allotted for the probes to reach equilibrium at the new depth before new scans were taken. SCANNER averaged three temperature readings to produce each temperature recorded for a scan. The number of scans taken during each run varied from 6-15, depending upon the current speed.

Five sets of four dye samples were taken during each run. These were taken simultaneously with the temperature scans to provide field

samples over the depth of the water column.

Overhead slide pictures of the wake and side view slide pictures of the discharge jet and flow field were taken during each run. Two photo stations were used when an experiment consisted of two runs (see Figure 7). With the laboratory lights out, side view slide pictures were taken, beginning when the dye front was visible and terminating when the last mirror section passed the light slit. Next, the laboratory lights were turned on and the overhead slide pictures of the plant wake were taken. If the experiment consisted of two runs, then the tow speed was changed and this procedure was repeated.

4.2 Data Reduction

Three types of data were collected from each experiment: 1) fluorescent dye samples, 2) slide photographs,* 3) thermistor temperature measurements. Each type of data has been reduced to a useable form for the 75 stratified current runs analyzed.

4.2.1 Fluorescent Dye Samples

Fluorescent dye samples taken from the intake line, discharge line and flow field were diluted as necessary for analysis with the fluorometer. Concentration measurements were evaluated using a calibration curve constructed just prior to the set of stratified current experiments. These measurements were used to determine direct recirculation (intake concentration/discharge concentration) and centerline dilution at 450 m (prototype) directly behind the power plant. The latter was defined as the discharge concentration divided by the maximum concentration of the field samples.

*During certain experiments motion pictures were also taken. These have been made into a movie but were not used for data analysis.

4.2.2 Slide Photographs

Approximately twelve side view and five overhead color slide photographs were taken for each run (tow speed) using the photographic apparatus described in Section 3.8. A photo-enlarger was used to trace the visible dye boundaries, as seen in the slide photographs, onto paper. The side view slides for each experiment were superimposed so that the complete set of photographs could be combined into one tracing. A reference grid, based on the fiber optic dot spacing and the surface and bottom boundary lines, was drawn over this tracing. Appendix I shows the complete set of side view tracings used for analysis. Appendix II shows tracings of the overhead pictures of the dye plume outline, grouped by discharge and stratification type, to show the effect of current speed on the plume shape. The reference grids for these drawings utilized the grid of black crosses on the basin floor which showed up in the photographs. Parallax corrections were applied using this grid in projecting the overhead pictures (see Figure 13a) to the plan views shown in Appendix II.

4.2.3 Temperature Data

4.2.3.1 Calibrations

The validity of results based on the temperature measurements (especially intake temperatures) can only be defended if the temperature data are considered accurate. The significance of small differences in temperature (<1.0°C), in terms of OTEC power production, requires that the thermistor probes be carefully calibrated to eliminate equipment errors.

Before the series of tests, each probe was calibrated at four different temperatures (10°C, 20°C, 30°C, 40°C) using a constant temperature bath (accuracy: 0.05°C). Each probe's measured temperature was adjusted based on a calibration constant found from linear interpolation between the four calibration points. Calibration checks were performed on all probes throughout the experimental series to adjust the four calibration points. These checks were performed at a single temperature and resulted in a uniform adjustment of each of the four calibration points. A uniform adjustment was justified on the basis of the demonstrated linearity of the probes.

Thermistor probe readings for the intake and discharge flow lines were checked after each experiment against a mercury thermometer (accuracy: 0.05°C) placed in the actual intake or discharge port. In this way a change in the calibration constants was used to account for the change in water temperature between the location of the probes (in the flow lines) and the actual intake or discharge point. This change could be as much as 0.5°C.

The sets of profile probes were checked periodically by comparing each probe reading with a thermometer as both were simultaneously exposed to a stream of water held at a constant temperature.

The field probes were checked for calibration during every experiment. Prior to the start of the experiment, the probe support frame (stage 2 of the towing carriage) was positioned so that the field probes were at a constant elevation near the surface. Since there were two probes at each horizontal location, this positioning took place twice. The difference between the mean probe temperature and the temperature of each individual probe defined the calibration adjustments for that

experiment. A typical experiment had about 10% of its probe calibrations adjusted by 0.1°C. Any probe requiring an adjustment of more than about 0.3°C was considered bad and was either replaced or repaired.

On the basis of the above procedures it is estimated that the calibrated accuracy of the intake, discharge and profile probes was about 0.1°C (reflecting the accuracy of the mercury thermometer and the repeatability of the individual probes). The calibrated accuracy of the field probes was estimated at 0.15°C because the calibration relied on the horizontal uniformity of the upper layer of the water column.

4.2.3.2 Temperature Data Manipulations

Each experimental temperature reading stored on the data aquisition system's disk storage unit was acutally an average of three temperatures that were scanned over a three second time interval. This was useful in averaging out turbulent temperature fluctuations. A computer program (TRANSFER written in BASIC) was used to transfer all of the experimental raw (not calibrated) data into MIT's Multics computer system (Honeywell 6180 computer) using the RS232 modem as an output terminal. Computer programs on the Multics system calibrated the data and produced two complete sets of results for each experiment: 1) temperatures in °C, 2) densities in gm/cm^3. A third data set compared measurements with a predicted horizontally uniform stratification based on profile probe measurements taken prior to the start of the experiment. By taking a series of these, small profile changes over time could be predicted by extrapolation. The value of this data set rests on the good

horizontal uniformity experienced during tests (see Figure 15).

A graphics program (PL1 language) was used to examine each of the data sets. Temperature or density maps for any plane in the basin could be created; the program could average the data spatially or in time. Generally three types of planes were examined; 1) horizontal plane views, 2) vertical plane views along the tow axis, and 3) vertical plane views perpendicular to the tow axis. This program was also used to print out temperature profiles, density profiles and time histories of the intake and discharge probe temperatures.

The three data sets corresponding to each experiment have been stored on magnetic tape, and are readily retrievable for further manipulation and analysis.

V. EXPERIMENTAL RESULTS AND ANALYSIS

5.1 Run Conditions

The experimental run conditions were designed to examine the external flow and temperature fields induced in a flowing-stratified ocean by a schematic OTEC plant characterized by the parameter ranges in Figure 4. Table 2 gives an overview of the experimental series which was conducted. Although a broad range of parameter variations was examined, these experiments were not meant to represent a comprehensive set of plant operating conditions. Rather, the experimental series was oriented towards investigating which ocean/plant operating conditions could adversely affect power production by inducing recirculation. To accomplish this, base case plant configurations for the evaporator discharge (exp. # 3A) and mixed discharge (exp. # 5A) concepts were established. Then the parameters selected for variation were changed, individually or in pairs, about the base case experiment. The stagnant-stratified tests [Adams et al., 1979] indicated little or no recirculation for the generic OTEC plant configurations examined. Thus, variations in current speed were felt to be of primary interest for a given plant configuration and mixed layer depth. Horizontal and vertical discharge angles were also varied within this context; however, the basin bottom was seen to limit the trajectory in four of these runs (26A, 26B, 27B, 28A). Finally, it should be noted that the nominal plant size is based on a flow rate of $Q_i = 5\ m^3/MWe\text{-}sec$.

The numerical values of the dimensional parameters resulting from the experimental schematizations (Table 2) are given in Table 3. Although it was not possible to obtain the same ocean profile on successive experiments, the mixed layer depths can be classified into three distinct groups:

TABLE 2: EXPERIMENTAL PARAMETER SCHEMATIZATION

Run #	Net Power (MW)[1]	Type of Discharge				Discharge Depth h_d	Discharge Angles[2]		Discharge Area A_o[3]	Mixed Layer Depth, H	Current[4] Speed, V (m/sec)
		Mix	Evap.	Radial	4-Jet[5]		α_H	α_V			
1A	400		X	X		M	-	0	BC	M	.15
1B	400		X	X		M	-	0	BC	M	.51
3A[6]	400		X	X		M	-	0	BC	M	.28
3B	400		X	X		M	-	0	BC	M	.40
4A	400	X		X		M	-	0	BC	M	.15
4B	400	X		X		M	-	0	BC	M	.51
5A[7]	400	X		X		M	-	0	BC	M	.28
5B	400	X		X		M	-	0	BC	M	.40
6A	600		X	X		M	-	0	BC	M	.28
6B	600		X	X		M	-	0	BC	M	.40
7A	400		X	X		M	-	0	BC	S	.28
7B	400		X	X		M	-	0	BC	S	.51
8A	600		X	X		M	-	0	BC	S	.28
8B	600		X	X		M	-	0	BC	S	.51
10	400		X	X		M	-	0	BC	S	1.00
11	600		X	X		M	-	0	BC	S	1.00
12	400		X	X		M	-	0	BC	S	1.00
13	600		X	X		M	-	0	BC	S	1.00
14	400		X	X		M	-	0	BC	M	.87
15A	200		X	X		M	-	0	1/2BC	M	.28

TABLE 2 (continued)

Run #	Net Power (MW)[1]	Type of Discharge				Discharge Depth h_d	Discharge Angles[2]		Discharge Area A_o[3]	Mixed Layer Depth, H	Current[4] Speed, V (m/sec)
		Mix	Evap	Radial	4-Jet[5]		α_H	α_V			
15B	200		X	X		M	-	0	1/2BC	M	.51
16	200		X	X		M	-	0	1/2BC	M	.87
17	200		X	X		M	-	0	1/2BC	M	1.00
18A	200	X		X		M	-	0	1/2BC	M	.28
18B	200	X		X		M	-	0	1/2BC	M	.51
19A	200		X	X		M	-	0	1/2BC	L	.28
19B	200		X	X		M	-	0	1/2BC	L	.51
20A	400		X	X		M	-	0	BC	L	.28
20B	400		X	X		M	-	0	BC	L	.51
22A	400		X	X		S	-	0	BC	M	.28
22B	400		X	X		S	-	0	BC	M	.51
23A	400	X		X		S	-	0	BC	M	.28
23B	400	X		X		S	-	0	BC	M	.51
24A	200	X		X		S	-	0	BC	M	.28
24B	200	X		X		S	-	0	BC	M	.51
25A	200		X	X		S	0	0	BC	M	.28
25B	200		X	X		S	0	0	BC	M	.51
26A	400		X		X	S	±45	45°↓	BC	M	.28
26B	400		X		X	S	±45	45°↓	BC	M	.51

TABLE 2 (continued)

Run #	Net Power (MW)[1]	Type of Discharge				Discharge Depth h_d	Discharge Angles		Discharge Area A_o [3]	Mixed Layer Depth, H	Current[4] Speed, V (m/sec)
		Mix	Evap.	Radial	4-Jet[5]		α_H	α_V			
27A	400		X		X	S	0	45°↓	BC	M	.28
27B	400		X		X	S	0	45°↓	BC	M	.51
28A	400		X		X	S	0	45°↓	BC	M	.51
28B	400		X		X	S	0	45°↓	BC	M	.87
29A	400		X		X	S	0	0	BC	M	.28
29B	400		X		X	S	0	0	BC	M	.51
30A	400		X		X	M	0	0	BC	M	.51
30B	400		X		X	M	0	0	BC	M	.87
31A	400		X		X	M	0	0	BC	M	.15
31B	400		X		X	M	0	0	BC	M	.87
32A	400		X		X	M	0	0	1/4BC	M	.28
32B	400		X		X	M	0	0	1/4BC	M	.51
33A	400		X		X	M	90°	0	1/4BC	M	.28
33B	400		X		X	M	90°	0	1/4BC	M	.51
34A	400		X		X	M	180°	0	1/4BC	M	.28
34B	400		X		X	M	180°	0	1/4BC	M	.51
35A	400		X	X		M	-	0	2BC	M	.28
35B	400		X	X		M	-	0	2BC	M	.51
36A	400		X	X		M	-	0	2BC	M	.28
36B	400		X	X		M	-	0	2BC	M	.51

TABLE 2 (continued)

Run #	Net Power (MW)[1]	Type of Discharge				Discharge Depth h_d	Discharge Angles[2]		Discharge Area A_o [3]	Mixed Layer Depth, H	Current[4] Speed, V (m/sec)
		Mix	Evap	Radial	4-Jet[5]		α_H	α_V			
37A	400		X	X		M	_	0	2BC	M	.15
37B	400		X	X		M	_	0	2BC	M	.87
38A	400	X		X		M	_	0	2BC	M	.28
38B	400	X		X		M	_	0	2BC	M	.51
39A	400		X	X		M	_	0	3BC	M	.28
39B	400		X	X		M	_	0	3BC	M	.51
40A	400		X	X		M	_	0	3BC	M	.15
40B	400		X	X		M	_	0	3BC	M	.87
41A	400		X	X		M	_	0	3BC	M	.51
41B	400		X	X		M	_	0	3BC	M	.87
42A	400	X		X		M	_	0	3BC	M	.28
42B	400	X		X		M	_	0	3BC	M	.51
43A	400		X		X	M	0	0	3BC	M	.28
43B	400		X		X	M	0	0	3BC	M	.51
44A	400		X		X	M	0	0	3BC	M	.15
44B	400		X		X	M	0	0	3BC	M	.87
45A	400	X			X	M	0	0	3BC	M	.28
45B	400	X			X	M	0	0	3BC	M	.51

Footnotes:

1 Based on $Q_i = 5M^3$/MW-sec

2 α_H = horizontal angle between current and upstream facing jet;
α_V^H = vertical angle with respect to the horizontal

L - large
M - medium
S - small

TABLE 2 (continued)

Footnotes (continued)

3 BC = Base Case area
4 Prototype values
5 Runs 32A to 34B simulate individual port discharges; Runs 26A and 26B simulate a 4-jet configuration with α_V = 45° and ports at α_H = 45°, 135°, 225° and 315°; all other 4-jet discharges have ports at α_V = 0° and α_H = 0°, 90°, 180°, 270°.
6 Base Case experiment for non-mixed discharge
7 Base Case experiment for mixed discharge

TABLE 3: EXPERIMENTAL PARAMETERS (Prototype dimensions except for R)

	PLANT										OCEAN				
Run #	Q_i (m^3/sec)	u_o (m/sec)	A_o (m^2)	h_i (m)	h_d (m)	h_o (m)	b_o (m)	T'_o (°C)	F^*_o	R (model)	H (m)	$\Delta\rho_a x10^4$ (g/cm^3)	V (m/s)	$T_{amb}(z=h_i)$ (°C)	$T(z=h_d)$ (°C)
1A	2000	3.5	71	9	76	1.98	-						.15		
1B	2000	3.5	71	9	76	1.98	-						.51		
3A	2000	3.5	71	8	75	1.98	-	28.0	21.0↑	6400	47	22.8	.28	30.4	26.7
3B	2000	3.5	71	8	75	1.98	-	28.0	21.0↑	6400	47	22.6	.40	30.1	26.7
4A	2000	7.0	71	9	76	1.98	-	24.3	24.1↓	11800	48	24.7	.15	32.6	28.1
4B	2000	7.0	71	9	76	1.98	-	24.3	24.1↓	11800	48	24.4	.51	32.5	28.1
5A	2000	7.0	71	11	78	1.98	-	24.9	23.2↓	12000	47	23.0	.28	32.5	29.0
5B	2000	7.0	71	11	78	1.98	-	24.9	23.2↓	12000	47	22.8	.40	32.4	29.0
6A	3000	5.3	71	9	76	1.98	-	30.7	26.4↑	10200	45	24.0	.28	33.0	29.1
6B	3000	5.3	71	9	76	1.98	-	30.7	26.0↑	10200	45	23.8	.51	32.8	29.1
7A	2000	3.5	71	9	75	1.98	-	30.7	19.8↑	6800	41	24.2	.28	33.2	29.4
7B	2000	3.5	71	9	75	1.98	-	30.8	19.4↑	6800	41	24.0	.51	33.0	29.4
8A	3000	5.3	71	9	76	1.98	-	31.1	27.8↑	10300	41	24.1	.28	33.8	29.7
8B	3000	5.3	71	9	76	1.98	-	31.1	27.8↑	10300	41	23.9	.51	33.5	29.7
10	2000	3.5	71	9	76	1.98	-	32.2	17.0↑	7000	36	24.4	1.0	34.2	30.5
11	3000	5.3	71	9	76	1.98	-	32.2	26.9↑	10500	35	24.9	1.0	35.0	31.6
12	2000	3.5	71	9	76	1.98	-	33.0	18.2↑	7100	35	24.9	1.0	35.3	31.5
13	3000	5.3	71	9	76	1.98	-	32.8	23.0↑	10600	31	23.4	1.0	34.6	30.8
14	2000	3.5	71	9	76	1.98	-	31.7	23.0↑	6900	50	19.1	.87	33.1	30.8

TABLE 3 (continued)

	PLANT										OCEAN				
Run #	Q_i (m^3/sec)	u_o (m/sec)	A_o (m^2)	h_i (m)	h_d (m)	h_o (m)	b_o (m)	T'_o (°C)	F_o^*	R (model)	H (m)	$\Delta\rho_a \times 10^4$ (g/cm^3)	V (m/s)	$T_{amb}(z=h_i)$ (°C)	$T_{amb}(z=h_d)$ (°C)
15A	1000	3.5	36	9	76	.99	-	30.3	25.0↑	3400	45	23.5	.28	32.6	29.1
15B	1000	3.5	36	9	76	.99	-	30.4	23.5↑	3400	45	23.2	.51	32.6	29.1
16	1000	3.5	36	9	76	.99	-	30.1	23.4↑	3400	48	24.0	.87	32.3	28.8
17	1000	3.5	36	9	75	.99	-	30.7	32.0↑	3400	51	24.9	1.0	33.3	30.0
18A	1000	7.0	36	9	76	.99	-	25.3	24.4↓	6000	50	24.9	.28	33.3	30.2
18B	1000	7.0	36	9	76	.99	-	25.4	24.9↓	6100	50	24.8	.51	33.2	30.2
19A	1000	3.5	36	9	76	.99	-	31.2	24.9↓	3400	64	24.5	.28	33.9	32.2
19B	1000	3.5	36	9	76	.99	-	31.2	24.9↓	3400	64	24.3	.51	33.9	32.2
20A	2000	3.5	71	9	76	1.98	-	30.6	47.3↓	6800	61	24.3	.28	32.9	30.8
20B	2000	3.5	71	9	76	1.98	-	30.6	48.8↓	6800	61	24.1	.51	32.9	30.8
22A	2000	3.5	71	10	38	1.98	-	25.9	17.4↓	6100	50	22.7	.28	27.8	27.7
22B	2000	3.5	71	10	38	1.98	-	25.8	17.5↓	6100	50	22.6	.51	27.7	27.6
23A	2000	7.0	71	9	37	1.98	-	17.3	16.5↓	10000	52	22.7	.28	27.0	27.0
23B	2000	7.0	71	9	37	1.98	-	17.2	16.5↓	9900	52	22.4	.51	26.9	26.9
24A	1000	3.5	71	9	38	1.98	-	12.5	8.1↓	4400	49	23.3	.28	24.5	24.5
24B	1000	3.5	71	9	38	1.98	-	12.5	8.2↓	4400	49	23.0	.51	24.5	24.4
25A	1000	1.8	71	8	37	1.98	-	22.0	8.1↓	2800	56	22.7	.28	24.4	24.4
25B	1000	1.8	71	8	37	1.98	-	22.1	8.3↓	2800	56	22.5	.51	24.3	24.3
26A	2000	3.9	64	9	53	5.99	10.74	23.1	25.2↓	9100	57	22.5	.28	24.8	24.4
26B	2000	3.9	64	9	53	5.99	10.74	23.1	25.2↓	9100	57	22.3	.51	24.7	24.4

TABLE 3 (continued)

	PLANT										OCEAN				
Run #	Q_i (m^3/sec)	u_o (m/sec)	A_o (m^2)	h_i (m)	h_d (m)	h_o (m)	b_o (m)	T'_o (°C)	F^*_o	R (model)	H (m)	$\Delta\rho_a x10^4$ (g/cm^3)	V (m/s)	$T_{amb}(z=h_i)$ (°C)	$T_{amb}(z=h_d)$ (°C)
27A	2000	3.9	64	9	52	5.99	10.74	22.0	146.3↓	8800	52	22.4	.28	23.3	22.0
27B	2000	3.9	64	9	52	5.99	10.74	22.1	253.4↑	8800	52	22.3	.51	23.1	22.0
28A	2000	3.9	64	9	53	5.99	10.74	21.9	21.9↓	8800	54	23.7	.51	24.5	23.6
28B	2000	3.9	64	9	53	5.99	10.74	21.9	22.0↓	8800	54	23.5	.87	24.4	23.6
29A	2000	3.9	64	8	74	5.99	10.74	22.0	30.7↑	8800	50	23.6	.28	24.5	21.1
29B	2000	3.9	64	8	74	5.99	10.74	22.0	30.9↑	8800	50	23.2	.51	24.5	21.1
30A	2000	3.9	64	8	74	5.99	10.74	21.8	32.6↑	8800	55	23.5	.51	24.3	20.9
30B	2000	3.9	64	8	74	5.99	10.74	21.8	32.4↑	8800	55	23.1	.87	24.3	20.9
31A	2000	3.9	64	8	74	5.99	10.74	21.8	24.3↑	8800	49	23.6	.15	24.4	20.3
31B	2000	3.9	64	8	74	5.99	10.74	21.8	24.4↑	8800	49	23.4	.87	24.2	20.3
32A	2000	3.9	64	8	74	5.99	10.74	22.0	32.1↑	8800	53	23.6	.28	24.5	21.2
32B	2000	3.9	64	8	74	5.99	10.74	22.1	30.3↑	8900	53	23.3	.51	24.4	21.2
33A	2000	3.9	64	9	75	5.99	10.74	23.4	19.7↑	9100	55	23.6	.28	24.5	21.3
33B	2000	3.9	64	9	75	5.99	10.74	23.7	18.6↑	9200	55	23.3	.51	24.5	21.3
34A	2000	3.9	64	9	75	5.99	10.74	22.2	28.2↑	8900	55	23.6	.28	24.5	21.1
34B	2000	3.9	64	9	75	5.99	10.74	22.3	26.9↑	8900	55	23.5	.51	24.5	21.1
35A	2000	2.1	120	10	78	3.33	-	22.0	11.9↑	5600	54	23.9	.28	24.6	20.7
35B	2000	2.1	120	10	78	3.33	-	22.0	11.8↑	5600	54	23.7	.51	24.5	20.7
36A	2000	2.1	120	9	77	3.33	-	22.7	10.2↑	5700	49	23.8	.28	25.3	21.0
36B	2000	2.1	120	9	77	3.33	-	22.7	10.2↑	5700	49	23.4	.51	25.2	21.0

TABLE 3 (continued)

	PLANT										OCEAN				
Run #	Q_i (m^3/sec)	u_o (m/sec)	A_o (m^2)	h_i (m)	h_d (m)	h_o (m)	b_o (m)	T'_o (°C)	F^*_o	R (model)	H (m)	$\Delta\rho_a x10^4$ (g/cm^3)	V (m/s)	$T_{amb}(z=h_i)$ (°C)	$T_{amb}(z=h_d)$ (°C)
37A	2000	2.1	120	9	77	3.33	-	23.0	9.4↑	5700	49	23.4	.15	25.3	20.9
37B	2000	2.1	120	9	77	3.33	-	23.0	9.3↑	5700	49	23.2	.75	25.3	20.9
38A	2000	4.2	120	9	77	3.33	-	14.3	11.3↓	9200	50	23.6	.28	25.4	21.3
38B	2000	4.2	120	9	77	3.33	-	14.3	11.3↓	9200	50	23.4	.51	25.4	21.3
39A	2000	1.6	159	9	77	4.43	-	22.7	9.0↑	5700	50	24.1	.28	25.9	21.7
39B	2000	1.6	159	9	77	4.43	-	22.8	8.8↑	5700	50	23.6	.51	25.9	21.7
40A	2000	1.6	159	9	77	4.43	-	23.9	6.2 ↑	5800	47	25.6	.15	26.9	21.7
40B	2000	1.6	159	9	77	4.43	-	23.9	5.2 ↑	5800	47	25.1	.75	26.8	21.7
41A	2000	1.6	159	9	77	4.43	-	24.3	8.6 ↑	5900	52	25.1	.51	27.4	21.4
41B	2000	1.6	159	9	77	4.43	-	24.3	8.6 ↑	5900	52	24.6	.75	27.4	21.4
42A	2000	3.1	159	10	78	4.43	-	16.8	8.2 ↓	9800	47	23.7	.28	27.0	23.6
42B	2000	3.1	159	10	78	4.43	-	16.8	8.2 ↓	9800	47	23.0	.51	26.9	23.6
43A	2000	1.9	132	9	75	12.19	10.86	23.4	14.0 ↑	5900	47	24.0	.28	26.8	22.7
43B	2000	1.9	132	9	75	12.19	10.86	23.4	14.0 ↑	5900	47	23.5	.51	26.7	22.7
44A	2000	1.9	132	9	76	12.19	10.86	24.9	9.2 ↑	6100	51	25.1	.15	27.5	23.4
44B	2000	1.9	132	9	76	12.19	10.86	24.9	9.1 ↑	6100	51	24.5	.75	27.4	23.4
45A	2000	3.8	132	9	76	12.19	10.86	17.1	9.4 ↓	10100	46	24.8	.28	27.7	23.8
45B	2000	3.8	132	9	76	12.19	10.86	17.1	9.4 ↓	10100	46	24.1	.51	27.7	23.8

~30 m, ~50 m, ~70 m (10, 16, 23 cm in the model). In all cases, a top to bottom density difference $\Delta\rho_a$ of approximately 2.2 x 10^{-3} g/cm^3 was achieved. It should be noted that $T'_{amb}(z=h_i)$ represents a vertical as well as horizontal average of the temperatures in the mixed layer. This was done to reduce the influence of water surface cooling over the length of an experiment.

The values of $\Delta\rho_a$ and T' indicated in Table 3 deserve further explanation. In the ocean, density is a function of temperature and salinity, $\rho = \rho[T,S]$. Jet behavior responds to differences in density rather than temperature. Thus, because ambient temperatures used in the experiments varied, experimentally measured temperatures (T) were cast in terms of density differences, using the density at a depth of 165 m (model depth of 55 cm) as a reference. Thus, in general

$$\Delta\rho' = \rho[T_{amb}(z=165m),\ S=0\,^{o}/_{oo}] - \rho[T, S=0\,^{o}/_{oo}]$$

For example, the top to bottom temperature difference ($\Delta\rho_a$) used to describe the ambient profiles is

$$\Delta\rho_a = \Delta\rho'(z=0) = \rho[T_{amb}(z=165m),\ S=0\,^{o}/_{oo}] - \rho[T_{amb}(z=0),\ S=0\,^{o}/_{oo}]$$

Furthermore, since one is more able to identify with ocean temperatures than with density differences, the values of $\Delta\rho'$ were converted to characteristic "tropical ocean" temperatures (denoted by primes) as well. A tropical ocean with uniform salinity of 35 $^{0}/_{00}$ and a temperature of 17°C at a depth of 165 m was assumed. Thus associated with every temperature T (and thus density difference $\Delta\rho'$) a value of T' was defined for which

$$\Delta\rho' = \rho[T'=17°C,\ S=35\,^{o}/_{oo}] - \rho[T',\ S=35\,^{o}/_{oo}]$$

5.2 Data Summary

Table 4 presents a summary of the results which can be expressed in parameter form. The measurement source for finding the parameter is denoted by a D, P, or T (dye, photographic, or temperature measurements) in the column heading. The parameters which are listed include:

h_{eq}: equilibrium depth of the wake centerline at x = -450 m (prototype) as seen in the side view photographic tracings.

t_{450}: thickness of the wake at x = -450 meters (prototype) as seen in the side view photographic tracings.

W_{450}: width of the wake at x = -450 m (prototype) as seen in the plan view photographic tracings.

X_s: distance to the stagnation point as seen in the plan view photographic tracings.

S_c: centerline dilution as determined from measurements of discharge and plume centerline dye concentrations at x=-450m (prototype).

S_{ave}: $\frac{W_{450} t_{450} V}{Q_o}$ as derived from photographic measurements of W_{450} and t_{450}.

λ: (direct) recirculation fraction - ratio of dye concentration measurements at the intake and discharge points.

$\Delta T_i'$: The difference between the evaporator intake temperature and the average of the temperatures in the mixed layer near the evaporator intake.

$= [T_i' - T_{amb}(z=h_i)]$

$\Delta\rho_o$: discharge density difference

$= [\rho_o - \rho_{amb}(z=h_d)]$

TABLE 4: EXPERIMENTAL RESULTS (Prototype dimensions)

Run #	Type of Disch.	Power MWe	Disch. Angles α_H	Disch. Angles α_V	V (m/s)	H(T) (m)	$\Delta\rho_o x10^4$ (T) (g/cm^3)	$Nx10^2$ (T) (s^{-1})	h_d (m)	h_{eq}(P) (m)	t_{450} (P) (m)	W_{450}(P) (m)	X_s(P) (m)	S_c(D)	S_{ave}(P)	λ(D)	$\Delta T_i'$(T) (°C)
1A	R-E	400	-	0	.15	-	-	-	76.1	66.1	33	1665	540	-	4.2	.002	-
1B	R-E	400	-	0	.51	-	-	-	76.1	-	127	-	105	-	-	.073	-
3A	R-E	400	-	0	.28	47.4	+3.40	1.57	74.5	65.9	44	1148	270	5.7	6.9	.006	-0.17
3B	R-E	400	-	0	.40	47.4	+3.40	1.57	74.5	74.5	55	750	160	5.1	8.2	.063	-0.55
4A	R-M	400	-	0	.15	48.0	-10.31	1.51	76.1	74.9	45	4125	1275	8.7	7.1	.005	-0.40
4B	R-M	400	-	0	.51	48.0	-10.31	1.51	76.1	71.2	70	870	180	4.9	7.8	.004	-0.46
5A	R-M	400	-	0	.28	47.4	-11.14	1.54	77.9	85.2	65	1770	335	6.2	7.9	.006	-0.55
5B	R-M	400	-	0	.40	47.4	-11.14	1.54	77.9	80.9	80	975	240	7.1	7.7	.002	-0.50
6A	R-E	600	-	0	.28	45.3	+4.82	1.60	75.6	69.2	60	1800	540	6.8	9.9	.008	-0.07
6B	R-E	600	-	0	.51	45.3	+4.97	1.60	75.6	57.8	83	680	165	6.9	9.7	.10	-0.86
7A	R-E	400	-	0	.28	41.4	+3.80	1.24	75.4	62.5	46	833	228	5.7	5.3	.002	-0.05
7B	R-E	400	-	0	.51	41.4	+3.95	1.24	75.4	66.2	67	581	120	5.0	10.0	.07	-0.55
8A	R-E	600	-	0	.28	41.4	+4.36	1.24	75.6	71.3	62	420	1215	6.1	6.9	.063	-0.15
8B	R-E	600	-	0	.51	41.1	+4.36	1.24	75.6	58.0	79	773	150	5.2	10.4	.079	0.00
10	R-E	400	-	0	1.00	36.0	+5.20	1.36	75.8	55.7	71	473	65	7.2	16.8	.007	-0.28
11	R-E	600	-	0	1.00	35.4	+2.20	1.40	75.8	49.2	77	630	92	7.0	16.2	.028	-0.53
12	R-E	400	-	0	1.00	34.5	+4.53	1.28	75.7	57.9	59	473	65	9.4	14.0	.008	-0.43
13	R-E	600	-	0	1.00	30.6	+6.38	1.08	75.7	47.0	85	548	94	9.7	15.5	.019	-0.60
14	R-E	400	-	0	.87	50.4	+1.89	1.32	75.8	54.4	85	585	90	7.5	21.7	.020	-0.44

TABLE 4 (continued)

Run #	Type of Disch.	Power MWe	Disch. Angles α_H	Disch. Angles α_V	V (m/s)	H(T) (m)	$\Delta\rho_o x10^4$ (T) (g/cm^3)	$Nx10^2$ (T) (s^{-1})	h_d (m)	h_{eq}(P) (m)	t_{450} (P) (m)	W_{450}(P) (m)	X_s(P) (m)	S_c(D)	S_{ave}(P)	λ(D)	$\Delta T_i'$(T) (°C)
15A	R-E	200	-	0	.28	45.3	+3.38	1.51	75.8	63.5	39	1088	260	7.9	11.7	.002	-0.42
15B	R-E	200	-	0	.51	45.3	+3.84	1.51	75.8	64.6	36	615	100	6.9	11.4	.004	-0.32
16	R-E	200	-	0	.87	48.0	+3.86	1.49	75.8	63.9	51	450	75	6.4	20.0	.010	-0.37
17	R-E	200	-	0	1.00	50.7	+2.06	1.54	75.4	68.6	48	345	55	9.9	16.6	.002	-0.25
18A	R-M	200	-	0	.28	50.1	-14.15	1.60	75.5	92.4	62	1500	470	37.4	12.8	.001	-0.80
18B	R-M	200	-	0	.51	50.1	-13.64	1.60	75.5	81.5	73	653	150	46.5	12.2	.001	-0.40
19A	R-E	200	-	0	.28	63.6	-3.42	1.77	75.8	92.1	51	1613	415	12.8	22.6	.003	-0.39
19B	R-E	200	-	0	.51	63.6	-3.42	1.77	75.8	83.9	52	1170	220	13.7	31.2	.017	-0.45
20A	R-E	400	-	0	.28	60.6	-.67	1.69	75.7	86.7	56	1575	390	5.7	12.1	.001	-0.34
20B	R-E	400	-	0	.51	60.6	-.63	1.69	75.7	84.0	51	870	180	7.4	11.4	.001	-0.18
22A	R-E	400	-	0	.28	50.1	-4.92	0.99	38.0	38.0	82	780	107	9.6	8.8	.25	-0.95
22B	R-E	400	-	0	.51	50.1	-4.91	0.99	38.0	38.0	77	458	105	6.9	9.0	.25	-0.80
23A	R-M	400	-	0	.28	51.5	-22.06	1.10	37.4	74.5	62	1310	288	5.9	5.6	.38	-4.84
23B	R-M	400	-	0	.51	51.5	-21.96	1.10	37.4	69.5	108	758	142	6.7	10.5	.25	-3.74
24A	R-M	200	-	0	.28	49.3	-22.85	1.20	37.5	86.8	74	1283	350	7.5	13.1	.001	-0.04
24B	R-M	200	-	0	.51	49.3	-22.40	1.20	37.5	67.7	68	765	155	7.3	13.3	.011	-0.87
25A	R-E	200	0	0	.28	55.7	-5.69	1.10	36.5	32.1	62	750	100	6.9	12.8	.24	-1.01
25B	R-E	200	0	0	.51	55.7	-5.46	1.10	36.5	31.9	68	469	50	7.6	16.4	.25	-0.79
26A	4-E	400	±45°	±45° ↓	.28	57.2	-3.03	1.28	52.5	-	100	1283	74	7.5	17.6	.001	-0.02

TABLE 4 (continued)

Run #	Type of Disch.	Power MWe	Disch. Angles α_H	Disch. Angles α_V	V (m/s)	H(T) (m)	$\Delta\rho_o x10^4$ (T) (g/cm^3)	$Nx10^2$ (T) (s^{-1})	h_d (m)	h_{eq}(P) (m)	t_{450} (P) (m)	W_{450}(P) (m)	X_s(P) (m)	S_c(D)	S_{ave}(P)	λ(D)	$\Delta T_i'$(T) (°C)
26B	4-E	400	±45°	↕45°	.51	57.2	-3.03	1.28	52.5	-	109	645	40	7.9	18.0	.001	-0.01
27A	4-E	400	0	↕45°	.28	52.4	-0.09	1.21	52.2	-	80	1013	372	6.3	11.1	.006	-0.07
27B	4-E	400	0	↕45°	.51	52.4	+0.03	1.21	52.2	-	81	623	218	7.1	12.9	-	-0.02
28A	4-E	400	0	↕45°	.51	53.6	-4.00	1.17	52.5	-	76	743	232	11.7	14.5	.003	-0.04
28B	4-E	400	0	↕45°	.87	53.6	-3.98	1.17	52.5	-	91	413	124	7.5	16.4	.001	-0.03
29A	4-E	400	0	0	.28	50.3	+2.05	1.62	74.4	61.5	68	1073	545	5.6	10.0	.013	-0.28
29B	4-E	400	0	0	.51	50.3	+2.02	1.62	74.4	62.8	69	885	400	5.4	15.7	-	-0.35
30A	4-E	400	0	0	.51	54.5	+1.81	1.63	74.4	72.9	77	870	315	6.6	17.2	.036	-0.60
30B	4-E	400	0	0	.87	54.5	+1.83	1.63	74.4	66.3	75	585	277	7.5	19.1	-	-0.64
31A	4-E	400	0	0	.15	49.1	+3.26	1.57	74.4	62.4	60	1350	890	5.7	6.2	.008	-0.05
31B	4-E	400	0	0	.87	49.1	+3.23	1.57	74.4	66.3	77	623	267	5.7	20.8	.018	-0.16
32A	1-E	400	0	0	.28	53.3	+1.87	1.53	73.5	73.5	22	1028	792	78.6	12.4	.002	-0.06
32B	1-E	400	0	0	.51	53.3	+2.10	1.53	73.5	69.2	69	530	810	11.7	57.3	.017	-0.36
33A	1-E	400	90	0	.28	54.8	+4.95	1.71	74.7	-	-	638	-	551.6	-	.004	-0.07
33B	1-E	400	90	0	.51	54.8	+5.58	1.71	74.7	-	-	405	-	105.6	-	.0004	-0.12
34A	1-E	400	180	0	.28	55.1	+2.42	1.71	74.7	70.4	62	248	-	10.5	8.5	.002	-0.15
34B	1-E	400	180	0	.51	55.1	+2.65	1.71	74.7	74.7	56	195	-	6.6	11.7	.001	-0.14
35A	R-E	400	-	0	.28	53.8	+2.86	1.67	77.9	76.9	43	-	185	4.1	-	.019	-0.25
35B	R-E	400	-	0	.51	53.8	+2.93	1.67	77.9	65.0	58	-	80	4.9	-	.091	-0.52

TABLE 4 (continued)

Run #	Type of Disch	Power MWe	Disch. Angles α_H	Disch. Angles α_V	V (m/s)	H(T) (m)	$\Delta\rho_o x10^4$ (T) (g/cm^3)	$Nx10^2$ (T) (s^{-1})	h_d (m)	h_{eq}(P) (m)	t_{450} (P) (m)	W_{450}(P) (m)	X_s(P) (m)	S_c(D)	S_{ave}(P)	λ(D)	$\Delta T_i'$(T) (°C)
36A	R-E	400	-	0	.28	49.0	+3.90	1.69	77.2	72.9	48	1200	179	4.4	7.9	.027	-0.42
36B	R-E	400	-	0	.51	49.0	+3.90	1.69	77.2	51.5	91	660	80	3.5	15.4	.089	-0.67
37A	R-E	400	-	0	.15	49.0	+4.62	1.67	76.9	72.6	43	2025	385	5.2	6.7	.002	-0.11
37B	R-E	400	-	0	.87	49.0	+4.66	1.67	76.9	52.9	78	503	74	5.0	14.7	.020	-0.23
38A	R-M	400	-	0	.28	50.3	-12.76	1.72	77.3	94.0	65	1740	330	8.9	7.8	.002	-0.10
38B	R-M	400	-	0	.51	50.3	-12.75	1.72	77.3	112.4	99	713	152	5.7	9.1	.003	-0.18
39A	R-E	400	-	0	.28	50.4	+2.45	1.39	77.1	72.8	45	1080	165	4.6	6.7	.046	-0.55
39B	R-E	400	-	0	.51	50.4	+2.57	1.39	77.1	68.3	51	638	76	3.3	8.3	.068	-0.68
40A	R-E	400	-	0	.15	47.0	+5.19	1.72	77.3	63.8	42	1560	421	2.6	5.0	.006	-0.30
40B	R-E	400	-	0	.87	47.0	+5.19	1.72	77.3	66.2	63	495	64	-	11.7	-	-0.59
41A	R-E	400	-	0	.51	51.8	+6.74	1.67	77.1	64.6	61	615	116	4.1	9.6	.088	-0.86
41B	R-E	400	-	0	.87	51.8	+6.77	1.67	77.1	63.3	71	480	60	4.1	12.8	.054	-0.50
42A	R-M	400	-	0	.28	47.0	-11.84	1.62	78.0	-	-	1238	382	3.4	-	.002	-0.30
42B	R-M	400	-	0	.51	47.0	-11.77	1.62	78.0	57.4	82	671	123	3.7	7.1	.002	-0.33
43A	4-E	400	0	0	.28	47.2	+1.61	1.67	75.2	70.9	48	975	464	4.3	6.4	.046	-0.51
43B	4-E	400	0	0	.51	47.2	+1.61	1.67	75.2	68.8	63	578	303	6.3	9.3	.041	-0.58
44A	4-E	400	0	0	.15	50.9	+3.71	1.67	75.8	63.8	55	1290	990	3.9	5.4	.051	-0.56
44B	4-E	400	0	0	.87	50.9	+3.78	1.67	75.8	62.9	69	465	118	3.7	12.0	.119	-0.01
45A	4-M	400	0	0	.28	45.5	-14.23	1.69	75.9	87.9	73	1305	945	3.8	6.5	.004	-0.40
45B	4-M	400	0	0	.51	45.5	-14.25	1.69	75.9	83.6	87	1058	473	3.8	11.8	.002	-0.31

TABLE 4 (continued)

bbreviations used in table:

R-E	Radial, Evaporator Discharge
R-M	Radial, Mixed Discharge
4-E	4 Separate Jets, Evaporator Discharge
4-M	4 Separate Jets, Mixed Discharge
1-E	1 Separate Jet, Evaporator Discharge
(T)	derived from Temperature data
(P)	derived from Photographic data
(D)	derived from Dye data

where ρ_o is the density of the discharge flow.

N: Brunt-Väisälä frequency

$$= \sqrt{\frac{g}{\rho_o} \frac{\partial \rho}{\partial z}}$$

where $g = 9.8\ m/s^2$ and $\partial\rho/\partial z$ is estimated from the density profiles at $z = h_d$ (See Appendix III).

In addition to the tabulated data discussed above, three appendices are included. Appendix I contains tracings of the discharge plume taken from the side view photographs with a 30 m x 30 m (prototype dimensions) grid labeling. In each side view tracing, the current is moving from right to left relative to the model.

Appendix II contains tracings of the wake plan views as taken from the overhead photographs. The grid labeling refers to prototype dimensions.

Appendix III contains the spatially averaged ambient density profiles for all of the experiments as derived from the temperature data. The locations of the intake and discharge ports are denoted by arrows labeled "I" and "D" respectively. The grid labeling refers to prototype dimensions.

5.3 Discussion of Results as Related to OTEC Plant and Site Parameters

The major thrust of this experimental study has been to investigate the sensitivity of recirculation and near field plume dynamics to variations in OTEC plant design and ambient ocean conditions. This sensitivity is presented below. An attempt is made in the following section to further interpret some of the results based on dimensional analysis.

5.3.1 OTEC Plant Recirculation as Influenced by OTEC Plant and Site Parameters

The influence of individual design parameters is most easily described in terms of the experimental data and the observed flow field interactions. Since all of the experimental results exist as either figures in the appendices or numerical data in Table 4, no attempt has been made to present and analyze all of the comparisons which can be made among experiments. Rather, in Figures 24 through 28, a subset of the experiments has been chosen to demonstrate the influence of various design parameters on direct recirculation λ (measured concentration of dye in the intake flow relative to the discharge dye concentration) and intake temperature depression $\Delta T_i'$ as a function of current speed. All of the experiments described herein utilized an annular intake structure, located near the surface as described in Section 3.2. It should be noted that because of experimental variability, curves drawn through the data points must be viewed as a means of highlighting the data points rather as than as definitive functions.

Figure 24 illustrates the dependence of recirculation over a range of current speeds on power plant size. Each plant is characterized as having radial evaporator discharge ports located at a medium discharge depth, operating in an ambient ocean characterized by a medium mixed layer depth and current speeds ranging from 0.0 m/s to 1.0 m/s (note: 0.0 m/s results were taken from the stagnant water tests [Adams, et al., 1979]). Both Figures 24a and 24b support the conclusion that peak direct and indirect recirculation increases with the size of the plant.

Figure 24a: Influence of Power Plant Size on Direct Recirculation Over a Range of Current Speeds

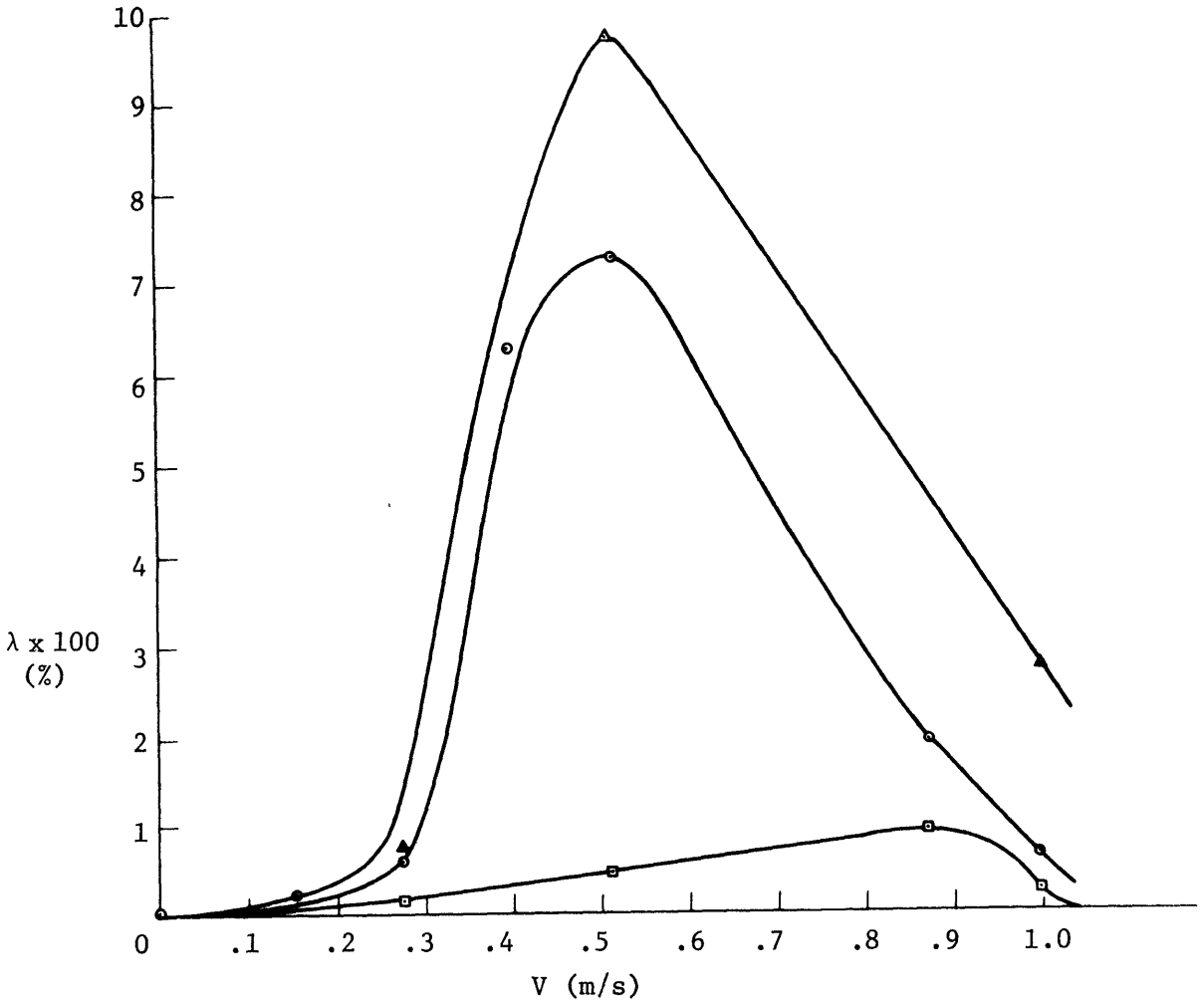

⊙ 400 MWe plant; evaporator discharge; medium mixed layer depth medium discharge depth; radial port

△ 600 MWe plant; evaporator discharge; medium mixed layer depth medium discharge depth; radial port

⊡ 200 MWe plant; evaporator discharge; medium mixed layer depth medium discharge depth; radial port

Figure 24b: Influence of Power Plant Size on Intake Temperature Depression over a Range of Current Speeds

⊙ 400 MWe plant; evaporator discharge; medium mixed layer depth; medium discharge depth; radial

△ 600 MWe plant; evaporator discharge; medium mixed layer depth; medium discharge depth; radial port

⊡ 200 MWe plant; evaporator discharge; medium mixed layer depth; medium discharge depth; radial port

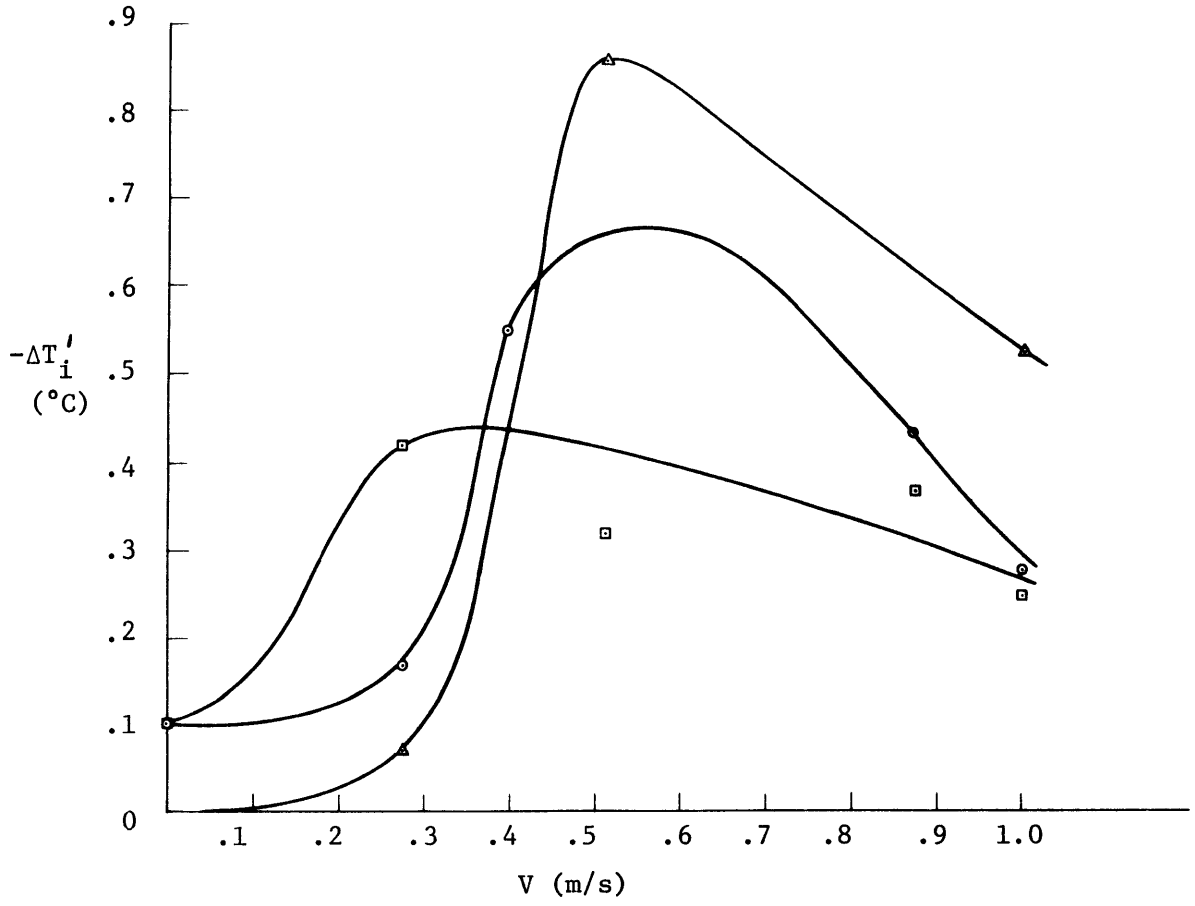

Peak direct recirculation varies from about 1% to about 10% as plant size ranges from 200 MWe to 600 MWe while peak intake temperature depression ranges from about .4 to .9 ^{o}C. In both cases the peak occurs at an ambient current speed of about 0.5 m/s. The maximum temperature depression of 0.9^{o}C can be assumed to result in about a 10% loss in net generating capacity (Allender, et. al., 1978).

The peaks in the $\lambda(V)$ and $\Delta T_i'(V)$ plots of Figure 24 are similar to those observed in other tests of this series in which the plant discharges a positively buoyant jet into the thermocline beneath the surface mixed layer. Similar peaks were also observed in experiments conducted at Hydronautics (Sundaram et. al., 1977, 1978) although a more complete comparison between the Hydronautics and the MIT tests is not possible due to the differences in experimental set-ups and parameter ranges. The mechanism for recirculation in these cases appears to involve an interplay between plume buoyancy and ambient current drag - hence it is designated as current-induced recirculation. This is distinguished from the other type of recirculation - designated as confinement-induced - which was occasionally observed under condition of shallow discharge into the mixed layer, and which involved an interplay between plume (negative) buoyancy and confinement due to the free surface.

For a positively buoyant discharge beneath the mixed layer, the jet entrains relatively cool ambient water (a source of indirect recirculation). The positive buoyancy causes the discharge jet to rise seeking a neutrally buoyant position in the thermocline. (The equilibrium plume positions will always be beneath the mixed layer because both the discharge and the entrainment temperatures are colder than the temperature of the mixed layer.) For low current speeds (.1 to .3 m/s for these configurations) the

stability of the density stratification tends to inhibit vertical perturbations (such as billowing), causing the jet to collapse and spread laterally without significant recirculation (see tracings in Appendix I). Intermediate current speeds (.4 to .6 m/s) push the already rising jet upwards diluting the jet through billowing action and causing recirculation of the diluted jet discharge; the inhibiting effects of the density stratification are not sufficient to offset the force of these perturbations. This process is unsteady as is confirmed by side view observations which indicate intermittent billowing of the plume and by raw intake dye concentration measurements which often showed considerable temporal variability before they were averaged to the reported values. At high current speeds (greater than .8 m/s for these configurations) the momentum of the current sweeps the plume backwards before it has a chance to rise or billow significantly. Combined with the greater availability of ambient water, this leads to a substantial reduction in direct recirculation and a somewhat smaller reduction in intake temperature depression.

Figure 25 illustrates two generic discharge configurations -- mixed versus non-mixed discharges -- and variations in (radial) port discharge area for 400 MWe plants discharging at a medium discharge height into a flowing-stratified ocean with a medium mixed layer depth. The non-mixed (evaporator flow only) discharges are positively buoyant relative to the ambient fluid; the mixed (evaporator and condenser flows mixed in the plant) discharges are negatively buoyant. Thus the non-mixed discharges tend to be lifted (and billowed) up into the mixed layer by the current while the negatively buoyant jets tend to sink and are swept down by the current. As a result, the mixed discharge designs for these cases show

very little direct recirculation. However, the intake temperature depressions for the mixed discharge designs are significant - of the order of 50% of those associated with the non-mixed designs. The relatively high intake temperature depressions for the mixed discharges can be attributed to two factors. First, any mixed discharge water that is directly recirculated back into the intake is much cooler than the comparable non-mixed jet. Second, the mixed discharges have twice the flow of the non-mixed configuration; thus they perturb and entrain a larger volume of water resulting in a lower temperature of any water indirectly recirculated to the intake.

Comparison of other run pairs in Table 4 reveals similar results: whereas the mixed discharge designs generally show little direct recirculation, they exhibit comparable, though usually smaller, intake temperature depression compared with non-mixed discharge designs. Yet, it should be noted that in one set of runs (22A, 22B, 23A, 24B involving a shallow discharge into the surface mixed layer) substantial direct recirculation ($.25 < \lambda < .40$) was observed for both mixed and non-mixed discharged. As discussed in Section 5.4 the mechanism for this recirculation appears to be more associated with the confinement due to the free surface than with billowing associated with the current. At any rate, substantial intake temperature reduction were observed in the two tests with a mixed discharge (~4-5^{o}C vs. ~1^{o}C for the non-mixed discharge). It is thus concluded that mixed discharges should be avoided in situations where significant direct recirculation is possible. In the absence of direct recirculation, use of a mixed discharge may result in smaller evaporater intake temperature depressions than would occur with a non-mixed discharge at the same elevation. However, temperature depressions may still occur due to various indirect effects.

Figure 25a: A Comparison Between Mixed and Evaporator Radial Discharges Over a Range of Discharge Areas as they Affect Direct Recirculation

400 MWe plant; medium mixed layer depth; medium discharge depth; radial ports

non-mixed ——— mixed – – – –

⊙ base case area
△ 2x base case area
⊡ 3x base case area

● base case area
X 2x base case area
✳ 3x base case area

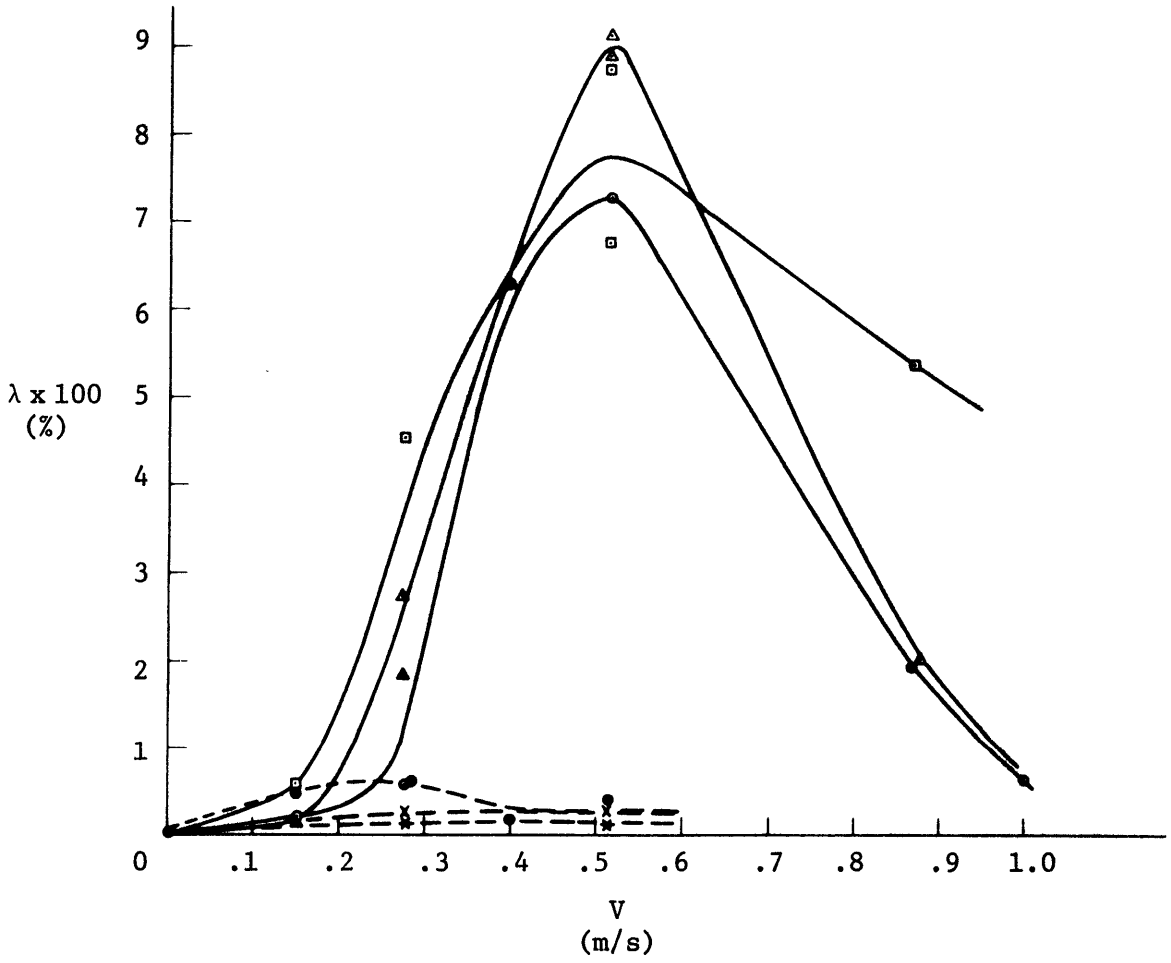

Figure 25b: A Comparison Between Mixed and Evaporator Radial Discharges Over a Range of Discharge Areas as they Affect Intake Temperature Depression

400 MWe plant; medium mixed layer depth; medium discharge depth; radial ports

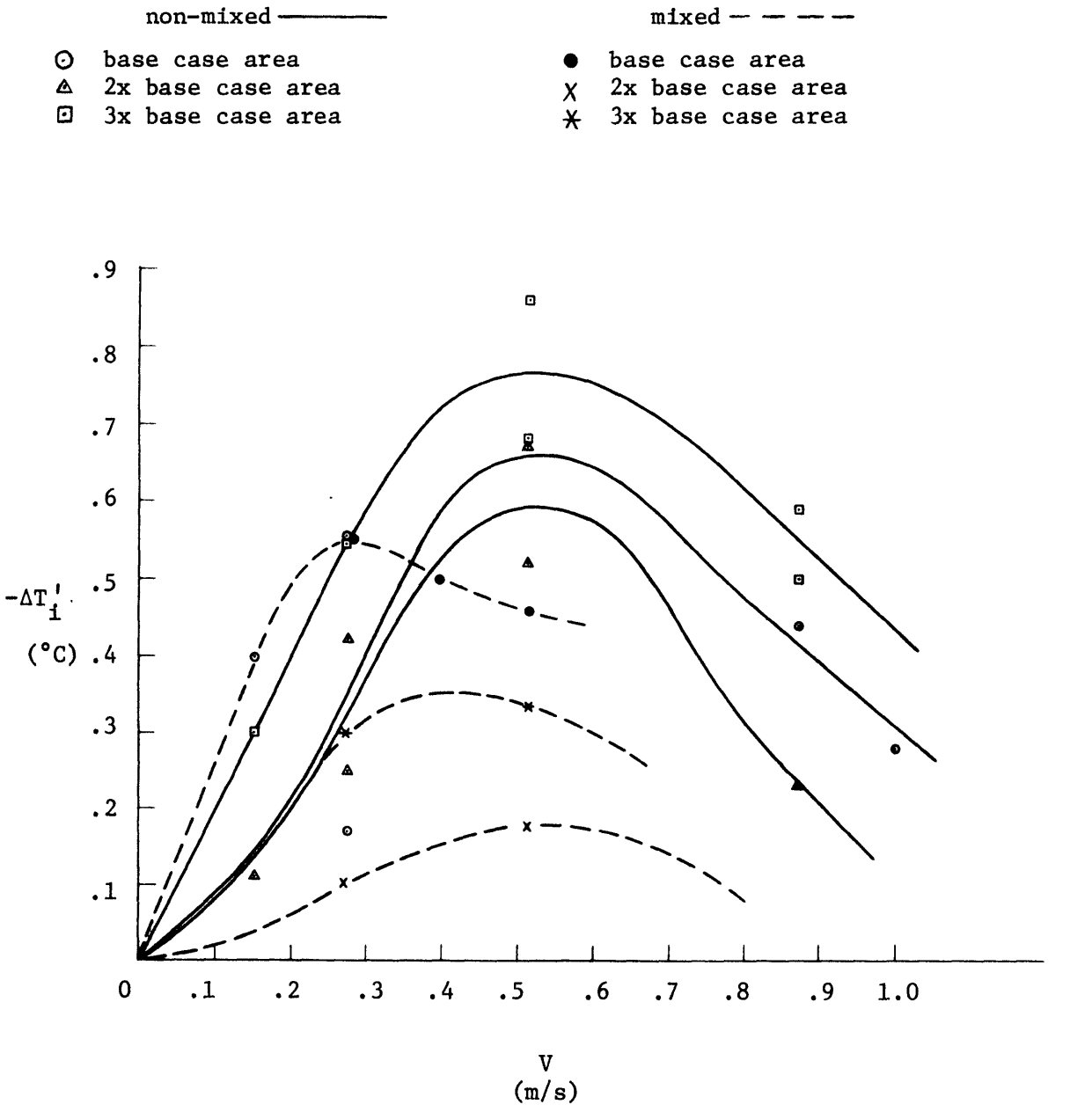

The effect of increasing the discharge port area for a given plant size (and hence flow rate) is to decrease the discharge velocity, thereby decreasing the discharge momentum. Figure 25a indicates that peak direct recirculation is comparable for all three discharge areas within the respective mixed and non-mixed groupings. However, reducing the discharge velocity seems to promote jet instability and intermittent billowing, particularly in the intermediate range of current speeds. This effect was observed visually during the experiments and is supported by the apparently random hierarchy of sensitivity to discharge area in Figure 25b.

Figure 26 illustrates the effect of varying the mixed layer depth on recirculation for a 400 MWe plant (with a radial evaporator discharge at a medium discharge height). The density profiles associated with the three types of mixed layer depths are shown in Appendix III. At a medium discharge depth, the discharge jet is positively buoyant with respect to density profiles characterized by shallow and medium mixed layer depths but negatively buoyant with respect to those characterized by a deep mixed layer depth. The positively buoyant jets (shallow and medium mixed layer depths) behave as previously described. Recirculation occurs due to the combined effects of positive plume buoyancy and the uplift and plume billowing created by the ambient current. Thus peak direct recirculation and intake temperature depression occur at intermediate current speeds.

With the deep mixed layer depths the jet is negatively buoyant and sinks. Thus the previously described current-induced recirculation mechanism is absent, and the discharge depth is sufficiently deep to prevent recirculation due to free surface confinement. As a result Figure 26 shows little intake temperature depression and essentially no direct recirculation for this case.

Figure 26a: The Influence of Varying Mixed Layer Depth on Direct Recirculation Over a Range of Current Speeds for a 400 MWe Plant with a Radial Evaporator Discharge at a Medium Discharge Depth

△ 400 MWe plant; evaporator discharge; deep mixed layer depth; medium discharge depth; radial port

⊙ 400 MWe plant; evaporator discharge; medium mixed layer depth; medium discharge depth; radial port

⊡ 400 MWe plant; evaporator discharge; shallow mixed layer depth; medium discharge depth; radial port

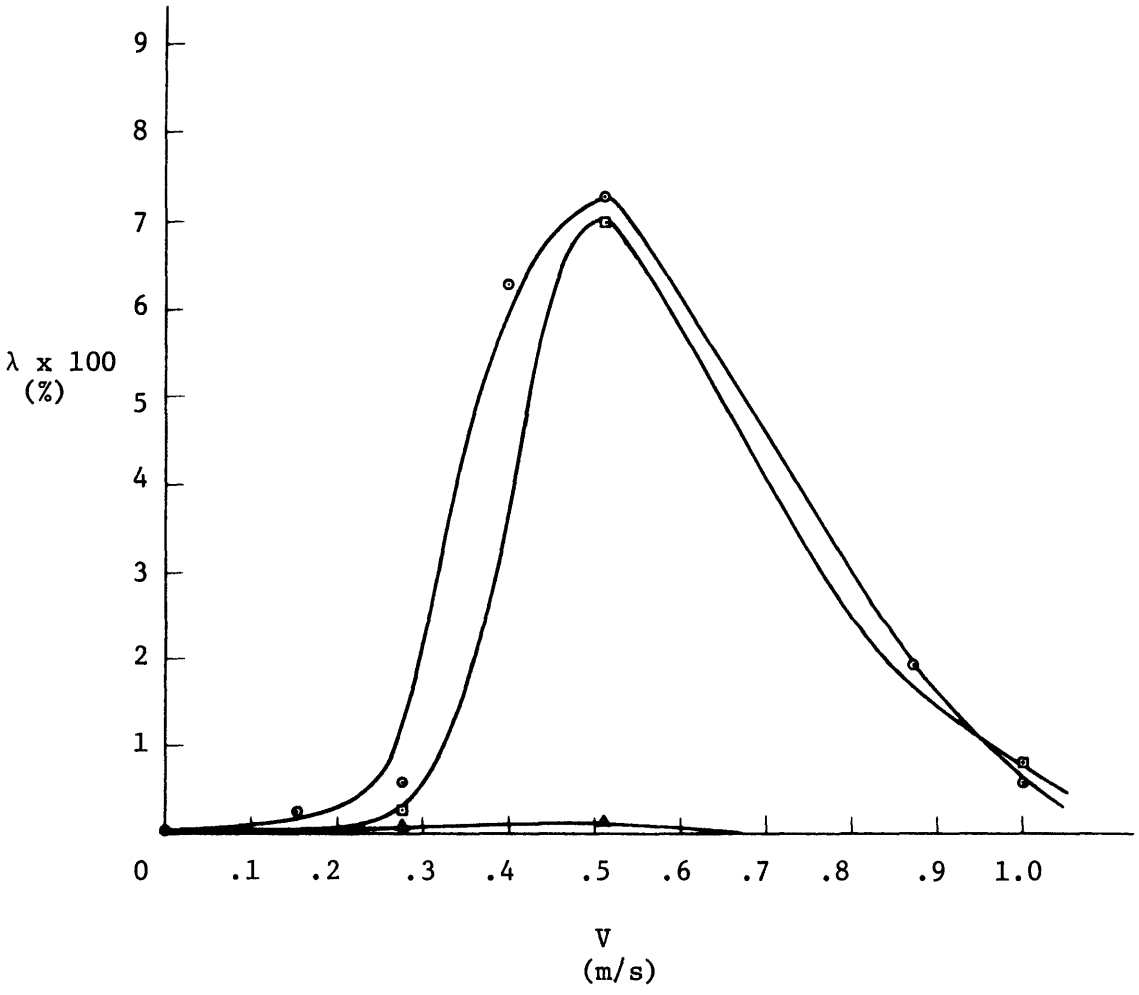

Figure 26b: The Influence of Varying Mixed Layer Depth on Intake Temperature Depression Over a Range of Current Speeds for a 400 MWe Plant with a Radial Evaporator Discharge at a Medium Discharge Depth

△ 400 MWe plant; evaporator discharge; deep mixed layer depth; medium discharge depth; radial port

⊙ 400 MWe plant; evaporator discharge; medium mixed layer depth; medium discharge depth; radial port

⊡ 400 MWe plant; evaporator discharge; shallow mixed layer depth; medium discharge depth; radial port

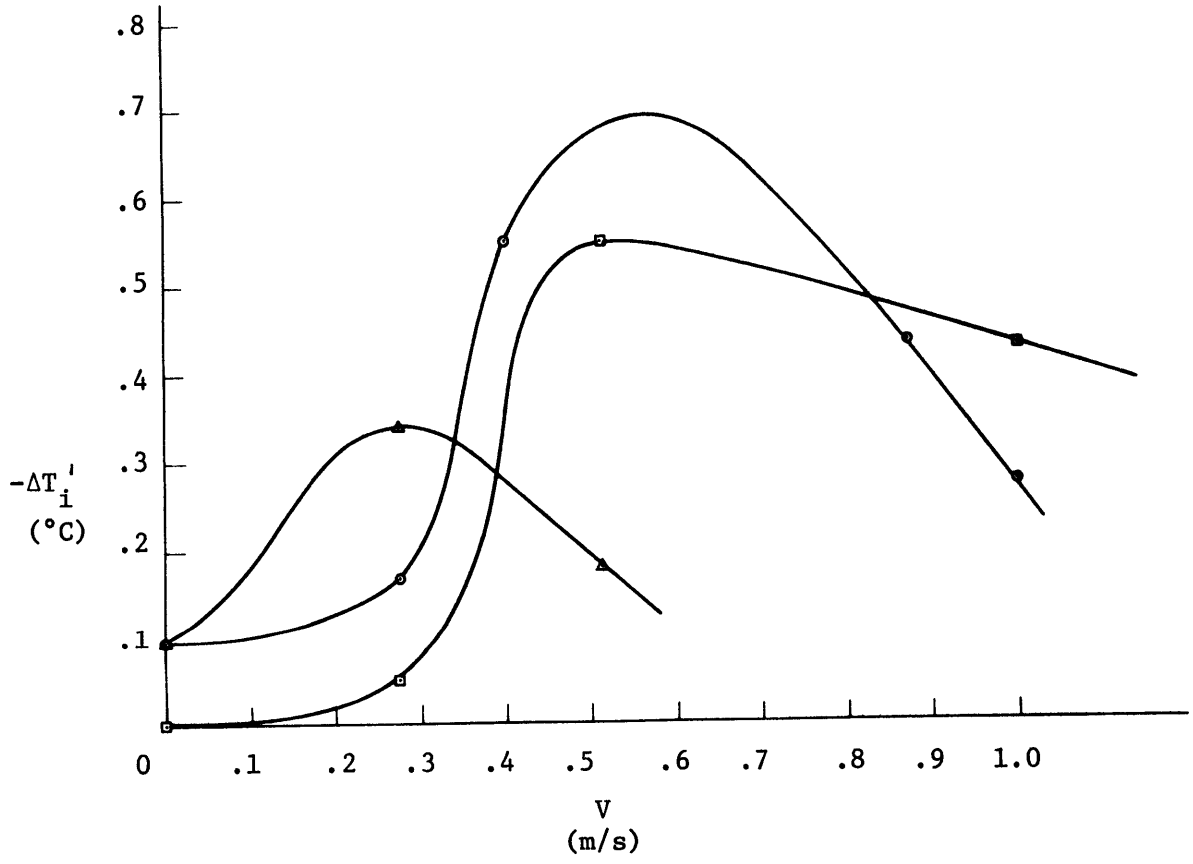

Figure 27 shows the effect of varying discharge depth, for mixed and non-mixed discharges. In each case, a 400 MWe plant is discharging into an ocean with a medium mixed layer depth. As discussed previously in the case of medium discharge depth, the non-mixed discharge shows modest direct recirculation ($\lambda \lesssim 8\%$) and intake temperature depression ($|\Delta T_i'| \lesssim .7^{o}F$) while the mixed discharge displays negligible direct recirculation and modest intake temperature depression ($|\Delta T_i'| \lesssim 0.5^{o}F$). Direct recirculation in these cases is caused by an interplay between positive plume buoyancy and ambient current drag.

In the case of the shallow discharge depth (into the mixed layer), behavior is quite different. Both mixed and non-mixed discharges are negatively buoyant. Recirculation, then, must occur as a result of forces which counteract the negative buoyancy of the plume. The major force is suspected to be the low pressure above the plume created by confinement due to the free surface. For the case of stagnant water and an infinite mixed layer depth, this case corresponds to that studied by Fry et. al. (1981).

Fry et. al. observed two types of behavior depending on discharge velocity. For low discharge velocities the negatively buoyant jet will fall relative to the intake level. Between the free surface and the jet, water flowing to maintain the intake and jet entrainment demands will be unconstrained. As the discharge velocity is increased, the demand for entrainment flow increases; thus the velocity of the flow between the jet and the free surface increases. Applying Bernoulli's equation between a point far upstream of the plant and a point above the jet near the intake dictates that increasing the discharge velocity will lower the pressure in the region between the surface and the jet. Above a critical discharge

Figure 27a: Effect of Varying Discharge Depth for Mixed and Non-Mixed Discharges on Direct Recirculation Over a Range of Current Speeds

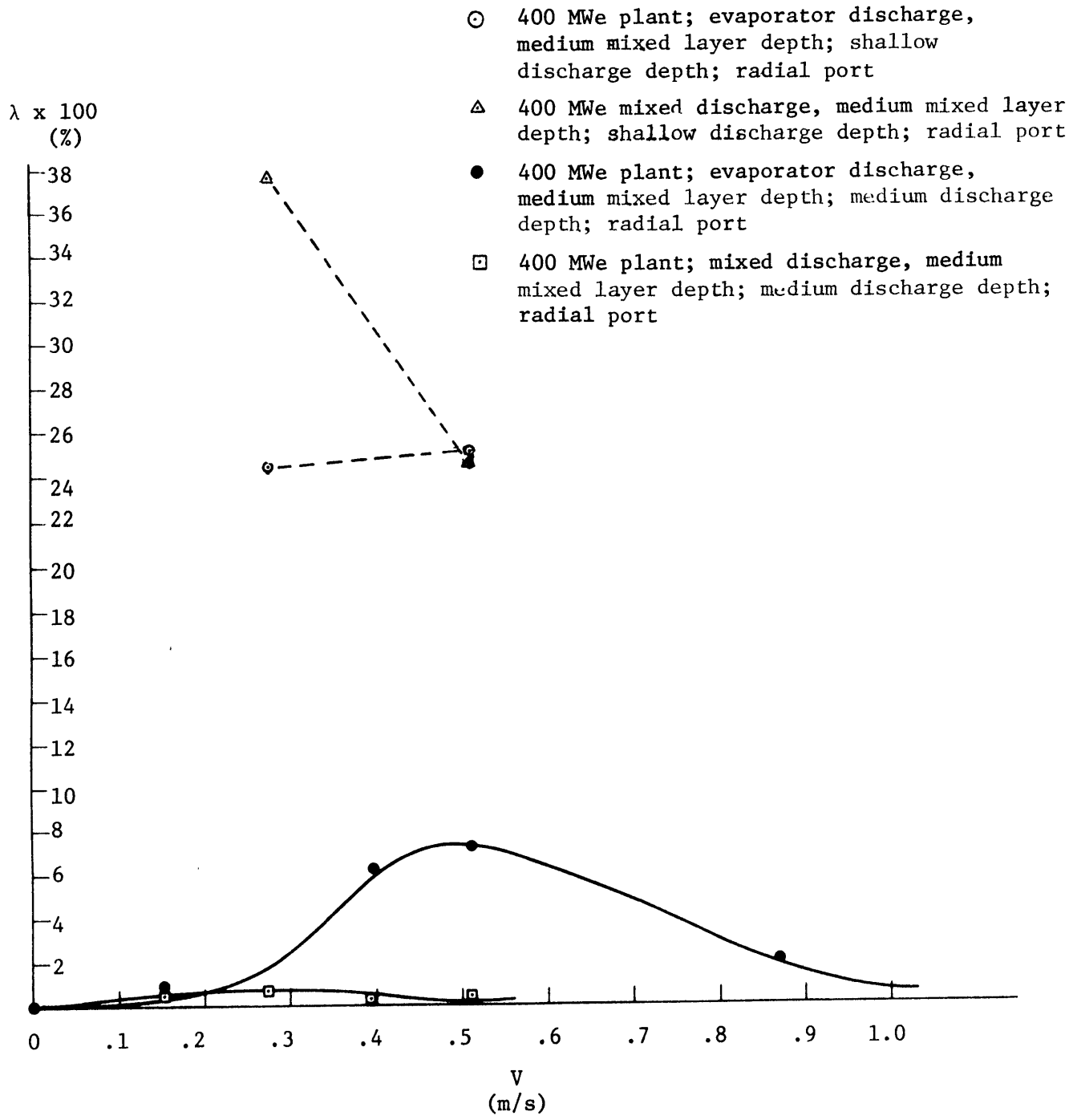

Figure 27b: Effect of Varying Discharge Depth for Mixed and Non-Mixed Discharges on Intake Temperature Depression Over a Range of Current Speeds

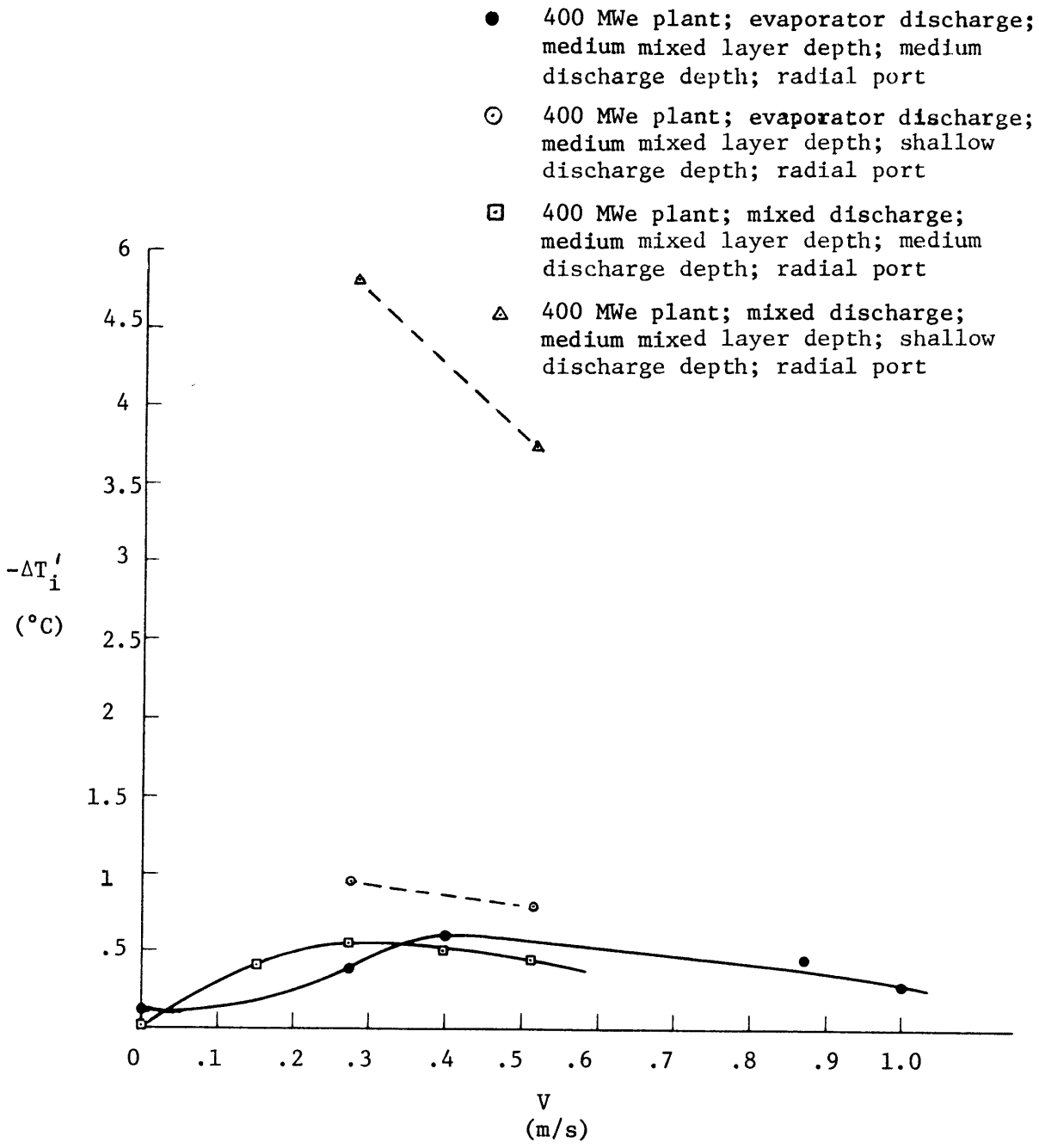

velocity, the pressure loss induces jet attachment in which case the intake flow is drawn essentially from diluted discharge flow. The criteria developed by Fry et. al (1981) to govern this transition are presented in Section 5.4.

The effects of an ambient current and a finite mixed layer depth may alter the tendency for recirculation. The finite mixed layer depth serves as a diffusion floor which narrows the region between the plume and the free surface. Thus it is possible that recirculation could occur at combinations of discharge submergence, buoyancy and momentum which would not result in recirculation in the case of an infinite mixed layer depth. However, any entrainment of colder water from beneath this floor will counteract this effect. The presence of an ambient current may also increase the probability of recirculation because of the tendency of the current to promote plume billowing. However, it is clear that an ambient current increases the plume dilution resulting in a decrease in both direct recirculation and intake temperature depression.

The results presented in Figure 27 are consistent with the heuristic description presented above and with the more quantitative analysis presented in Section 5.4. Note, however, that no experiments were performed in stagnant water(for the 400 MWe plants with a shallow discharge depth and a medium mixed layer depth).

From the standpoint of OTEC operations, it is very important to note the large magnitude of the recirculation which occurs as a result of these shallow submergence discharges. Unlike the current-induced recirculation found to occur with discharges beneath the mixed layer, and associated with intermittent turbulent billowing, the confinement-induced

recirculation is associated with steady recirculation of the mean jet flow. This results in large values of direct recirculation (maximum $\lambda \sim 25 - 40\%$) and corresponding values of intake temperature depression (maximum $|\Delta T_i'| \sim 1^oC$ for the non-mixed and $4 - 5^oC$ for the mixed discharge). The large value of intake temperature depression would certainly make this particular mixed discharge design unacceptable.

Figure 28 compares non-mixed and mixed discharges from 400 MWe plants with radial and separate discharge ports of varying port area. The ocean is schematized as having a medium mixed layer depth with current speeds ranging up to 1 m/s.

A comparison of the evaporator discharges with base case area indicates that less direct recirculation is associated with the 4-jet configuration than with the radial case. Figure 28b indicates that the intake temperature depressions are comparable although there are no significant trends.

Jets discharging through the larger area parts exhibited considerable instability in the presence of a current, especially in the case of the evaporator discharge where the plume was positively buoyant. For the case with large discharge ports, the relatively low jet momentum, compared with that of the ambient currents, resulted in excessive billowing and intermittency. The random behavior associated with the large discharge ports is demonstrated by the point spread in Figure 28.

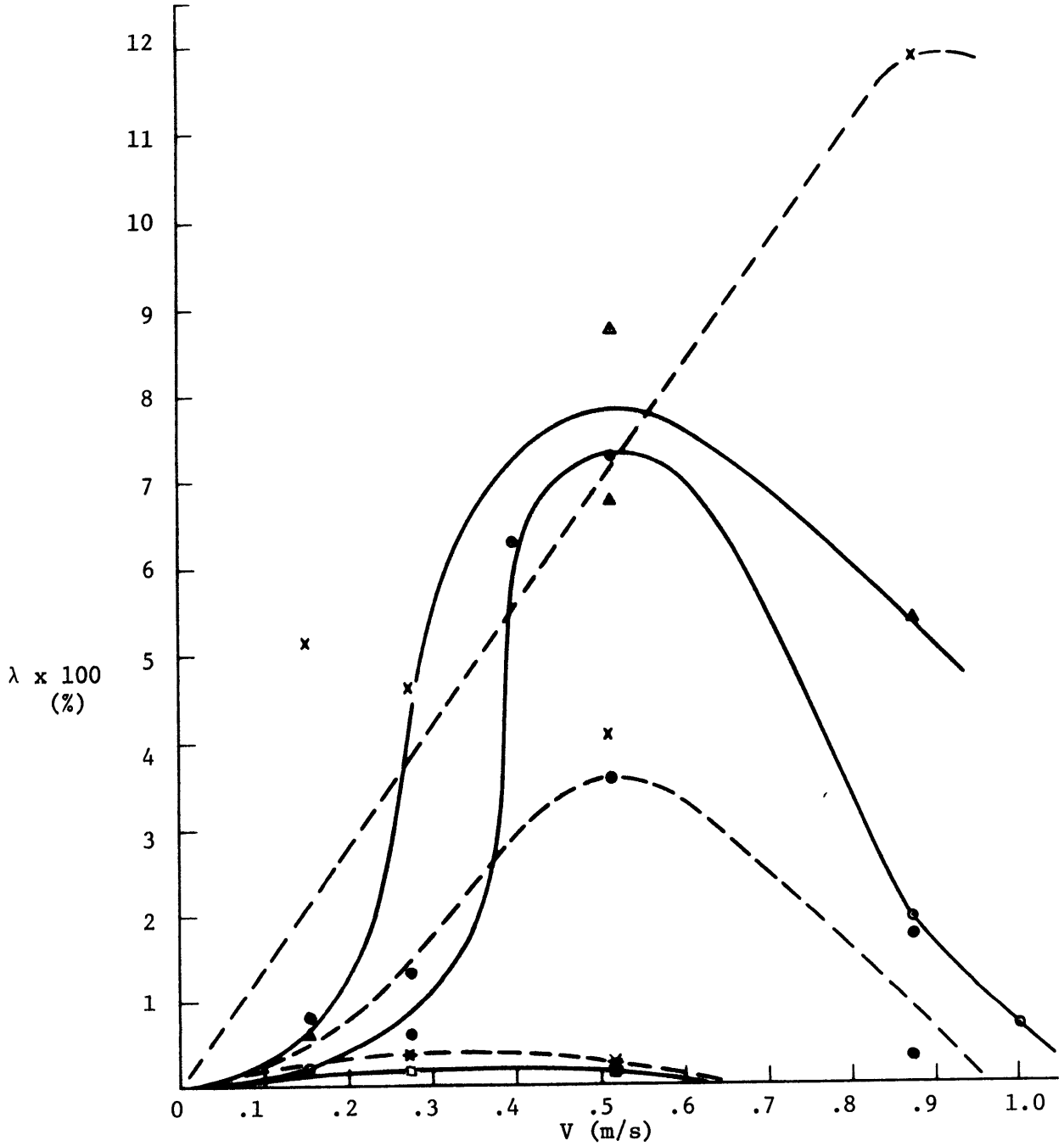

Figure 28a: A Comparison of Radial Versus Separate Ports with Variations in Mixed Versus Non-Mixed Discharge Configurations and Port Size (Direct Recirculation Versus Current Speed)

Radial Ports

- ⊙ 400 evap.; med. mixed layer depth; med. disch.; base case area
- △ 400 evap.; med. mixed layer depth; med. disch.; 3x base case area
- ⊡ 400 mixed; med. mixed layer depth; med. disch.; 3x base case area

Separate Ports

- ● 400 evap.; med. mixed layer depth; med. disch.; base case area
- X 400 evap.; med. mixed layer depth; med. disch.; 3x base case area
- ✳ 400 mixed; med. mixed layer depth; med. disch.; 3x base case area

Figure 28b: A Comparison of Radial Versus Separate Ports with Variations in Mixed Versus Non-Mixed Discharge Configurations and Port Size (Intake Temperature Depression Versus Current Speed)

Radial Ports

⊙ 400 MWe plant; evaporator discharge; medium mixed layer depth; medium discharge depth; base case area

△ 400 MWe plant; evaporator discharge; medium mixed layer depth; medium discharge depth; 3x base case area

⊡ 400 MWe plant; mixed discharge; medium mixed layer depth; medium discharge depth; 3x base case area

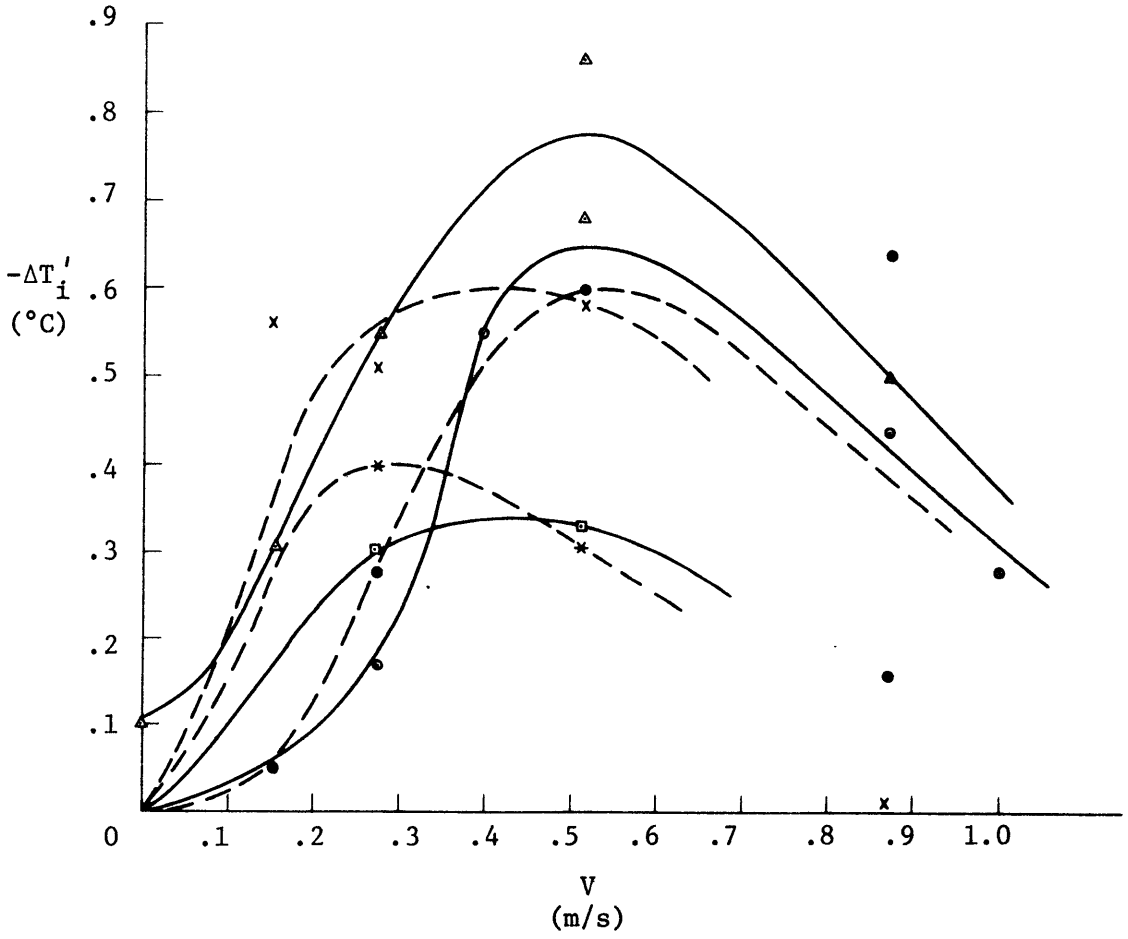

Separate Ports

● 400 MWe plant; evaporator discharge; medium mixed layer depth; medium discharge depth; base case area

X 400 MWe plant; evaporator discharge; medium mixed layer depth; medium discharge depth; 3x base case area

✳ 400 MWe plant; mixed discharge; medium mixed layer depth; medium discharge depth; 3x base case area

5.3.2 Dilution Analysis

Plume dilution is one of the most important environmental parameters associated with OTEC operations. Two direct measurements of dilutions were made and tabulated in Table 4: S_c and S_{ave}. Figure 29 is a plot of S_c versus S_{ave} for all radial and 4-jet discharge configurations examined. Because S_{ave} is calculated using the outside boundaries of the thickness and width of the wake, S_{ave} is expected to be larger than S_c for any given experiment (since this approach necessarily overestimates the cross-sectional area of the wake and ignores any non-homogeneity of mixing within the wake).* Figure 29 shows that in general this is the case. Thus, S_{ave} and S_c should provide estimates of the upper and lower bounds of the near field plant wake dilution. For example, using $(S_{ave} + S_c)/2$ for experiment 7B indicates that the concentration in the intermediate field of any chemicals contained in the discharge will be about 13% of the discharge concentration.

Another, indirect, measure of dilution can be estimated based on the measurements of direct and indirect recirculation. This can be illustrated in Figure 30 where it is assumed that the discharge has flow Q_o, temperature T_o and concentration c_o, and that it mixes with ambient water of average temperature T_{ao} and zero (dye) concentration before partially recirculating. Let the dilution, average temperature and average concentration at this point be S_N, T_N, c_N. The heat and mass (of dye) balances can be written as

*It should also be added that, due to discrete sampling, the estimate of S_c may not represent the true minimum dilution. Although the field samples were usually taken over the depth of the basin during a run, it was not unlikely for the field sample dye probe to be positioned slightly above or below the point a minimum dilution. The resulting error in estimating minimum dilution is estimated to be about 10%.

Figure 29: Plot of Centerline Dilution (c_o/c_f) Versus Average Dilution ($\frac{W_{450}t_{450}V}{Q_o}$).

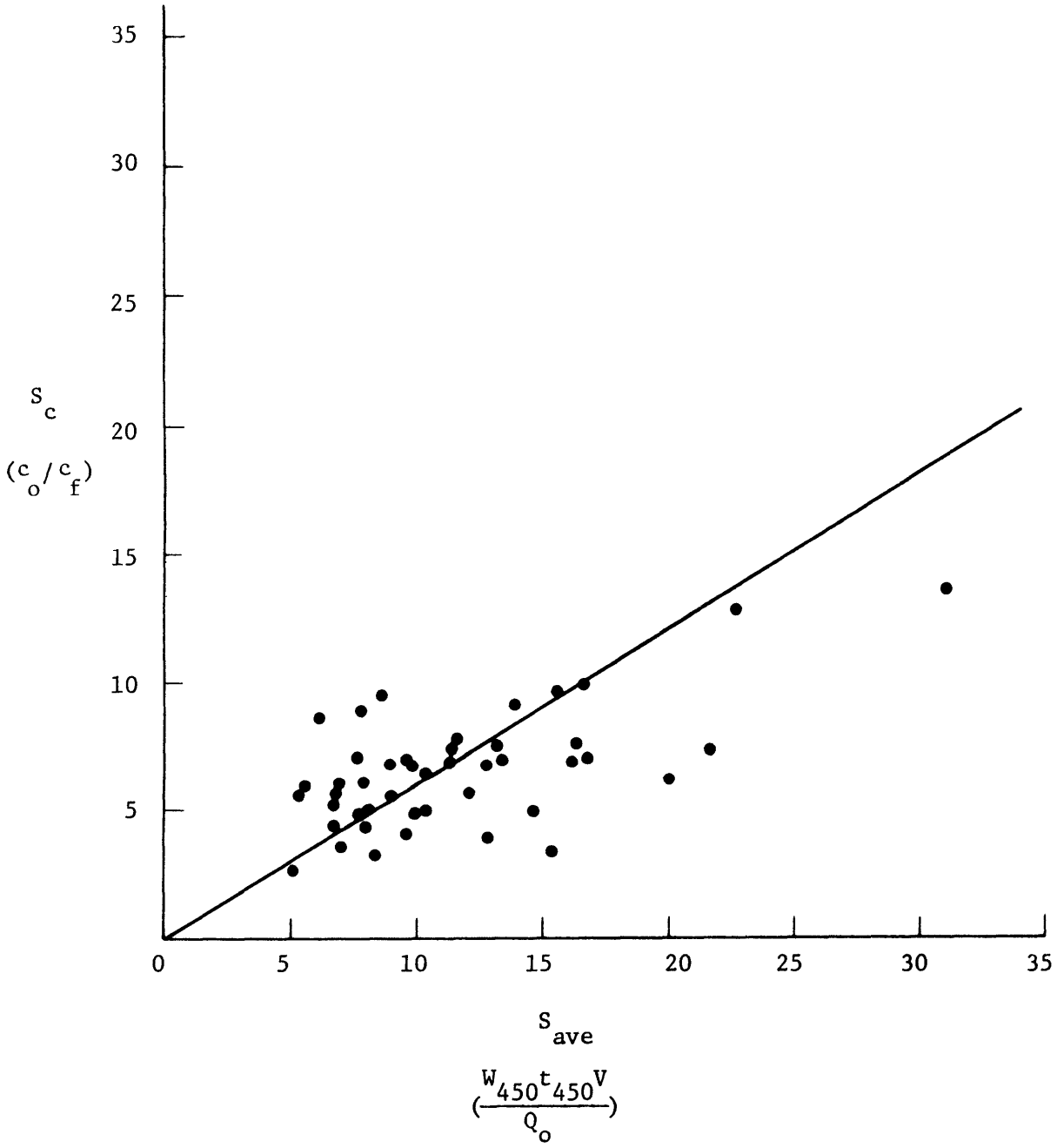

a) Radial Discharge Configuration

b) 4-Jet Discharge Configuration

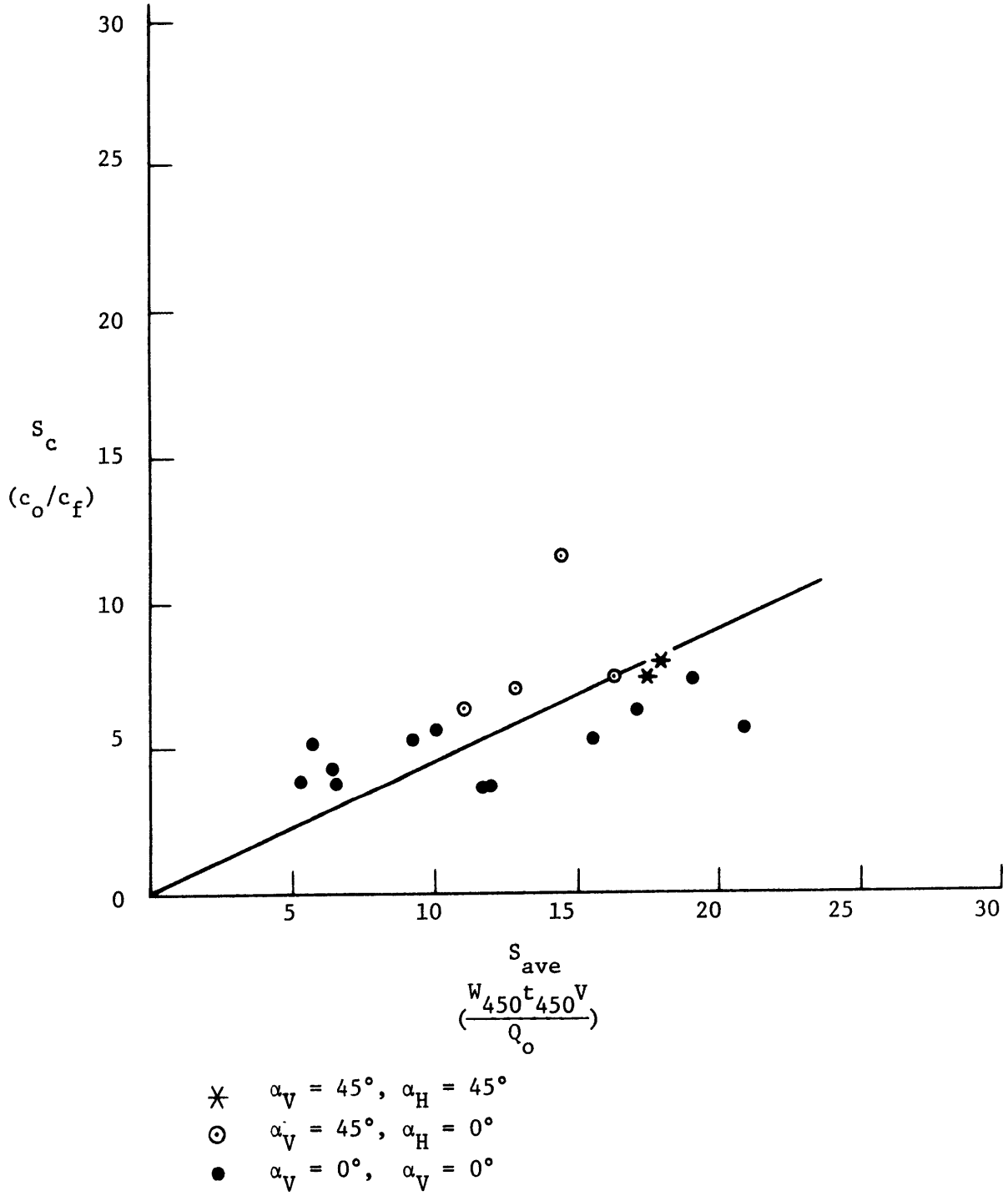

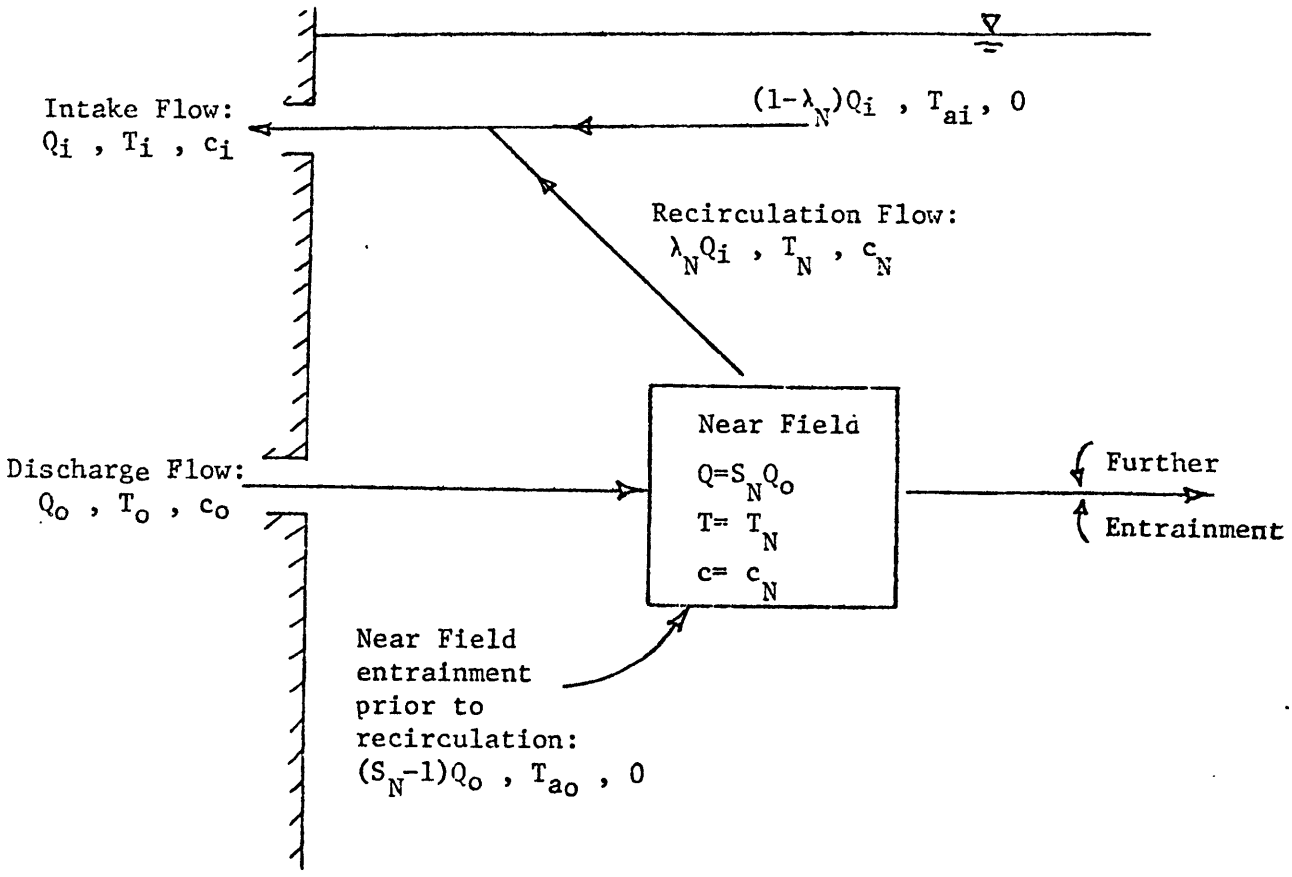

Figure 30: Schematic Representation of Near Field Recirculation (flow rate, temperature, and dye concentration noted for each flow)

$$Q_o T_o + (S_N - 1) Q_o T_{ao} = S_N Q_o T_N$$

$$Q_o c_o = S_N Q_o c_N$$

Now assume that a fraction λ_N of the intake flow is recirculated from this near field region while a fraction $(1 - \lambda_N)$ is drawn from the undisturbed water whose average temperature is T_{ai} and whose concentration is zero. Thus heat and mass balances at the intake can be written as

$$Q_i T_i = \lambda_N Q_i T_N + (1-\lambda_N) Q_i T_{ai}$$

$$Q_i c_i = \lambda_N Q_i c_N$$

Noting that c_i/c_o has been previously designated as λ, the above equations can be solved for

$$\lambda_N = \frac{\lambda(T_o - T_{ao}) - (T_i - T_{ai})}{T_{ai} - T_{ao}}$$

and

$$S_N = \frac{\lambda_N}{\lambda}$$

Approximating T_{ao} by T_{amb} $(z=h_d)$ and T_{ai} by T_{amb} $(z=h_i)$ these equations are evaluated in Table 5 for runs where the discharge port was located below the mixed layer depth. In general, the billowing action of the discharge jet induced by the current in front of the plant serves to reduce the effects of direct recirculation through jet dilution while enhancing any indirect recirculation by displacement of the ambient stratification and by enhancing the mixing with cold ambient water. Consider run 7B which is a case with significant direct recirculation. The results

Table 5 Analysis of Near Field Recirculation and Dilution for Discharge Ports Located Below the Mixed Layer Depth

Run #	T_{ai}	T_{ao}	T_i	T_o	λ	λ_N	S_N	S_c
1A	-	-	-	-	.002	-	-	-
1B	-	-	-	-	.073	-	-	-
3A	30.38	26.73	29.95	27.95	.006	.12	20.0	5.7
B	30.10	26.73	29.50	27.95	.063	.20	3.19	5.1
4A	32.55	28.11	32.15	24.25	.005	.09	17.15	8.7
B	32.54	28.11	32.08	24.25	.004	.096	24.1	4.9
5A	32.50	28.95	31.95	24.90	.006	.15	24.7	6.2
B	32.35	28.95	31.85	24.90	.002	.145	72.3	7.1
6A	32.96	29.05	32.89	30.65	.008	.021	2.65	6.8
B	32.80	29.05	31.94	30.70	.10	.273	2.73	6.9
7A	33.24	29.44	33.19	30.70	.002	.014	7.0	5.7
B	33.00	29.44	32.45	30.75	.07	.18	2.6	5.0
8A	33.80	29.66	33.65	31.10	.063	.058	1.92	6.1
B	33.45	29.66	32.45	31.10	.079	.294	3.72	5.2
10	34.18	30.50	33.90	32.15	.007	.079	11.32	7.2
11	34.98	31.50	34.45	32.20	.028	.158	5.64	7.0
12	35.30	31.54	34.87	32.95	.008	.117	14.67	9.4
13	34.55	30.75	33.95	32.75	.019	.168	8.84	9.7
14	33.14	30.81	32.70	31.40	.020	.194	9.70	7.5
15A	32.62	29.12	32.20	30.25	.002	.12	60.3	7.9
B	32.59	29.12	32.27	30.40	.004	.094	23.4	6.9
16	32.22	28.80	31.85	30.10	.010	.11	11.2	6.4
17	33.25	30.03	33.00	30.70	.002	.078	39.0	9.9
18A	33.30	30.19	32.50	25.25	.001	.256	256.0	37.4
B	33.20	30.19	32.80	25.35	.001	.131	131.0	46.5
19A	33.89	32.24	33.50	31.18	.003	.234	78.1	12.8
B	33.85	32.24	33.40	31.18	.017	.268	15.78	13.7
20A	32.92	30.77	32.58	30.58	.001	.158	158.1	5.7
B	32.86	30.77	32.68	30.60	.001	.086	86.0	7.4

Table 5 (continued)

Run #	T_{ai}	T_{ao}	T_i	T_o	λ	λ_N	S_N	S_c
22A	27.75	27.65	26.80	25.85	.25	-	-	9.6
B	27.70	27.60	26.90	25.80	.25	-	-	6.9
23A	26.99	26.96	22.15	17.26	.38	-	-	5.9
B	26.94	26.93	23.20	17.22	.25	-	-	6.7
24A	24.55	24.54	24.51	12.50	.001	-	-	7.5
B	24.47	24.44	23.60	12.53	.011	-	-	7.3
25A	24.41	24.38	23.40	22.00	.24	-	-	6.9
B	24.34	24.33	23.55	22.05	.25	-	-	7.6
26A	24.79	24.36	24.77	23.12	.001	.044	43.6	7.5
B	24.72	24.36	24.71	23.12	.001	.024	24.3	7.9
27A	23.33	22.04	23.26	22.0	.006	.054	9.01	6.3
B	23.13	22.04	23.11	22.05	-	-	-	7.1
28A	24.54	23.57	24.50	21.86	.003	.036	11.98	11.7
B	24.42	23.57	24.39	21.87	.001	.033	33.29	7.5
29A	24.52	21.06	24.24	21.98	.013	.084	6.49	5.6
B	24.48	21.06	24.13	21.97	-	-	-	5.4
30A	24.30	20.93	23.70	21.75	.036	.187	5.19	6.6
B	24.30	20.93	23.66	21.76	-	-	-	7.5
31A	24.35	20.28	24.30	21.78	.008	.015	1.90	5.7
B	24.22	20.28	24.06	21.77	.018	.047	2.63	5.7
32A	24.49	21.16	24.43	22.00	.002	.0185	9.26	78.6
B	24.42	21.16	24.06	22.10	.017	.115	6.78	11.7
33A	24.53	21.25	24.46	23.40	.004	.024	6.0	551.6
B	24.47	21.25	24.35	23.66	.0	.038	93.92	105.6
34A	24.50	21.12	24.35	22.20	.002	.045	22.51	10.5
B	24.46	21.12	24.32	22.30	.001	.042	42.3	6.6
35A	24.60	20.65	24.35	21.95	.019	.07	3.66	4.1
B	24.54	20.65	24.02	21.98	.091	.165	1.81	4.9
36A	25.27	20.97	24.85	22.70	.027	.109	4.02	4.4
B	25.16	20.97	24.49	22.70	.089	.197	2.21	3.5

Table 5 (continued)

Run #	T_{ai}	T_{ao}	T_i	T_o	λ	λ_N	S_N	S_c
37A	25.29	20.92	25.18	22.96	.002	.026	13.05	5.2
B	25.26	20.92	25.03	22.98	.020	.062	31.24	5.0
38A	25.44	21.30	25.34	14.30	.002	.021	10.39	8.9
B	25.42	21.30	25.24	14.31	.003	.039	12.87	5.7
39A	25.91	21.67	25.36	22.74	.046	.141	3.07	4.6
B	25.86	21.67	25.18	22.79	.068	.180	2.65	3.3
40A	26.90	21.70	26.60	23.91	.006	.060	10.04	2.6
B	26.81	21.70	26.22	23.91	-	-	-	-
41A	27.38	21.44	26.52	24.30	.088	.187	2.13	4.1
B	27.35	21.44	26.85	24.31	.054	.111	2.05	4.1
42A	26.95	23.63	26.65	16.80	.002	.086	43.12	3.4
B	26.89	23.63	26.56	16.84	.002	.097	48.53	3.7
43A	26.76	22.70	26.25	23.38	.046	.133	2.90	4.3
B	26.68	22.70	26.10	23.38	.041	.153	3.73	6.3
44A	27.51	23.42	26.95	24.91	.051	.155	3.05	3.9
B	27.37	23.42	27.36	24.94	.119	.048	.406	3.7
45A	27.71	23.83	27.31	17.08	.004	.096	24.03	3.8
B	27.67	23.83	27.36	17.07	.002	.077	38.6	3.8

of the recirculation analysis indicate that approximately 7% of the intake flow is directly recirculated from the discharge, 11% is entrainment flow which is recirculated along with the discharge flow and 82% is ambient water. A comparison between the measured centerline dilution (450 m behind the plant) S_c and the calculated near field dilution S_N indicates that most of the discharge mixing takes place after recirculation. In contrast, run number 3A is an example of an experiment where there was little direct recirculation (.6%) while 11.4% of the intake flow was jet entrainment water and 88% was ambient water. This mixing effect is indicated in the fact that the computed near field dilution (in front of the plant) is nearly four times larger than the measured centerline dilution at 450 m behind the plant.

In considering the results in Table 5, it is important to realize that the analysis cannot account for mixing induced by the presence of the power plant, near field mixing of negatively buoyant plumes which dive down (since the analysis relies on a change in intake temperature), indirect recirculation caused by displacement of the upper stratified layers, or the dynamics of the intake alone.

5.3.3 Analysis of Plume Characteristics

The shape and equilibrium depth of the plume at 450 m (prototype) behind the plant are given by the parameters t_{450}, W_{450} and h_{eq} in Table 4.

Note that there is a strong correlation between $h_{eq}-h_d$ and the buoyancy of the jet. For cases of horizontal discharge all positively buoyant plumes rose while all negatively buoyant plumes fell. Also, increasing the submergence of the discharge tends to lower the equilibrium position of the plume while decreasing the submergence tends to raise the

equilibrium position. In each case the equilibrium level is heavily dependent on the rate at which the discharge mixes with ambient water. To illustrate this point, consider the effect of discharging a negatively buoyant immiscible, isothermal fluid into a stagnant ambient environment characterized by a linear density gradient, $\frac{\partial \rho}{\partial z}$, and an average density ρ at the discharge elevation. If the discharge density differs from the ambient density by an amount $\Delta\rho_o$, the equilibrium level below the level of the discharge would be given by

$$\Delta h_o = \frac{(\Delta\rho_o/\rho)g}{N^2}$$

where

$$N^2 = \frac{g\partial\rho}{\rho\partial z}$$

However, the plant discharge jets do entrain ambient water resulting in an effective lowering of $\Delta\rho_o$; thus, most of the experiments provided in Table 4 exhibited a smaller displacement $\Delta h = (h_{eq}-h_d)$ than given by Δh_o. However, some experiments indicated that the measured Δh was larger than the corresponding Δh_o. This is attributed to strong jet deflection and to increase in the wake thickness induced by interactions of the discharge jet with the current; it occurred primarily in cases with large discharge (positive or negative) buoyancy.

5.3.4 Ambient Profile Perturbations

The tendency of the discharge plume to rise or fall until it can "hide" in ambient water of its own density makes it difficult to notice the effects of the plume on the ambient profiles. For this reason, no attempt

was made to monitor these effects with temperature measurements.

5.4 Further Data Interpretation through Dimensional Analysis

The flow fields generated by an OTEC plant in a flowing-stratified environment are highly three-dimensional. To describe these flows mathematically would require use of three-dimensional numerical techniques and turbulence representations which are not clearly understood. In lieu of attempting to solve an extremely difficult analytical problem, approximate descriptions of the flow fields generated by the physical model (see Section 5.3) are combined with dimensional analysis in an attempt to analyze the problem from a fluid mechanical perspective. A dimensional analysis of the flow fields generated by OTEC plants is not even straightforward due to the large number of parameters involved. However, our perspective has been that it is preferable to attempt a simplified analysis of a realistic problem than to over-simplify (the experimental set-up) so as to be able to perform a comprehensive analysis.

5.4.1 Governing Variables

The following analysis is limited to OTEC plants with horizontal radial discharges. Under these conditions any dependent measure of the flow field (e.g. wake geometry, dilution, recirculation) can be expressed as a function of the following independent variables

$$\phi = f(M_o, B_o, Q_o, Q_i, r_o, h_i, h_d, V, H, N) \qquad (5.1)$$

where ϕ = dependent parameter

$M_o = Q_o u_o$ = discharge momentum flux ($L^4 t^{-2}$)

$B_o = Q_o[\rho_o - \rho_{amb}(z=h_d)]g/\rho$ = discharge buoyancy flux ($L^4 t^{-3}$)

Q_o = discharge volume flux ($L^3 t^{-1}$)

Q_i = intake volume flux ($L^3 t^{-1}$)

r_o = plant radius (L)

h_d = discharge depth (L)

h_i = intake depth (L)

V = current speed (Lt^{-1})

H = mixed layer depth (L)

$N = (\frac{1}{\rho} \frac{\partial \rho}{\partial z} g)^{1/2}$ = Brunt - Väisälä frequency (t^{-1})

There are a total of ten independent variables in two dimensions. These can be combined to form nine dimensional variables in one dimension, e.g., length, or eight dimensionless variables. Comparison of various length scales allows one to identify, for a particular flow field characteristic, which parameters are most important, and thus allows the problem to be simplified.

5.4.2 Definition of Length Scales

Four of the independent variables in Eq. (5.1) already have dimensions of length. The six independent variables of Eq. (5.1) involving dimensions of length and time can be combined to form five length scales:

$\ell_B = M_o^{3/4} |B_o|^{-1/2}$ (buoyancy length scale)*

$\ell_Q = Q_o M_o^{-1/2}$ (discharge length scale)

$\ell_{Q_i} = Q_i M_o^{-1/2}$ (intake length scale)

---

* ℓ_B is positive if $B_o > 0$ (i.e., negatively buoyant plume) and negative if $B_o < 0$ (i.e., positively buoyant plume)

$$\ell_V = M_o^{1/2} V^{-1} \qquad \text{(current length scale)}$$

$$\ell_S = M_o^{1/4} N^{-1/2} \qquad \text{(stratification length scale)}$$

The values for each experiment of each of these lengths is tabulated in Table 6. The discharge momentum flux M_o has been chosen as the repeating variable in this exercise because discharge momentum is one variable which is presumed to always be important in the near field. The significance of the other variables can be determined in relation to M_o at various distances from the plant. Variables such as Q_o and Q_i which are combined with M_o to a negative power to form length scales will become insignificant at distances from the plant which are large compared with that length scale. For example the discharge flow rate Q_o is expected to be insignificant at distances $x >> l_Q$. Variables such as B_o, V and N which are combined with M_o to a positive power to form a length scale are <u>insignificant</u> only at distances which are small compared with the particular length scale. If the near field is defined as the region which is dominated by discharge momentum, then limits to the near field can be associated with discharge buoyancy, ambient current or ambient stratification. This is a rather narrow definition of near field, but one which might govern the applicability of various jet model formulations (e.g. integral jet models). The significance of the three length scales characterizing these variables is discussed further.

<u>Current Length Scale</u> (ℓ_V)

A non-buoyant horizontal radial jet discharged into a uniform ambient fluid of velocity V will penetrate a certain distance before being

TABLE 6: IMPORTANT INDEPENDENT VARIABLES AND LENGTH SCALES (Prototype Dimensions)

Run #	M_o (m^4/s^2)	B_o (m^4/s^3)	Q_o (m^3/s)	Q_i (m^3/s)	$Nx10^2$ (1/s)	V (m/s)	h_d (m)	ℓ_V (m)	ℓ_S (m)	ℓ_B (m) 1	ℓ_Q (m)	ℓ_{Q_i} (m)
1A	7040	-	2000	2000	-	.15	76.1	584.	-	-	23.8	23.8
1B	7040	-	2000	2000	-	.51	76.1	163.	-	-	23.8	23.8
3A	7040	6.7	2000	2000	1.72	.28	74.5	305.	70.	+300.	23.8	23.8
3B	7040	6.7	2000	2000	1.72	.40	74.5	211.	70.	+300.	23.8	23.8
4A	28160	-40.6	4000	2000	1.13	.15	76.1	1096.	122.	-340.	23.8	11.9
4B	28160	-40.6	4000	2000	1.13	.51	76.1	327.	122.	-340.	23.8	11.9
5A	28160	-43.9	4000	2000	1.17	.28	77.9	610.	120.	-330.	23.8	11.9
5B	28160	-43.9	4000	2000	1.17	.40	77.9	422.	120.	-330.	23.8	11.9
6A	15840	14.2	3000	3000	1.72	.28	75.6	457.	86.	+380.	23.8	23.8
6B	15840	14.7	3000	3000	1.66	.51	75.6	245.	87.	+370.	23.8	23.8
7A	7040	7.5	2000	2000	1.40	.28	75.4	305.	77.	+280.	23.8	23.8
7B	7040	7.8	2000	2000	1.33	.51	75.4	163.	79.	+280.	23.8	23.8
8A	15840	12.9	3000	3000	1.40	.28	75.6	457.	95.	+390.	23.8	23.8
8B	15840	12.9	3000	3000	1.40	.51	75.6	245.	95.	+390.	23.8	23.8
10	7040	10.2	2000	2000	1.47	1.00	75.8	83.	75.	+240.	23.8	23.8
11	15840	8.3	3000	3000	1.29	1.00	75.8	125.	99.	+490.	23.8	23.8
12	7040	8.9	2000	2000	1.33	1.00	75.7	83.	79.	+260.	23.8	23.8
13	15840	18.8	3000	3000	1.40	1.00	75.7	125.	95.	+330.	23.8	23.8
14	7040	5.6	2000	2000	1.36	.87	75.8	96.	78.	+400.	23.8	23.8
15A	3520	3.3	1000	1000	1.57	.28	75.8	215.	61.	+250.	16.9	16.9

TABLE 6 (continued)

Run #	M_o (m^4/s^2)	B_o (m^4/s^3)	Q_o (m^3/s)	Q_i (m^3/s)	$Nx10^2$ (1/s)	V (m/s)	h_d (m)	ℓ_V (m)	ℓ_S (m)	ℓ_B (m) 1	ℓ_Q (m)	ℓ_{Q_i} (m)
15B	3520	3.8	1000	1000	1.63	.51	75.8	115.7	60.	+240.	16.9	16.9
16	3520	3.8	1000	1000	1.66	.87	75.8	68.1	60.	+230.	16.9	16.9
17	3520	2.0	1000	1000	1.60	1.00	75.4	59.3	61.	+320.	16.9	16.9
18A	14080	-27.8	2000	1000	1.33	.28	75.5	431.5	95.	-245.	16.9	8.4
18B	14080	-26.8	2000	1000	1.36	.51	75.5	231.3	93.	-250.	16.9	8.4
19A	7040	-6.6	2000	2000	1.85	.28	75.8	432.	81.	-290.	16.9	16.9
19B	7040	-6.6	2000	2000	1.85	.51	75.8	231.	81.	-290.	16.9	16.9
20A	7040	-1.3	2000	2000	1.80	.28	75.7	305.1	68.	-650.	23.8	23.8
20B	7040	-1.3	2000	2000	1.80	.51	75.7	163.6	68.	-700.	23.8	23.8
22A	7040	-9.7	2000	2000	1.40	.28	38.0	305.1	77.	-250.	23.8	23.8
22B	7040	-9.7	2000	2000	1.40	.51	38.0	163.6	77.	-250.	23.8	23.8
23A	28160	-86.7	4000	2000	1.33	.28	37.4	610.2	112.	-230.	23.8	11.9
23B	28160	-86.4	4000	2000	1.33	.51	37.4	327.1	112.	-230.	23.8	11.9
24A	7040	-44.9	2000	1000	1.36	.28	37.5	305.1	78.	-115.	23.8	11.9
24B	7040	-44.0	2000	1000	1.33	.51	37.5	163.6	79.	-115.	23.8	11.9
25A	1760	-5.6	1000	1000	1.33	.28	36.5	152.6	57.	-115.	23.8	23.8
25B	1760	-5.4	1000	1000	1.33	.51	36.5	81.8	57.	-120.	23.8	23.8
26A	7780	-6.0	2000	2000	1.28	.28	52.5	320.7	83.	-340.	22.7	22.7
26B	7780	-6.0	2000	2000	1.28	.51	52.5	171.9	83.	-340.	22.7	22.7
27A	7780	-0.18	2000	2000	1.21	.28	52.2	320.7	85.	-1970.	22.7	22.7
27B	7780	0.06	2000	2000	1.21	.51	52.2	171.9	85.	+3411.	22.7	22.7

TABLE 6 (continued)

Run #	M_o (m^4/s^2)	B_o (m^4/s^3)	Q_o (m^3/s)	Q_i (m^3/s)	$Nx10^2$ (1/s)	V (m/s)	h_d (m)	ℓ_V (m)	ℓ_S (m)	ℓ_B (m) 1	ℓ_Q (m)	ℓ_{Q_i} (m)
28A	7780	-7.9	2000	2000	1.17	.51	52.5	171.	87.	-300.	22.7	22.7
28B	7780	-7.8	2000	2000	1.17	.87	52.5	101.	87.	-300.	22.7	22.7
29A	7780	4.0	2000	2000	1.69	.28	74.4	320.	72.	+410.	22.7	22.7
29B	7780	4.0	2000	2000	1.69	.51	74.4	171.	72.	+420	22.7	22.7
30A	7780	3.6	2000	2000	1.69	.51	74.4	171.	72.	+440.	22.7	22.7
30B	7780	3.6	2000	2000	1.69	.87	74.4	101.	72.	+440.	22.7	22.7
31A	7780	6.4	2000	2000	1.69	.15	74.4	576.	72.	+320.	22.7	22.7
31B	7780	6.3	2000	2000	1.69	.87	74.4	101.	72.	+320.	22.7	22.7
32A	1945	0.92	500	2000	1.53	.28	73.5	320.	54.	+310.	11.3	45.3
32B	1945	1.0	500	2000	1.53	.51	73.5	171.	54.	+290.	11.3	45.3
33A	1945	2.4	500	2000	1.71	.28	74.7	320.	51.	+190.	11.3	45.3
33B	1945	2.7	500	2000	1.71	.51	74.7	171.	51.	+175.	11.3	45.3
34A	1945	1.1	500	2000	1.71	.28	74.7	320.	51.	+280.	11.3	45.3
34B	1945	1.3	500	2000	1.71	.51	74.7	171.	51.	+260.	11.3	45.3
35A	4180	5.6	2000	2000	1.69	.28	77.9	235.	62.	+220.	30.9	30.9
35B	4180	5.7	2000	2000	1.69	.51	77.9	126.	62.	+220.	30.9	30.9
36A	4180	7.7	2000	2000	1.71	.28	77.2	235.	61.	+190.	30.9	30.9
36B	4180	7.7	2000	2000	1.71	.51	77.2	126.	61.	+190.	30.9	30.9
37A	4180	9.1	2000	2000	1.60	.15	76.9	422.	64.	+175.	30.9	30.9
37B	4180	9.2	2000	2000	1.63	.75	76.9	86.	63.	+170.	30.9	30.9
38A	16720	-50.1	4000	2000	1.25	.28	77.3	470.	102.	-210.	30.9	15.5

TABLE 6 (continued)

Run #	M_o (m^4/s^2)	B_o (m^4/s^3)	Q_o (m^3/s)	Q_i (m^3/s)	$Nx10^2$ (1/s)	V (m/s)	h_d (m)	ℓ_V (m)	ℓ_S (m)	ℓ_B (m) [1]	ℓ_Q (m)	ℓ_{Q_i} (m)
38B	16720	-50.1	4000	2000	1.25	.51	77.3	252.	102.	-210.	30.9	15.5
39A	3140	4.8	2000	2000	1.63	.28	77.1	203.	59.	+190.	35.7	35.7
39B	3140	5.0	2000	2000	1.66	.51	77.1	109.	58.	+185.	35.7	35.7
40A	3140	10.2	2000	2000	1.74	.15	77.3	366.	57.	+130.	35.7	35.7
40B	3140	10.2	2000	2000	1.74	.75	77.3	74.	57.	+130.	35.7	35.7
41A	3140	5.3	2000	2000	1.74	.51	77.1	109.	57.	+175.	35.7	35.7
41B	3140	5.3	2000	2000	1.74	.75	77.1	74.	57.	+175.	35.7	35.7
42A	12560	-46.5	4000	2000	1.21	.28	78.0	407.	96.	-175.	35.7	17.8
42B	12560	-46.2	4000	2000	1.21	.51	78.0	218.	96.	-175.	35.7	17.8
43A	3780	3.2	2000	2000	1.66	.28	75.2	223.	61.	+275.	32.5	32.5
43B	3780	3.2	2000	2000	1.66	.51	75.2	119.	61.	+275.	32.5	32.5
44A	3780	7.3	2000	2000	1.66	.15	75.8	401.	61.	+180.	32.5	32.5
44B	3780	7.4	2000	2000	1.66	.75	75.8	82.	61.	+175.	32.5	32.5
45A	15120	-55.9	4000	2000	1.25	.28	75.9	447.	99.	-185.	32.5	16.3
45B	15120	-56.0	4000	2000	1.25	.51	75.9	239.	99.	-180.	32.5	16.3

[1] The buoyancy length scale ℓ_B has been squared to retain the sign of the jet buoyancy.
Thus $\ell_B^2 = M_o^{3/2} B_o^{-1}$

"swept back" by the current. Experiment 6B is a close approximation to this situation. From momentum conservation arguments, the upstream distance that such a jet will penetrate should be given by

$$X_s(X_s-r_o)V^2 \propto M_o$$

For $r_o^2 << \ell_V^2$ this results in

$$(X_s - \frac{r_o}{2}) \propto \ell_V \qquad (5.2)$$

An equation similar to Eq. (5.2) is plotted in Fig. 31 based on the experimentally observed values of X_s listed in Table 4. Error brackets indicated in Figure 31 represent uncertainty in the estimation of X_s of ± 5m. (prototype). The relationship

$$(X_s-r_o) = 0.53\ \ell_V \qquad (5.3)$$

provides a better fit to the data than Eq. (5.2) and will be utilized in the analysis below. The reason that Eq. (5.3) fits better than Eq. (5.2) is probably due to the preponderance of mixed discharges at large values of ℓ_V. Mixed discharges have greater (negative) buoyancy than evaporator discharges, thus leading to greater jet curvature, increased drag and shorter X_s.

Stratification Length Scale (ℓ_S)

A non-buoyant horizontal radial discharge into a stagnant linearly stratified ambient fluid will be characterized by a region (close to the discharge) of increasing vertical jet thickness. After achieving a maximum thickness, t_{max}, the jet will collapse to form a somewhat thinner

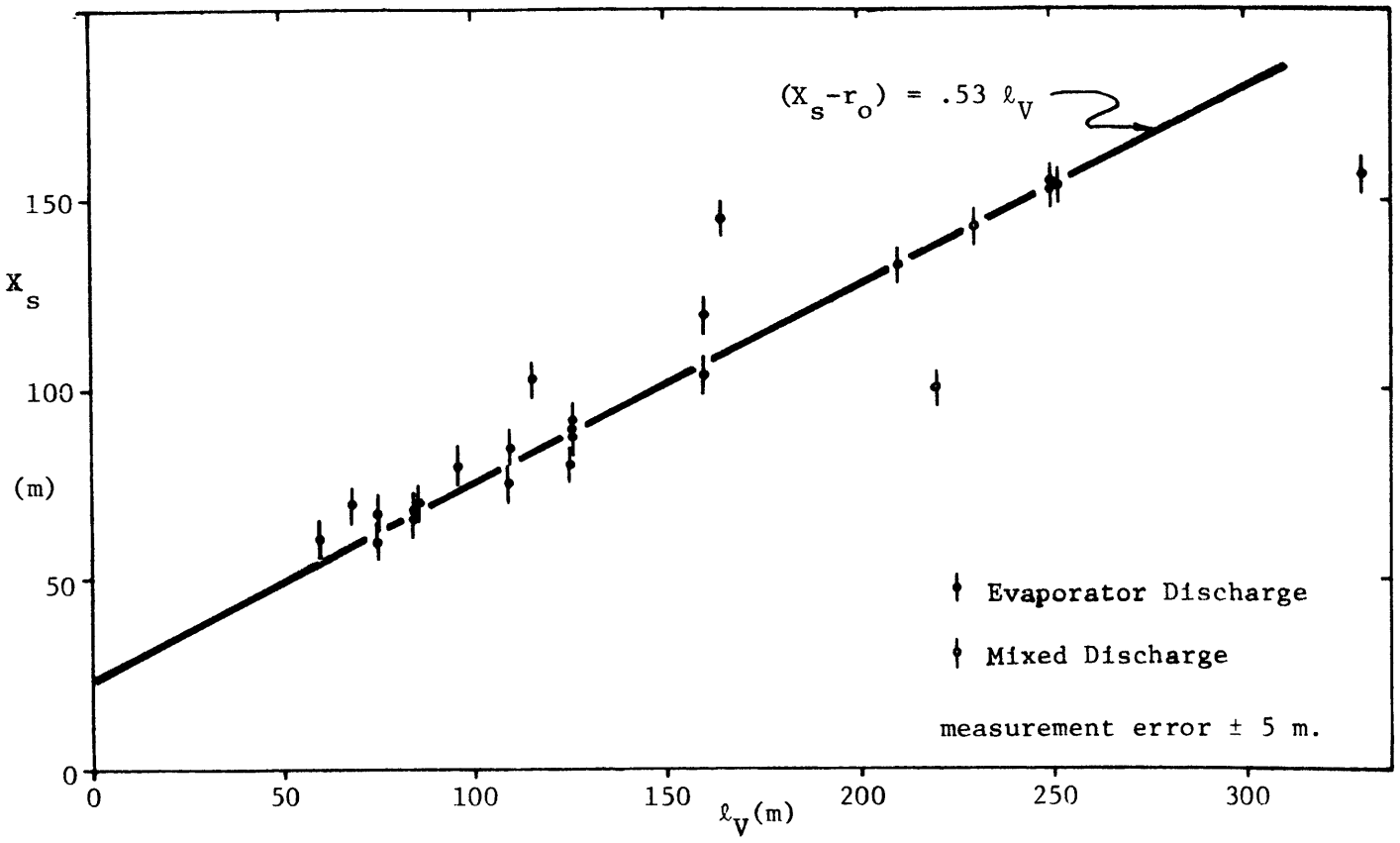

Figure 31 Upstream Penetration Distance of Experiments with "Swept Back" Conditions

intermediate layer. This behavior can be seen in the side-view photographs of the stagnant water experiments (Appendix I of Adams, et al., 1979) as well as the photographs from the present experiments conducted in a weak current. (See, e.g., Run A in Appendix I.) Using potential energy arguments, both the maximum thickness t_{max} and the distance to the maximum thickness $r(t_{max}) - r_o$ are expected to be proportional to the stratification length scale, ℓ_S. The distance to the point of maximum thickness observed in the stagnant water tests is plotted in Figure 32.

Buoyancy Length Scale, ℓ_B

The trajectory of a positively or negatively buoyant jet discharged into a stagnant, uniform ambient fluid will be characterized by the length scale ℓ_B. In most of the experiments reported, jet trajectory was dominated by either ambient current or ambient stratification effects, but buoyancy was still important.

At this point it is worthwhile to offer a second definition of ℓ_B. The value of B_o defined in Eq. (5.1) is based on the ambient density at the level of the discharge. An alternative definition is based on the ambient surface density,

$$B_o' = Q_o[\rho_o - \rho_{amb}(z=0)]g/\rho \qquad (5.4)$$

Whereas B_o and ℓ_B govern the initial trajectory of the jet, B_o' and the corresponding length scale $\ell_B' = M_o^{3/4} |B_o'|^{-1/2}$ provide better correlation with observed confinement-induced recirculation.

Ratio of ℓ_V/ℓ_S

The behavior of strongly current dominated experiments (e.g., 6B) and

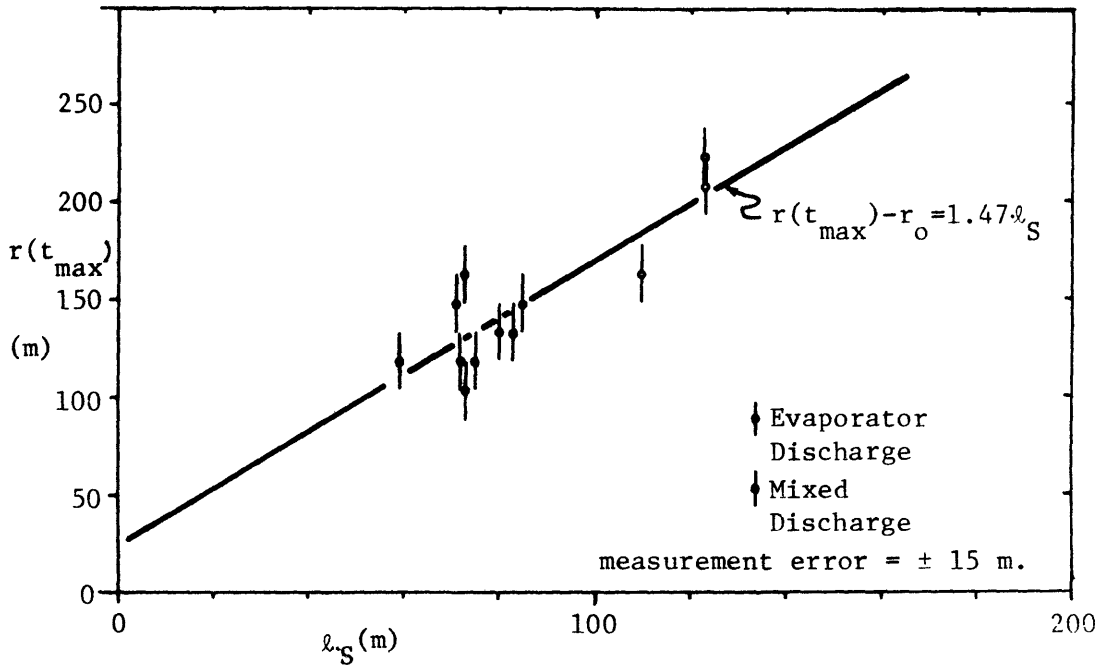

Figure 32 Distance to Point of Maximum Jet Thickness for Stagnant Water Tests

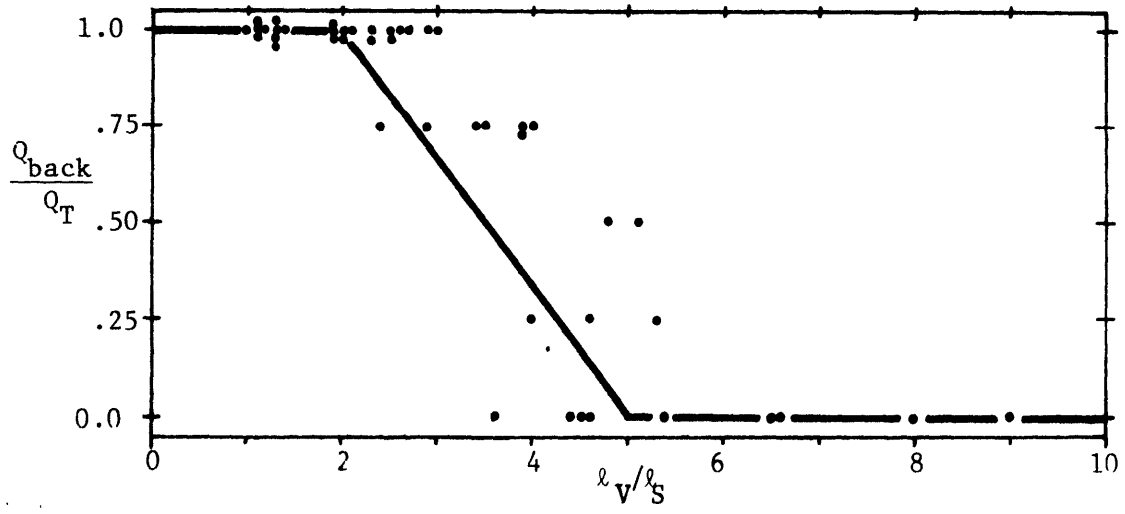

Figure 33 Quantification of the Distinction between Stratification and Current Dominated Experiments

stratification dominated experiments (e.g., 8A) is striking. Figure 33 is an attempt to quantify this distinction as a function of the ratio ℓ_V/ℓ_S. The variable which is plotted is the experimentally estimated fraction of the total near field flow Q_T which is swept back by the ambient current. This ratio is estimated from photographs in intervals of 25% and, while clearly subjec a definite relationship is observed with completely "swept back" conditions associated with low values of ℓ_V/ℓ_S (high V) and completely lateral return flow associated with large $_V/_S$ (small V). The following relationship has been fit to the data and is used in the subsequent recirculation analysis.

$$\frac{Q_{back}}{Q_T} = \begin{cases} 1.0 & 0 < \ell_V/\ell_S < 2 \\ 1.67 = .33\ \ell_V/\ell_S & 2 < \ell_V/\ell_S < 5 \\ 0 & 5 < \ell_V/\ell_S \end{cases} \qquad (5.5)$$

5.4.3 Recirculation Analysis

Two modes of recirculation were noted in the discussion of Section 5.3 and are depicted in Figure 34. Confinement-induced recirculation is associated with negatively buoyant jets discharged sufficiently close to the surface that the jet is bent upward due to dynamic pressure effects. As illustrated in Figure 34a the jet axis intersects the water surface at an appreciable angle thus guaranteeing that the intake will be completely covered ($\lambda_N = 1$). The theory and analysis performed by Fry et al.,(1981) for stagnant non-stratified ambient conditions indicates that the onset of this mode is governed primarily by the parameter h_d/ℓ_B' and secondarily by the parameters ℓ_{Q_i}/ℓ_Q (defined as k by Fry), ℓ_B'/ℓ_Q and ℓ_B'/r_o. This

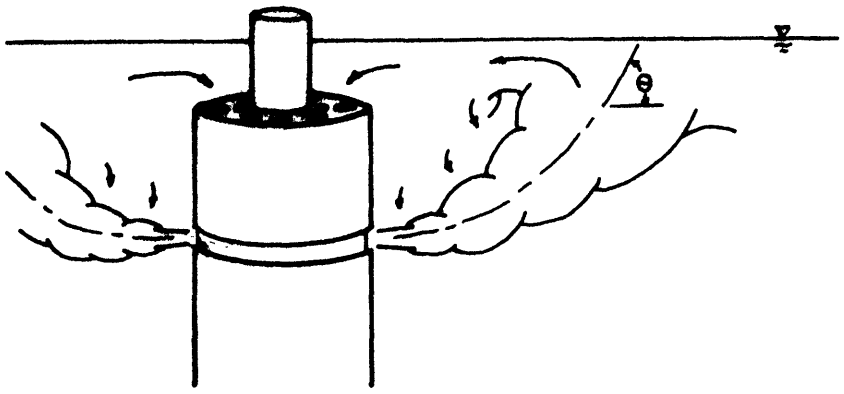

a. Confinement Induced Recirculation

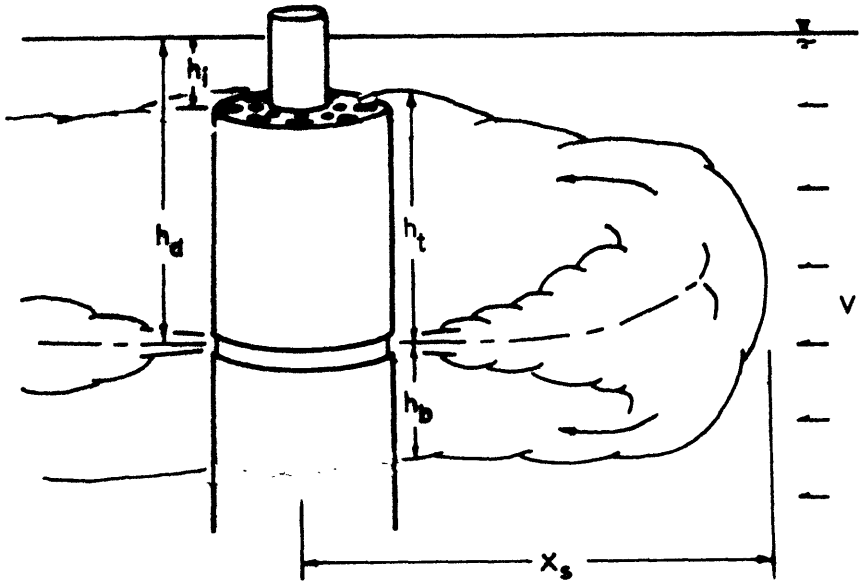

b. Current Induced Recirculation

Figure 34 Modes of Recirculation Definition Sketches

dependence is illustrated in Figure 35 a,b for the case of an evaporator discharge (k=1); similar curves could be drawn for the case of a mixed discharge. Two sets of curves (a and b) are required to describe this mode because of the hysteresis effect observed by Fry. Figure 35a gives the predicted value of h_d/ℓ_B' below which the jet was always observed to attach to the free surface (and thus to recirculate). Figure 35b gives the value of h_d/ℓ_B' above which the jet was always observed to be detached (and thus to not recirculate). For intermediate values of h_d/ℓ_B' the jet could be made to either attach or detach. Fry's analysis can not be applied directly to conditions with an ambient current, but observations of these experiments suggest that confinement-induced recirculation is limited to conditions for which

$$h_d/\ell_V \leq 0.5 \tag{5.6}$$

Current-induced recirculation involves a positively buoyant jet discharged at deeper submergence but lifted further by the dynamic effects of the ambient current. The jet is "swept back" before its axis intersects the free surface. Such a situation is portrayed in Figure 34b. In this case full coverage of the intake by the discharge flow (λ_N=1) is not guaranteed unless $h_t > (h_d - h_i)$. Unlike the confinement-induced recirculation, this mode is expected to occur in essentially the same form for the case of individual as well as radial port discharges.

In situations where the intake is fully covered (λ_N=1; confinement- or current-induced modes) the extent of direct recirculation λ should be inversely proportional to the jet dilution which, in turn, should be a function of the jet trajectory. In the absence of a current, this trajectory would be expected to scale with the length ℓ_H defined as

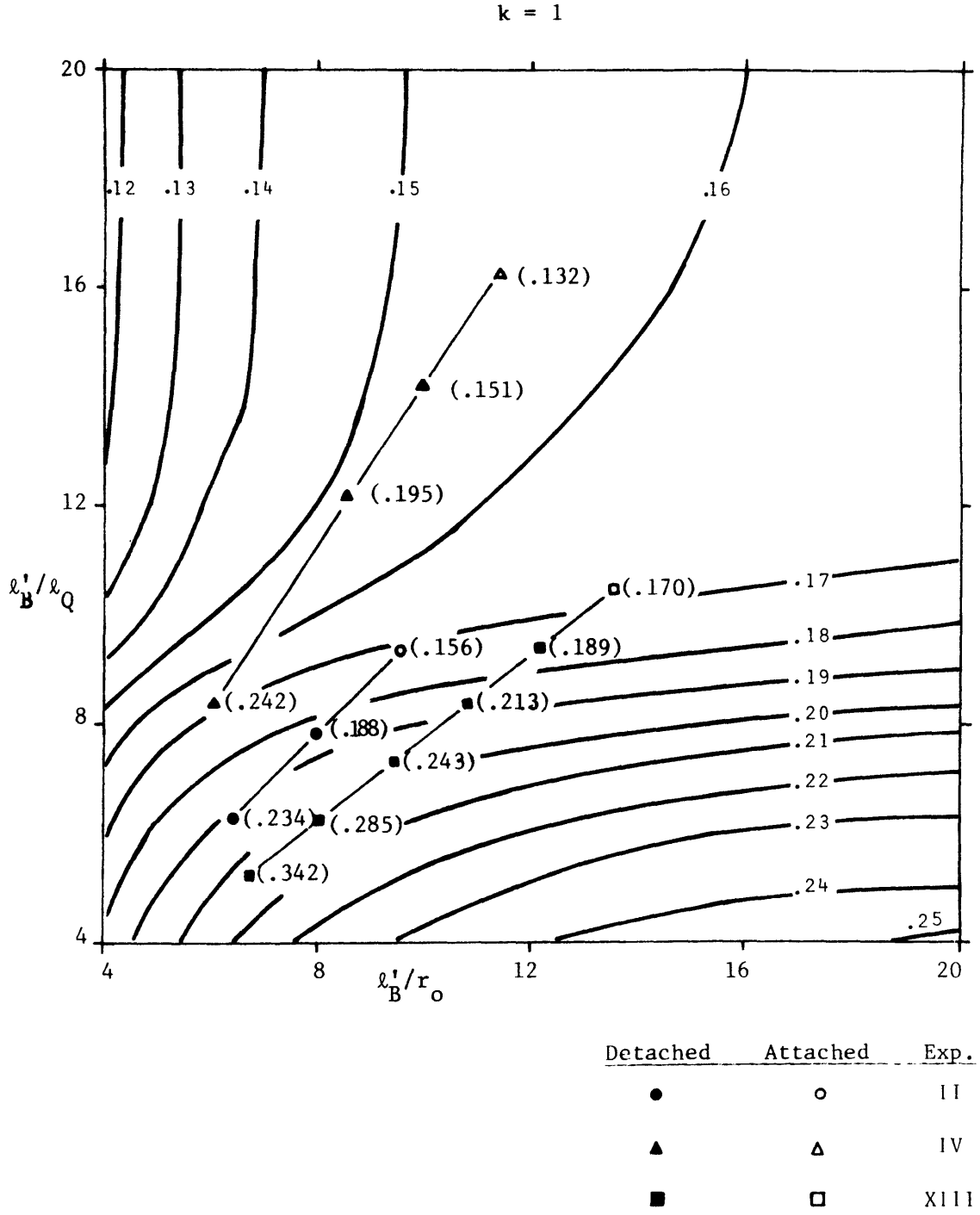

Figure 35a Integral Model Predictions and Experimental Data of h_d/ℓ'_B at Attachment (with Intake, k = 1)

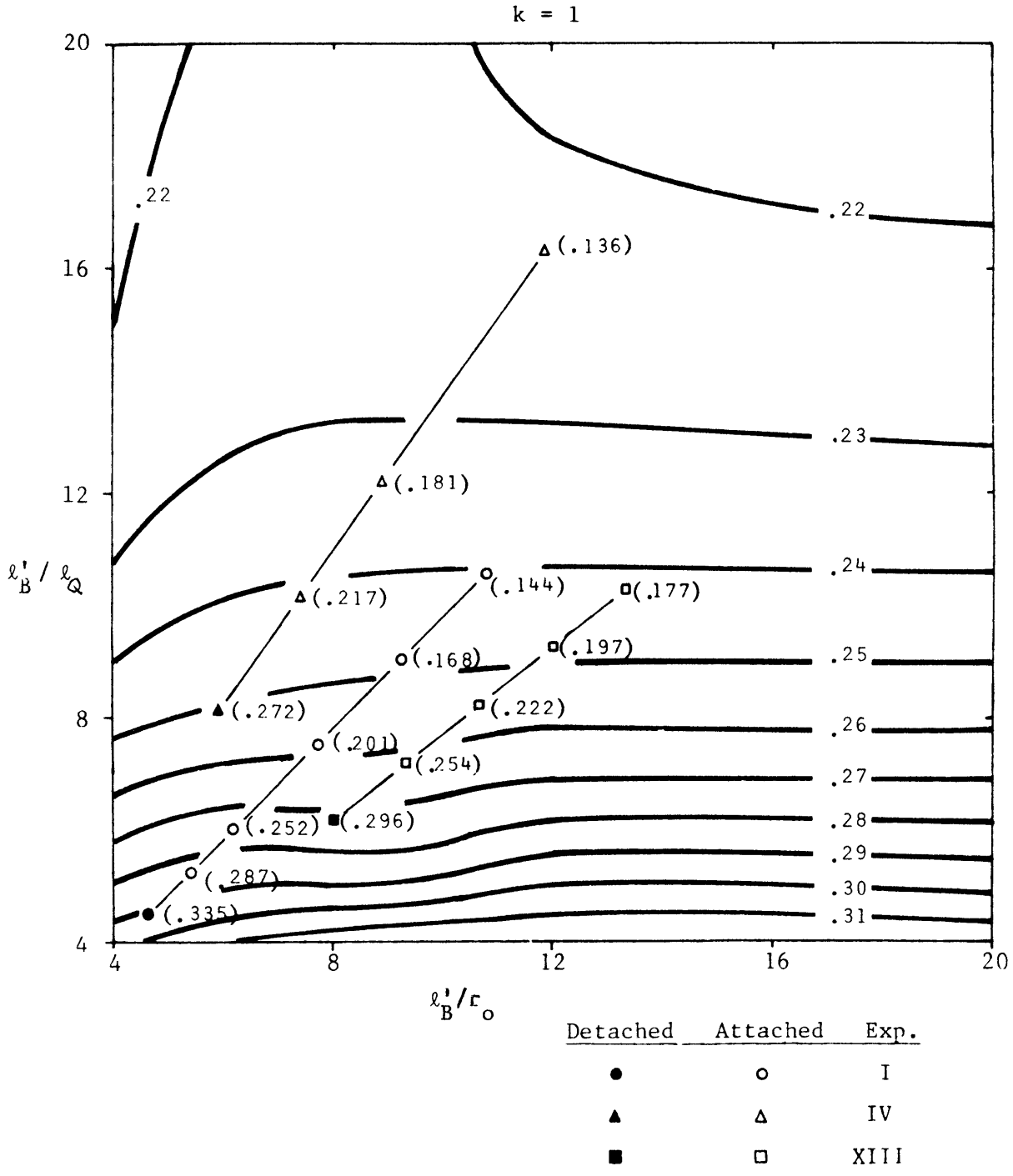

Figure 35b Integral Model Predictions and Experimental Data of h_d/ℓ_B' at Detachment (with Intake, k = 1)

$$\ell_H = h_o + \min \{h_d, h_t\} \tag{5.7}$$

See Figure 34b. Figure 36 plots $\lambda \ell_H/\ell_Q$ versus the parameter ℓ_q/ℓ_V. It is apparent that recirculation decreases (near field dilution increases) as current velocity increases and that recirculation is greater for the confinement-induced as opposed to the current-induced experiments, due to the higher dilution attained in the latter.

The variables h_t and h_b defined in Figure 34b are measured from the side-view photographs of Appendix I. Correlations of these variables with the governing length scales are used to help quantify recirculation as follows.

The total plume thickness at the position of the plant is $h_t + h_b$. Figure 37 plots $(h_t + h_b)/\ell_v$ versus the ratio ℓ_v/ℓ_s. For high current velocity (low ℓ_v/ℓ_s) a constant value of $(h_t + h_b)/h_b$ is expected while at low current speeds, zero total thickness is expected. The following straight-line relationships, consistent with the transition values of ℓ_V/ℓ_S defined in Fig. 33, were fit to the data of Figure 37:

$$\frac{h_t+h_b}{\ell_V} = \begin{cases} 0.6 & 0 < \ell_V/\ell_S < 2 \\ 1.0 - .2\,\ell_V/\ell_S & 2 < \ell_V/\ell_S < 5 \\ 0 & 5 < \ell_V/\ell_S < \infty \end{cases} \tag{5.8}$$

The net rise (fall) of the plume centerline at the position of the plant is given by $(h_t-h_b)/2$. Figure 38 shows this rise, normalized with respect to the total plume thickness, plotted versus ℓ_V/ℓ_B. Negatively buoyant plumes (positive ℓ_B) are expected to sink ($h_b > h_t$) while positively

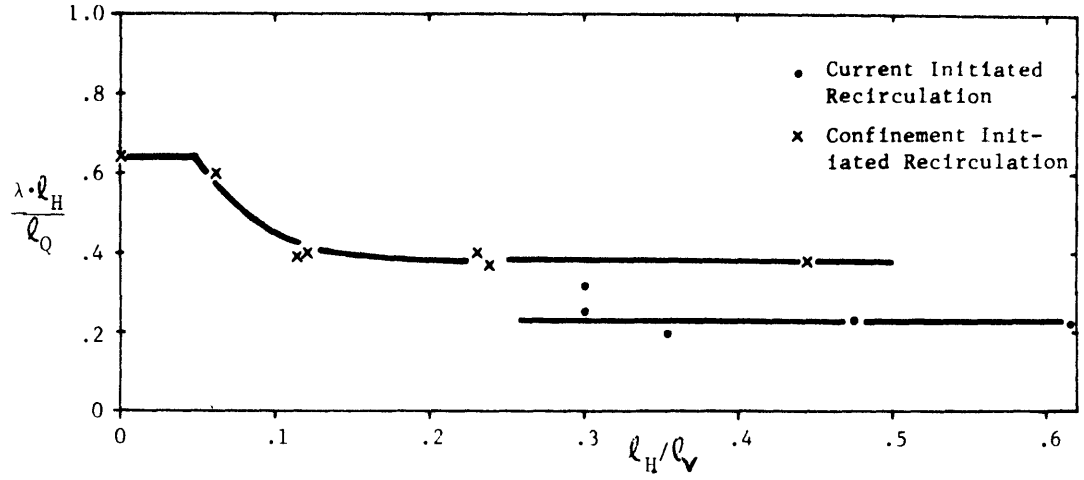

Figure 36 Normalized Recirculation for Experiments with Fully Covered Intakes

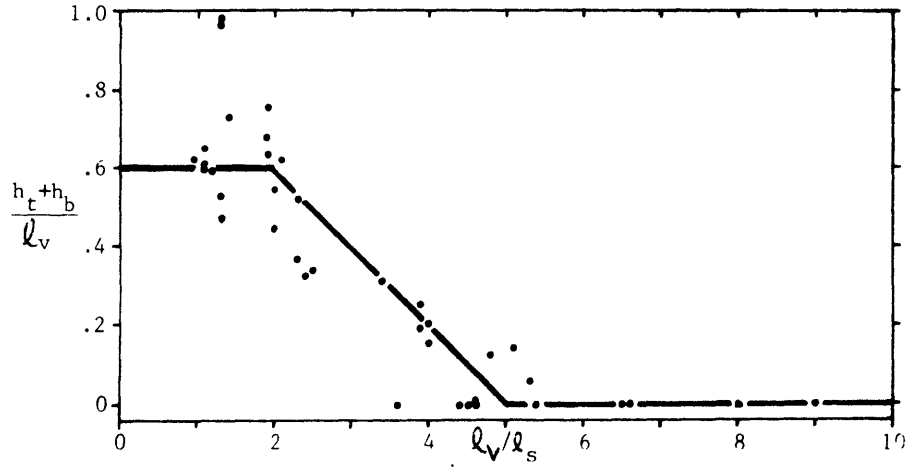

Figure 37 "Swept Back" Plume Thickness at the Position of the OTEC Plant

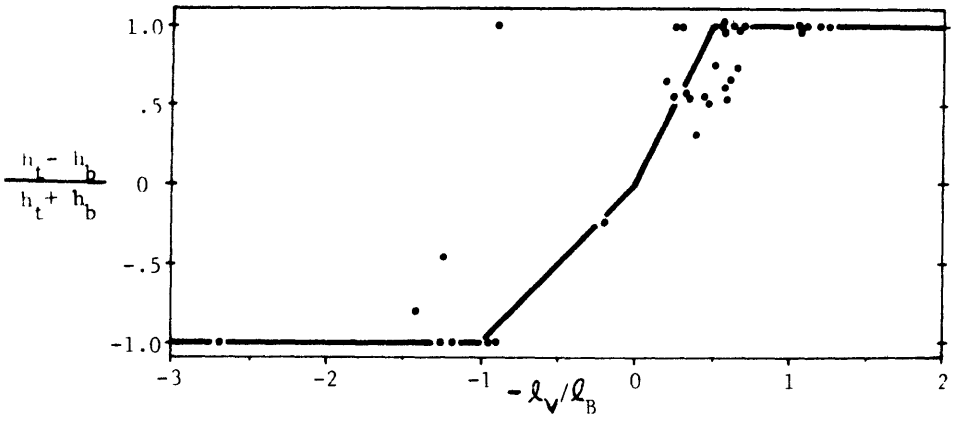

Figure 38 "Swept Back" Plume Rise or Fall at the Position of the OTEC Plant

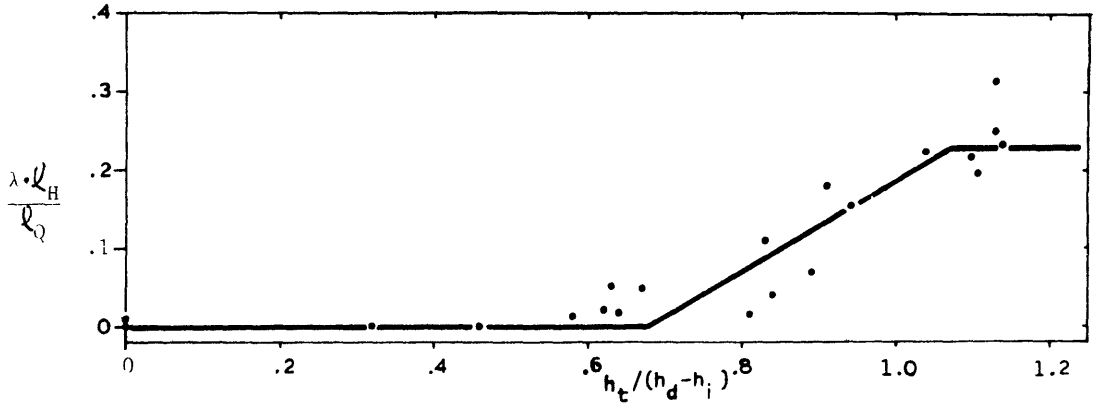

Figure 39 Normalized Recirculation for Fully "Swept Back" Plumes (Q_{back}/Q_T = 1.0)

buoyant plume (negative ℓ_B) are expected to rise. The following straight-line relationships, consistent with these trends, are fit to the data of Figure 38:

$$\frac{h_t-h_b}{h_t+h_b} = \begin{cases} -1 & -\infty < -\ell_V/\ell_B < -1 \\ \ell_V/\ell_B & -1 < -\ell_V/\ell_B < 0 \\ 2\ell_V/\ell_B & 0 < -\ell_V/\ell_B < .5 \\ 1 & .5 < -\ell_V/\ell_B < \infty \end{cases} \tag{5.9}$$

Full coverage of the intake (resulting in $\lambda_N = 1$) has been defined previously as occurring when

$$h_t \geq h_d - h_i \tag{5.10}$$

When inequality (5.10) is not satisfied, recirculation can still occur due to intermittent billowing of the plume. Remember that h_t and h_b are defined in terms of mean jet geometry. Figure 39 plots experimentally observed values (experiments where $Q_{back}/Q_T = 1.0$) of normalized recirculation versus $h_t/(h_d - h_i)$. Assuming $\lambda \sim Q_{back}/Q_T$ (if $Q_{back}/Q_T < 1$), straight-line relationships fit to this data are

$$\lambda \frac{\ell_H}{\ell_Q} = \begin{cases} 0.23[\frac{Q_{back}}{Q_T}] & 1.08 < h_t/(h_d-h_i) \\ 0.23[\frac{Q_{back}}{Q_T}]\ [-1.7 + 7.5\ \frac{h_t}{(h_d-h_i)}] & .68 < h_t/(h_d-h_i) < 1.08 \\ 0 & h_t/(h_d-h_i) < .68 \end{cases} \tag{5.11}$$

The non-zero value of λ for $h_t > .68(h_d - h_i)$ implies that intermittent

recirculation may still occur as long as the discharge-intake separation does not exceed 1.5 times the mean plume height h_t. This criterion is consistent with that used by Fry to define attachment in his studies of confinement initiated recirculation.

Equations (5.5), (5.6), (5.8), (5.9) and (5.11) and Figure 35a, b constitute a model to predict the extent of direct recirculation λ as a function of the various length scales characterizing the problem. A short computer program has been developed to evaluate these equations for each of the horizontal, radial discharge experiments. Predicted and observed values of recirculation are tabulated in Table 7 along with various other predicted measures of plume behavior. In general the agreement between prediction and observation is quite good.

To further illustrate the model predictions, Figure 40 plots contours of predicted recirculation versus discharge depth and current velocity for base case values of the other experimental parameters defined on Figure 41. Figure 40 is divided into three regions. The upper region (above the dashed line at h_d=40m) is defined by Figure 35a and Equation (5.6) and is where surface attachment (confinement-induced recirculation) is always expected. An intermediate region (between the dashed and solid lines) is defined by Figure 35b and Equation (5.6) and indicates where confinement-induced recirculation may be present. In the lowest region confinement-induced recirculation is not expected to occur. Current-induced recirculation is predicted mainly for the lowest region although some is predicted to occur in the intermediate region.

Also shown on the figure are experimentally observed values of recirculation. An experiment exhibiting recirculation was classified as

Table 7 Measured and Predicted Values of Direct Recirculation

Exp.	Experimental Measurements ℓ_V/ℓ_S	λ_{meas}	$\lambda_{pred.}$	Confinement Induced?	Model Predictions: Length Scale Domination ℓ_V	Intermediate	ℓ_S	Return Direction: Fully Up	Up	Down	Fully Down	Intake Coverage: Full	Intermittent	None
1A	8.3	.002	.000	No			X							X
1B	2.3	.073	.064	No		X		X				X		
3A	4.4	.006	.000	No		X		X						X
3B	3.0	.063	.049	No		X		X				X		
4A	9.0	.005	.000	No			X							X
4B	2.7	.004	.000	No		X				X				X
5A	5.1	.006	.000	No			X							X
5B	3.5	.002	.000	No		X					X			X
6A	5.3	.008	.000	No			X							X
6B	2.9	.100	.052	No		X		X				X		
7A	4.0	.002	.026	No		X		X					X	
7B	2.0	.070	.071	No		X		X				X		
8A	4.8	.063	.000	No		X		X						X
8B	2.6	.079	.058	No		X		X				X		
10	1.1	.007	.000	No	X				X					X
11	1.3	.028	.032	No	X				X				X	
12	1.1	.008	.000	No	X				X					X
13	1.3	.019	.059	No	X				X				X	
14	1.2	.020	.000	No	X				X					X
15A	3.6	.002	.024	No		X		X					X	
15B	1.9	.004	.049	No	X				X				X	
16	1.1	.010	.000	No	X				X					X
17	.97	.002	.000	No	X				X					X
18A	4.5	.001	.000	No		X					X			X
18B	2.5	.001	.000	No		X				X				X
19A	5.4	.003	.000	No		X					X			X
19B	2.9	.017	.000	No		X				X				X

TABLE 7 (continued)

Exp	Experimental Measurements ℓ_V/ℓ_S	λ_{meas}	$\lambda_{pred.}$	Confinement Induced?	Model Predictions: Length Scale Domination ℓ_V	Intermediate	ℓ_S	Return Direction: Fully Up	Up	Down	Fully Down	Intake Coverage: Full	Intermittent	None
20A	4.6	.001	.000	No		X				X				X
20B	2.4	.001	.000	No		X				X				X
22A	4.0	.250	.266	Yes				X				X		
22B	2.1	.250	.241	Yes				X				X		
23A	5.4	.380	.367	Yes				X				X		
23B	2.9	.250	.281	Yes				X				X		
24A	4.0	.001	.000	No		X					X			X
24B	2.1	.011	.000	No		X					X			X
25A	2.7	.240	.250	Yes				X				X		
25B	1.4	.250	.248	Yes				X				X		
35A	3.9	.019	.024	No		X		X					X	
35B	2.0	.091	.094	No		X		X				X		
36A	3.9	.027	.020	No		X		X					X	
36B	2.1	.089	.094	No		X		X				X		
37A	6.6	.002	.000	No			X							X
37B	1.4	.020	.000	No	X				X					X
38A	4.6	.002	.000	No		X					X			X
38B	2.5	.003	.000	No		X					X			X
39A	3.4	.046	.044	No		X		X					X	
39B	1.9	.068	.090	No	X			X					X	
40A	6.5	.006	.000	No			X	X						X
40B	1.3	-	.000	No	X				X					X
41A	1.9	.088	.090	No	X			X					X	
41B	1.3	.054	.000	No	X				X					X
42A	4.3	.002	.000	No		X					X			X
42B	2.3	.002	.000	No		X					X			X

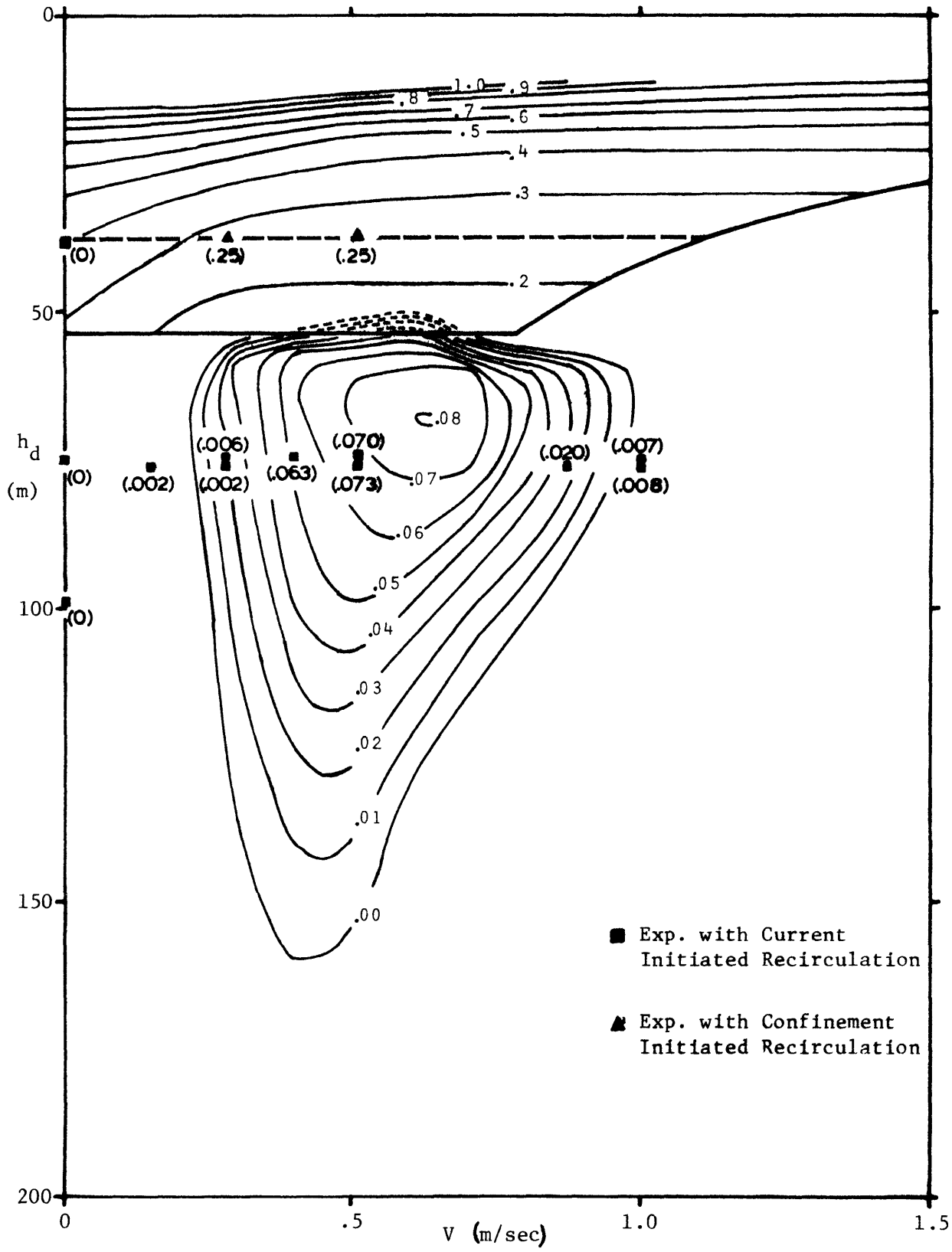

Figure 40 Model Predictions of Recirculation (λ) for the Evaporator Discharge of a Base Case 400 MW OTEC Plant

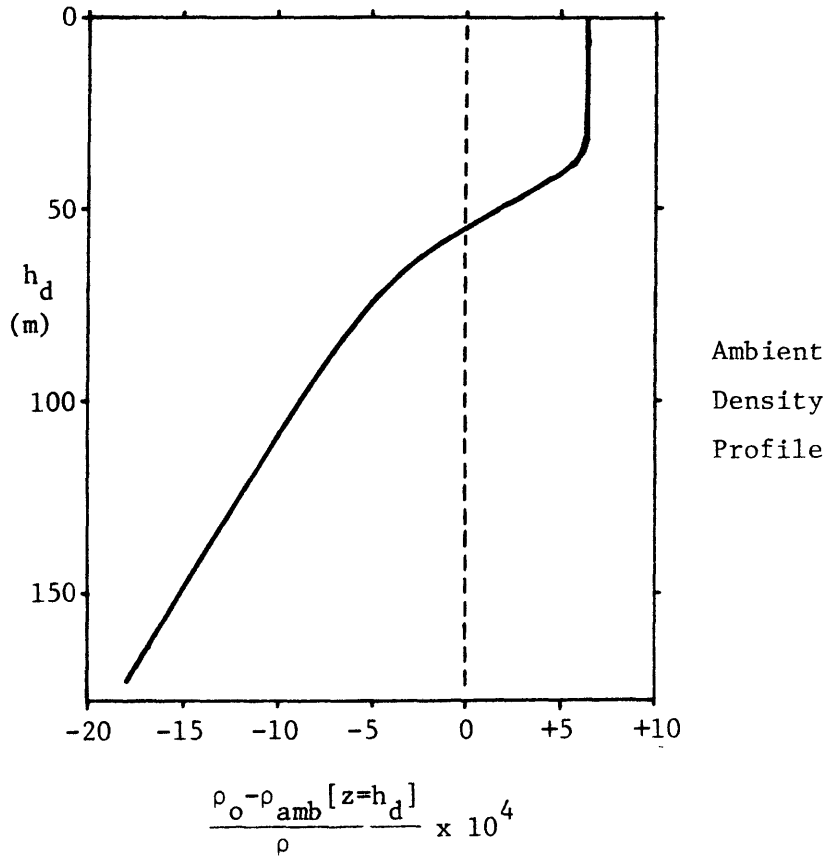

Warm Water Intake:

Depth = 9 m.
Flow = 2000 m^3/sec

Radial Evaporator Discharge:

Radius = 23 m.
½ Width = 2.0 m.
Depth = 11 - 200 m.
Flow = 2000 m^3/sec
Density = <see above>

Ambient Ocean:

Density Profile = <see above>
Current = 0 - 1.5 m/sec

Figure 41 Base Case 400 MW Evaporator Discharge Conditions

confinement-induced (triangles) or current-induced (squares) as a function of the jet angle at the point of impact with the surface (if any) as observed in the side-view photographs. (See Figure 34a) A value of $\theta \leq 90$ was used to define confinement-induced recirculation. Note that the parameters governing three experiments placed them in the overlap region. In two of these experiments, confinement-induced recirculation was observed while in one experiment current-induced recirculation was observed. The agreement between observed and predicted recirculation is good for both modes of recirculation.

Figure 40 can be used to summarize our present understanding of the recirculation phenomenon. Consider a discharge at h_d = 100 m. At low current speeds the near field is stratification-dominated and little of the discharge is swept back towards the intake. Increasing the current speed increases the quantity Q_{back} and results, in this example, in maximum recirculation at about .5 m/s. At higher speeds the plume is still swept back, but as indicated in Figure 37 the plume thickness diminishes, reducing the intake coverage. In this particular example, recirculation ceases at about 1 m/s.

Now consider a discharge into a fixed current speed of, say, 0.5 m/s. For discharge submergence below about 150 m., the plume is positively buoyant but the submergence is sufficient to prevent any coverage of the intake. As the discharge elevation is raised, the plume buoyancy is decreased but this effect is offset by the decrease in discharge-intake separation. Peak current-induced recirculation occurs for a discharge depth of about 75m. At some elevation above this depth, the discharge becomes negatively buoyant and the current will tend to pull the jet down

and away from the intake, thus avoiding recirculation. At higher discharge elevations (above about 50 m in this example), dynamic pressure effects are sufficient to overcome plume negative buoyancy leading to confinement-induced recirculation. In this example, the values of λ for this mode are in the range of 25% and above, or about three times the peak values predicted for current-induced recirculation.

5.4.4 Dilution Analysis

The length scales l_S and l_V have been shown to characterize the near field dimensions of the plume. From dimensional arguments, the induced near field flow can be estimated (to within a constant of proportionality) as

$$Q \sim M_o^{1/2} \ell_S \tag{5.12a}$$

$$Q \sim M_o^{1/2} \ell_V \tag{5.12b}$$

where the smaller (dominating) length (ℓ_S or ℓ_V) is used. The dilution S would be given by

$$S = \frac{Q}{Q_o} \sim \frac{(M_o^{1/2})\ \ell_S}{Q_o} \tag{5.13a}$$

for stratification-dominated runs, or

$$S = \frac{Q}{Q_o} \sim \frac{(M_o^{1/2})\ \ell_V}{Q_o} \tag{5.13b}$$

for current-dominated runs. Figures 42 and 43 are graphs of centerline dilution (S_c) and average dilution (S_{ave}) versus the dimensionally derived dilutions corresponding to the stratification- and current-dominated

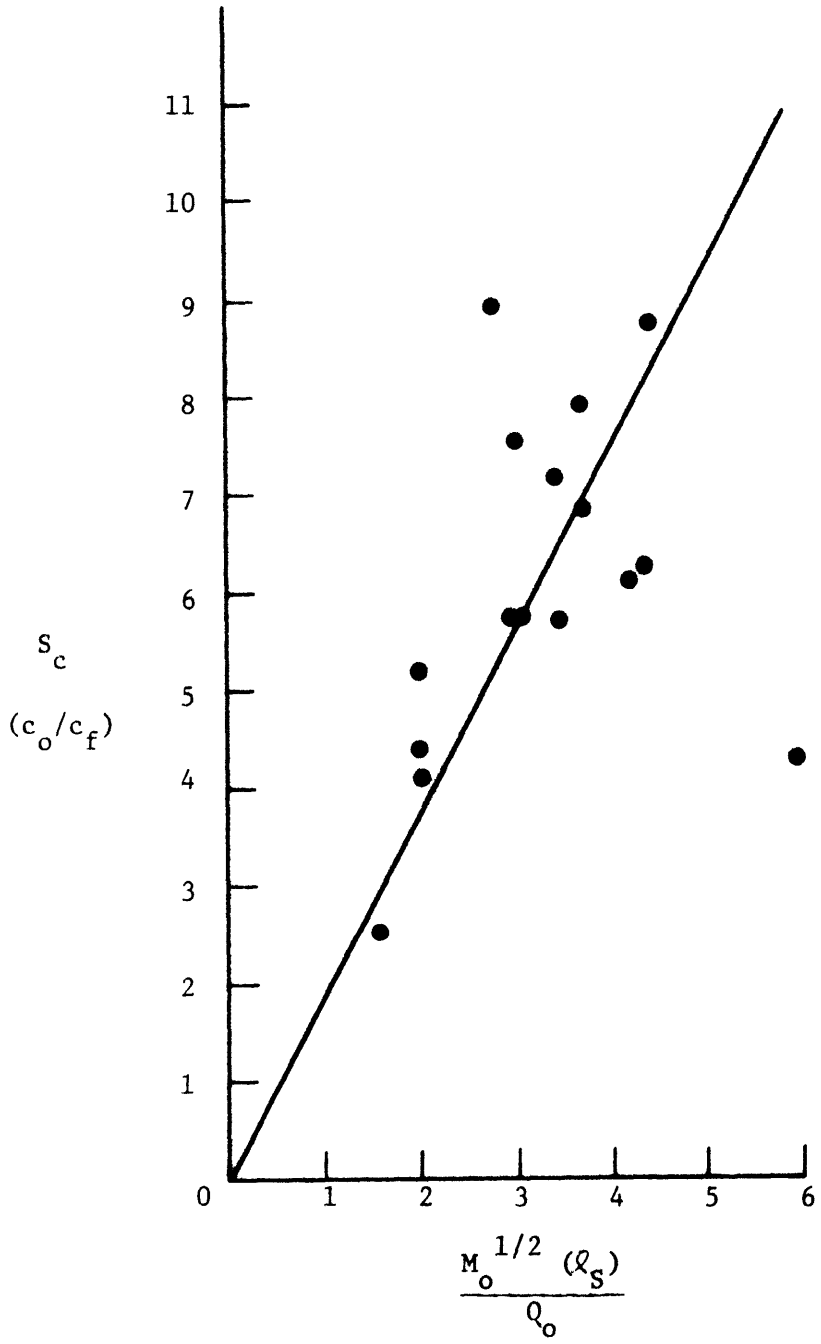

Figure 42a Centerline (S_c) Dilution Versus Dimensionally Derived Dilution for (Radial Port) Stratification Dominated Experiments

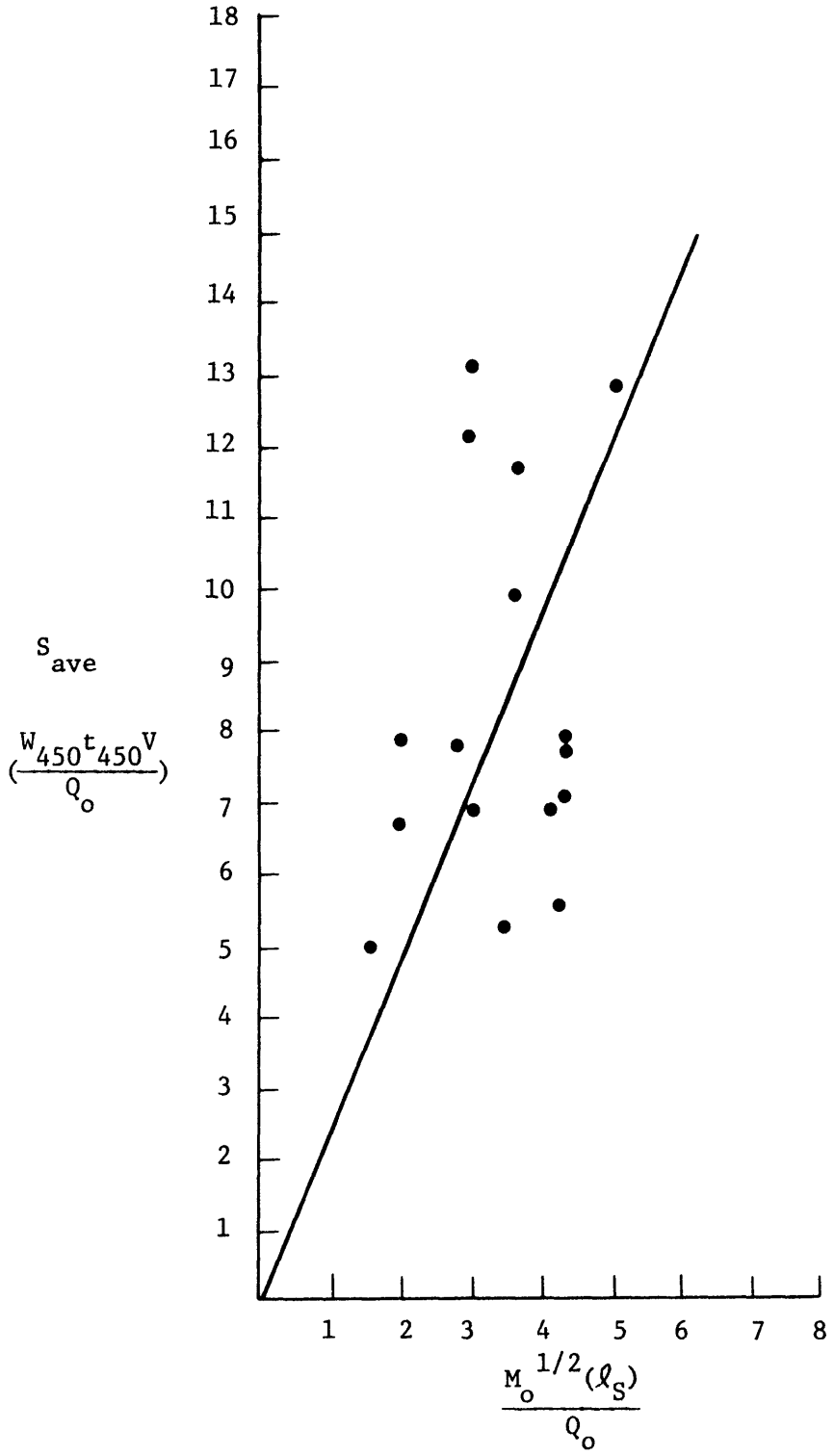

Figure 42b Average Dilution (S_{ave}) Versus Dimensionally Derived Dilution for (Radial Port) Stratification Dominated Experiments

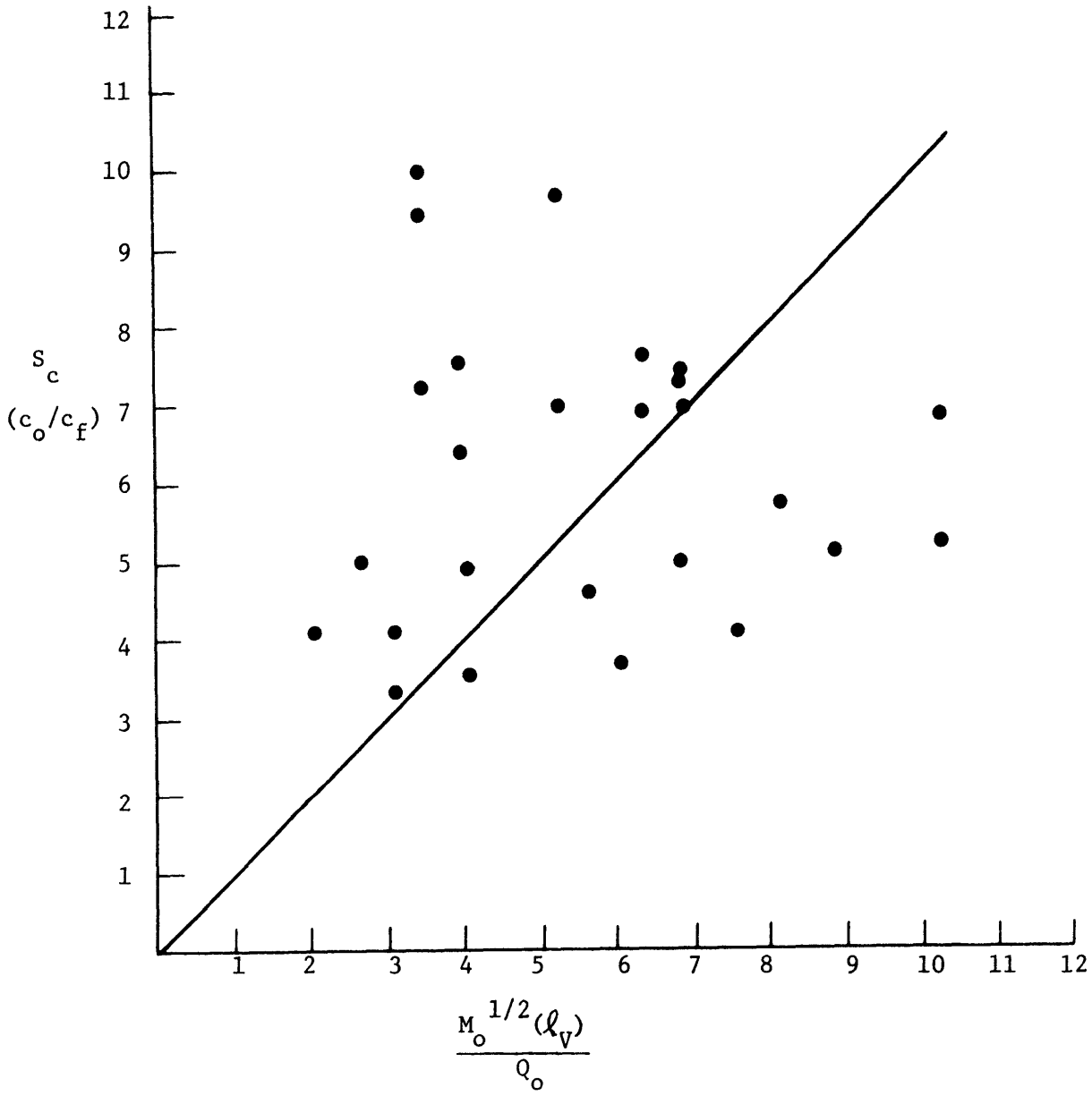

Figure 43a Centerline Dilution (S_c) Versus Dimensionally Derived Dilution for (Radial Port) Current Dominated Experiments

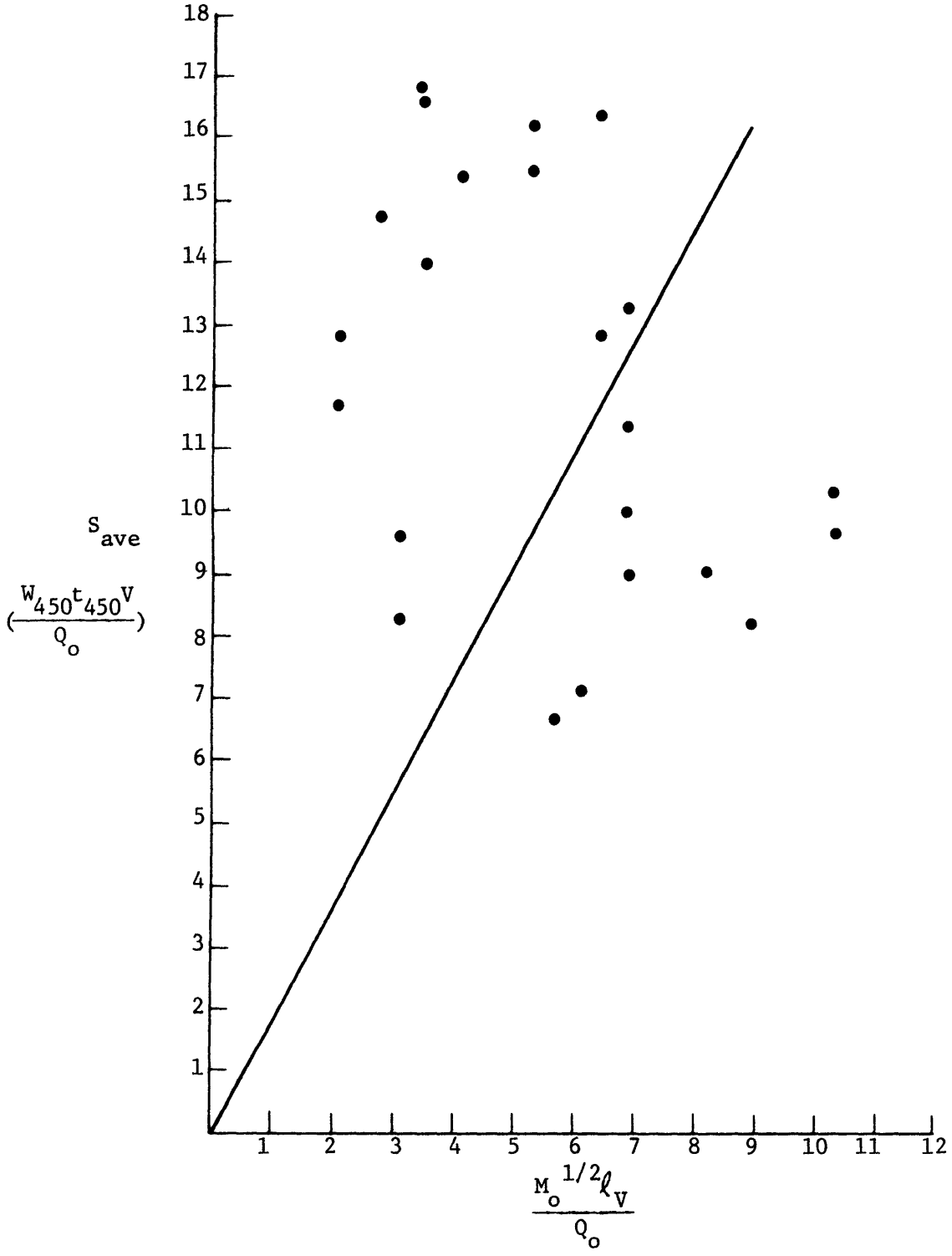

Figure 43b Average Dilution (S_{ave}) Versus Dimensionally Derived Dilution for (Radial Port) Current Dominated Experiments

experiments. Figure 42 indicates that both forms of measured dilution correlate fairly well with the derived dilution for stratification-dominated experiments. However, Figure 43 indicates that there is little correlation in the case of the current-dominated experiments. The effect of the current is to distort the near field resulting in a shorter ℓ_V upstream (windward side) of the plant than downstream (leeward side, where the current does not act against the flow of the discharge jets). The dimensionally derived dilution is proportional to the upstream ℓ_V; this relationship assumes that all mixing occurs within a radius of ℓ_V about the plant while in fact there is still considerable mixing outside of this distance behind the plant. Thus the observed point spread is not surprising, since a correlation between the measured dilution (at 450 meters behind the plant) and the derived dilution would imply that no mixing occurs outside of a distance ℓ_V from the plant.

5.4.5 Analysis of Additional Plume Characteristics

Data relating to the plume shape characteristics are available in Table 4 and Appendices I and II. Plume characteristics which are amenable to length scale analysis include the jet stagnation distance, lateral and vertical spreading of the plume and vertical displacement of the plume.

In Section 5.4.2 it was argued that plume geometry for current-dominated experiments (large V and ℓ_S/ℓ_V) was governed by the current length ℓ_V. For example, Figure 31 has shown a correlation between stagnation distance $X_s - r_o$ and ℓ_V. It is reasonable to assume that if the stagnation distance scales with ℓ_V, then the plume width should also scale with ℓ_V - at least over that portion of the plume in which discharge momentum is significant. In Figure 44 plume width (normalized by ℓ_V) has

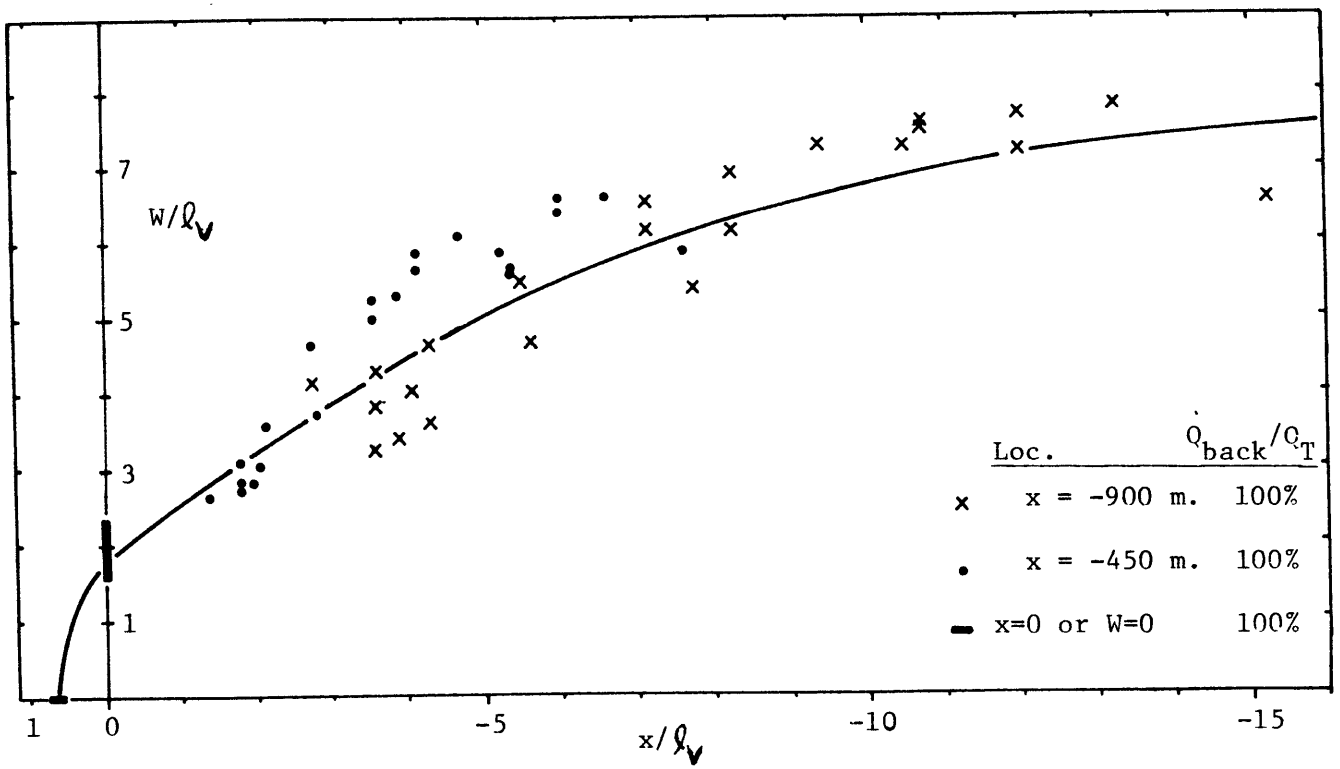

Figure 44 Normalized Plume Width versus Longitudinal Distance for Current Dominated Experiments.

been plotted versus longitudinal distance (normalized by ℓ_V) for the current-dominated experiments, i.e. those for which $Q_{back}/Q_T = 1.0$ in Figure 33. The widths used in Figure 43 have been derived from the overhead plume tracings of Appendix II at distances $X = X_S$, 0, -450 m., and -900 m. (prototype).

In Section 5.4.2 it was also argued that plume geometry for stratification-dominated experiments (small V and ℓ_S/ℓ_V) was governed by the stratification length ℓ_S. For example, Figure 32 has shown a correlation between the distance to the point of maximum plume thickness, $r(t_{max}) - r_o$, and ℓ_S for the stagnant water experiments. Figure 45 complements Figure 32 by plotting t_{max} versus ℓ_S for the same experiments. Figures 46 and 47 plot $(r(t_{max}) - r_o)/\ell_S$ and t_{max}/ℓ_S versus ℓ_S/ℓ_V for stratification-dominated experiments, i.e. those experiments with a weak current and characterized by values of Q_{back}/Q_T less than 1.0.

In stagnant or stratification-dominated experiments, an intermediate density layer will protrude upstream of $r(t_{max})$. It is reasoned below that this distance - and the shape of the wake in general - are scaled by ℓ_V for stratification-dominated experiments as well as for current-dominated experiment. In Section 5.4 it was shown that, for stratification-dominated experiments, dilution is limited mainly to $r < r(t_{max})$, and that the dilution at $r(t_{max})$ is proportional to ℓ_S/ℓ_Q. Thus the volume flux at this point would be proportional to $\ell_S Q_o/\ell_Q$. If the plume thickness at $r > r(t_{max})$ scales as t_{max} (i.e. is proportional to ℓ_S), then a characteristic lateral plume dimension is given by

$$W \sim \frac{\ell_S Q_o}{\ell_Q \ell_S V} = \ell_V \qquad (5.14)$$

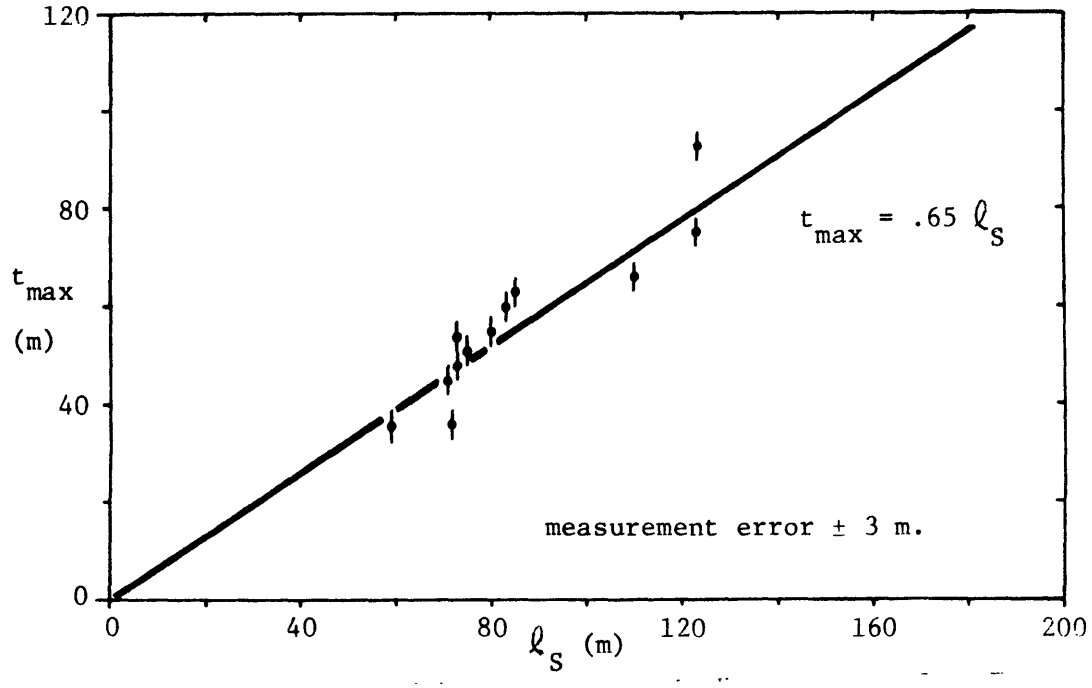

Figure 45 Maximum Near Field Plume Thickness versus ℓ_s for Stagnant Water Experiments

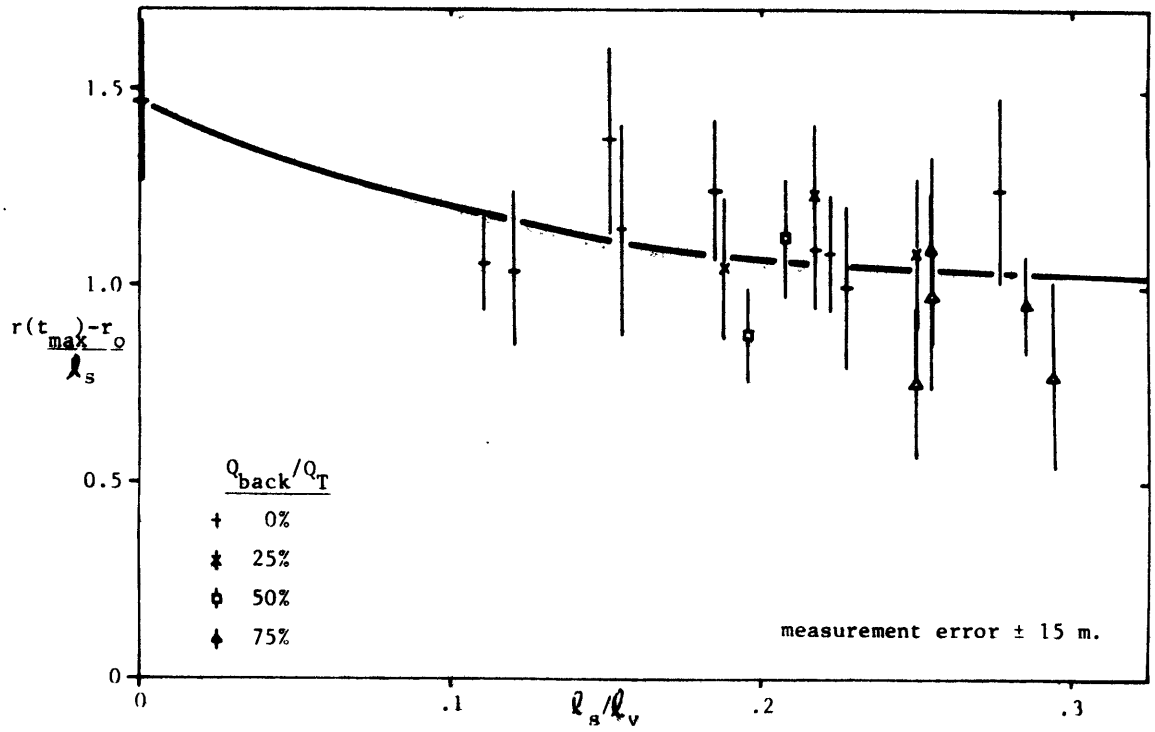

Figure 46 Distance to Maximum Near Field Plume Thickness for Stratification Dominated Experiments

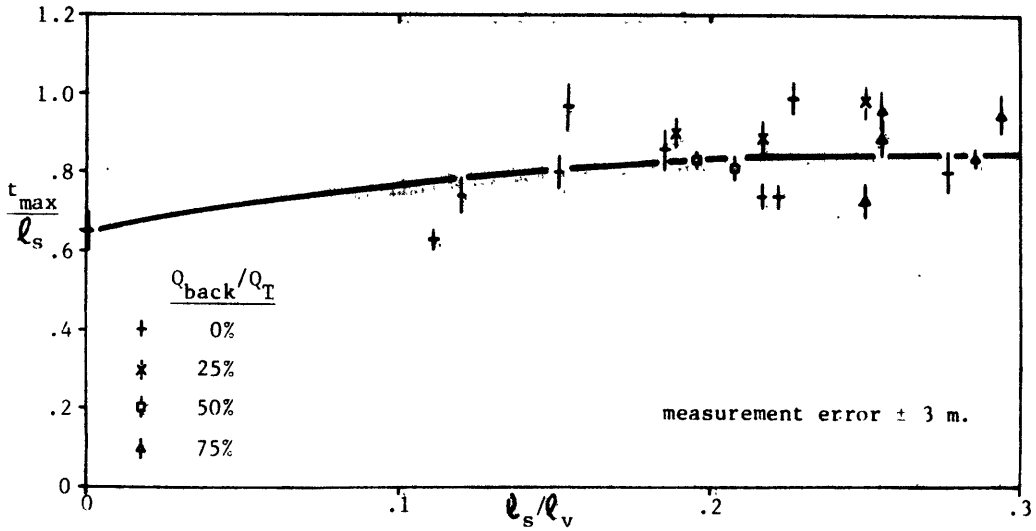

Figure 47 Maximum Near Field Plume Thickness for Stratification Dominated Experiments

This is the same relationship, though not necessarily with the same proportionality, that governs current-dominated experiments. The assumption that plume thickness at $r > r(t_{max})$ scales with ℓ_S is tested in Figure 48 a and b for the case of plume thickness at $x = -450$ m. Figure 48 a, based on the side-view tracings of the stagnant water experiments (Adams et al., 1979), shows a nearly constant value of the ratio t_{450}/ℓ_S. The increase in that ratio for the stratification-dominated experiments reported here ($Q_{back}/Q_T = 0$) is shown in Figure 48b.

If Equation 5.14 is valid, then other geometric measures, such as the distance to the point of stagnation, should scale similarly with ℓ_V. Figure 49 plots the stagnation length for all radial, horizontal discharge experiments versus the ratio ℓ_V/ℓ_S, indicating that the proportionality in Equation 5.14 appears greatest for stratification-dominated experiments. Figure 50, plotting plume width (normalized by ℓ_V) for the stratification-dominated experiments leads to the same conclusion. As with Figure 41, the widths used in Figure 50 have been derived from the overhead plume tracings of Appendix II at distances $x = X_S$, 0, -450 m., and -900 m. (prototype).

Section 5.4.3 defined $h_t - h_b$ as a measure of the plume elevation at the plant (x=0); this measure was used to help model recirculation. For purposes of environmental assessment, it is also desirable to identify plume elevation behind the plant where the plume has achieved gravitational equilibrium. If ambient current effects are not strong then the net rise (fall) of the plume $h_{eq} - h_d$ can be related to the buoyancy and stratification lengths, ℓ_B and ℓ_S. Consider an immiscible negatively buoyant fluid discharged into a linearly stratified ambient. The discharged fluid will fall a

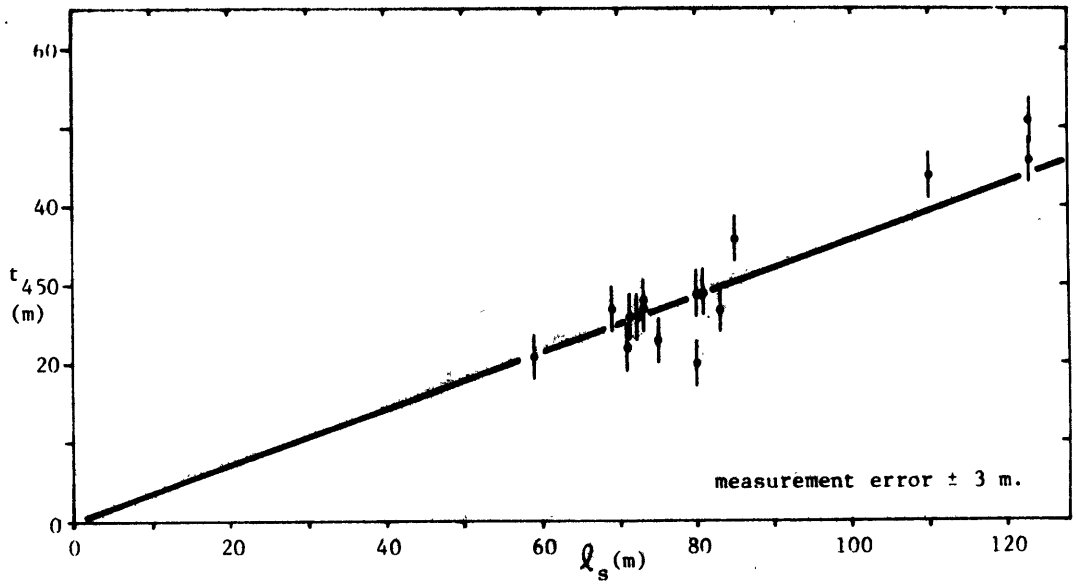

Figure 48a Plume Thickness for Stagnant Water Tests

Stagnant Tests

Tests with Current ($Q_{back}/Q_T = 0$)

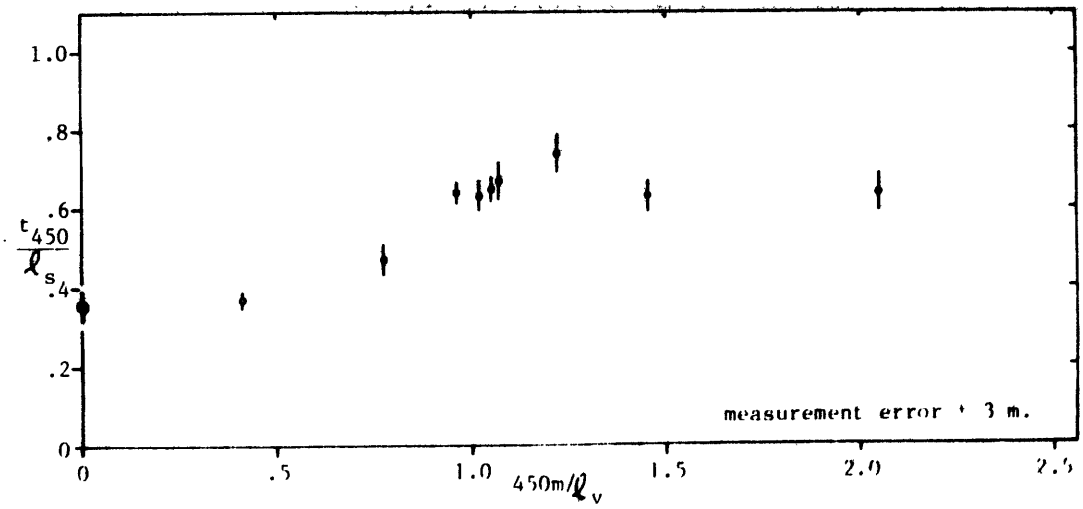

Figure 48b Plume Thickness 450 m. Downstream of Plant (for Experiments with $Q_{back}/Q_T = 0$)

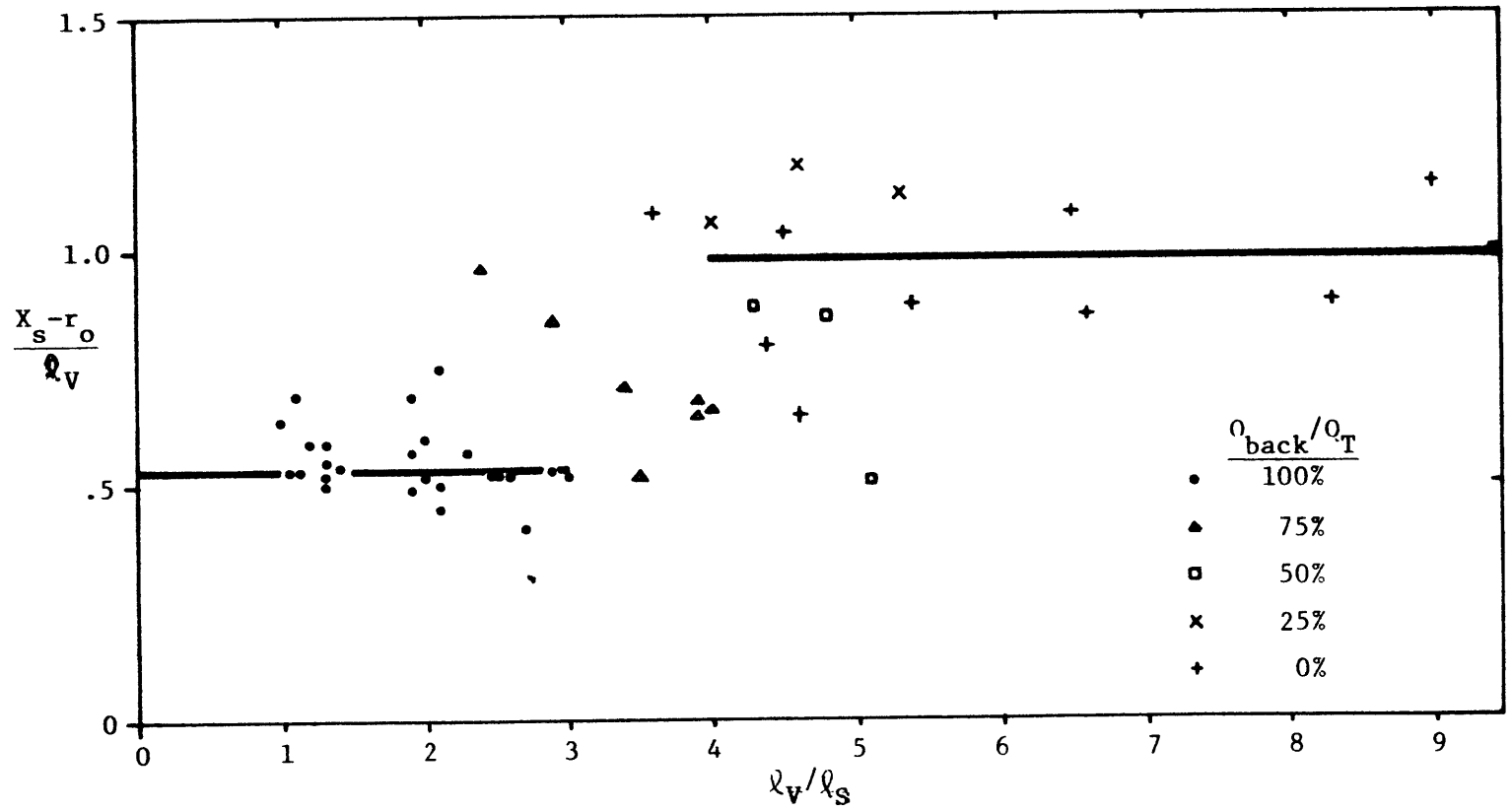

Figure 49 Stagnation Length for all Radial Horizontal Discharge Experiments

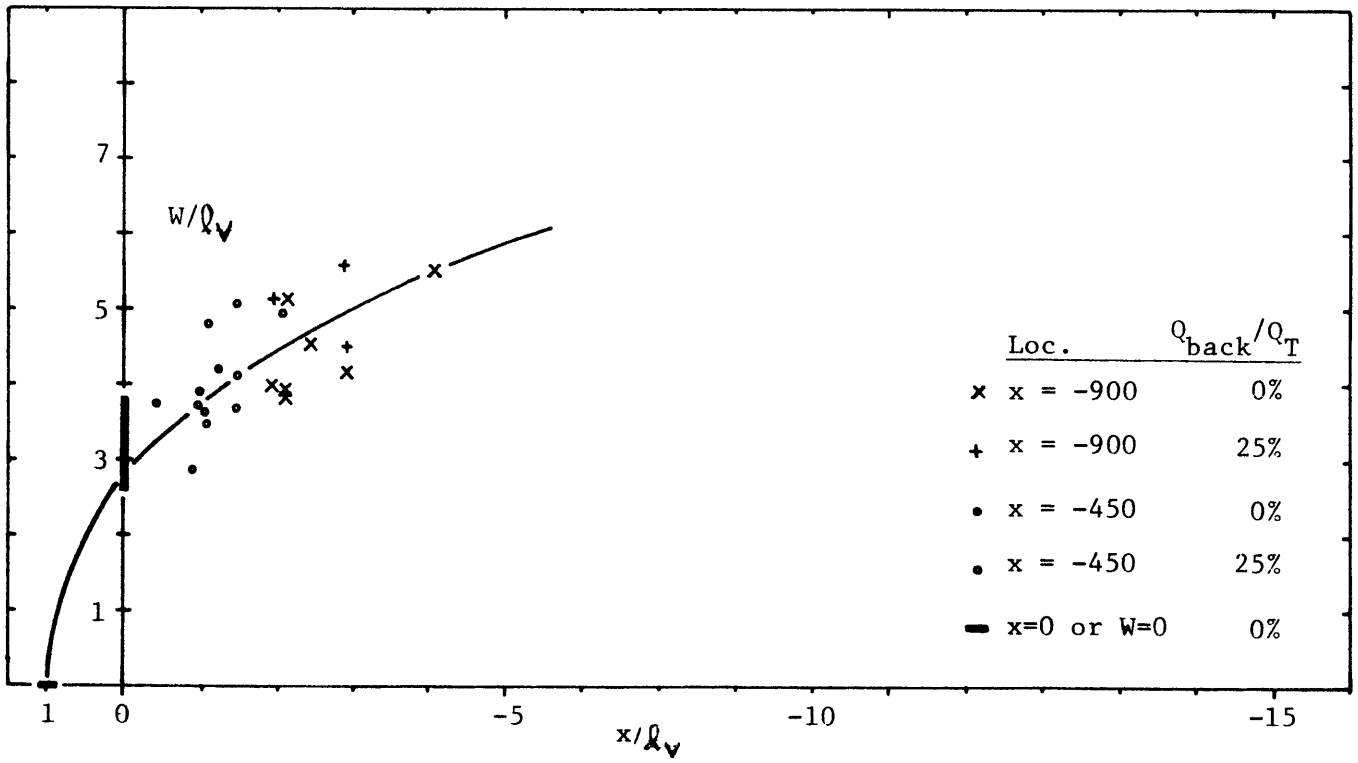

Figure 50 Normalized Plume Width versus Longitudinal Distance for Stratification Dominated Experiments

distance

$$h_{eq} - h_d = \frac{B_o}{N^2 Q_o} \tag{5.15}$$

Now consider that the discharged fluid is miscible and achieves a dilution

$$S \sim \frac{\ell_s}{\ell_Q} \tag{5.16}$$

due to mixing with ambient fluid at the level of the discharge. The effective discharge volume will then be SQ_o, the buoyancy flux will be unchanged, and thus the discharged fluid should fall a distance

$$h_{eq} - h_d = \frac{B_o \ell_Q}{N^2 \ell_S Q_o} = \frac{\ell_S^3}{\ell_B |\ell_B|} \tag{5.17}$$

Figure 51 plots observed values of $h_{eq} - h_d$ versus $\ell_S^3 / \ell_B |\ell_B|$ for both the stagnant water tests and the stratification-dominated tests. In each case the values of h_{eq} have been derived from the side-view photographs and have been plotted with error bars of ± 3 m (prototype). Figure 51 indicates reasonable agreement between data and Equation 5.17, especially for the stagnant water experiments.

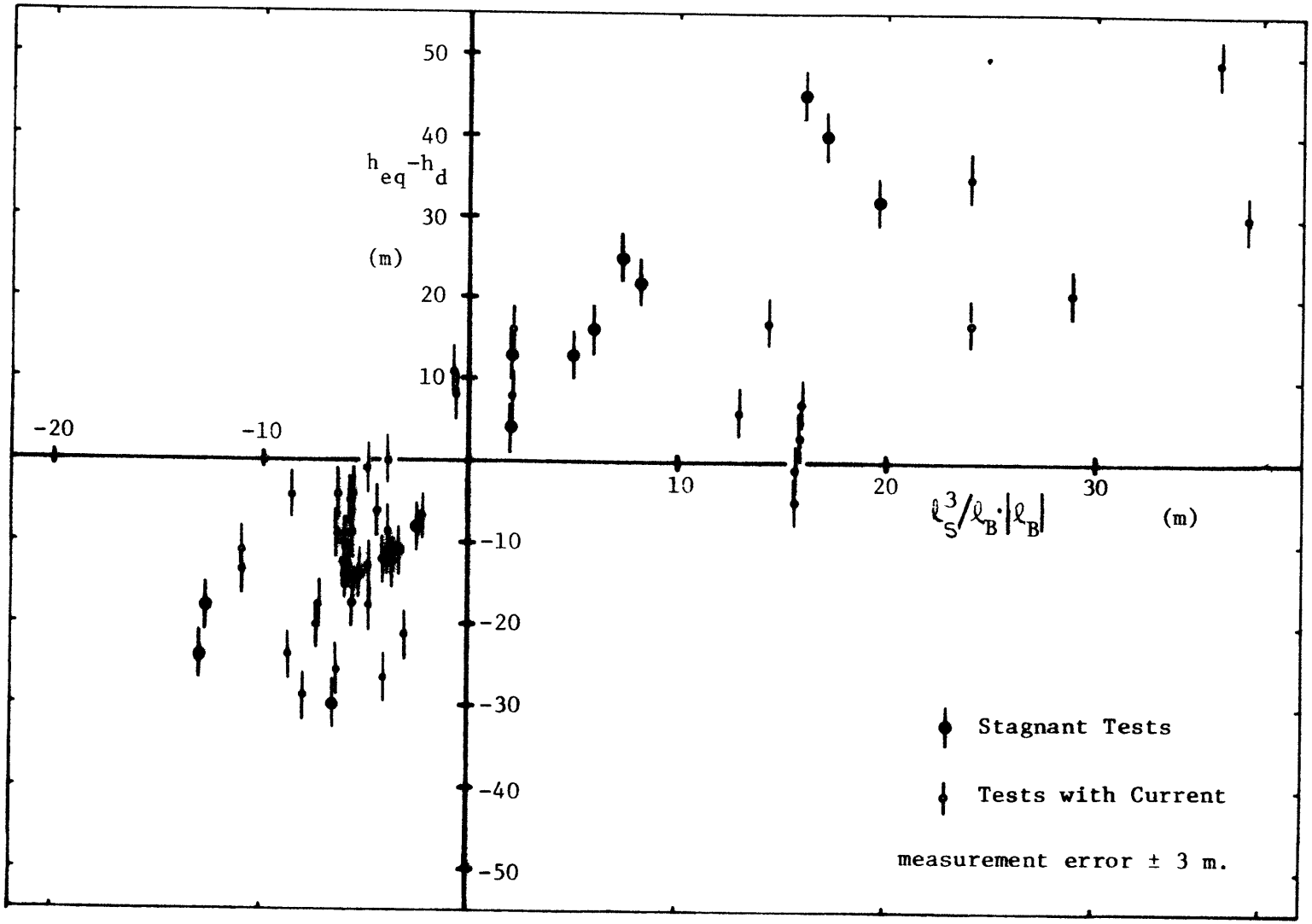

Figure 51 Observed Plume Rise or Fall for Ambient Current and Stagnant Water Experiments

VI. SUMMARY AND CONCLUSIONS

6.1 Summary

Ocean thermal energy conversion plants have been suggested as a means of producing power based on the thermal difference between the upper and lower temperature strata in a tropical ocean. The purpose of this study has been to examine, experimentally, the performance of generic OTEC plant designs under realistic operating conditions in order to determine the tendency for recirculation and to characterize plume transport to help in the assessment of environmental impact.

Both mixed and non-mixed discharge concepts were examined for power plant sizes ranging from 200 MWe to 600 MWe with nominal evaporator and condenser discharge flow rates of $5 m^3/s$-MWe. Discharge port designs considered include radial and separate (4-jet and single jet) configurations with variations in port elevation, discharge area and horizontal and vertical discharge angle (separate ports only). An axisymmetric, annular intake structure which promoted vertical downward inflow was located near the surface (in the mixed layer of the density profile) for all of the experiments.

Prototype ambient ocean conditions were modeled by towing the model OTEC plant through a temperature-stratified basin. Uniform current speeds ranging up to 1.0 m/s (prototype) were studied for oceans with continuously stratified density profiles characterized as having small, medium and large mixed layer depths.

Measurements included temperature, dye concentration and visual observation from still and motion pictures. Results derived from these measurements are presented in tables and graphs in prototype dimensions for direct use by OTEC designers. Many of the results are also analyzed and presented in non-dimensional terms to extend their generality.

6.2 Conclusions

The following conclusions are based on the experimental results and the dimensional analysis.

1. Recirculation can occur directly as the result of discharged water reaching the intake, or indirectly as the result of ambient water which interacts with the discharged flow before being drawn into the intake. Recirculation was characterized by the percent direct recirculation λ and by the intake temperature drop $\Delta T_i'$ (below the temperature of the ambient water at the level of the intake).

2. No significant recirculation was observed in any tests involving a discharge directed with a vertical (downward) component. For plants employing a horizontal discharge, recirculation was observed to be a complex function of a number of parameters.

3. Confinement-induced recirculation was observed under certain conditions of shallow discharge submergence and low to moderate current speeds. This recirculation occurs only for the radial slot discharges and results from negative pressures above the jet associated with the proximity of the free surface. Measured values of direct recirculation

fell in the range of λ = 25% - 40%. These values, and the parameter ranges under which this type of recirculation was observed, are consistent with mathematical predictions by Fry et al., (1981).

4. Current-induced recirculation was observed for certain combinations of ambient current speed and deeper discharge submergence (resulting in generally positive discharge buoyancy). Under this mode the plume was observed to billow upward resulting in either steady recirculation (for sufficiently small discharge-intake separation) or intermittent recirculation (for larger discharge-intake separation). Measured values of direct recirculation fell in the range of λ = 0 to 10% and were a strong function of current speed; maximum recirculation was observed at intermediate current speeds of about 0.5 m/s. Recirculation of this type was observed for both radial slot and multiple port discharge configurations, although somewhat greater recirculation was observed with the radial slot configuration.

5. Experiments employing mixed evaporator and condenser discharges resulted in significantly lower values of direct recirculation as compared with tests of separate (evaporator only) discharge. This decreased tendency for recirculation is due to the greater negative plume buoyancy resulting from the mixture of evaporator and condenser flows. However, intake temperatures were often observed to decrease for mixed discharges, even in the absence of direct recirculation. The intake temperature drops were often comparable (order of 0.5°C) with those observed in analogous tests with separate discharges and

are ascribed to various indirect effects associated with the larger discharge flows of the mixed discharge schemes.

6. Minimum measured plume dilutions were found to fall in the range of S = 5 to 10. This implies that the peak near field concentration of any discharged chemicals (e.g., biocides, products of corrosion, working fluid leaks) would be in the range of 10 to 20% of the discharge concentrations.

7. Many plume properties were successfully interpreted using length scale analysis. In addition to the various geometric length scales characterizing the plant, the following near field length scales were found to be most significant: current length scale formed from the discharge kinematic momentum flux and the ambient current speed, stratification length scale formed from the discharge kinematic momentum flux and the ambient density gradient, and the buoyancy length scale formed from the discharge kinematic momentum and buoyancy fluxes.

8. The ratio of stratification to current length scale was used to distinguish between current-dominated and stratification-dominated experiments. In the former (characterized by relatively large current speed) the discharge plume was swept back largely in the vertical plane which leads to the possibility of current-induced recirculation. In the latter (characterized by relatively low current speed) the discharge collapses in front of the plant forming an intermediate layer; the downstream flow is caused primarily by lateral circulation.

9. The horizontal and vertical extents of the discharge wake were found to be correlated with the current length scale. Different correlations were appropriate for current-dominated and stratification-dominated tests. Appropriate normalization of the outside plume dimensions by the current length scale allows many plume profiles to be collapsed onto one curve.

10. The rise or fall of the equilibrium plume elevation (above or below the discharge elevation) was found to be correlated with the ratio of the stratification length cubed divided by the buoyancy length squared. The proportionality is explainable based on simple mixing principles and allows one to quickly assess the ultimate level reached by various discharged substances (e.g., chemicals or nutrients).

11. The various length scales were used to develope a simple mathematical model describing direct recirculation. Comparison was made between predicted and observed recirculation for cases involving horizontal radial slot discharges. Good agreement was observed.

REFERENCES

Adams, E.E., D.J. Fry, D.H. Coxe, and D.R.F. Harleman, "Research on the External Fluid Mechanics of Ocean Thermal Energy Conversion Plants: Report Covering Experiments in Stagnant Water," R.M. Parsons Laboratory for Water Resources and Hydrodynamics, M.I.T. Technical Report No. 250, Cambridge (June, 1979).

Allender, J.H, J.D. Ditmars, R.A. Paddock, and K.D. Saunders, "OTEC Physical and Climatic Environmental Impacts: An Overview of Modeling Efforts and Needs," Proc. Fifth Ocean Thermal Energy Conversion (OTEC) Conf., Miami, pp. III-165 - III-189 (Feb. 20-22, 1978).

Bathen, K.H., R.M. Kamins, D. Kornreich, and J.E.T. Moncur, "An Evaluation of Oceanographic and Socio-Economic Aspects of a Nearshore Ocean Thermal Energy Conversion Pilot Plant in Subtropical Hawaiian Waters," University of Hawaii, Honolulu, Hawaii, Grant no. AER74-17421 A01 (April, 1975).

Claude, Georges, "Power from the Tropical Seas," Mechanical Engineering, 52, 1039-1044 (December, 1930).

Craya, A., "Theoretical Research on the Flow of Non-homogeneous Fluids," Houille blanche, January-February, 1949, pp. 44-45.

d'Arnsoval, A., "Utilization des Forces Naturales. Avenir de L'electricite," La Revue Scientifique, 370-372 (September 17, 1881).

Ditmars, J.D. and R.A. Paddock, "OTEC Physical and Climatic Environmental Impacts," Proc. Sixth Ocean Thermal Energy Conversion (OTEC) Conference, Washington D.C., pp. 13.11-1 - 13.11-8 (June 19-22, 1979).

Fry, D.J., "Effects of Oceanic Flow Patterns on the Thermal Efficiency of Ocean Thermal Energy Conversion (OTEC)," M.S. Thesis, Dept. of Civil Engineering, Carnegie-Mellon Univ., Pittsburgh (April, 1976).

Fry, D.J., "Jet Diffusion in Confined Regions," Ph.D. Thesis, Dept. of Civil Engineering, Massachusetts Institute of Technology, Cambridge, MA (July, 1980).

Fry, D.J. and E.E. Adams, "Jet Diffusion in Confined Regions" MIT Energy Laboratory Report No. MIT-EL 81-050, Cambridge, MA (September 1981).

Gabriel, P., "Experimental Research on the Flow of Non-homogeneous Fluids," Houille blanche, January-February, 1949, pp. 56-64.

Giannotti, J.G., "Thermal Mixing Consideration in OTEC Park Design (Partial Input, Task II)," Rept. No. 77-018-03, Giannotti and Buck Assoc., Inc., Annapolis, MD. (October, 1977).

Heronemus, W.E., et al., "Research Applied to Ocean Sited Power Plants," University of Massachusetts, Progress Report: NSF/RANN/SE/GI-34979/PR/744 (February, 1975).

Jirka, G.H., G. Abraham, D.R.F. Harleman, "An Assessment of Techniques for Hydrothermal Prediction," R.M. Parsons Laboratory for Water Resources and Hydrodynamics, Department of Civil Engineering, M.I.T. Technical Report No. 203, Cambridge, MA (1975).

Jirka, G.H., R.P. Johnson, D.J. Fry, and D.R.F. Harleman, "Ocean Thermal Energy Conversion Plants: Experimental and Analytical Study of Mixing and Recirculation," R.M. Parsons Laboratory for Water Resources and Hydrodynamics, M.I.T. Technical Report No. 231, Cambridge, MA (September, 1977)

Lockheed Missiles and Space Company, Inc., "OTEC Efflux Impact," Vol. II, Ocean Thermal Energy Conversion (OTEC) Power Plant Technical and Economic Feasibility," NSF Report No. NSF/RANN/SE/GI-C937/FR/75/1, (April, 1975).

Mangarella, P.A., "An Analysis of the Fluid Motion into the Condenser Intake of a 400 MWe Ocean Thermal Difference Power Plant," NSF Rept. No. NSF/RANN/SE/GI-34979/TR/75/3, University of Massachusetts, Amherst, MA (March, 1975).

McCaffrey, E.F., Electronics Engineer, R.M. Parsons Laboratory for Water Resources and Hydrodynamics, personal communication (May, 1980).

Miller, Arthur R., "Ranges and Extremes of the Natural Environment Related to Design Criteria for Ocean Thermal Energy Conversion Plants," Woods Hole Oceanographic Institute (October, 1977).

Molinari, R.L., and J.F. Festa, "Ocean Thermal and Velocity Characteristics of the Gulf of Mexico Relative to the Placement of a Moored OTEC Plant," Atlantic Oceanographic and Meteorological Laboratories, Miami, FL (October, 1978).

"Ocean Thermal Energy Program; Research on an Evaluation and Test Program," TRW Systems Group, Contract No. NSF C958 (February, 1975).

Proceedings of the Third Ocean Thermal Energy Conversion Conference, Houston, TX (May, 1975).

Proceedings of the Fourth Ocean Thermal Energy Conversion Conference, University of New Orleans, New Orleans, LA (July, 1977).

Proceedings of the Fifth Ocean Thermal Energy Conversion Conference, Miami Beach, FL (February, 1978).

Proceedings of the Sixth Ocean Thermal Energy Conversion Conference, Washington D.C. (June, 1979)

Roberts, G.O., S.A. Piacsek, and J. Toomre, "Two-Dimensional Numerical Model of the Near Field Flow for an Ocean Thermal Power Plant. Part III. Simulation of the Lockheed Baseline Design," Naval Research Lab., Report No. NRL-GFD/OTEC 6-76 (December, 1976).

Sundaram, T.R., S.K. Kapur, A.M. Sinnarwalla, and E. Sambuco, "The External Flow Field Associated with the Operation of an Ocean Thermal Power Plant," Hydronautics, Inc., Report No. COO-2348-1 (December, 1977).

Sundaram, T.R., S.K. Kapur, and A.M. Sinnarwalla, "Some Further Experimental Results on the External Flow Field of an OTEC Power Plant," Hydronautics, Inc., Report No. COO-2348-2 (April, 1978).

Van Dusen, E., and P.A. Mangarella, "An Analysis of the Thermal and Nutrient Properties of the Condenser Discharge Plume Created by an Ocean Thermal Difference Power Plant," NSF Report No. NSF/RANN/SE/GI-34979/TR/74/2, University of Massachusetts, Amherst, MA (October, 1974).

Wolf, A.W., "OTEC Thermal Resource Report," Ocean Data Systems, Inc., Monterey, CA, Contract No. ET-78-C-01-2898 (May, 1979).

APPENDIX I

SIDE VIEW PHOTOGRAPHIC TRACINGS OF THE DISCHARGE PLUME

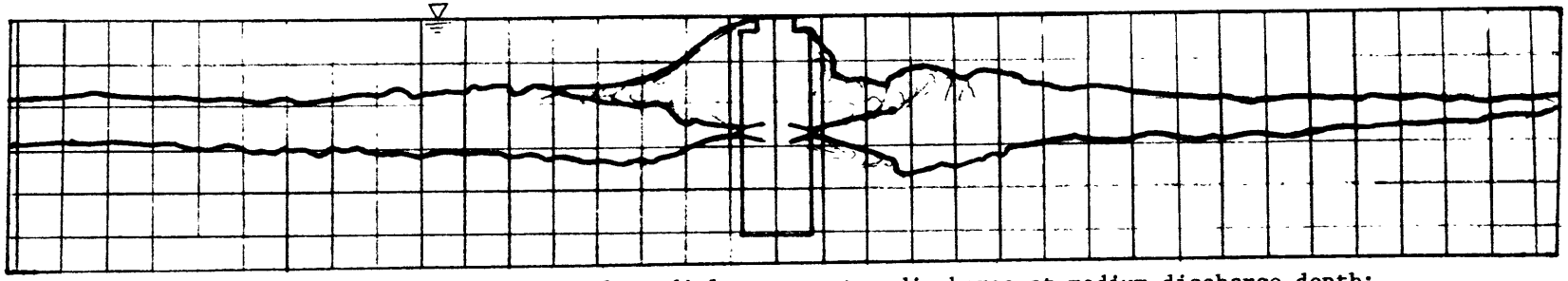

Run 1A: 400 MWe plant; horizontal, radial, evaporator discharge at medium discharge depth; medium mixed layer depth; current speed = .15 m/s. Grid spacing = 30 m.

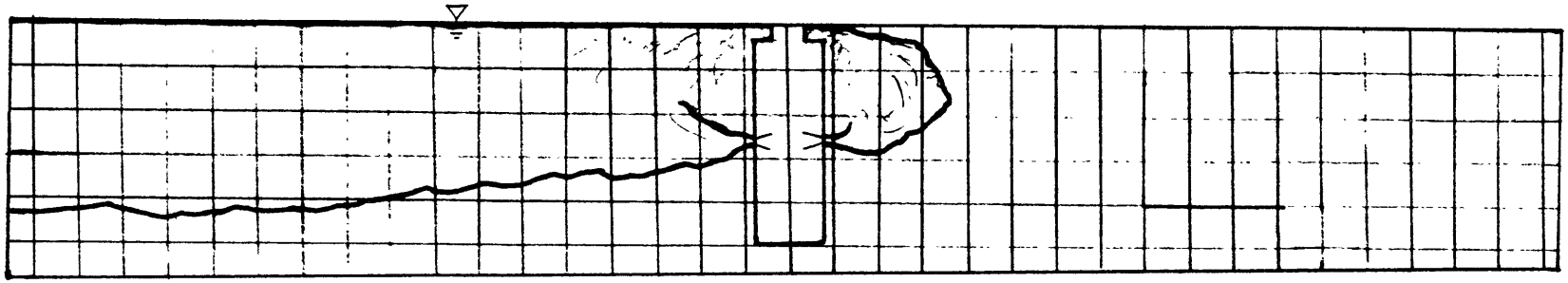

Run 1B: 400 MWe plant; horizontal, radial, evaporator discharge at medium discharge depth; medium mixed layer depth; current speed = .51 m/s. Grid spacing = 30 m.

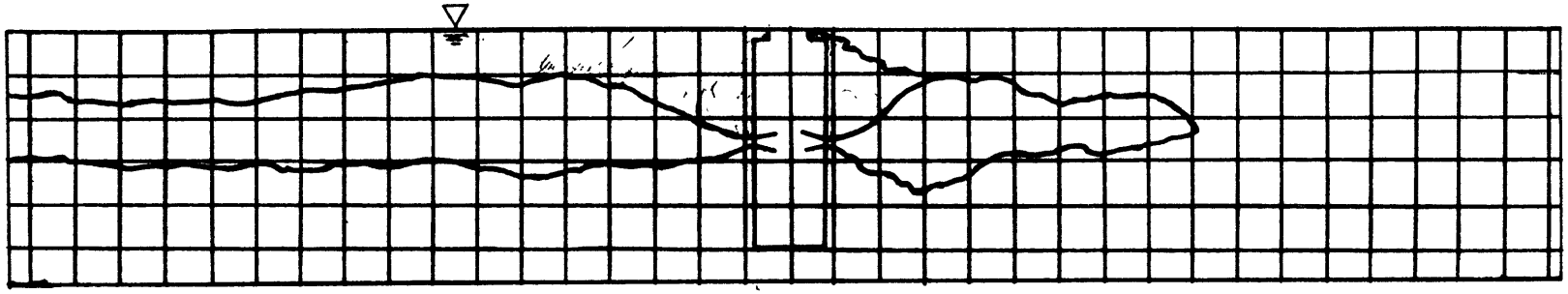

Run 3A: 400 MWe plant; horizontal, radial, evaporator discharge at medium discharge depth; medium mixed layer depth; current speed = .27 m/s. Grid spacing = 30 m.

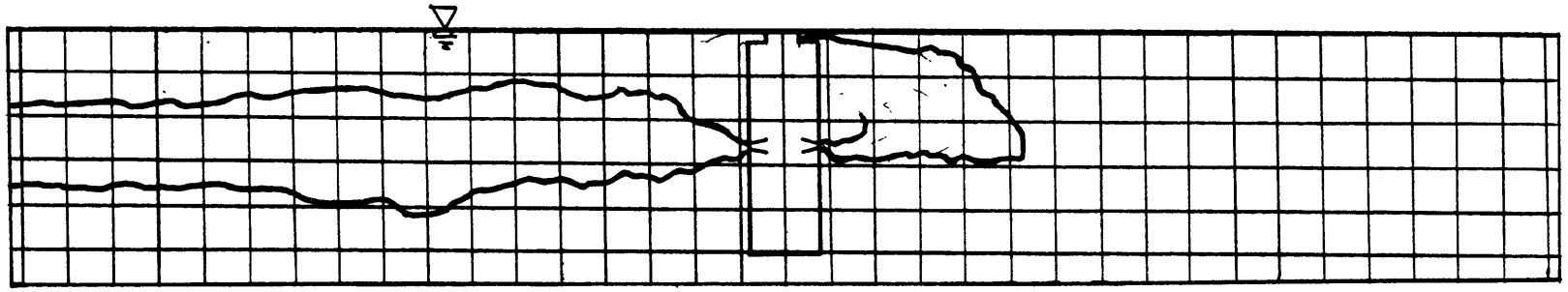

Run 3B: 400 MWe plant; horizontal, radial, evaporator discharge at medium discharge depth; medium mixed layer depth; current speed = .40 m/s. Grid spacing = 30 m.

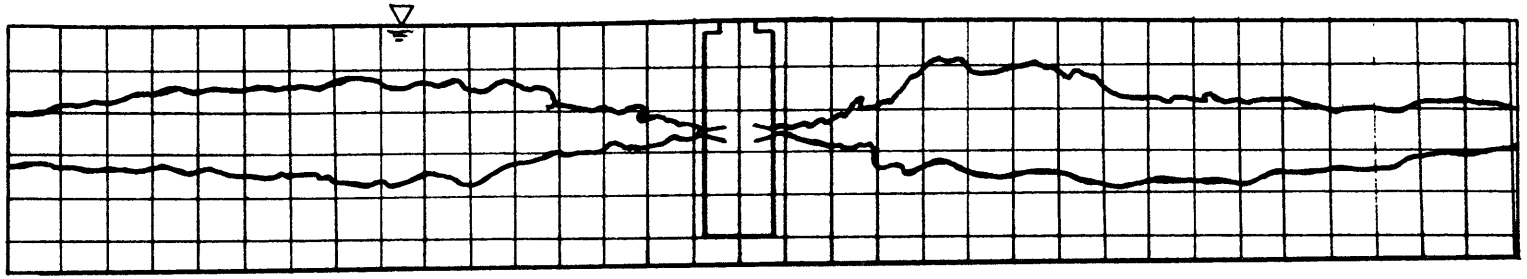

Run 4A: 400 MWe plant; horizontal, radial, mixed discharge at medium discharge depth; medium mixed layer depth; current speed = .15 m/s. Grid spacing = 30 m.

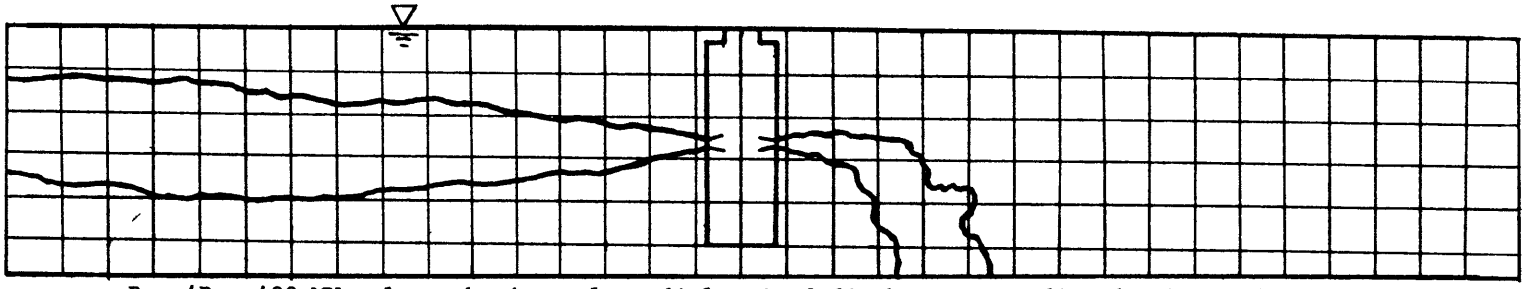

Run 4B: 400 MWe plant; horizontal, radial, mixed discharge at medium discharge depth; medium mixed layer depth; current speed = .51 m/s. Grid spacing = 30 m.

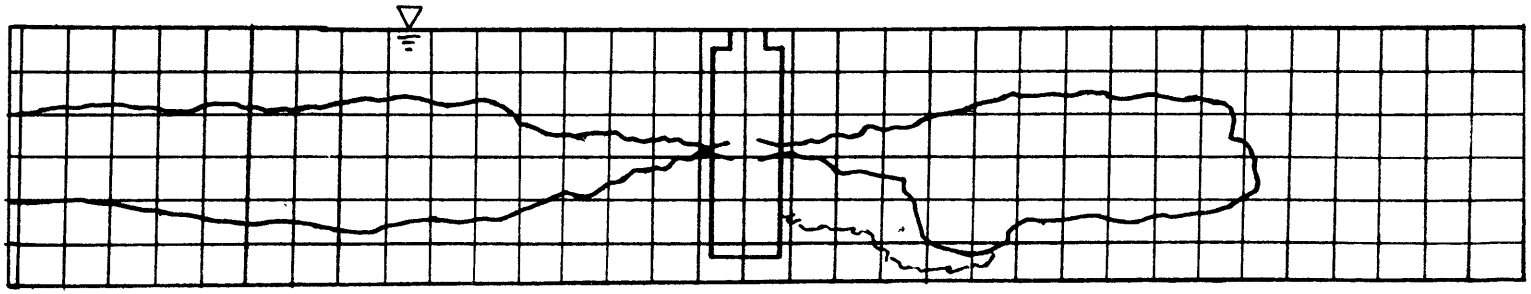

Run 5A: 400 MWe plant; horizontal, radial, mixed discharge at medium discharge depth; medium mixed layer depth; current speed = .27 m/s. Grid spacing = 30 m.

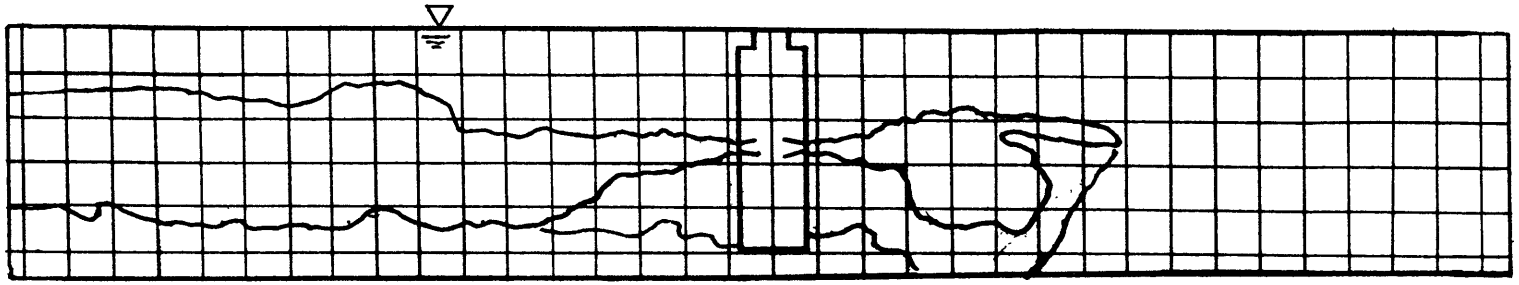

Run 5B: 400 MWe plant; horizontal, radial, mixed discharge at medium discharge depth; medium mixed layer depth; current speed = .40 m/s. Grid spacing = 30 m.

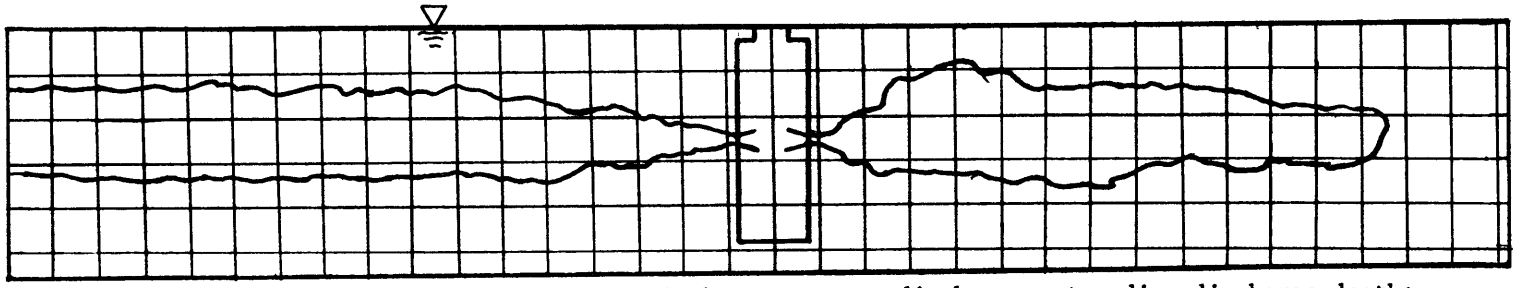

Run 6A: 600 MWe plant; horizontal, radial, evaporator discharge at medium discharge depth; medium mixed layer depth; current speed = .27 m/s. Grid spacing = 30 m.

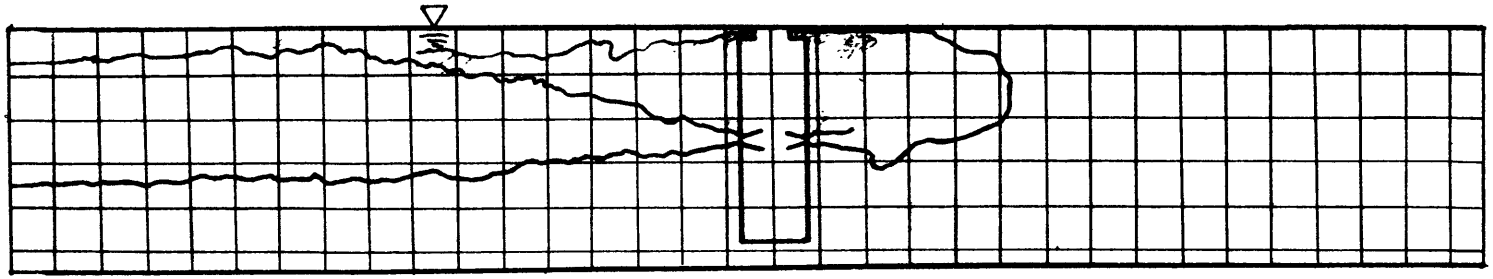

Run 6B: 600 MWe plant; horizontal, radial, evaporator discharge at medium discharge depth; medium mixed layer depth; current speed = .51 m/s. Grid spacing = 30 m.

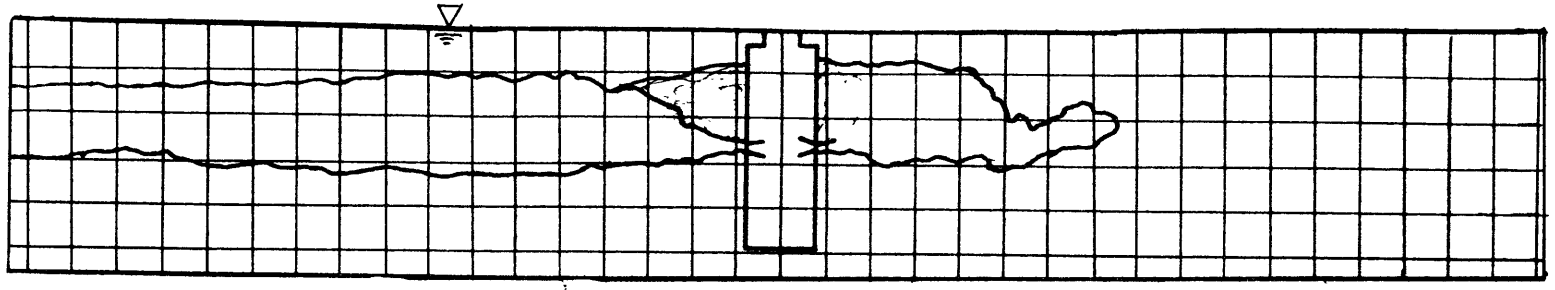

Run 7A: 400 MWe plant; horizontal, radial, evaporator discharge at medium discharge depth; shallow mixed layer depth; current speed = .27 m/s. Grid spacing = 30 m.

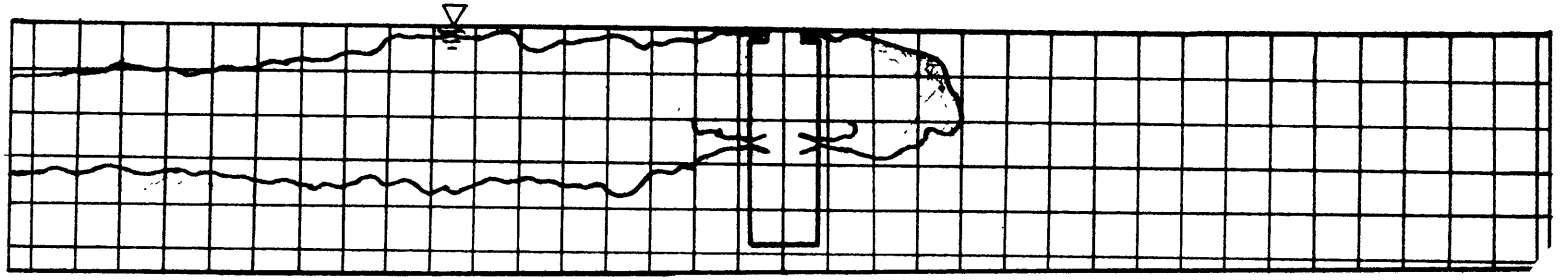

Run 7B: 400 MWe plant; horizontal, radial, evaporator discharge at medium discharge depth; shallow mixed layer depth; current speed = .51 m/s. Grid spacing = 30 m.

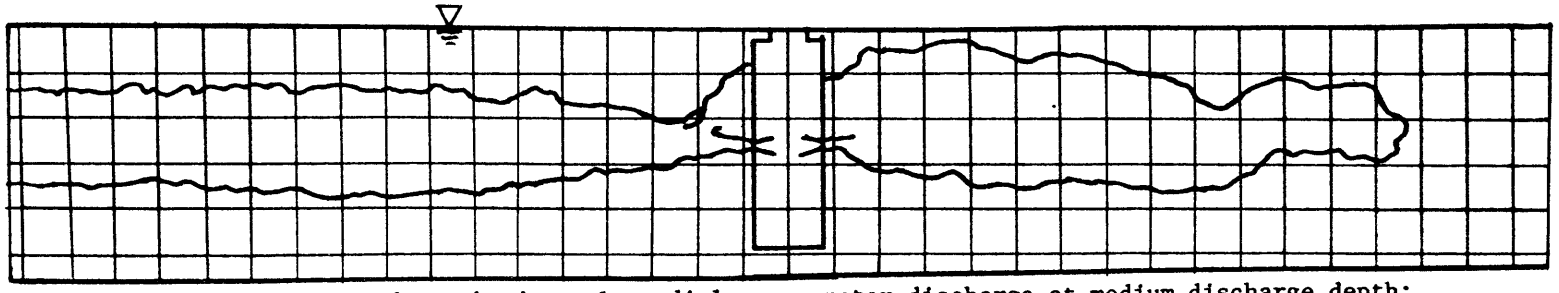

Run 8A: 600 MWe plant; horizontal, radial, evaporator discharge at medium discharge depth; shallow mixed layer depth; current speed = .27 m/s. Grid spacing = 30 m.

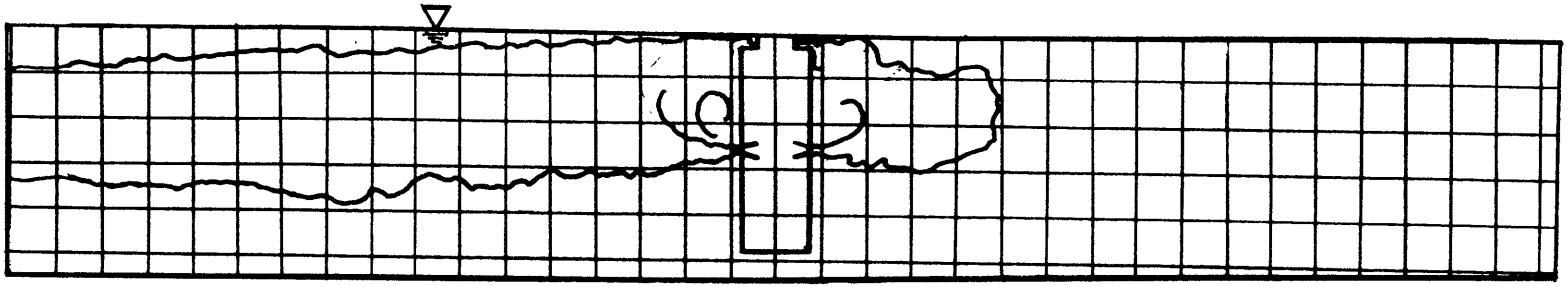

Run 8B: 600 MWe plant; horizontal, radial, evaporator discharge at medium discharge depth; shallow mixed layer depth; current speed = .51 m/s. Grid spacing = 30 m.

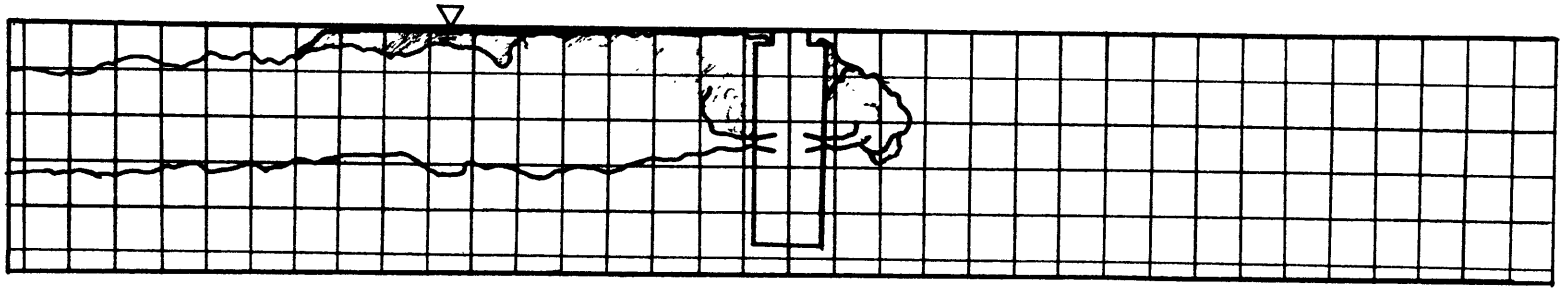

Run 9: Aborted

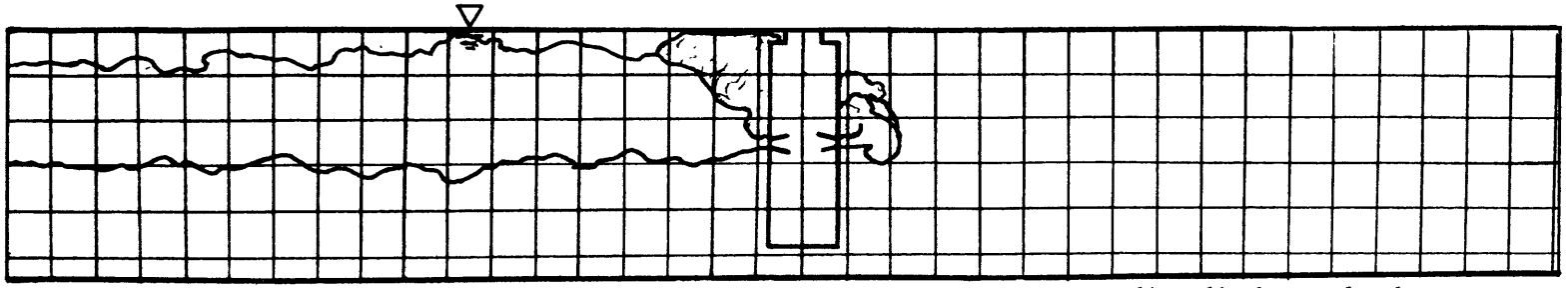

Run 10: 400 MWe plant; horizontal, radial, evaporator discharge at medium discharge depth; medium mixed layer depth; current speed = 1.0 m/s. Grid spacing = 30 m.

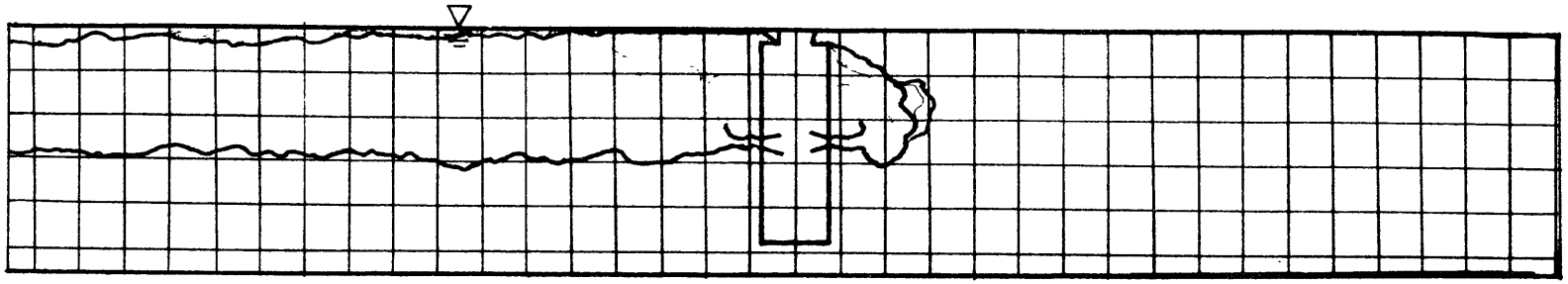

Run 11: 600 MWe plant; horizontal, radial, evaporator discharge at medium discharge depth; medium mixed layer depth; current speed = 1.0 m/s. Grid spacing = 30 m.

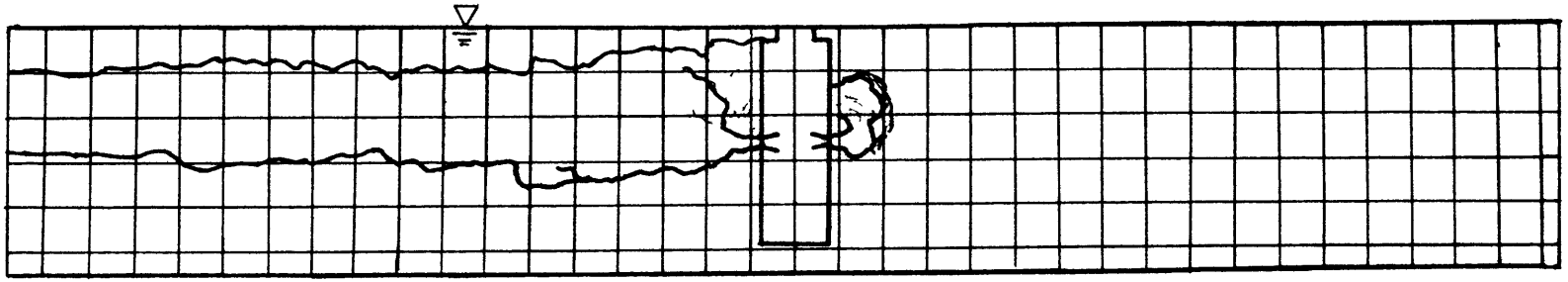

Run 12: 400 MWe plant; horizontal, radial, shallow discharge at medium discharge depth; shallow mixed layer depth; current speed = 1.0 m/s. Grid spacing = 30 m.

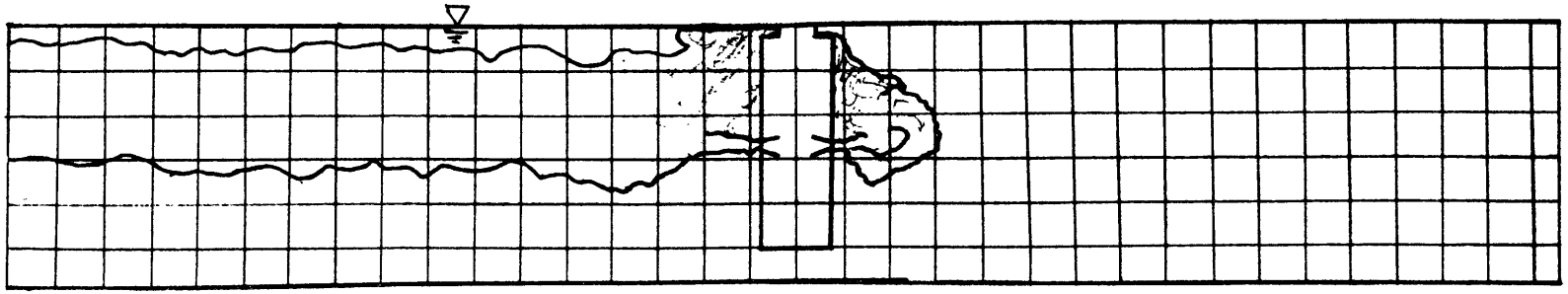

Run 13: 600 MWe plant; horizontal, radial, evaporator discharge at medium discharge depth; shallow mixed layer depth; current speed = 1.0 m/s. Grid spacing = 30 m.

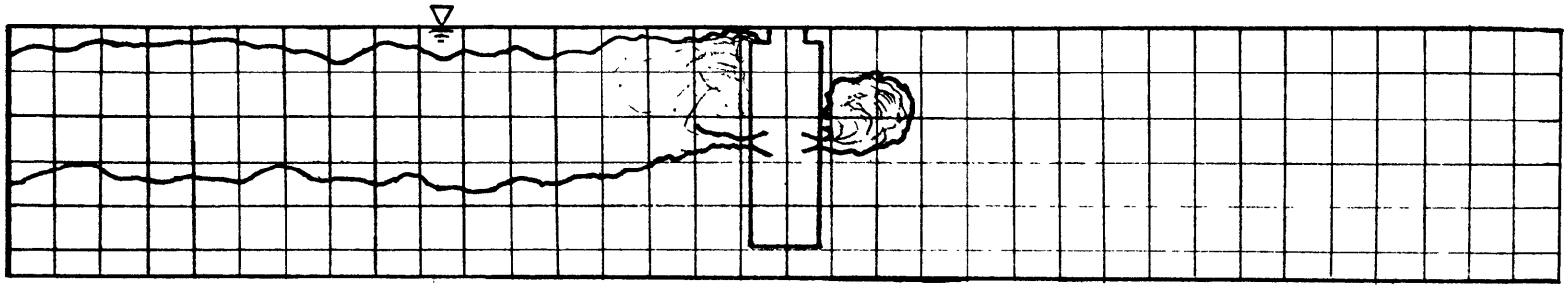

Run 14: 400 MWe plant; horizontal, radial, evaporator discharge at medium discharge depth; medium mixed layer depth; current speed = .87 m/s. Grid spacing = 30 m.

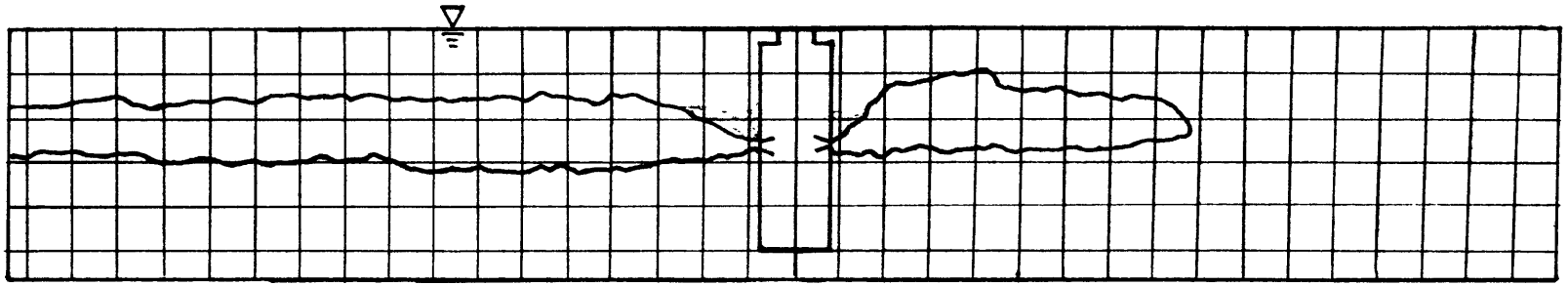

Run 15A: 200 MWe plant; horizontal, radial, evaporator discharge at medium discharge depth; medium mixed layer depth; current speed = .27 m/s. Grid spacing = 30 m.

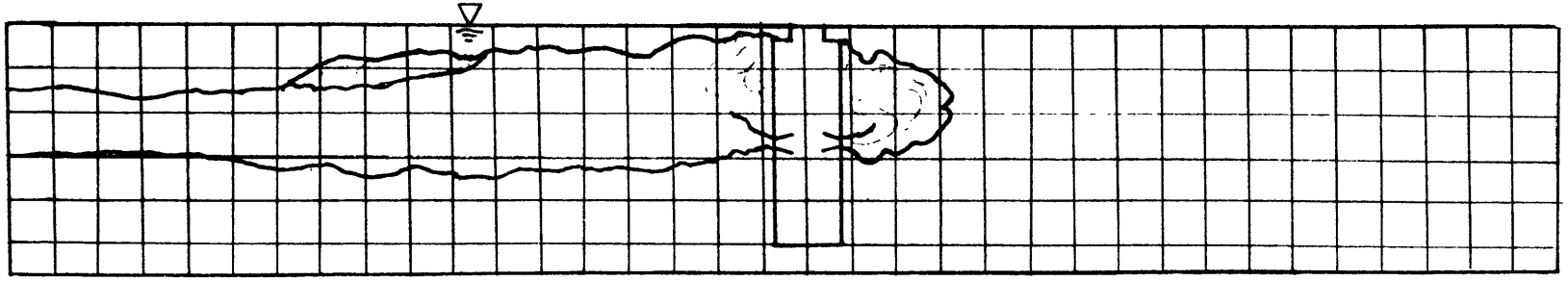

Run 15B: 200 MWe plant; horizontal, radial, evaporator discharge at medium discharge depth; medium mixed layer depth; current speed = .51 m/s. Grid spacing = 30 m.

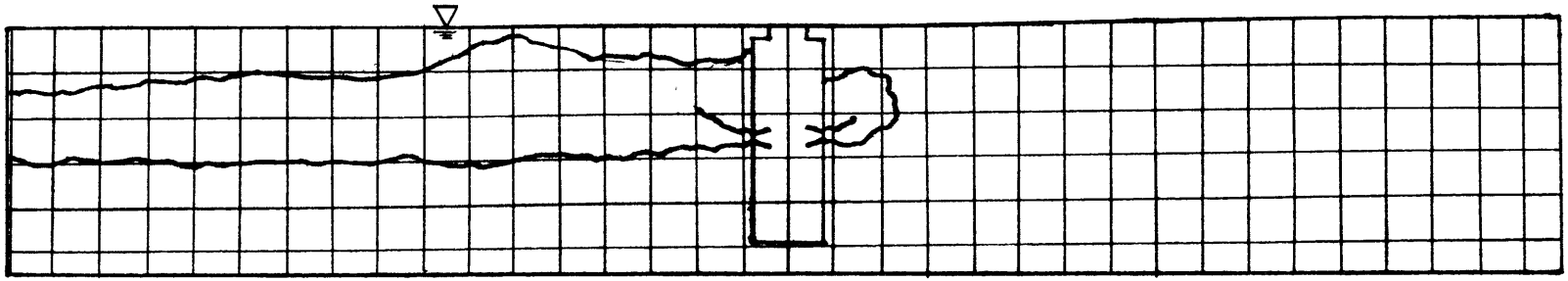

Run 16: 200 MWe plant; horizontal, radial, evaporator discharge at medium discharge depth; medium mixed layer depth; current speed = .87 m/s. Grid spacing = 30 m.

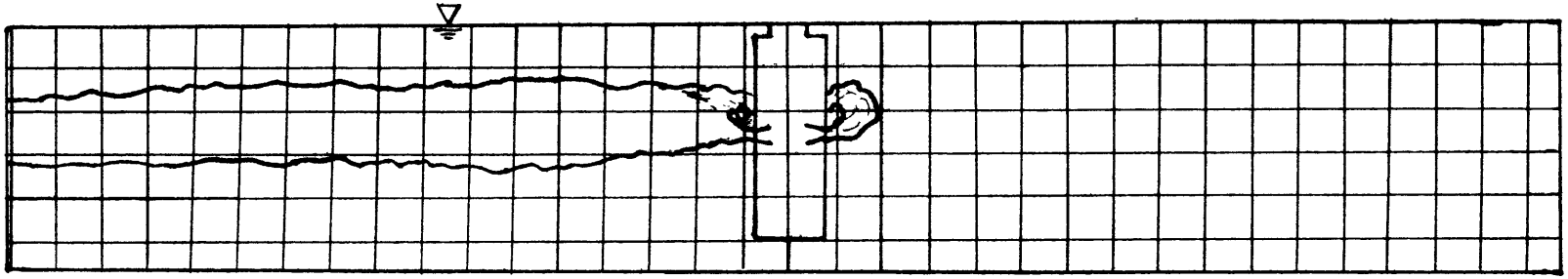

Run 17: 200 MWe plant; horizontal, radial, evaporator discharge at medium discharge depth; medium mixed layer depth; current speed = 1.0 m/s. Grid spacing = 30 m.

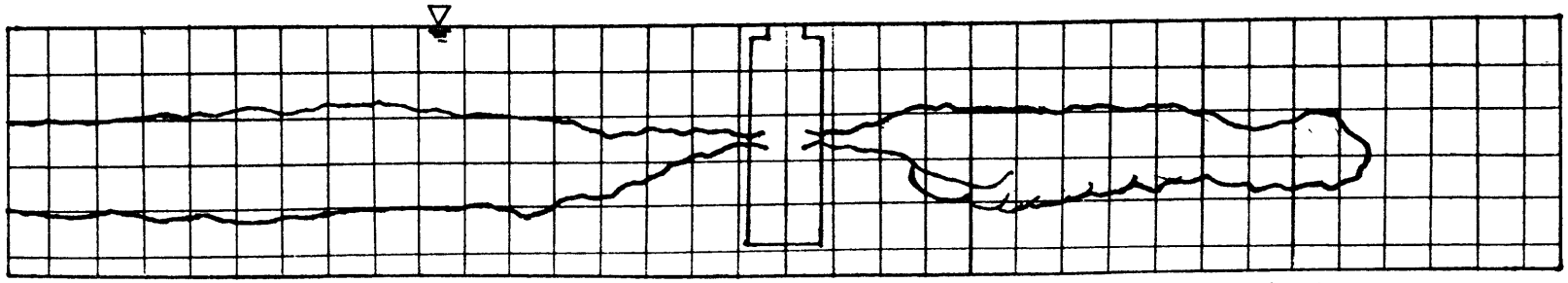

Run 18A: 200 MWe plant; horizontal, radial, mixed discharge at medium discharge depth; medium mixed layer depth; current speed = .27 m/s. Grid spacing = 30 m.

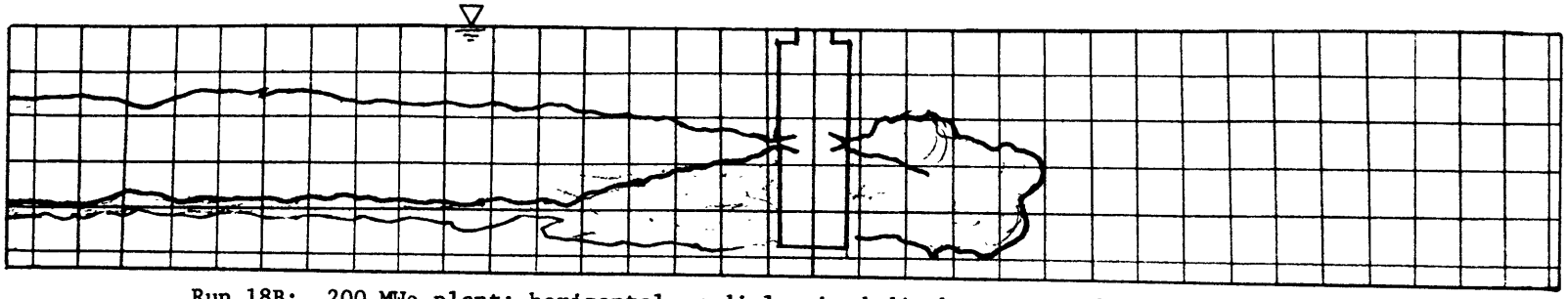

Run 18B: 200 MWe plant; horizontal, radial, mixed discharge at medium discharge depth; medium mixed layer depth; current speed = .51 m/s. Grid spacing = 30 m.

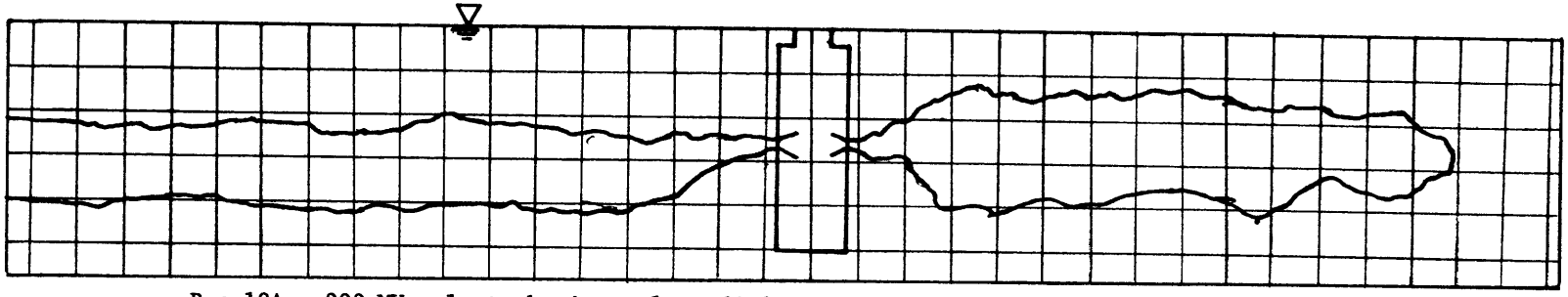

Run 19A: 200 MWe plant; horizontal, radial, evaporator discharge at medium discharge depth; deep mixed layer depth; current speed = .27 m/s. Grid spacing = 30 m.

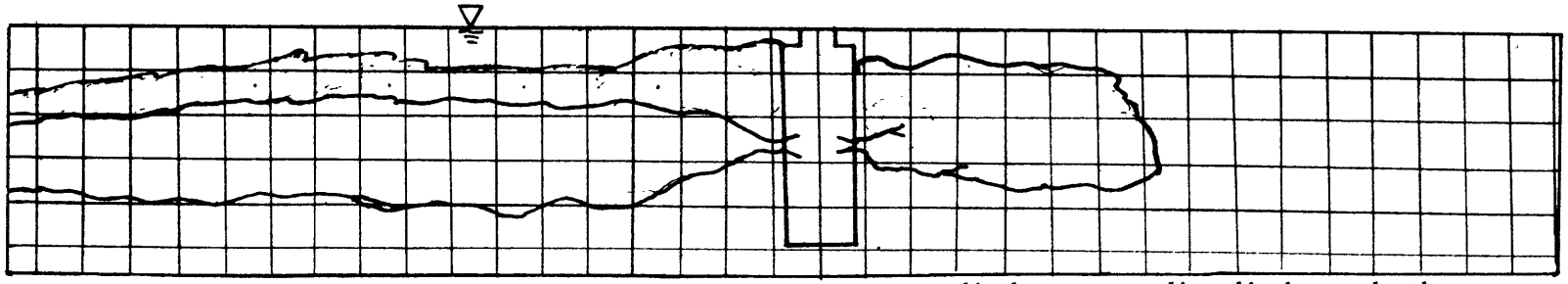

Run 19B: 200 MWe plant; horizontal, radial, evaporator discharge at medium discharge depth; deep mixed layer depth; current speed = .51 m/s. Grid spacing = 30 m.

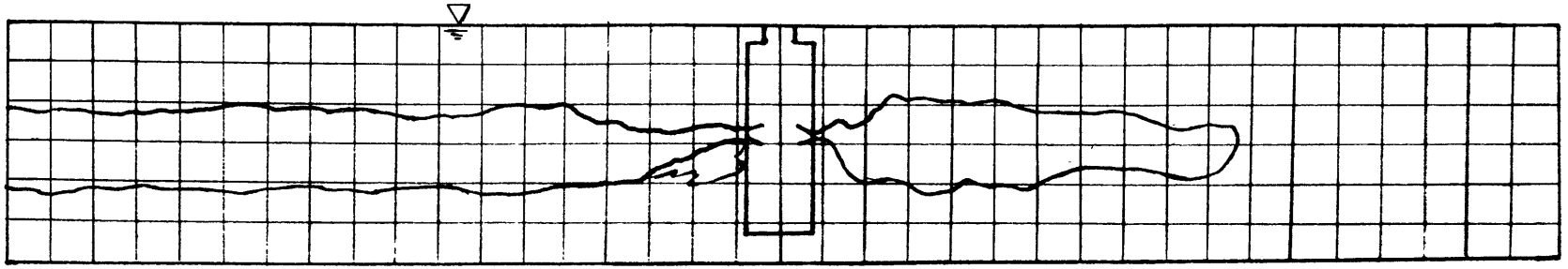

Run 20A: 400 MWe plant; horizontal, radial, evaporator discharge at medium discharge depth; deep mixed layer depth; current speed = .27 m/s. Grid spacing = 30 m.

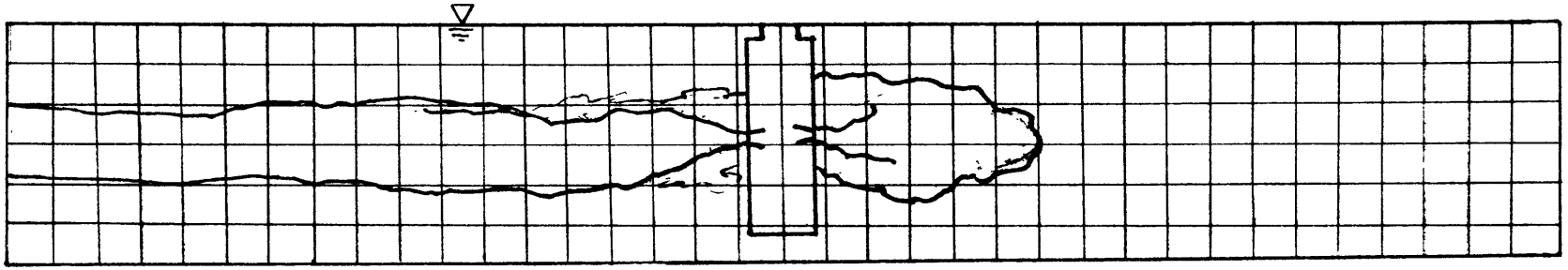

Run 20B: 400 MWe plant; horizontal, radial, evaporator discharge at medium discharge depth; deep mixed layer depth; current speed = .51 m/s. Grid spacing = 30 m.

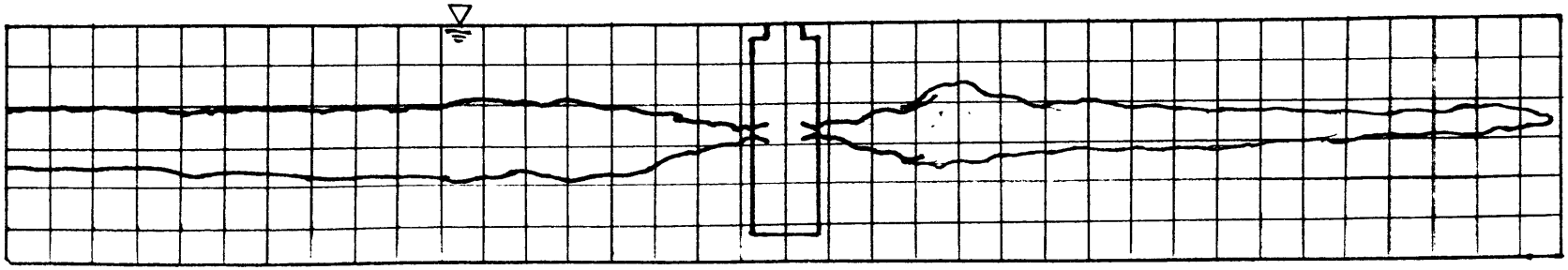

Run 21A: Aborted

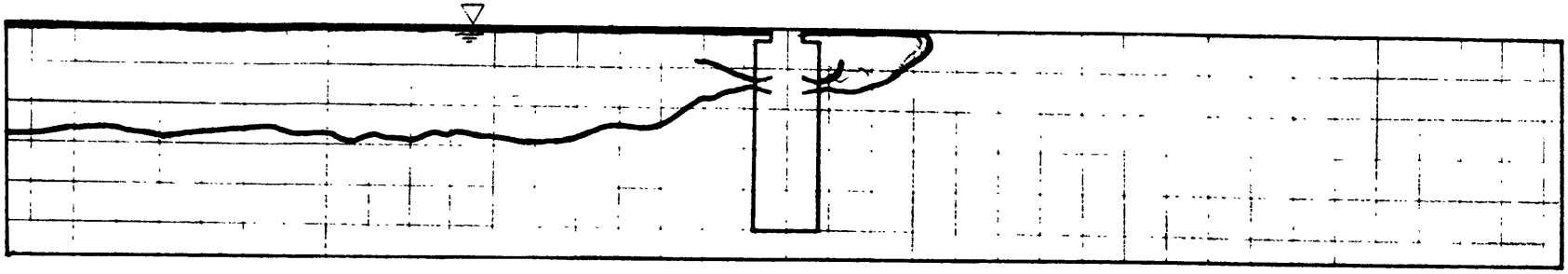

Run 22A: 400 MWe plant; horizontal, radial, evaporator discharge at shallow discharge depth; medium mixed layer depth; current speed = .28 m/s. Grid spacing = 30 m.

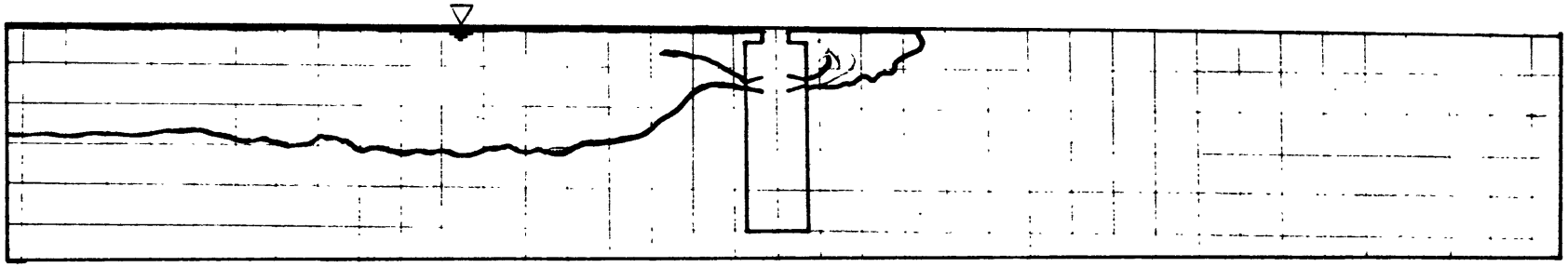

Run 22B: 400 MWe plant; horizontal, radial, evaporator discharge at shallow discharge depth; medium mixed layer depth; current speed = .51 m/s. Grid spacing = 30 m.

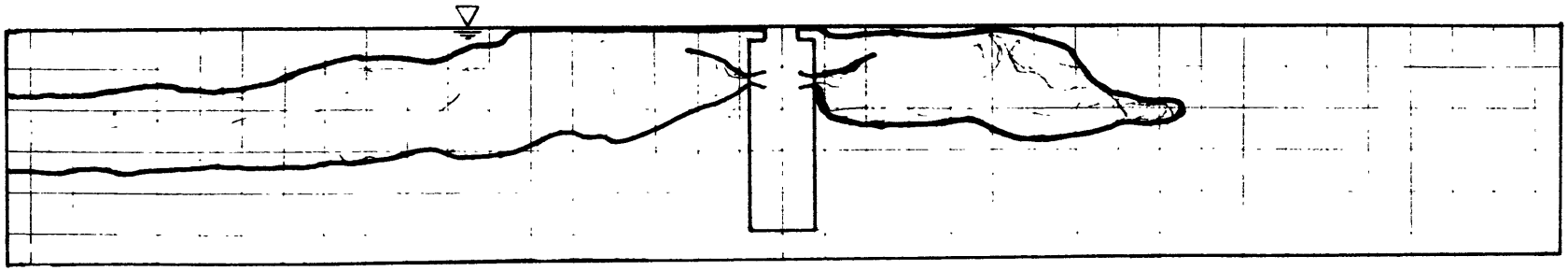

Ran 23A: 400 MWe plant; horizontal, radial, mixed discharge at shallow discharge depth; medium mixed layer depth; current speed = .28 m/s. Grid spacing = 30 m.

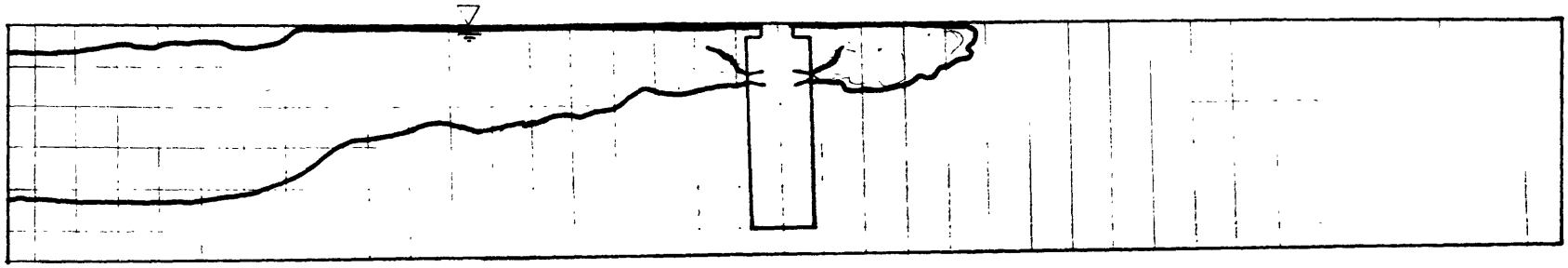

Run 23B: 400 MWe plant; horizontal, radial, mixed discharge at shallow discharge depth; medium mixed layer depth; current speed = .51 m/s. Grid spacing = 30 m.

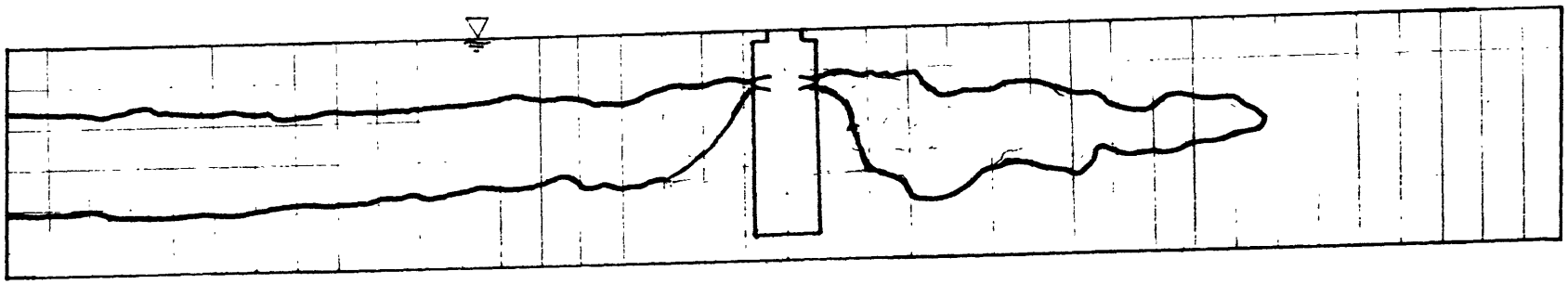

Run 24A: 200 MWe plant; horizontal, radial, mixed discharge at shallow discharge depth; medium mixed layer depth; current speed = .28 m/s. Grid spacing = 30 m.

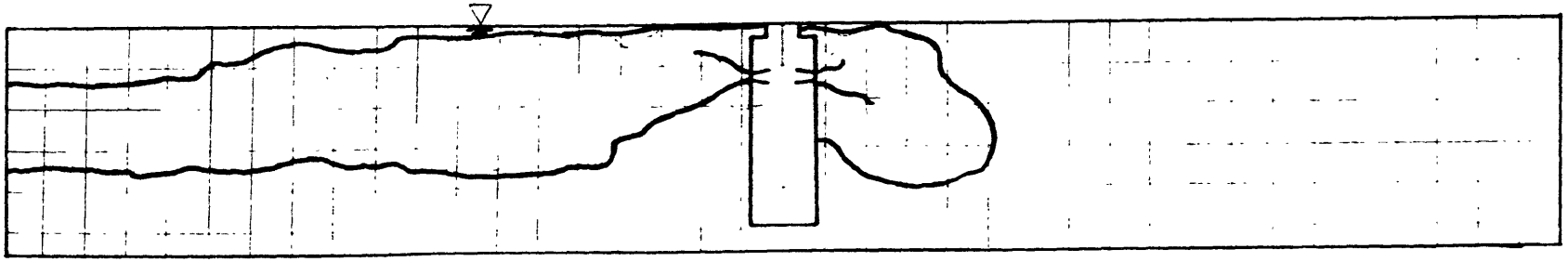

Run 24B: 200 MWe plant; horizontal, radial, mixed discharge at shallow discharge depth; medium mixed layer depth; current speed = .51 m/s. Grid spacing = 30 m.

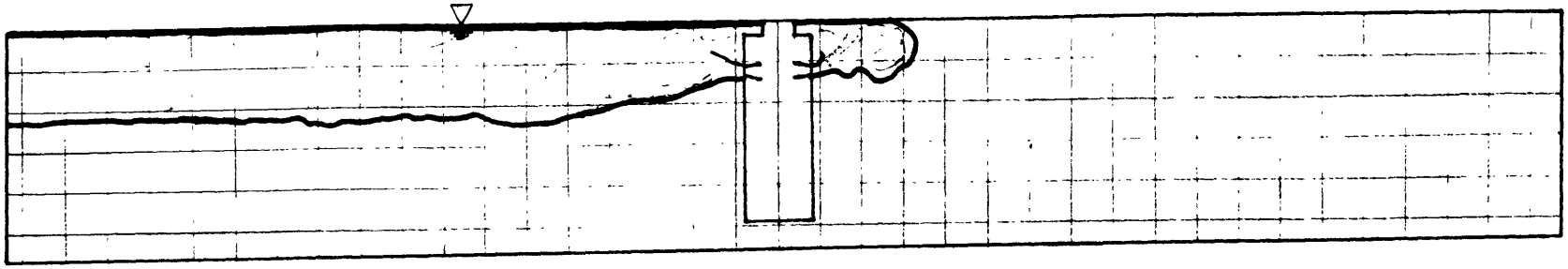

Run 25A: 200 MWe plant; horizontal, radial, evaporator discharge at shallow discharge depth; medium mixed layer depth; current speed = .28 m/s. Grid spacing = 30 m.

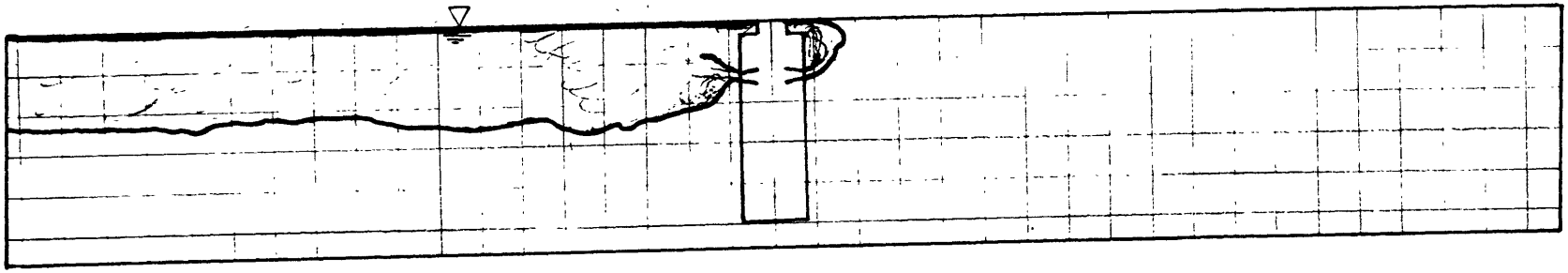

Run 25B: 200 MWe plant; horizontal, radial, evaporator discharge at shallow discharge depth; medium mixed layer depth; current speed = .51 m/s. Grid spacing = 30 m.

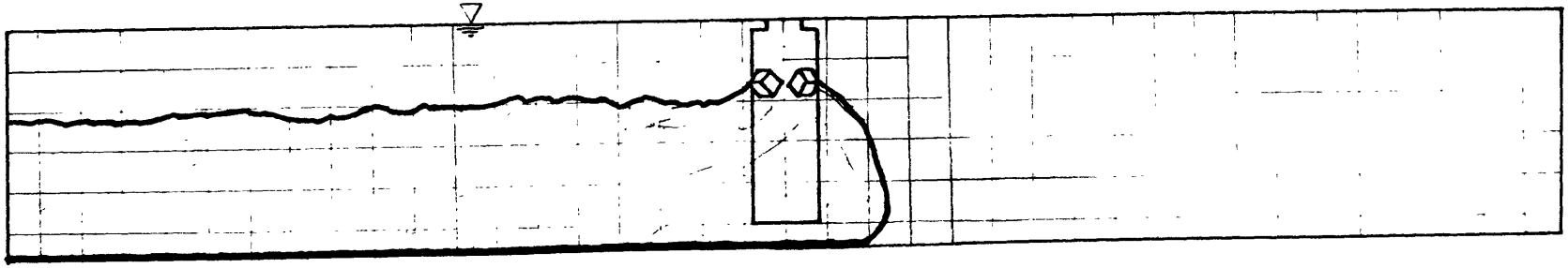

Run 26A: 400 MWe plant; α_H=45°, α_V=45°; 4-jet evaporator discharge at shallow discharge depth; medium mixed layer depth; current speed = .28 m/s; Grid spacing = 30 m.

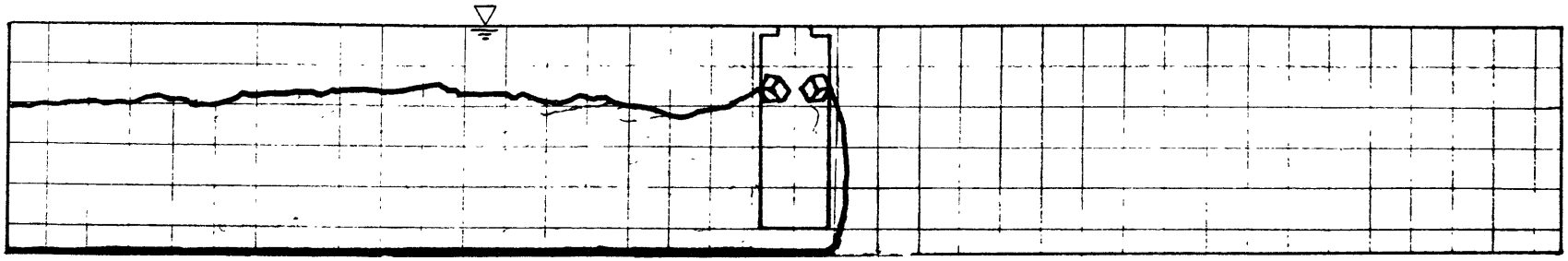

Run 26B: 400 MWe plant; α_H=45°, α_V=45°; 4-jet, evaporator discharge at shallow discharge depth; medium mixed layer depth; current speed = .51 m/s. Grid spacing = 30 m.

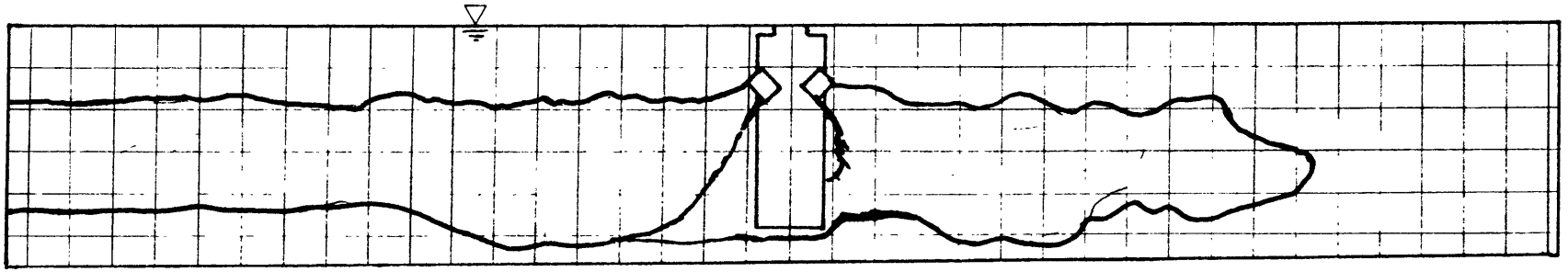

Run 27A: 400 MWe plant; α_H=0°, α_V=45°; 4-jet, evaporator discharge at shallow discharge depth; medium mixed layer depth; current speed = .28 m/s. Grid spacing = 30 m.

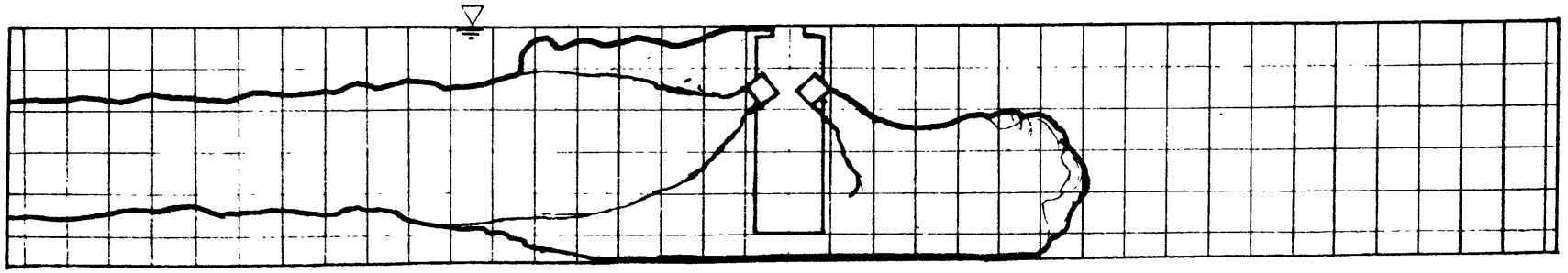

Run 27B: 400 MWe plant: α_H=0°, α_V=45°; 4-jet, evaporator discharge at shallow discharge depth; medium mixed layer depth; current speed = .51 m/s. Grid spacing = 30 m.

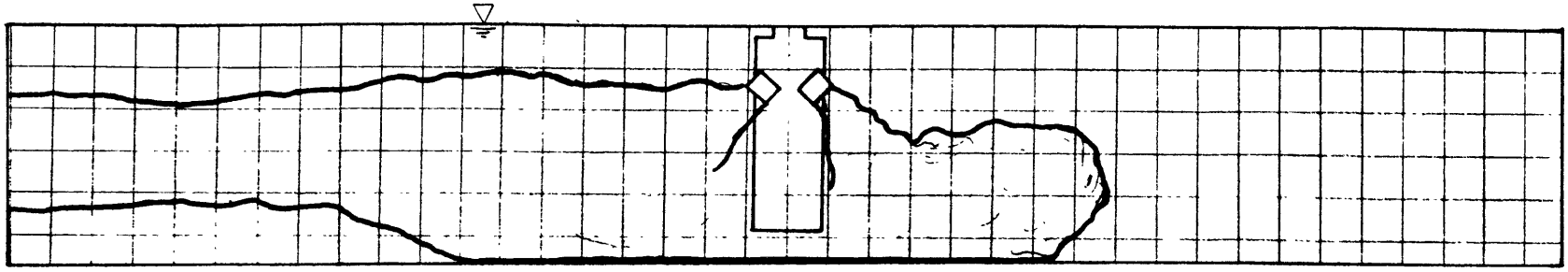

Run 28A: 400 MWe plant; α_H=0°, α_V=45°; 4-jet, evaporator discharge at shallow discharge depth; medium mixed layer depth; current speed = .51 m/s. Grid spacing = 30 m.

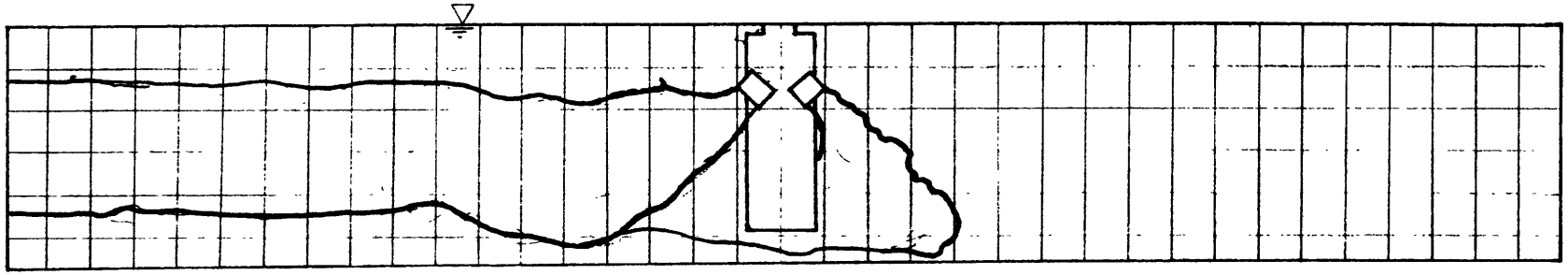

Run 28B: 400 MWe plant; α_H=0°, α_V=45°; 4-jet, evaporator discharge at shallow discharge depth; medium mixed layer depth; current speed = .87 m/s. Grid spacing = 30 m.

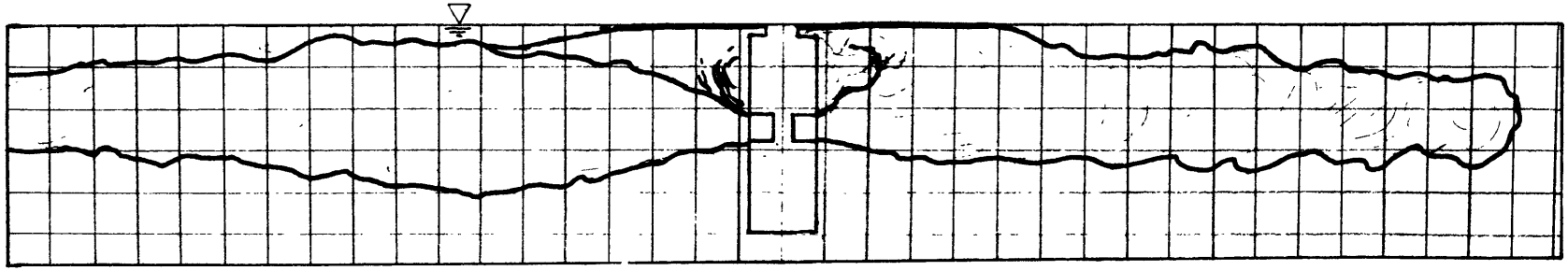

Run 29A: 400 MWe plant; horizontal, 4-jet, evaporator discharge at medium discharge depth; medium mixed layer depth; current speed = .28 m/s. Grid spacing = 30 m.

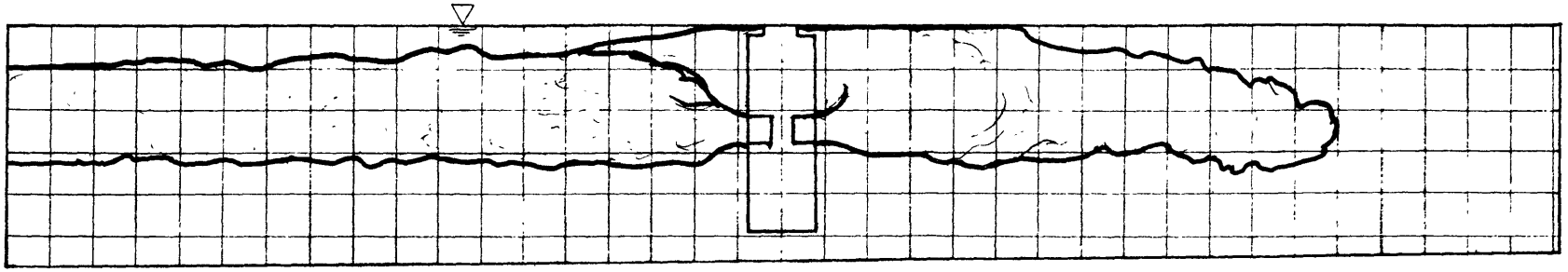

Run 29B: 400 MWe plant; horizontal, 4-jet, evaporator discharge at medium discharge depth; medium mixed layer depth; current speed = .51 m/s. Grid spacing = 30 m.

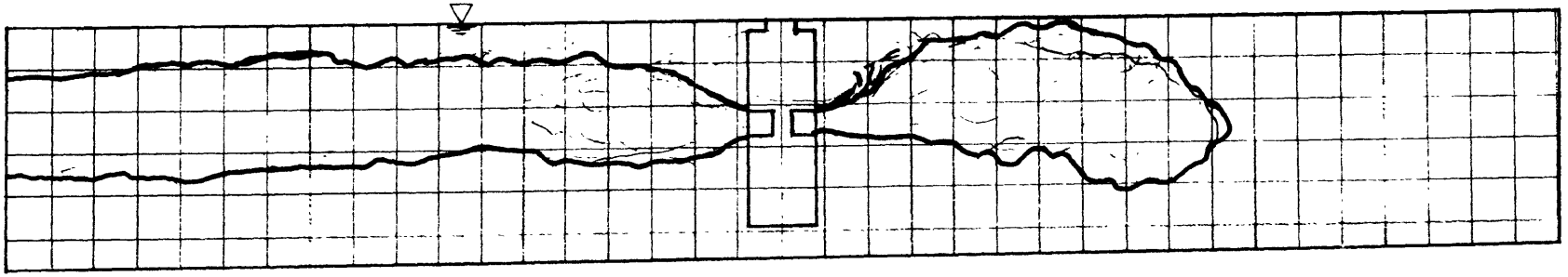

Run 30A: 400 MWe plant; horizontal, 4-jet, evaporator discharge at medium discharge depth; medium mixed layer depth; current speed = .51 m/s. Grid spacing = 30 m.

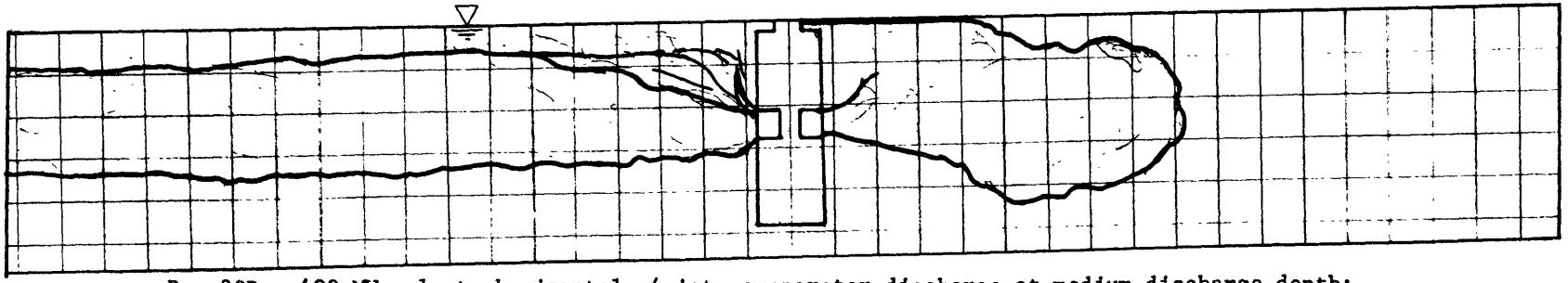

Run 30B: 400 MWe plant; horizontal, 4-jet, evaporator discharge at medium discharge depth; medium mixed layer depth; current speed = .87 m/s. Grid spacing = 30 m.

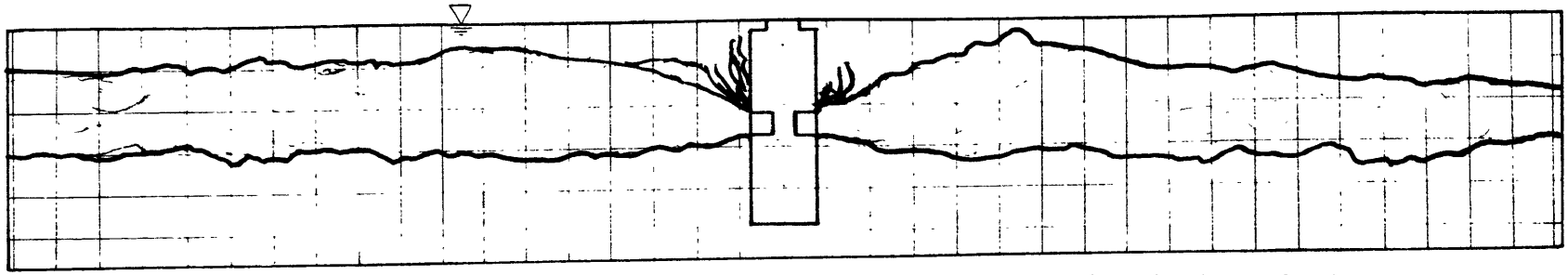

Run 31A: 400 MWe plant; horizontal, 4-jet, evaporator discharge at medium discharge depth; medium mixed layer depth; current speed = .15 m/s. Grid spacing = 30 m.

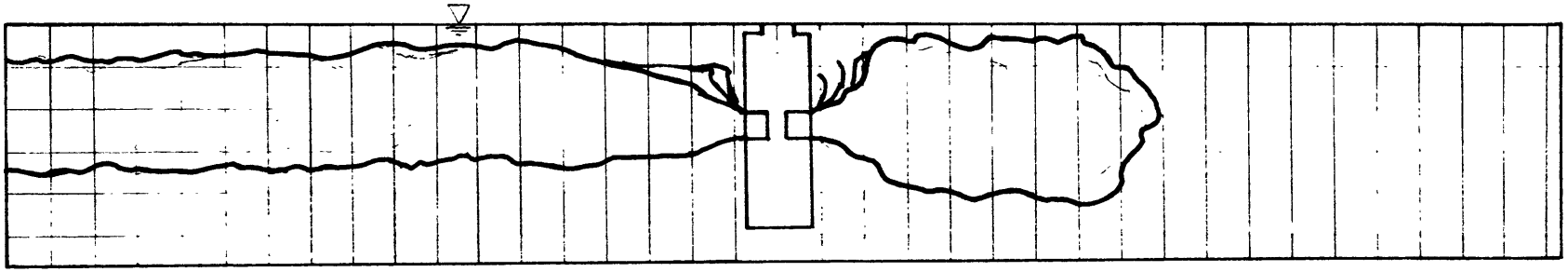

Run 31B: 400 MWe plant; horizontal, 4-jet, evaporator discharge at medium discharge depth; medium mixed layer depth; current speed = .87 m/s. Grid spacing = 30 m.

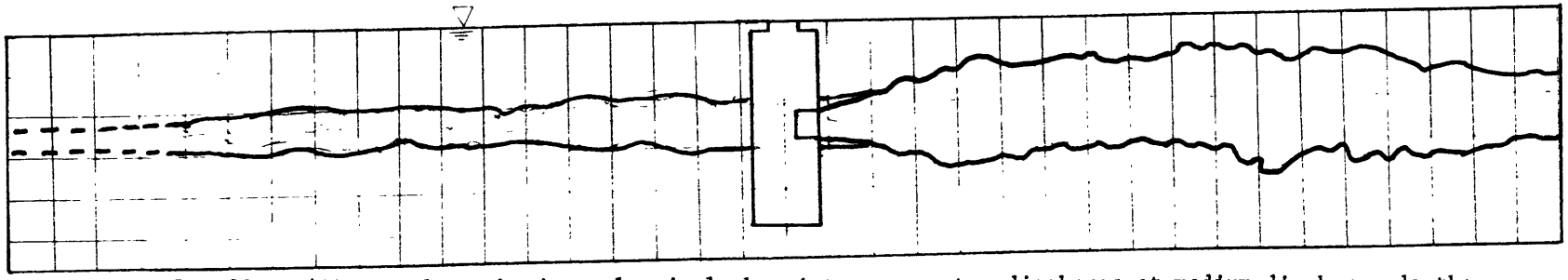

Run 32A: 400 MWe plant; horizontal, single bow jet, evaporator discharge at medium discharge depth; medium mixed layer depth; current speed = .28 m/s. Grid spacing = 30 m.

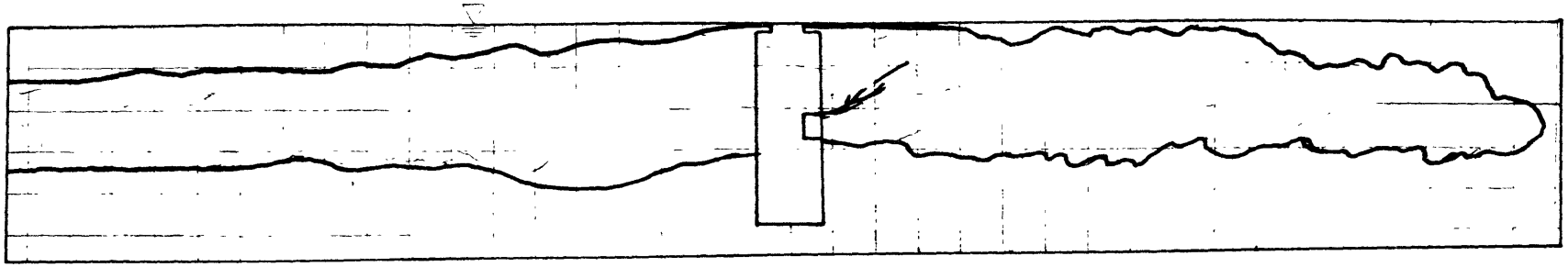

Run 32B: 400 MWe plant; horizontal, single bow jet, evaporator discharge at medium discharge depth; medium mixed layer depth; current speed = .51 m/s. Grid spacing = 30 m.

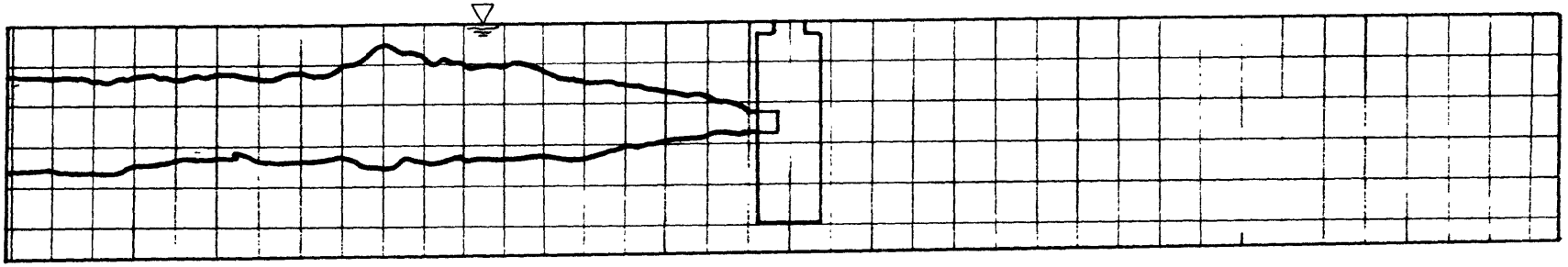

Run 34A: 400 MWe plant; horizontal, single stern jet, evaporator discharge at medium discharge depth; medium mixed layer depth; current speed = .28 m/s. Grid spacing = 30 m.

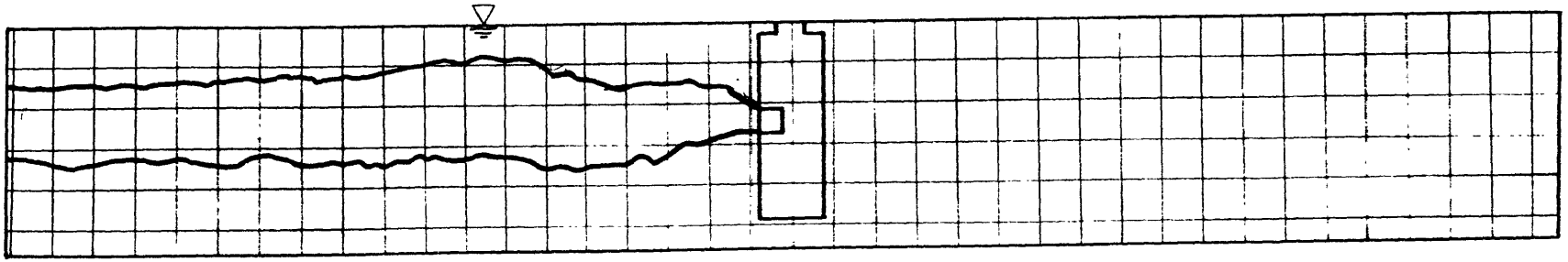

Run 34B: 400 MWe plant; horizontal, single stern jet, evaporator discharge at medium discharge depth; medium mixed layer depth; current speed = .51 m/s. Grid spacing = 30 m.

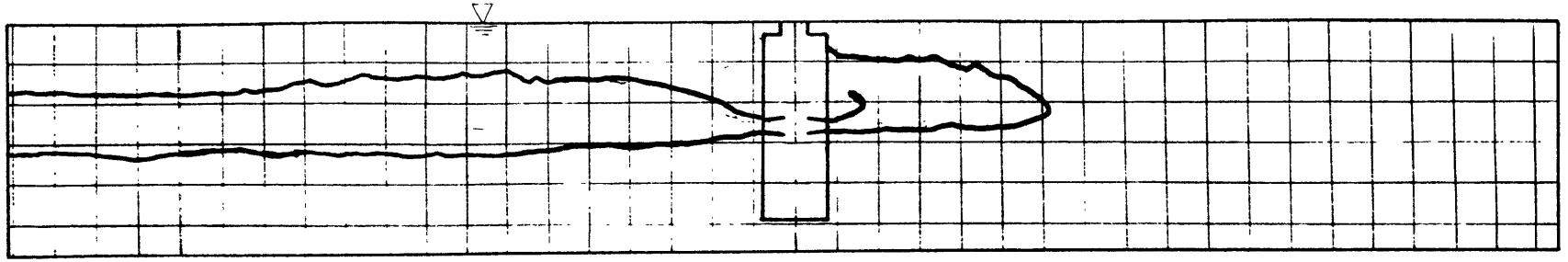

Run 35A: 400 MWe plant; horizontal, radial, evaporator discharge at medium discharge depth; medium mixed layer depth; current speed = .28 m/s. Grid spacing = 30 m.

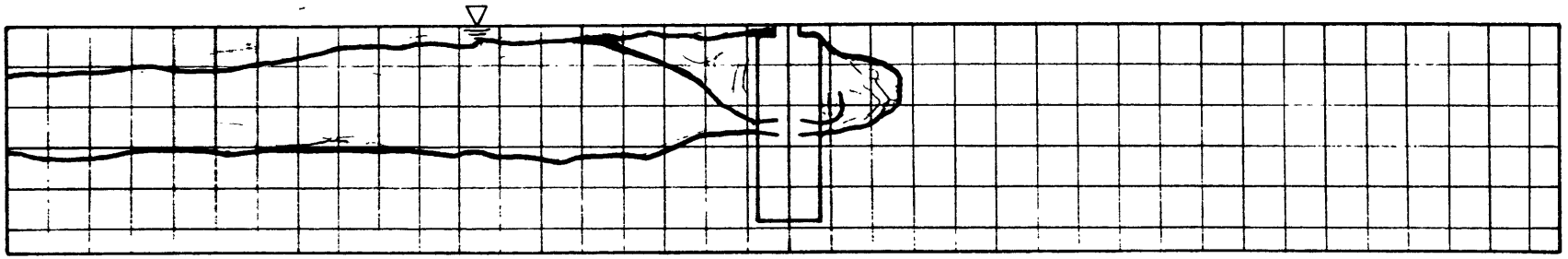

Run 35B: 400 MWe plant; horizontal, radial, evaporator discharge at medium discharge depth; medium mixed layer depth; current speed = .51 m/s. Grid spacing = 30 m.

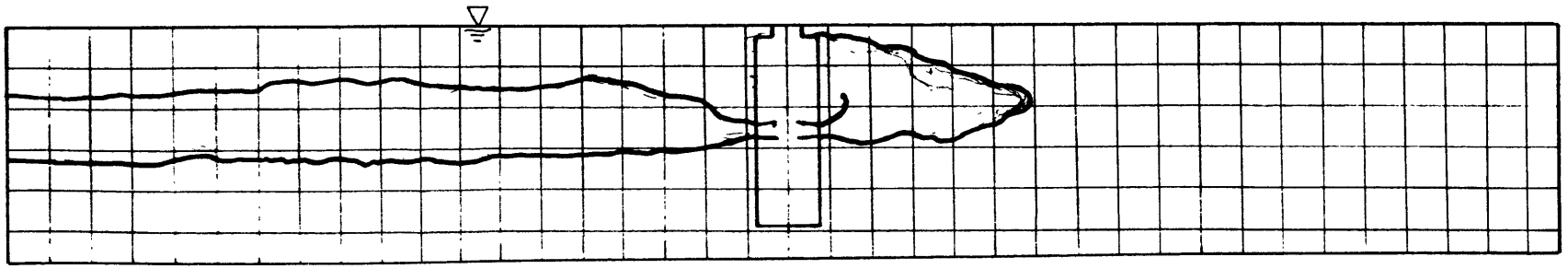

Run 36A: 400 MWe plant; horizontal, radial, evaporator discharge at medium discharge depth; medium mixed layer depth; current speed = .28 m/s. Grid spacing = 30 m.

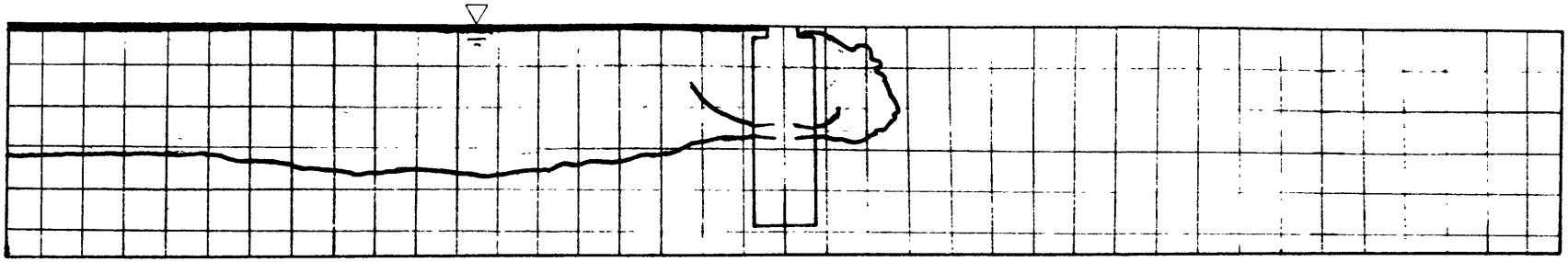

Run 36B: 400 MWe plant; horizontal, radial, evaporator discharge at medium discharge depth; medium mixed layer depth; current speed = .51 m/s. Grid spacing = 30 m.

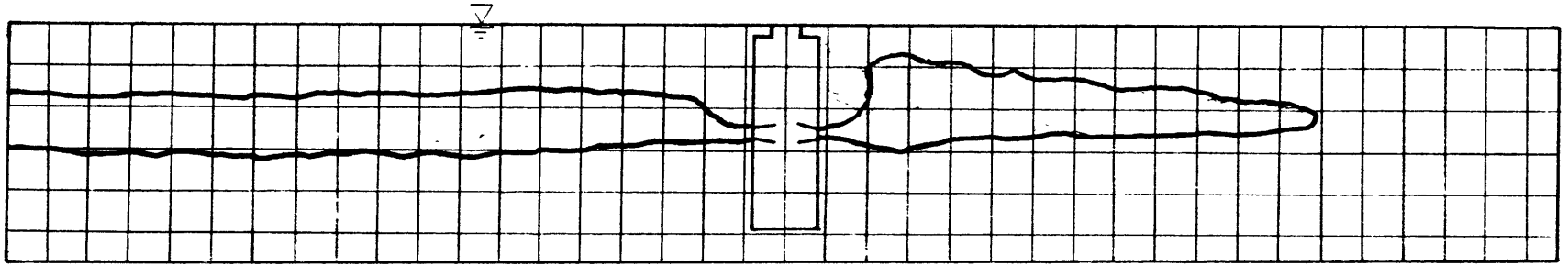

Run 37A: 400 MWe plant; horizontal, radial, evaporator discharge at medium discharge depth; medium mixed layer depth; current speed = .15 m/s. Grid spacing = 30 m.

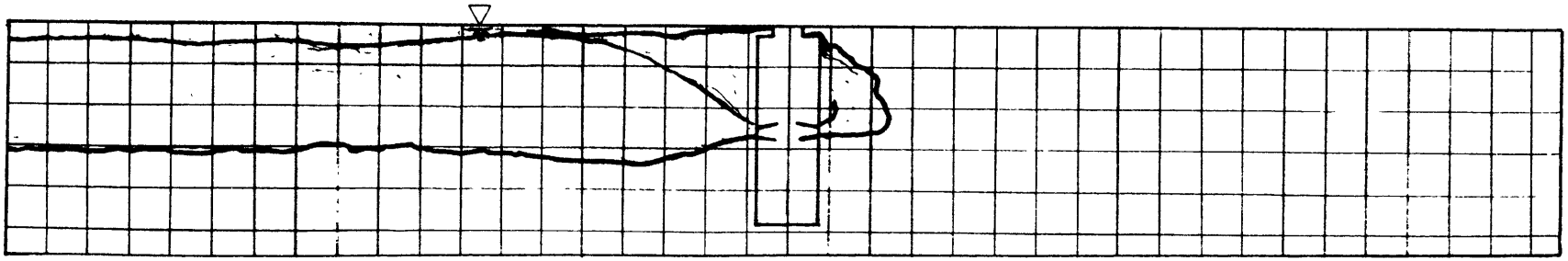

Run 37B: 400 MWe plant; horizontal, radial, evaporator discharge at medium discharge depth; medium mixed layer depth; current speed = .87 m/s. Grid spacing = 30 m.

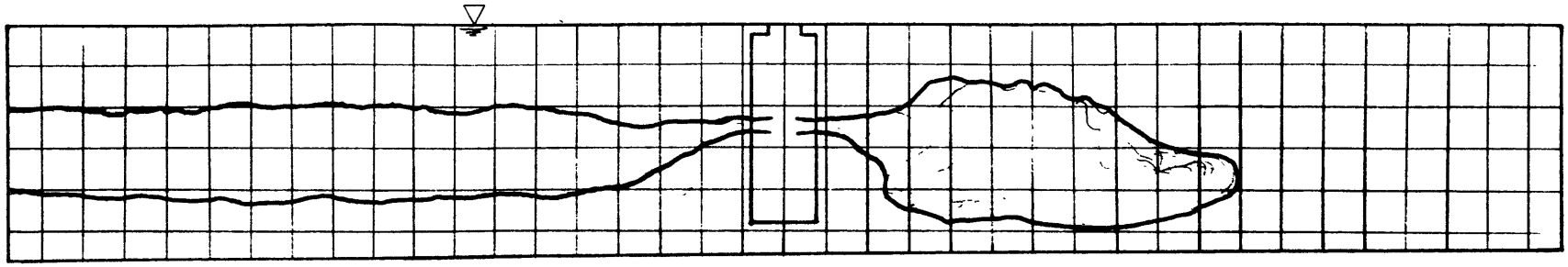

Run 38A: 400 MWe plant; horizontal, radial, mixed discharge at medium discharge depth; medium mixed layer depth; current speed = .28 m/s. Grid spacing = 30 m.

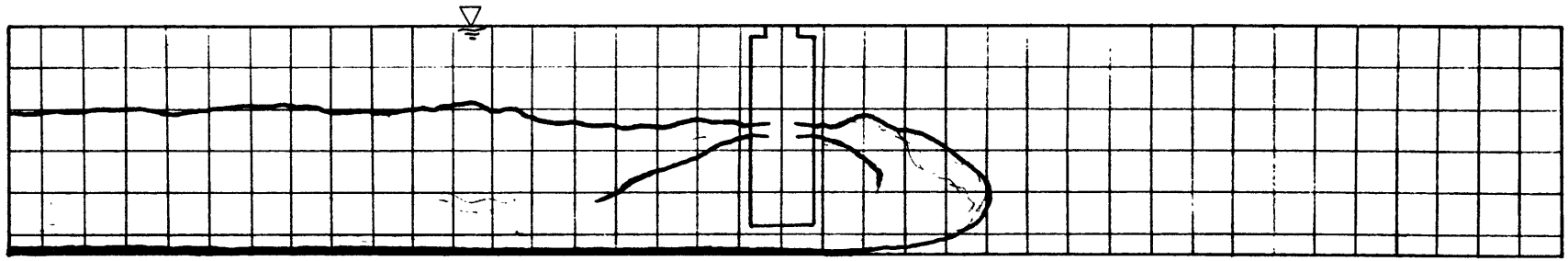

Run 38B: 400 MWe plant; horizontal, radial, mixed discharge at medium discharge depth; medium mixed layer depth; current speed = .51 m/s. Grid spacing = 30 m.

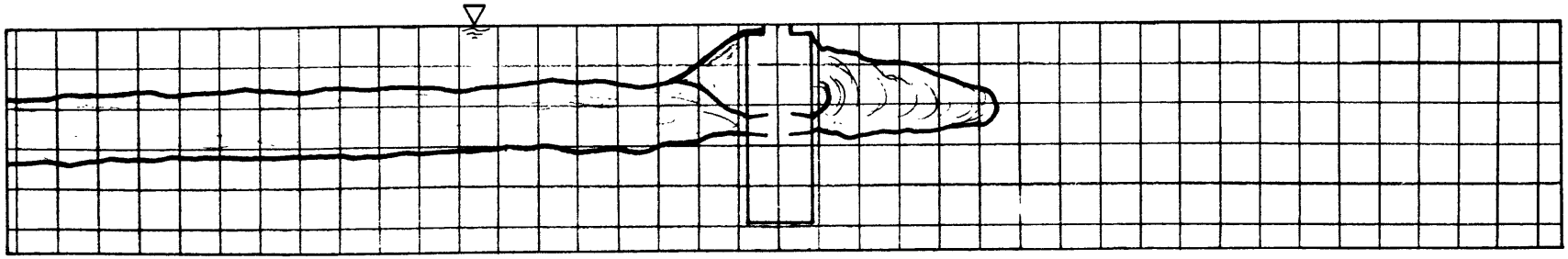

Run 39A: 400 MWe plant; horizontal, radial, evaporator discharge at medium discharge depth; medium mixed layer depth; current speed = .28 m/s. Grid spacing = 30 m.

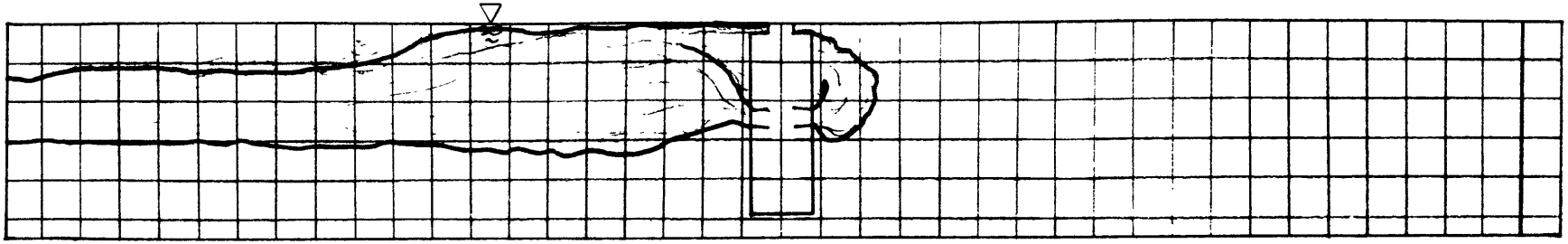

Run 39B: 400 MWe plant; horizontal, radial, evaporator discharge at medium discharge depth; medium mixed layer depth; current speed = .51 m/s. Grid spacing = 30 m.

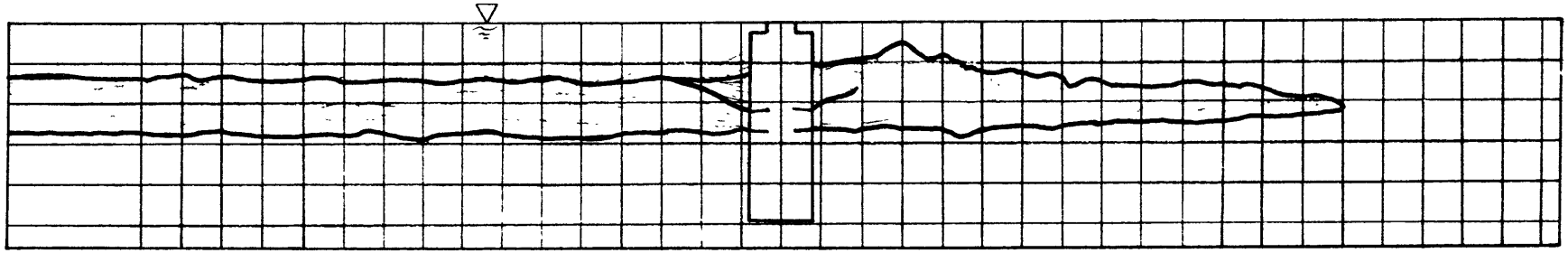

Run 40A: 400 MWe plant; horizontal, radial, evaporator discharge at medium discharge depth; medium mixed layer depth; current speed = .15 m/s. Grid spacing = 30 m.

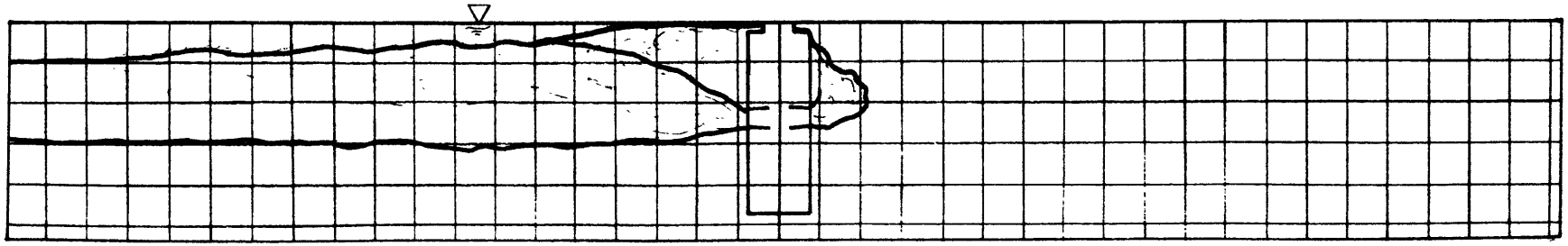

Run 40B: 400 MWe plant; horizontal, radial, evaporator discharge at medium discharge depth; medium mixed layer depth; current speed = .87 m/s. Grid spacing = 30 m.

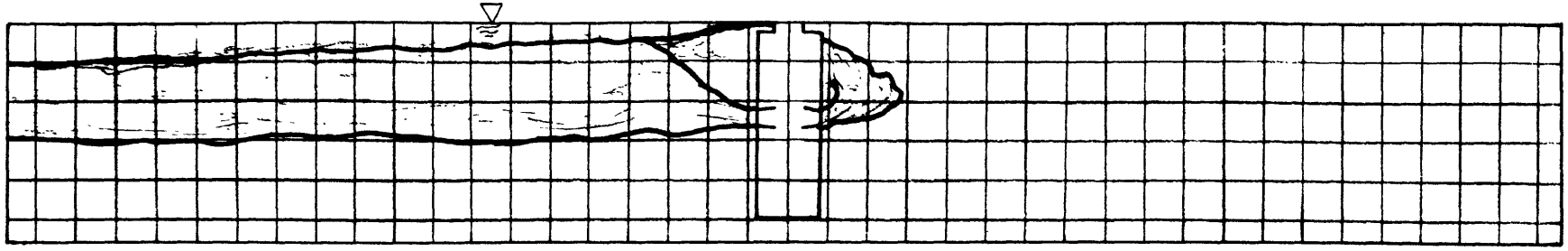

Run 41A: 400 MWe plant; horizontal, radial, evaporator discharge at medium discharge depth; medium mixed layer depth; current speed = .51 m/s. Grid spacing = 30 m.

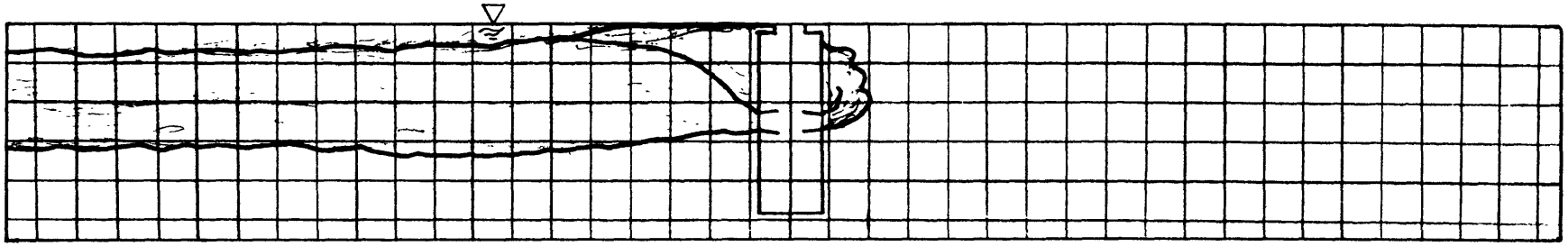

Run 41B: 400 MWe plant; horizontal, radial, evaporator discharge at medium discharge depth; medium mixed layer dpeth; current speed = .87 m/s. Grid spacing = 30 m.

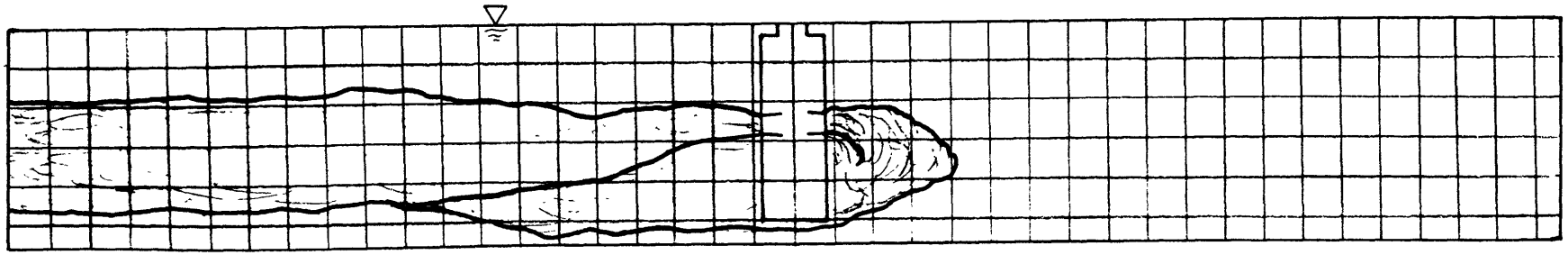

Run 42B: 400 MWe plant; horizontal, radial, mixed discharge at medium discharge depth; medium mixed layer depth; current speed = .51 m/s. Grid spacing = 30 m.

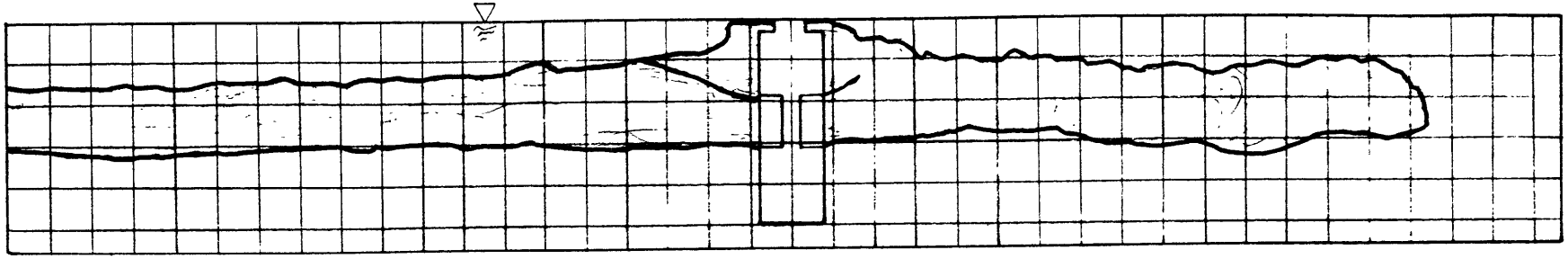

Run 43A: 400 MWe plant; horizontal, 4-port, evaporator discharge at medium discharge depth; medium mixed layer depth; current speed = .28 m/s. Grid spacing = 30 m.

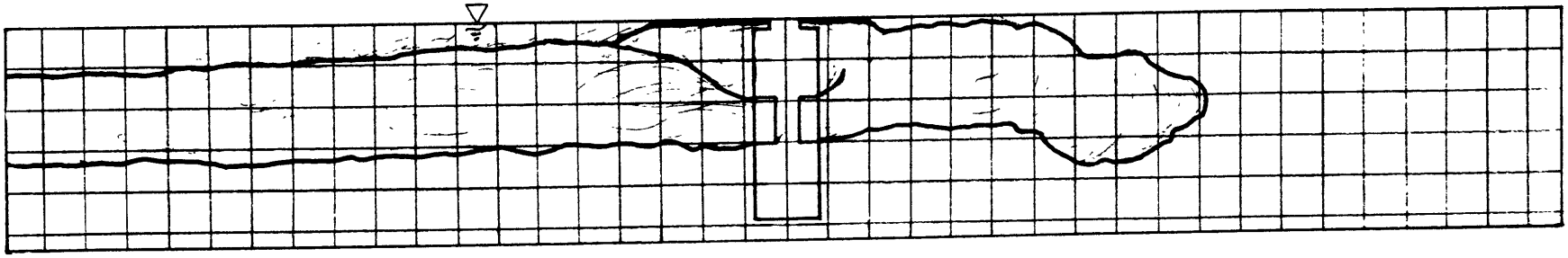

Run 43B: 400 MWe plant; horizontal, 4-port, evaporator discharge at medium discharge depth; medium mixed layer depth; current speed = .51 m/s. Grid spacing = 30 m.

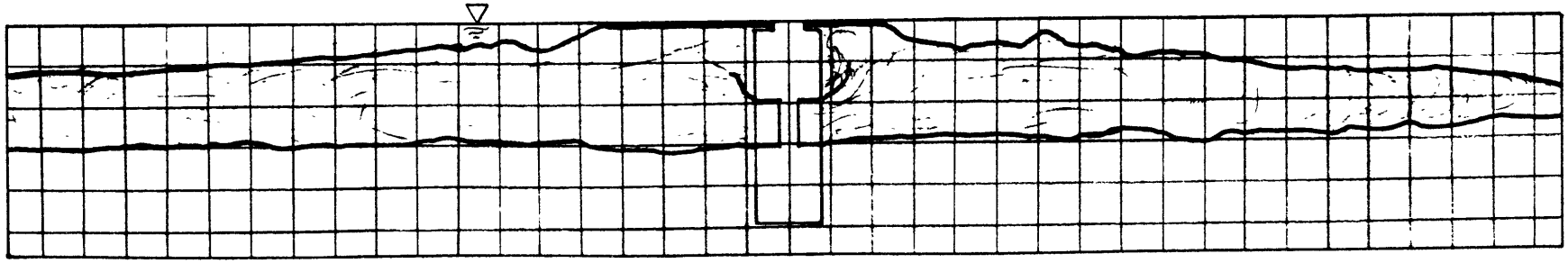

Run 44A: 400 MWe plant; horizontal, 4-port, evaporator discharge at medium discharge depth; medium mixed layer depth; current speed = .15 m/s. Grid spacing = 30 m.

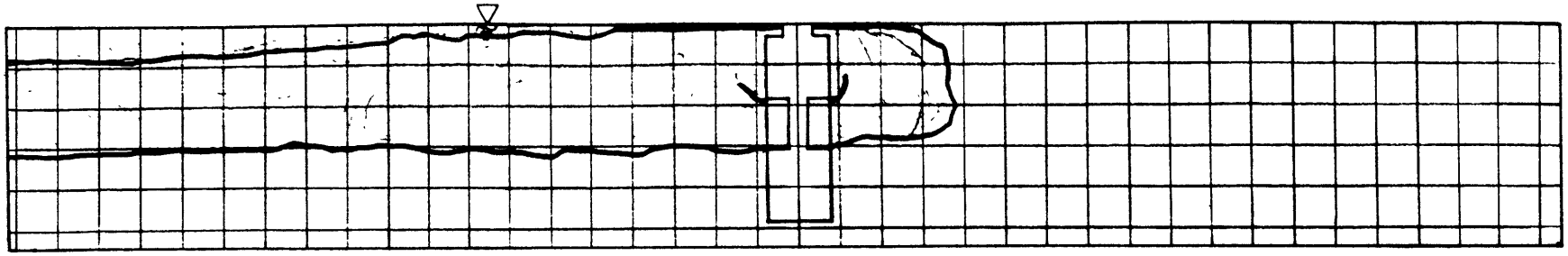

Run 44B: 400 MWe plant; horizontal, 4-port, evaporator discharge at medium discharge depth; medium mixed layer depth; current speed = .87 m/s. Grid spacing = 30 m.

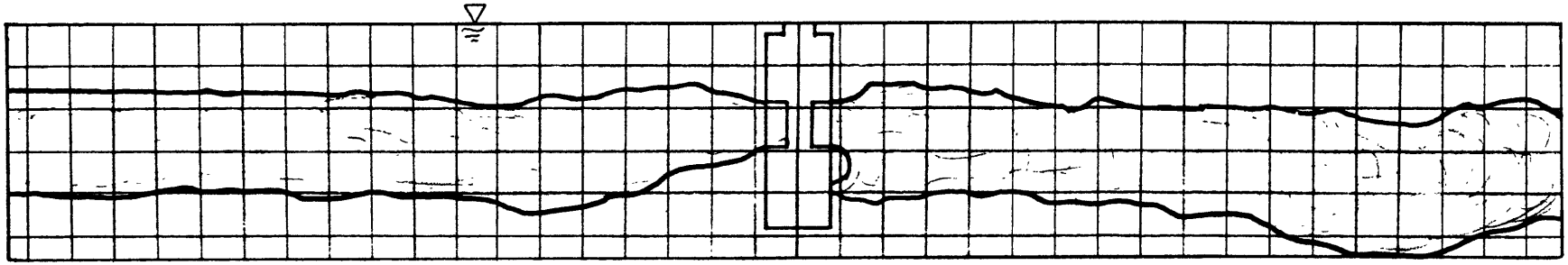

Run 45A: 400 MWe plant; horizontal, radial, mixed discharge at medium discharge depth; medium mixed layer depth; current speed = .28 m/s. Grid spacing = 30 m.

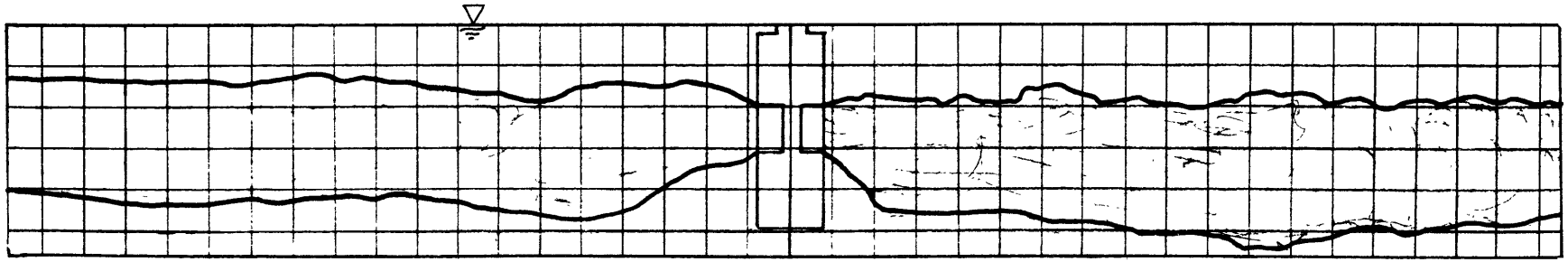

Run 45B: 400 MWe plant; horizontal, radial, mixed discharge at medium discharge depth; medium mixed layer depth; current speed = .51 m/s. Grid spacing = 30 m.

APPENDIX II

OVERHEAD VIEW PHOTOGRAPHIC TRACINGS OF THE DISCHARGE WAKE

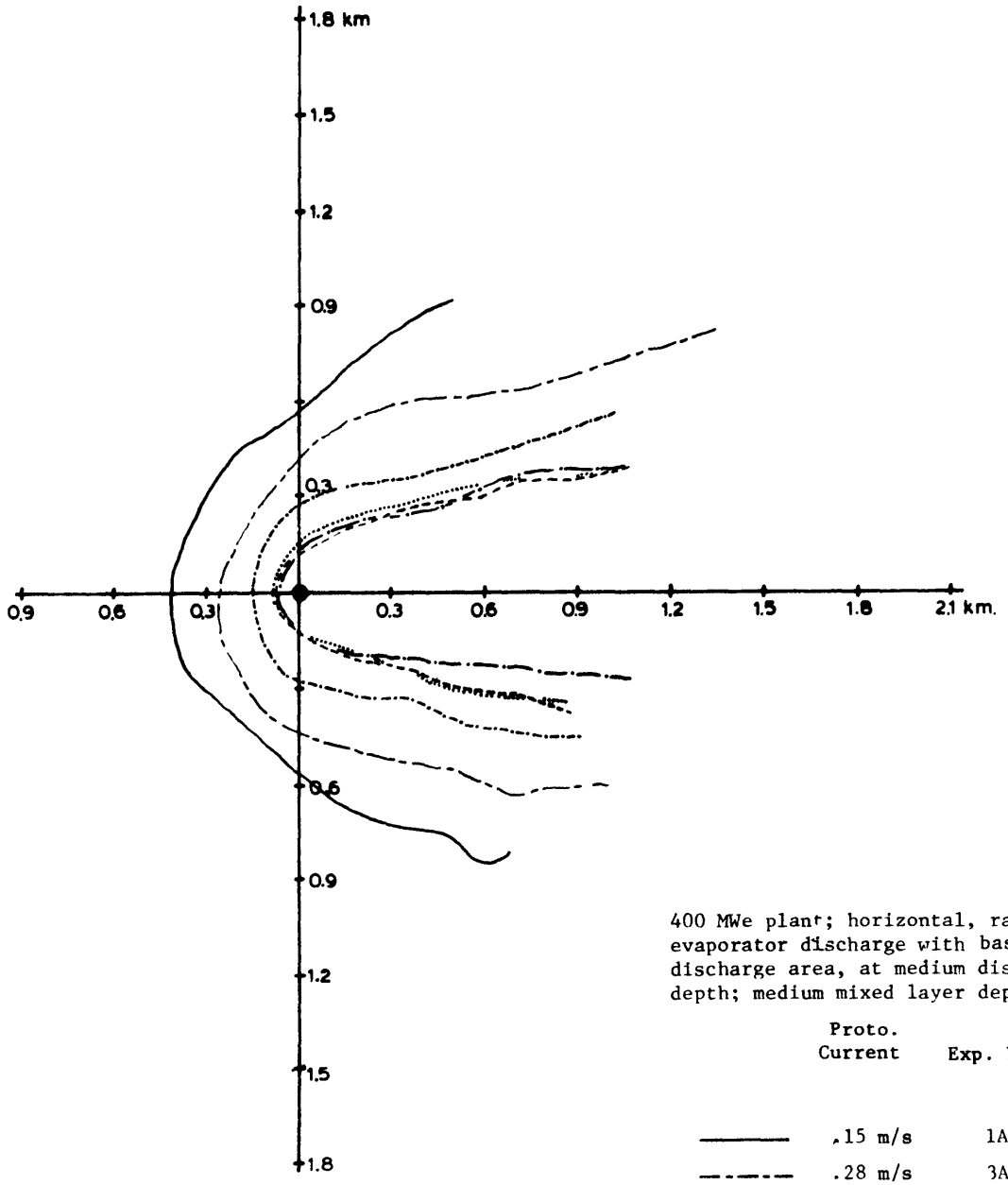

400 MWe plant; horizontal, radial, evaporator discharge with base case discharge area, at medium discharge depth; medium mixed layer depth

	Proto. Current	Exp. No.
———	.15 m/s	1A
— - — - —	.28 m/s	3A
—·—·—·—	.40 m/s	3B
.....	.87 m/s	14
- - - - - - - -	1.0 m/s	9
—·—·—	1.0 m/s	10

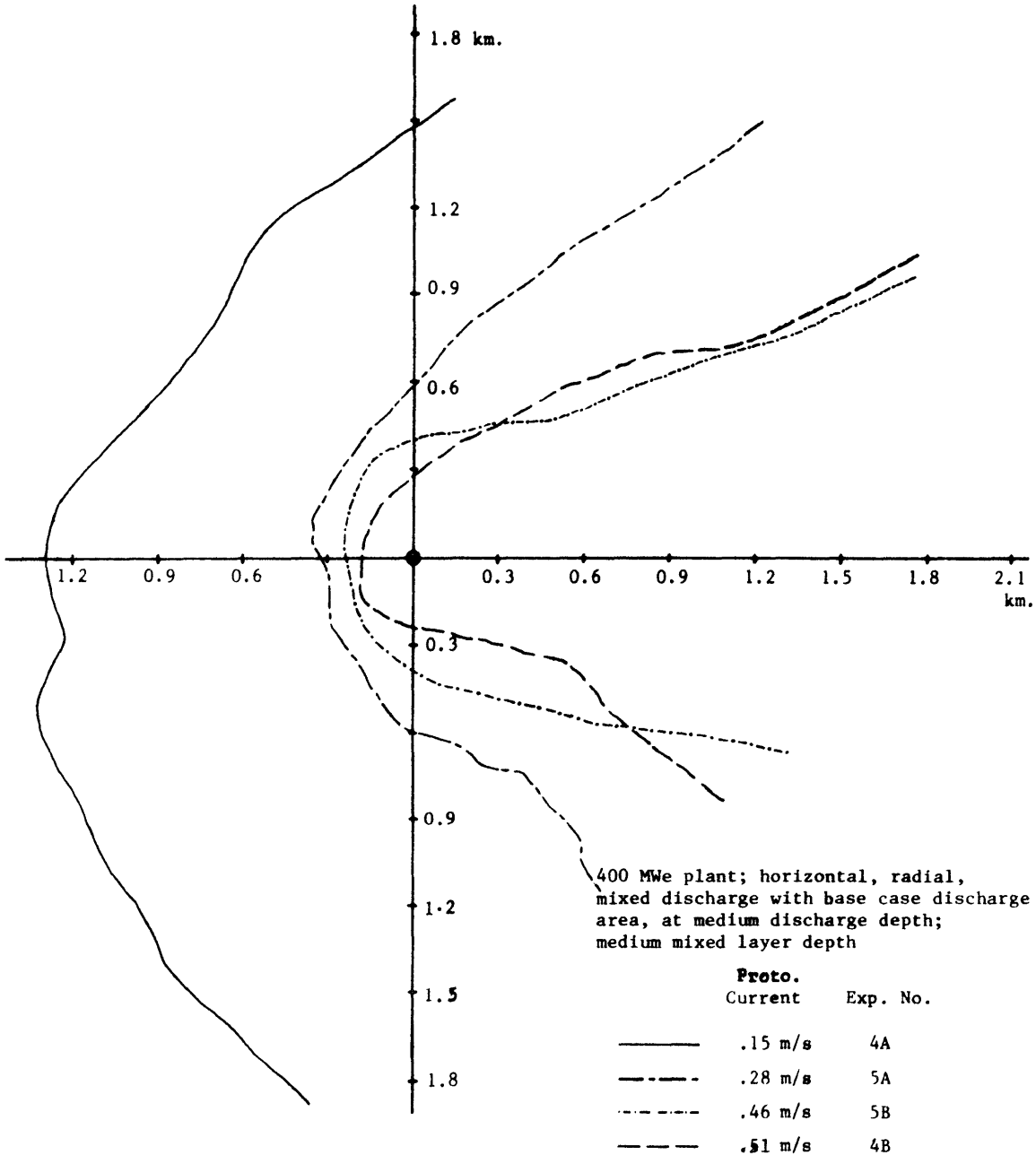
1.8 km.
1.2
0.9
0.6
0.3
0.6
0.9
1.2
1.5
1.8
2.1
km.
0.3
0.9
1.2
1.5
1.8
400 MWe plant; horizontal, radial, mixed discharge with base case discharge area, at medium discharge depth; medium mixed layer depth
Proto. Current
Exp. No.
.15 m/s
4A
.28 m/s
5A
.46 m/s
5B
.51 m/s
4B

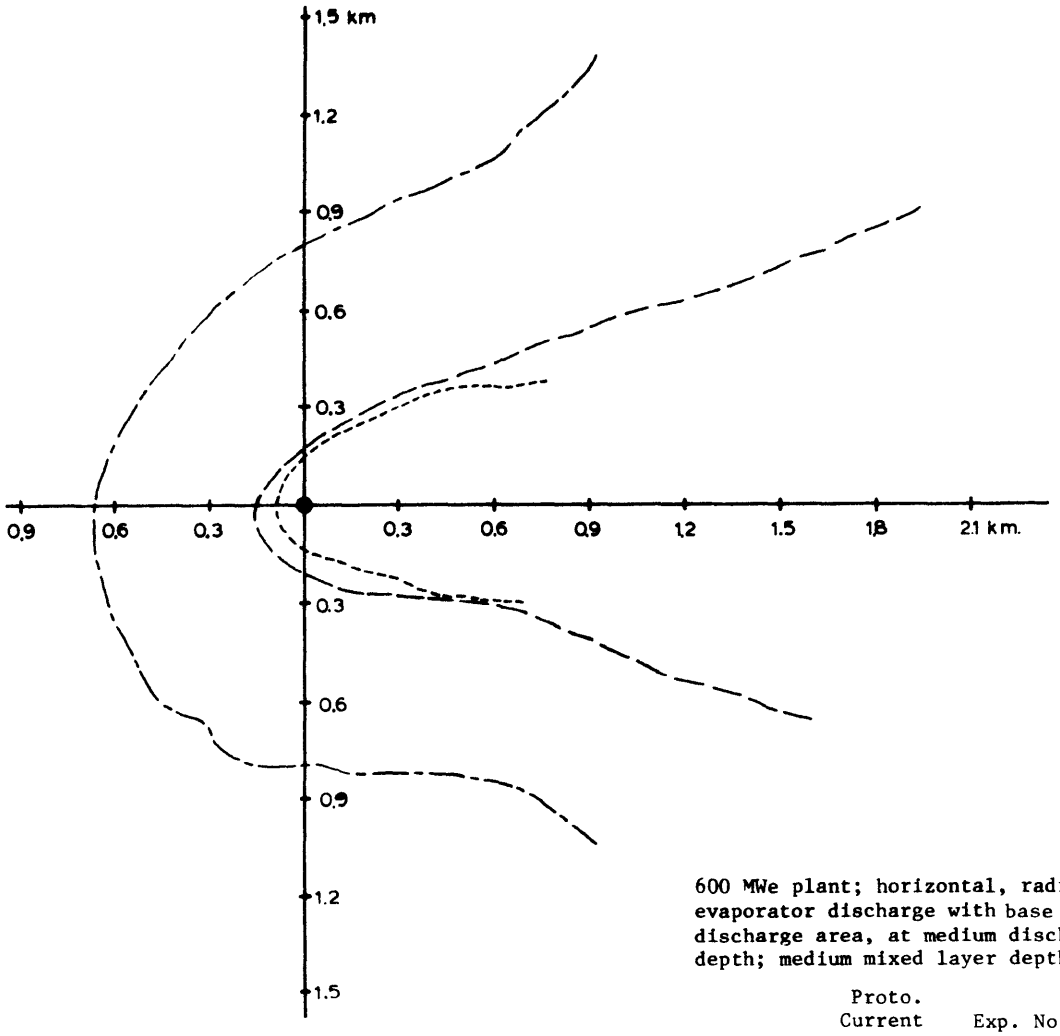

600 MWe plant; horizontal, radial, evaporator discharge with base case discharge area, at medium discharge depth; medium mixed layer depth

	Proto. Current	Exp. No.
—·—·—	.28 m/s	6A
— — —	.51 m/s	6B
-------	1.0 m/s	11

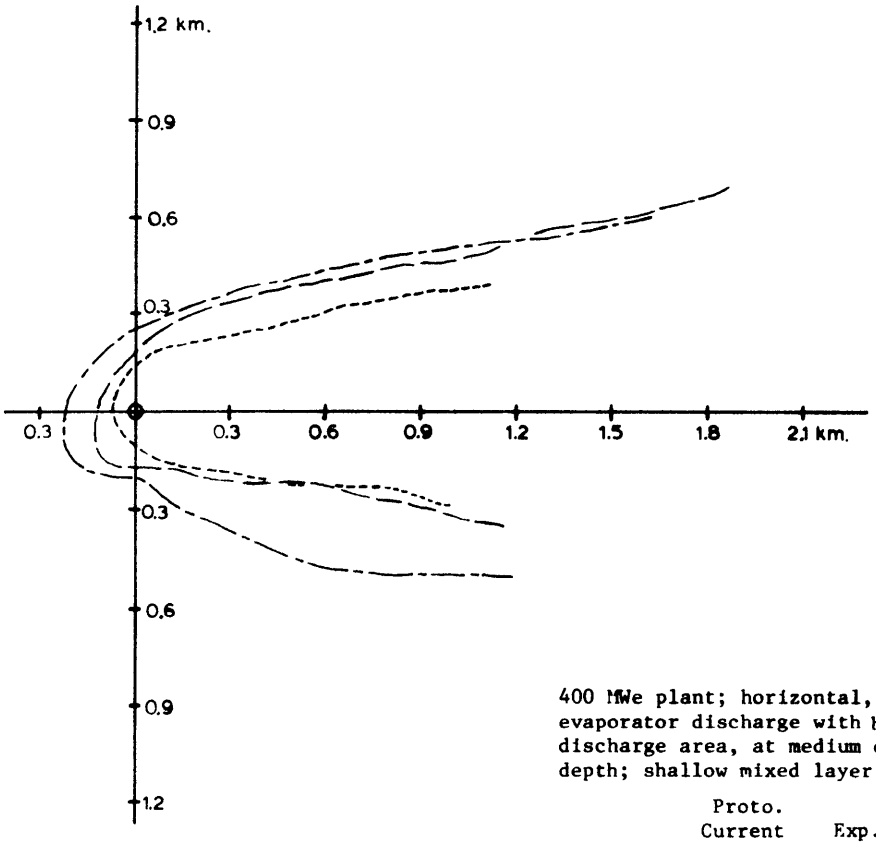

400 MWe plant; horizontal, radial, evaporator discharge with base case discharge area, at medium discharge depth; shallow mixed layer depth

	Proto. Current	Exp. No.
——-——-	.28 m/s	7A
—— ——	.51 m/s	7B
--------	1.0 m/s	12

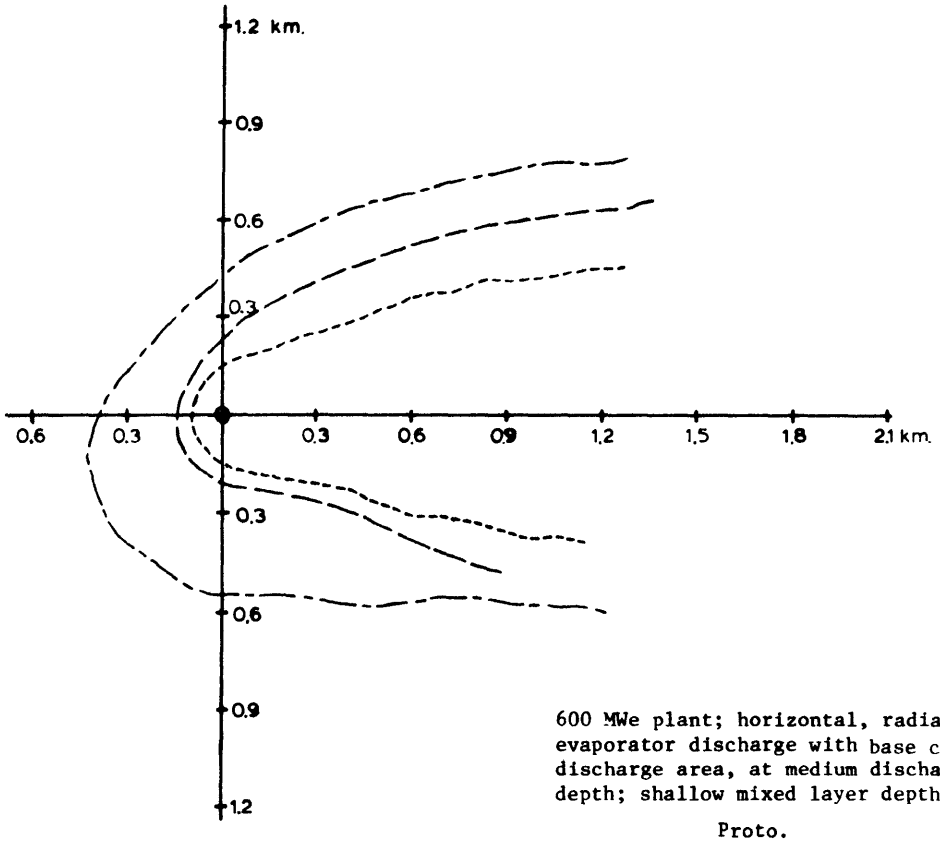

600 MWe plant; horizontal, radial, evaporator discharge with base case discharge area, at medium discharge depth; shallow mixed layer depth

	Proto. Current	Exp. No.
— · — · —	.28 m/s	8A
— — —	.51 m/s	8B
----------	1.0 m/s	13

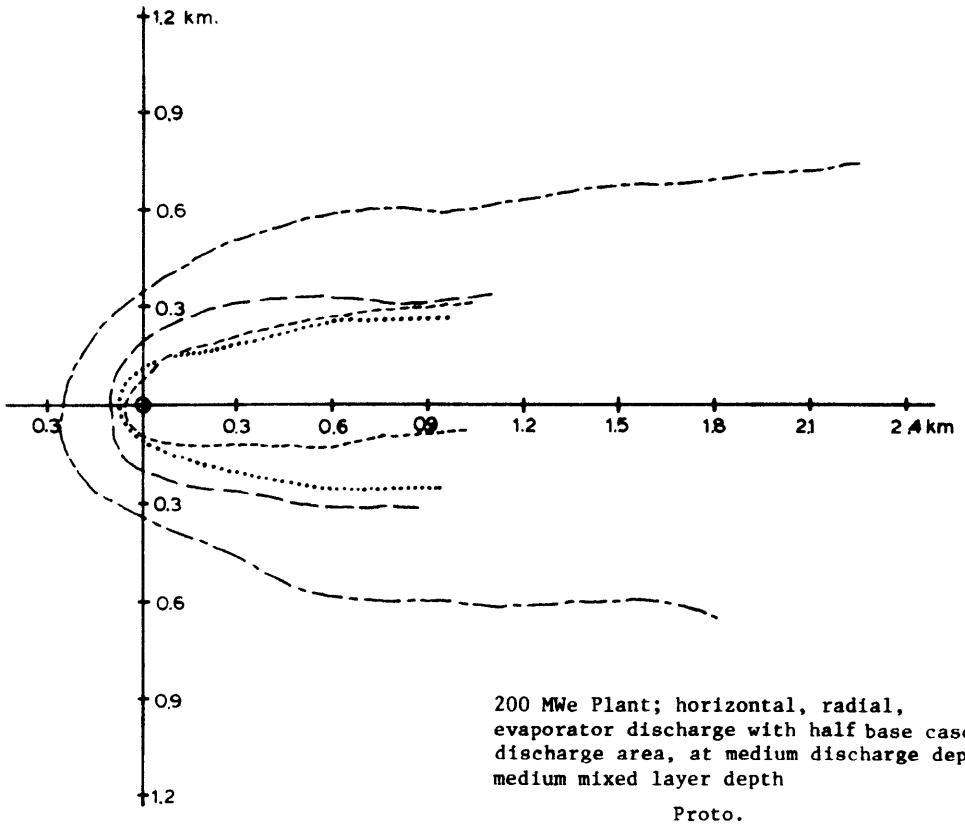

200 MWe Plant; horizontal, radial, evaporator discharge with half base case discharge area, at medium discharge depth; medium mixed layer depth

	Proto. Current	Exp. No.
— - — -	.28 m/s	15A
— — —	.51 m/s	15B
.....	.87 m/s	16
--------	1.0 m/s	17

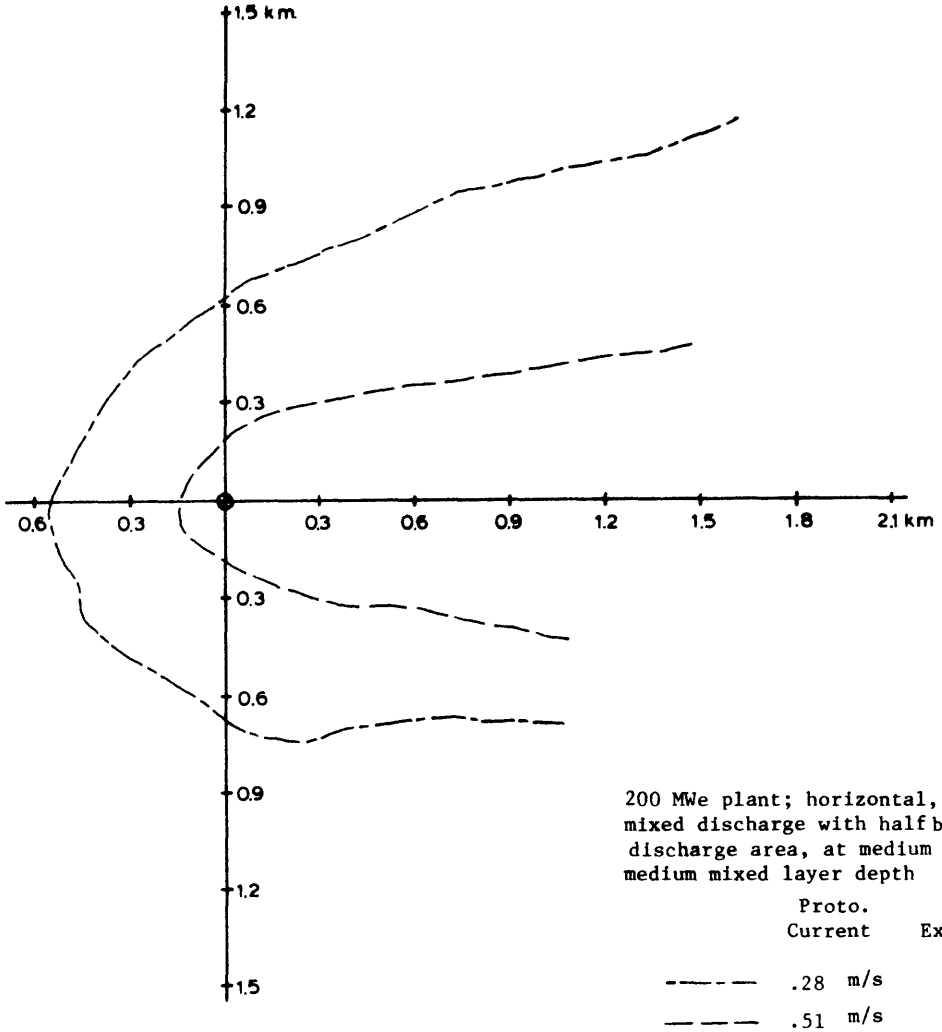

200 MWe plant; horizontal, radial, mixed discharge with half base case discharge area, at medium discharge depth; medium mixed layer depth

	Proto. Current	Exp. No.
- - - -	.28 m/s	18A
— — —	.51 m/s	18B

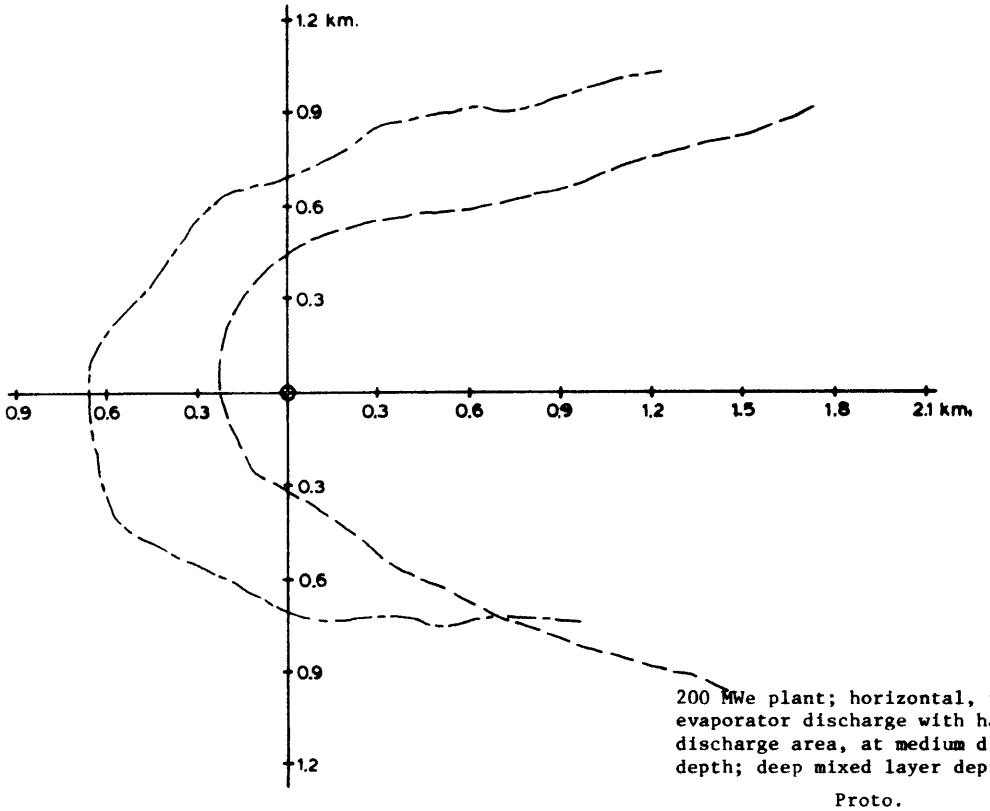

200 MWe plant; horizontal, radial, evaporator discharge with half base case discharge area, at medium discharge depth; deep mixed layer depth

	Proto. Current	Exp. No.
—·—·—	.28 m/s	19A
— — —	.51 m/s	19B

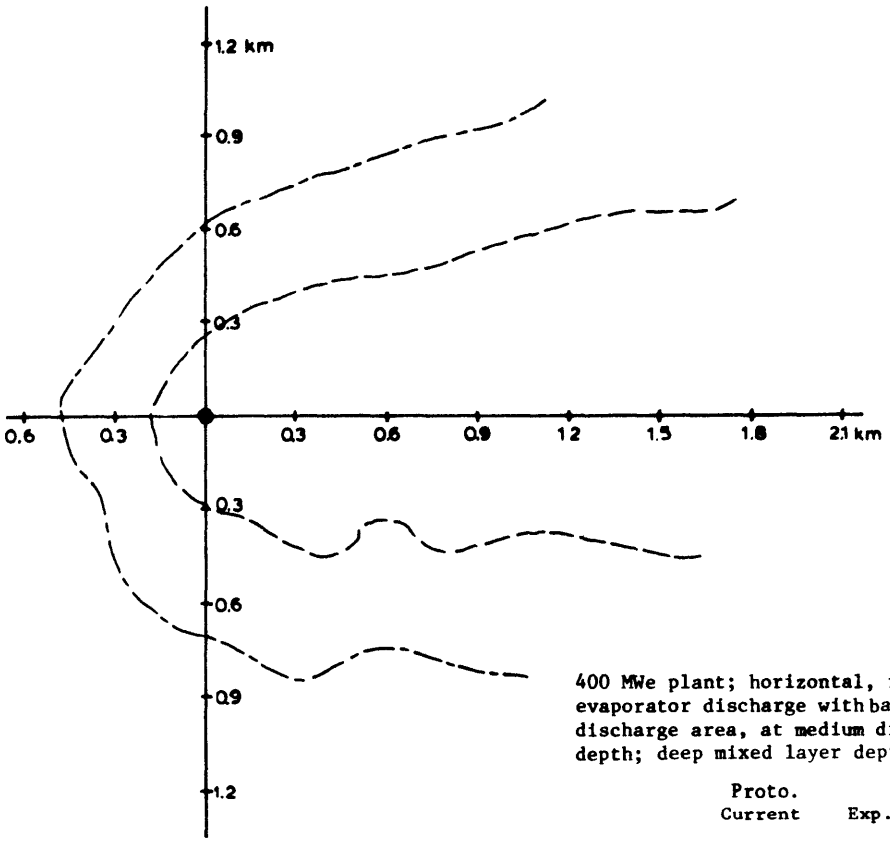

400 MWe plant; horizontal, radial, evaporator discharge with base case discharge area, at medium discharge depth; deep mixed layer depth

	Proto. Current	Exp. No.
—·—·—	.28 m/s	20A
— — —	.51 m/s	20B

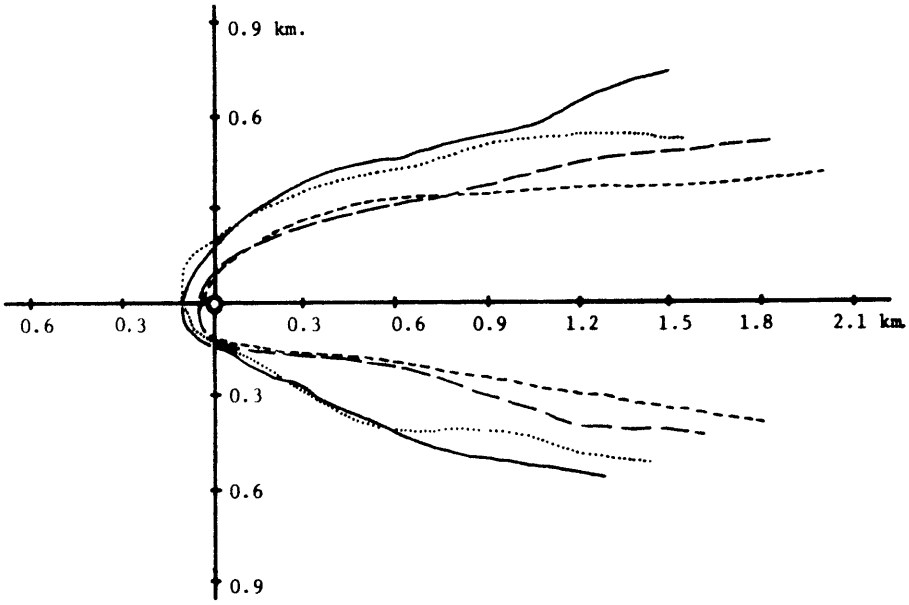

Horizontal, radial, evaporator discharge with base case discharge area, at shallow discharge depth; medium mixed layer depth

Proto. Current	Exp. No.	Net Power (MWe)
—— .28 m/s	22A	400
···· .28 m/s	25A	200
— — .51 m/s	22B	400
------ .51 m/s	25B	200

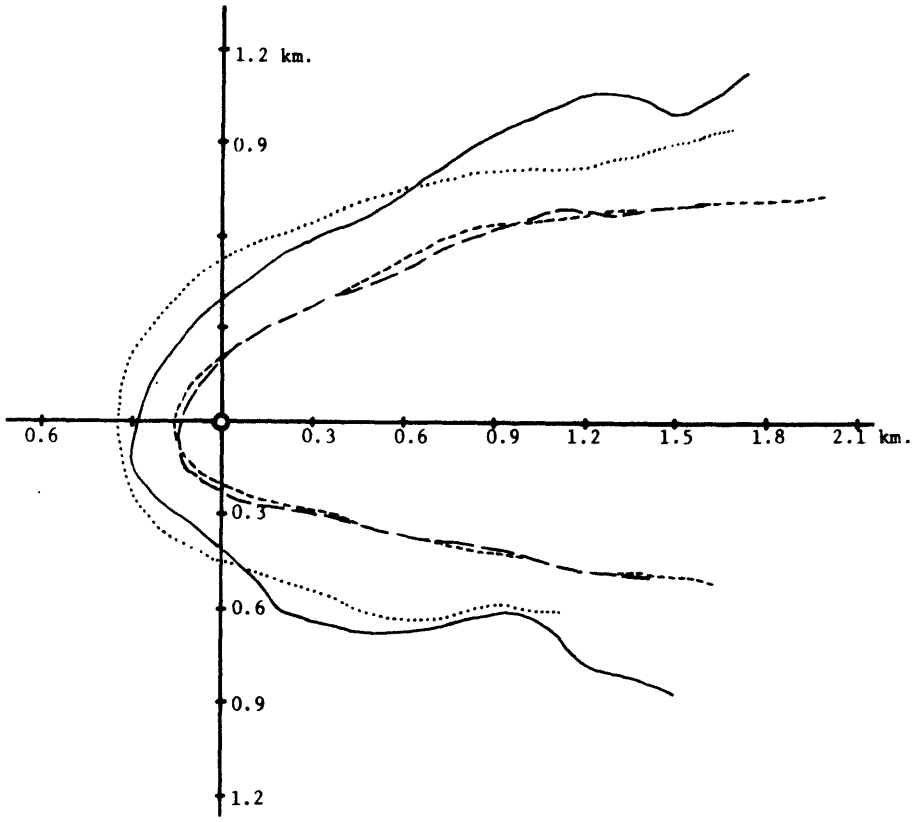

Horizontal, radial, mixed discharge with base case discharge area, at shallow discharge depth; medium mixed layer depth

	Proto. Current	Exp. No.	Net Power (MWe)
———	.28 m/s	23A	400
.....	.28 m/s	24A	200
------	.51 m/s	24B	200
— —	.51 m/s	23B	400

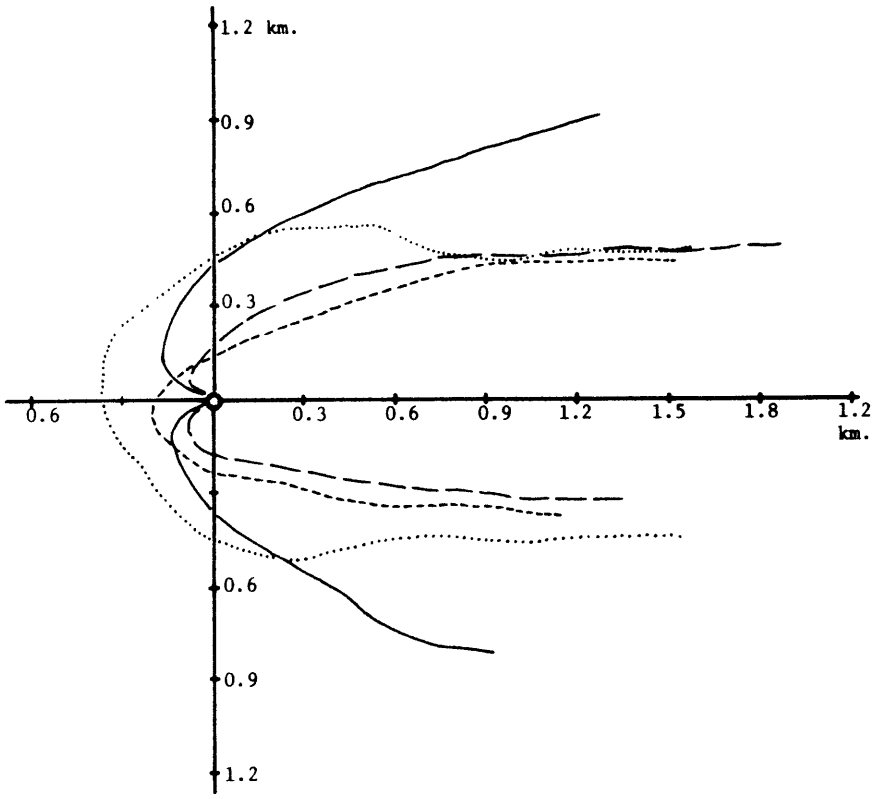

400 MWe plant; 4-jet, evaporator discharge with base case area, at shallow discharge depth; medium mixed layer depth

	Proto. Current	Exp. No.	α_{H}[1]	α_{V}
———	.28 m/s	26A	45°	45°
— —	.51 m/s	26B	45°	45°
. . . .	.28 m/s	27A	0°	45°
------	.51 m/s	27B	0°	45°

[1] See Table 3

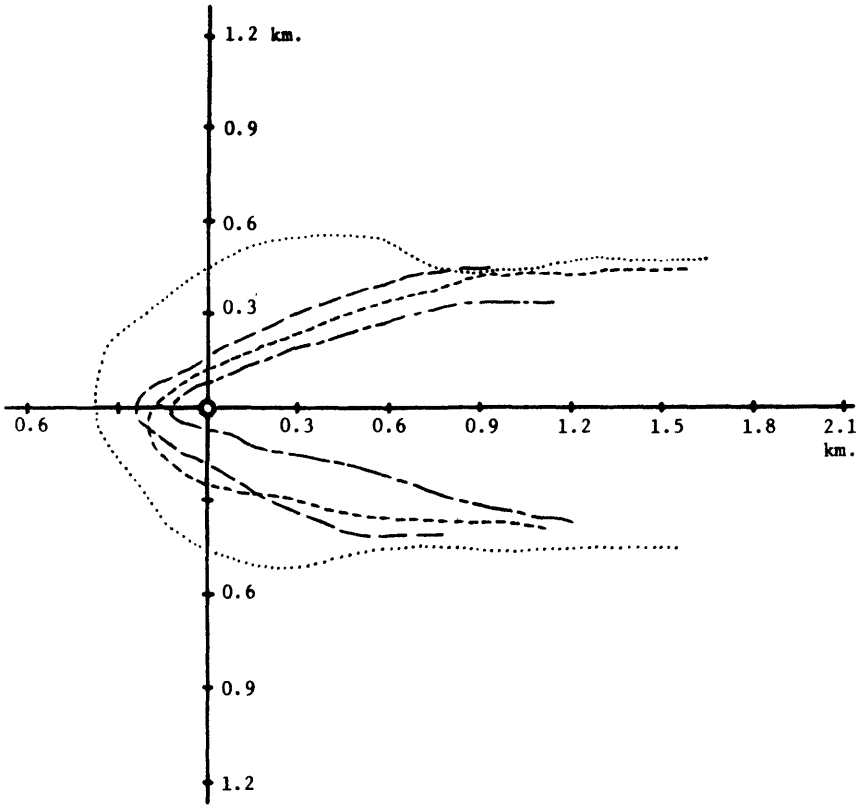

400 MWe plant; 4-jet, evaporator discharge with base case discharge area, at shallow discharge depth; medium mixed layer depth

	Proto. Current	Exp. No.	α_H	α_V
.....	.28 m/s	27A	0°	45°
-----	.51 m/s	27B	0°	45°
—— ——	.51 m/s	28A	0°	45°
—— - ——	.87 m/s	28B	0°	45°

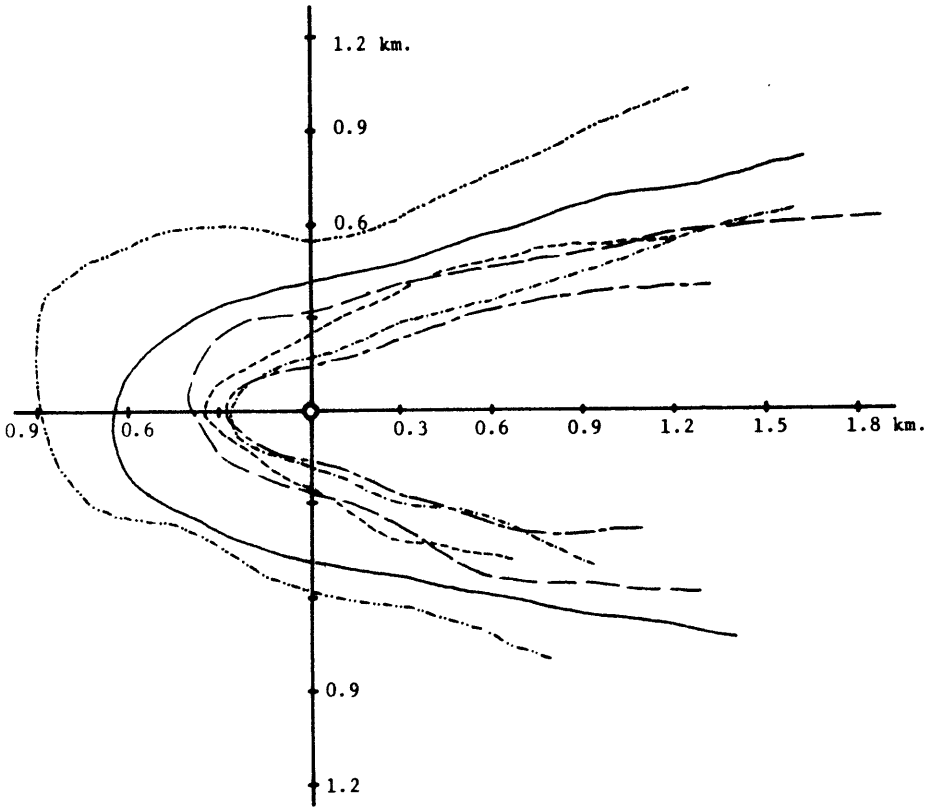

400 MWe plant; horizontal, 4-jet discharge with base case discharge area, at medium discharge depth; medium mixed layer depth

	Proto. Current	Exp. No.
-·-·-·-	.15 m/s	31A
———	.28 m/s	29A
— —	.51 m/s	29B
------	.51 m/s	30A
—·—·—	.87 m/s	30B
-·-·-·-	.87 m/s	31B

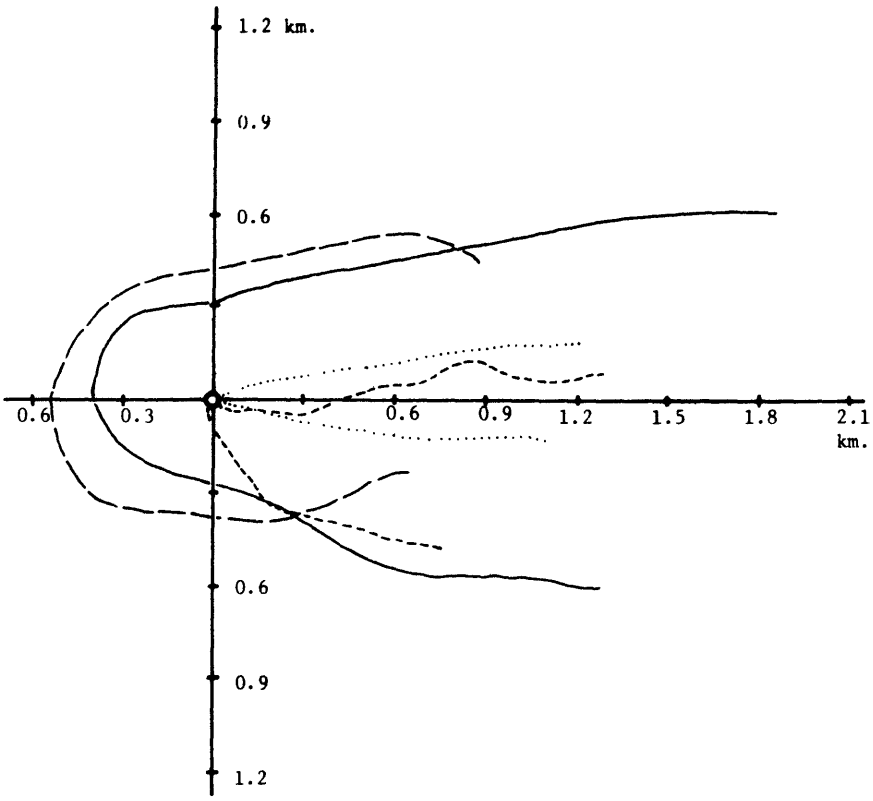

400 MWe plant; horizontal, evaporator discharge with base case discharge ports, at medium discharge depth; medium mixed layer depth

	Proto. Current	Exp. No.	Port Type
— —	.51 m/s	32B	1-bow jet
———	.51 m/s	29B	4-jet
------	.51 m/s	33B	1-port jet
.....	.51 m/s	34B	1-aft jet

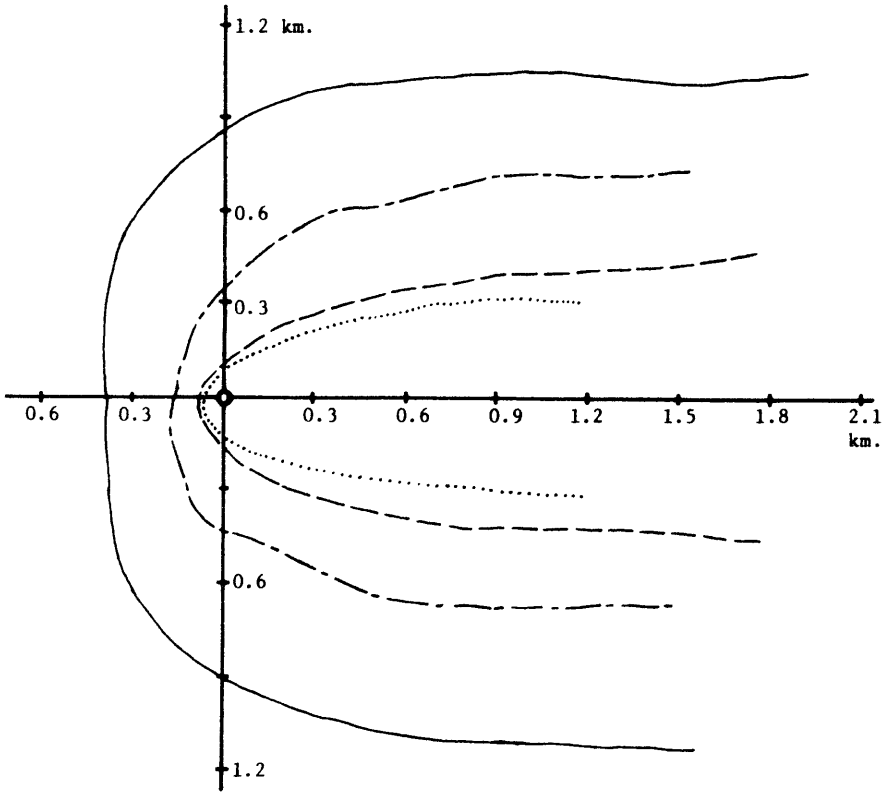

400 MWe plant; horizontal, radial discharge with twice base case discharge area, at medium discharge depth; medium mixed layer depth

	Proto. Current	Exp. No.
———	.15 m/s	37A
—·—·—	.28 m/s	36A
— — —	.51 m/s	36B
·· ··· ····	.87 m/s	37B

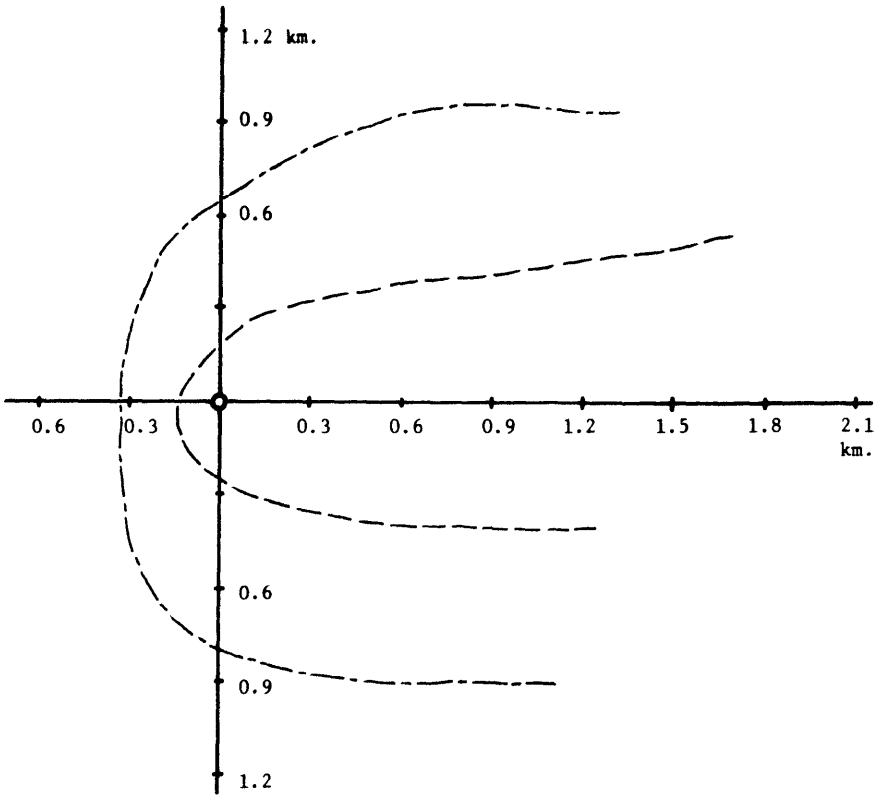

400 MWe plant; horizontal radial, mixed discharge with twice base case discharge area, at medium discharge depth; medium mixed layer

	Proto. Current	Exp. No.
—·—	.28 m/s	38A
— —	.51 m/s	38B

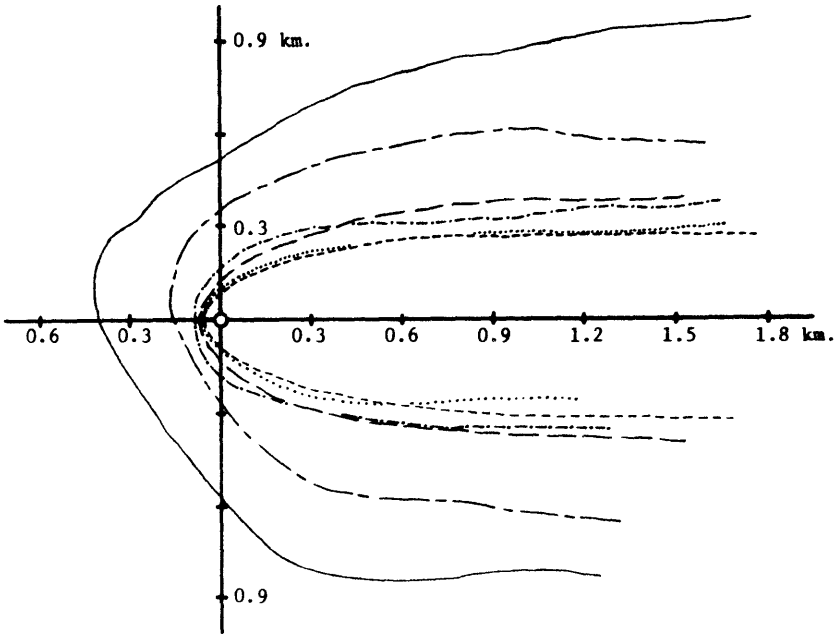

400 MWe plant; horizontal, radial, evaporator discharge with 3 times base case discharge area, at medium discharge depth; medium mixed layer depth

	Proto. Current	Exp. No.
———	.15 m/s	40A
—— ——	.28 m/s	39A
—— — —	.51 m/s	41A
—— ——	.51 m/s	39B
	.87 m/s	40B
-------	.87 m/s	41B

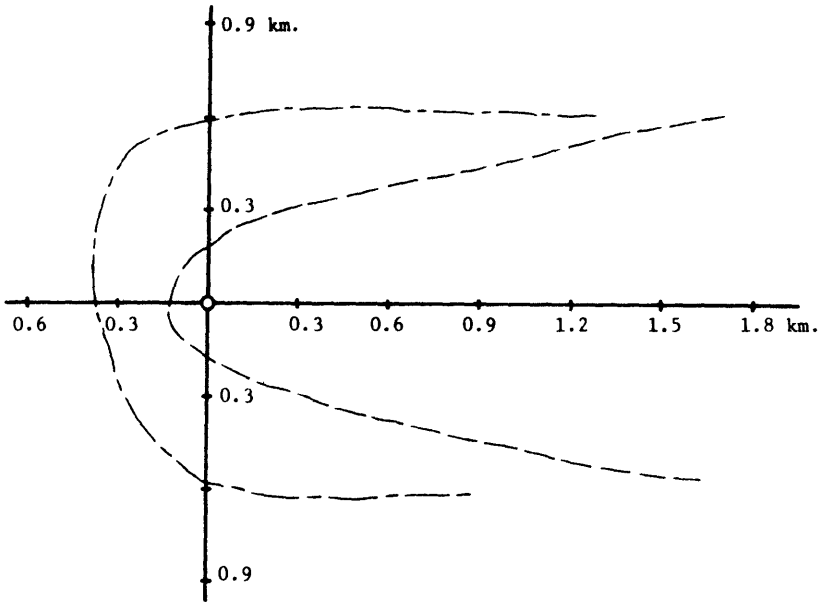

400 MWe plant; horizontal, radial, mixed discharge with 3 times base case area, at medium discharge depth; medium mixed layer depth

	Proto. Current	Exp. No.
—·—	.28 m/s	42A
— —	.51 m/s	42B

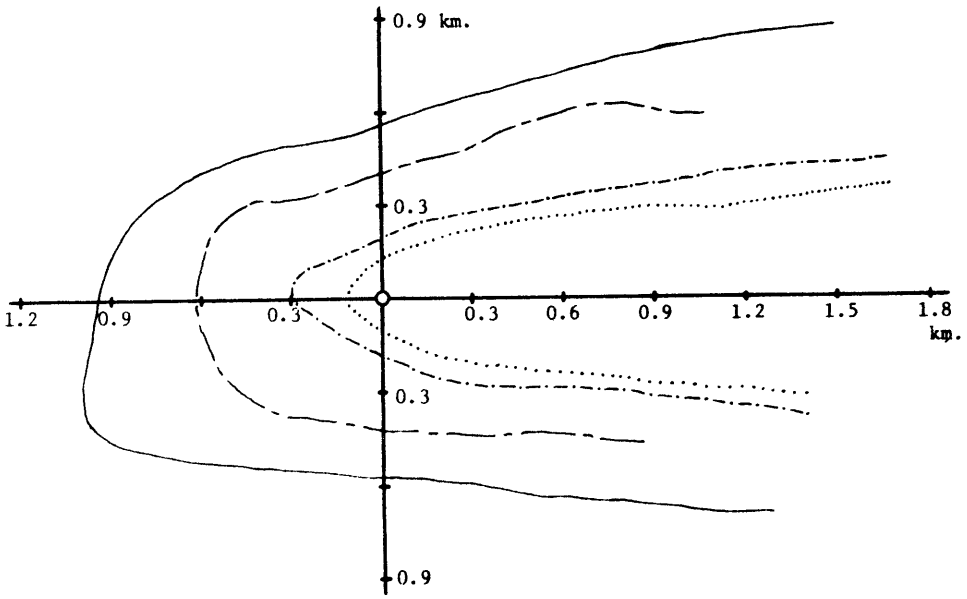

400 MWe plant; horizontal, 4-jet, evaporator discharge with 3 times base case discharge area, at medium discharge depth; medium mixed layer depth

	Proto. Current	Exp. No.
———	.15 m/s	44A
— — —	.28 m/s	43A
—·—·—	.51 m/s	43B
·····	.87 m/s	44B

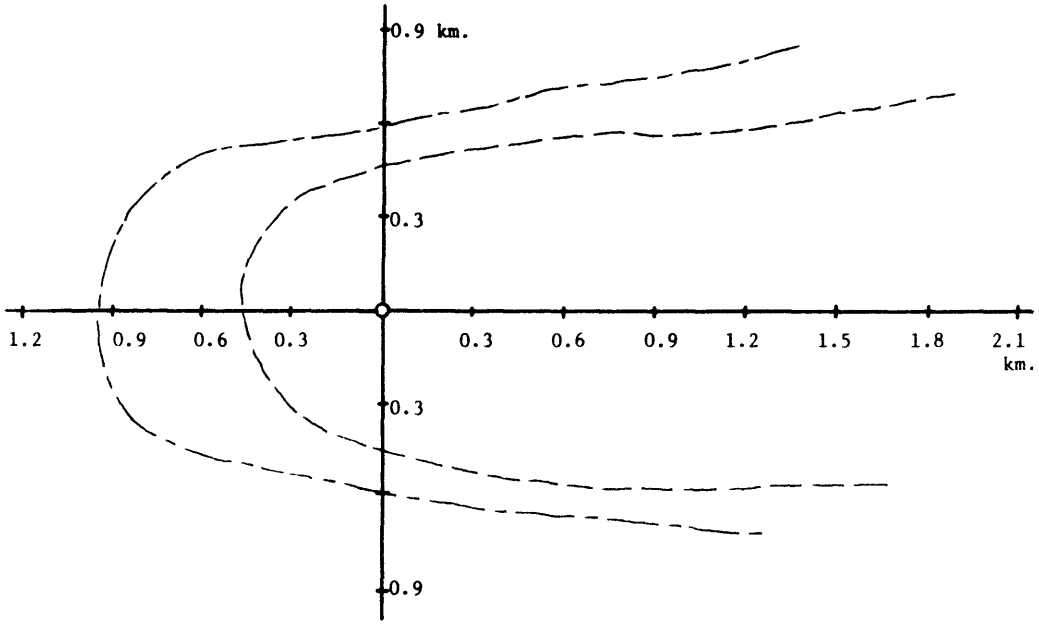

400 MWe plant; horizontal, 4-jet, mixed discharge with 3 times base case discharge area, at medium discharge depth; medium mixed layer depth

	Proto. Current	Exp. No.
—·—	.28 m/s	45A
——	.51 m/s	45B

APPENDIX III

EXPERIMENTAL (SPATIALLY AVERAGED) DENSITY PROFILES

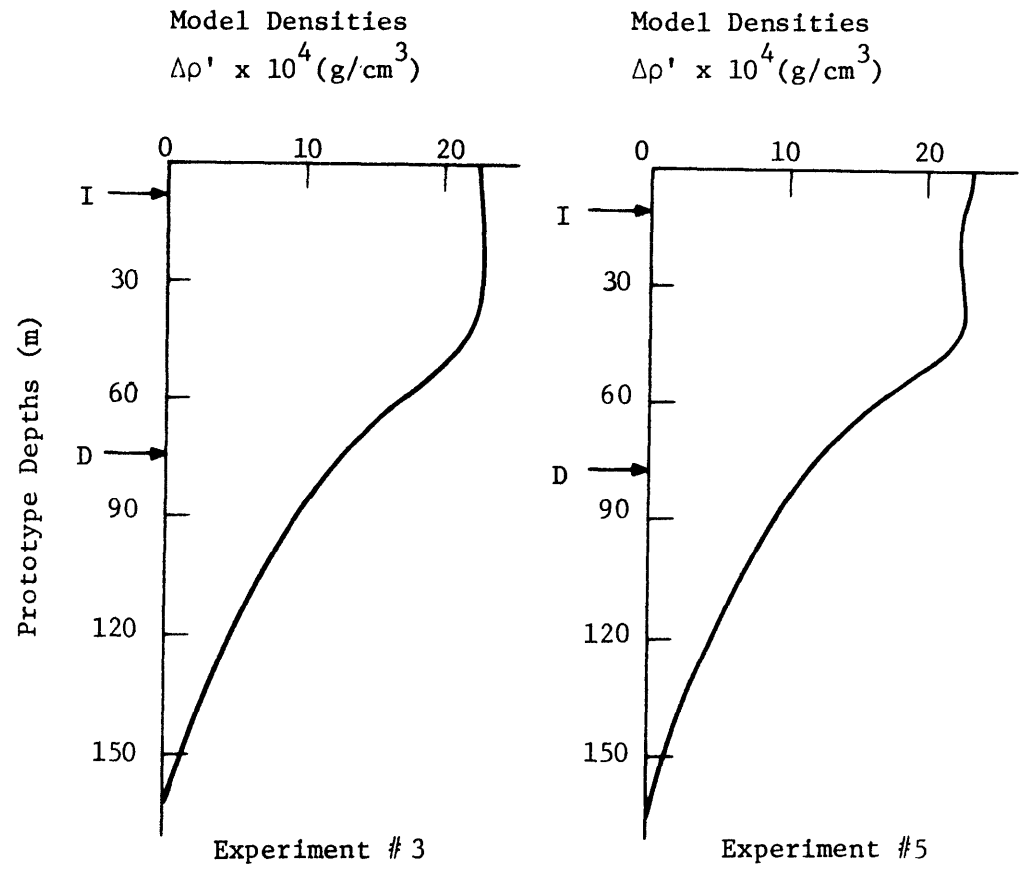
Model Densities
$\Delta\rho' \times 10^4 (g/cm^3)$
0
10
20
I
30
60
D
90
120
150
Prototype Depths (m)
Experiment # 3
Model Densities
$\Delta\rho' \times 10^4 (g/cm^3)$
0
10
20
I
30
60
D
90
120
150
Experiment #5

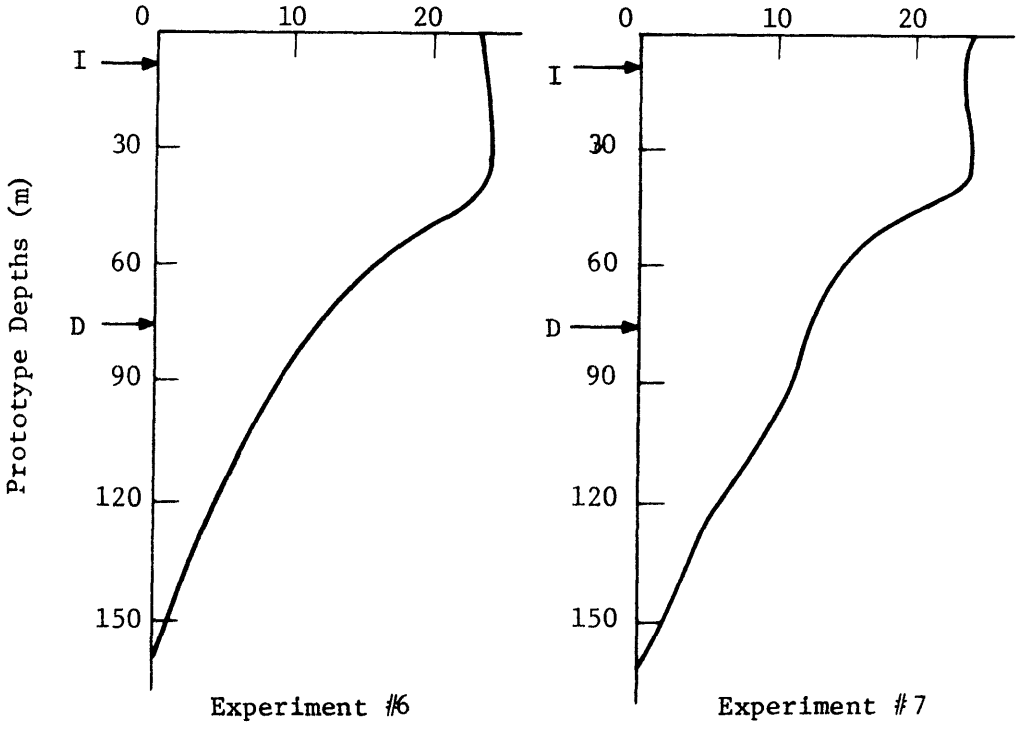
0
10
20
I
30
60
D
90
120
150
Prototype Depths (m)
Experiment #6
0
10
20
I
30
60
D
90
120
150
Experiment # 7

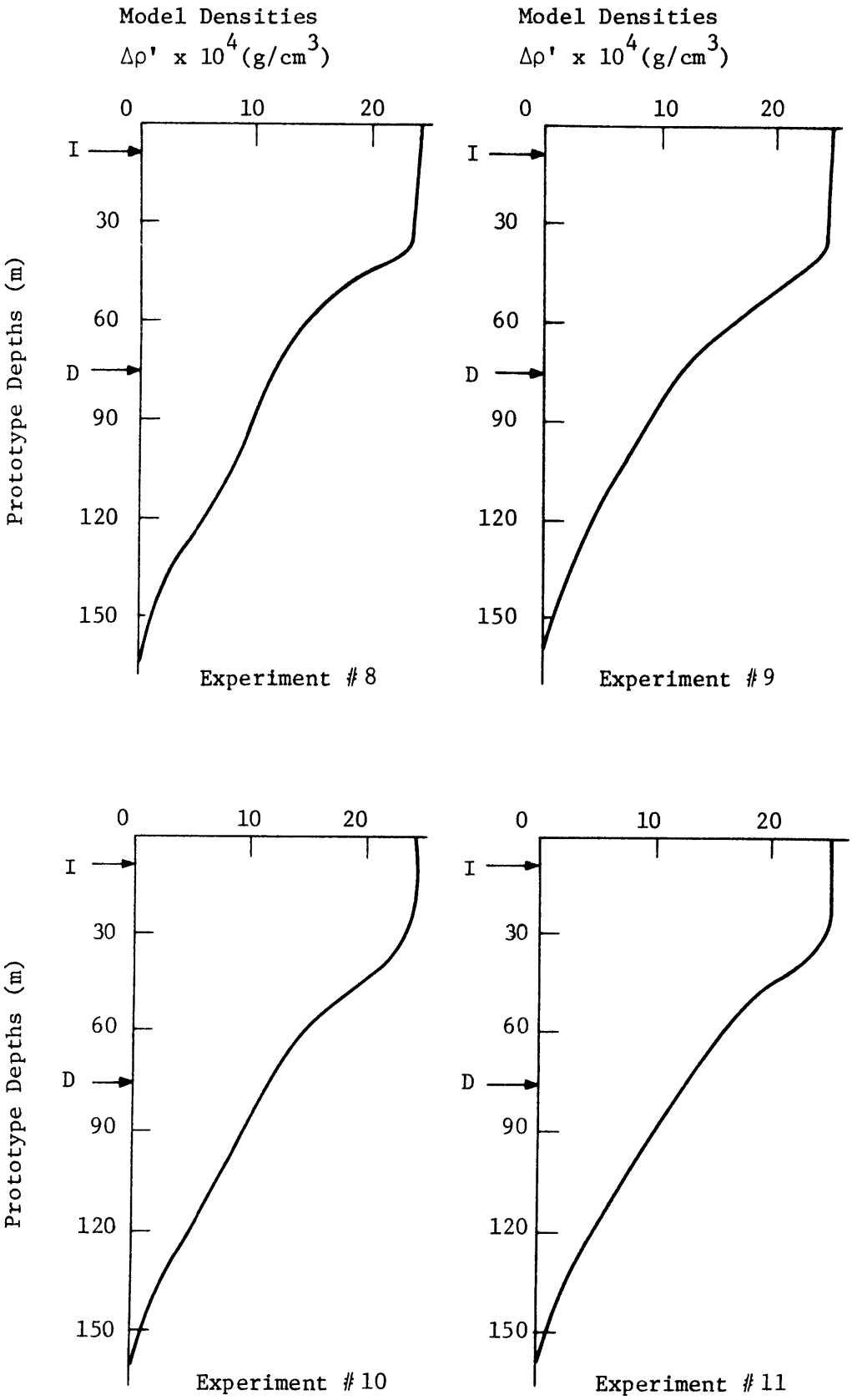
Model Densities
$\Delta\rho' \times 10^4 (g/cm^3)$
0
10
20
I
30
60
D
90
120
150
Prototype Depths (m)
Experiment # 8
Model Densities
$\Delta\rho' \times 10^4 (g/cm^3)$
Experiment # 9
Experiment # 10
Experiment # 11

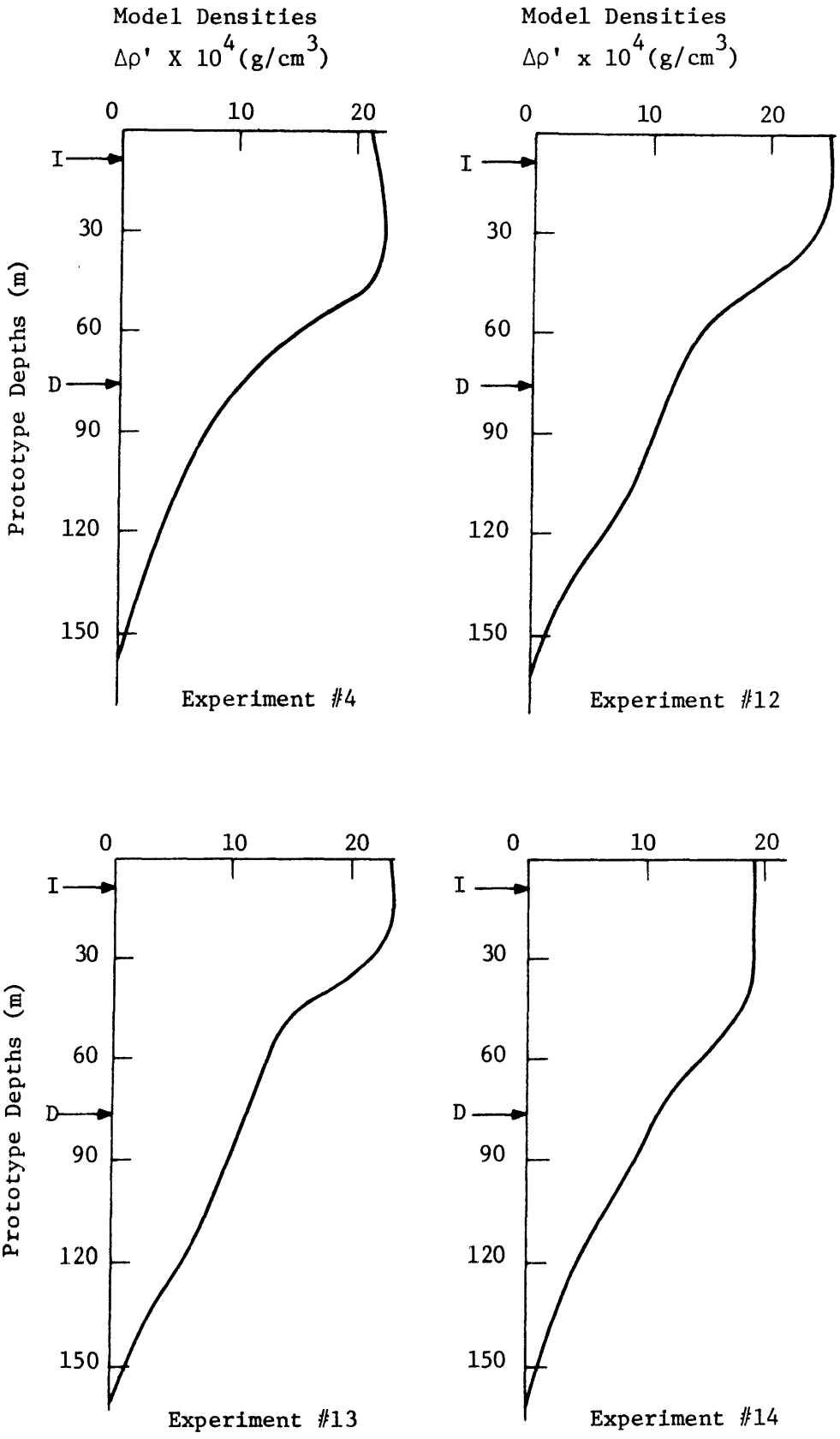
Model Densities
Δρ' X 10^4(g/cm^3)
0
10
20
I
30
60
D
90
120
150
Prototype Depths (m)
Experiment #4
Model Densities
Δρ' x 10^4(g/cm^3)
0
10
20
I
30
60
D
90
120
150
Experiment #12
0
10
20
I
30
60
D
90
120
150
Prototype Depths (m)
Experiment #13
0
10
20
I
30
60
D
90
120
150
Experiment #14

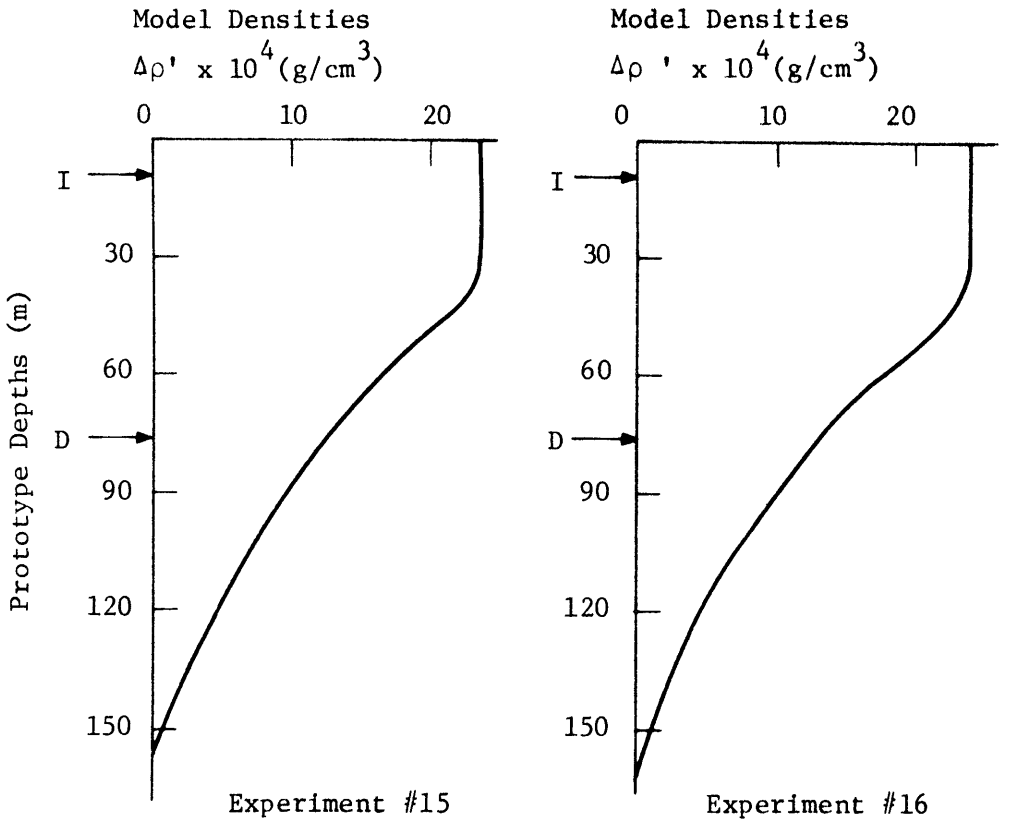
Model Densities
$\Delta\rho'$ x 10^4 (g/cm^3)
0
10
20
I
30
60
D
90
120
150
Prototype Depths (m)
Experiment #15
Model Densities
$\Delta\rho$ ' x 10^4 (g/cm^3)
0
10
20
I
30
60
D
90
120
150
Experiment #16

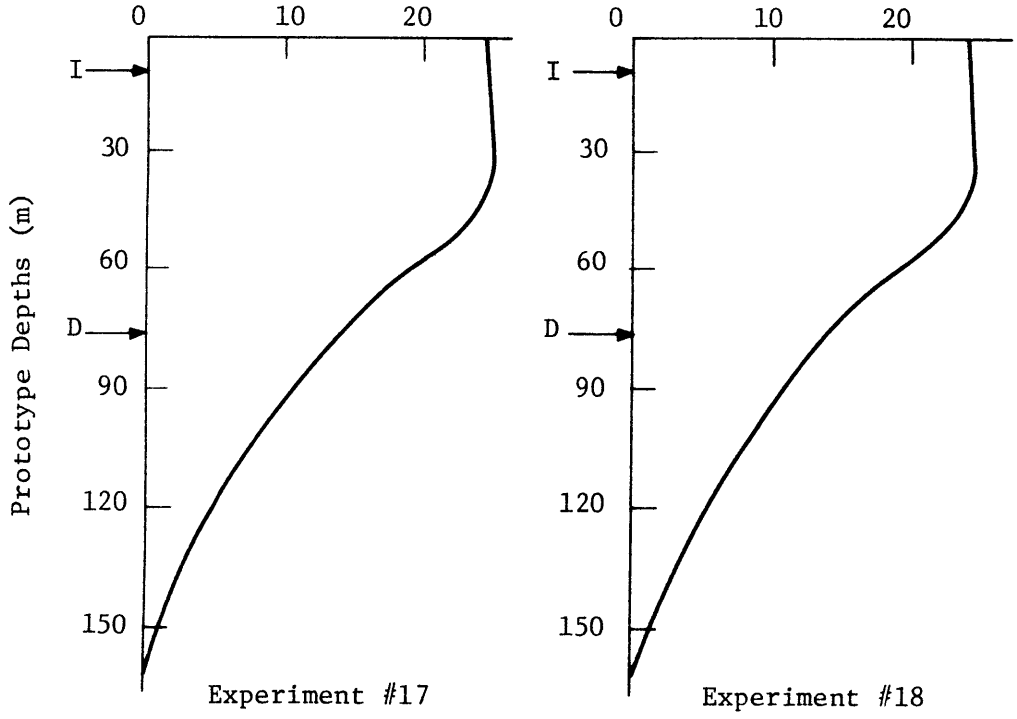
0
10
20
I
30
60
D
90
120
150
Prototype Depths (m)
Experiment #17
0
10
20
I
30
60
D
90
120
150
Experiment #18

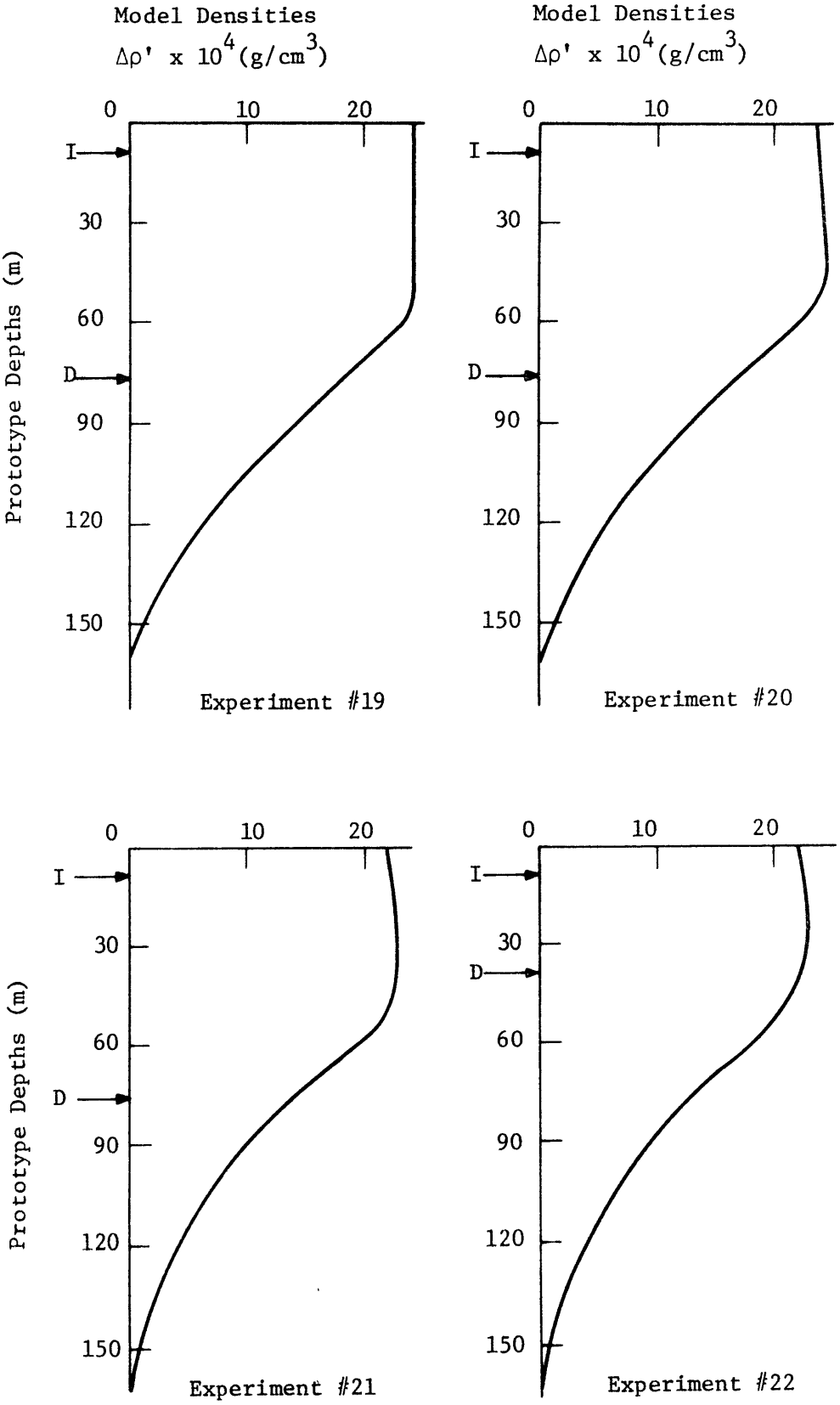
Model Densities
Δρ' x 10^4 (g/cm^3)
0
10
20
I
D
30
60
90
120
150
Prototype Depths (m)
Experiment #19
Model Densities
Δρ' x 10^4 (g/cm^3)
Experiment #20
Experiment #21
Experiment #22

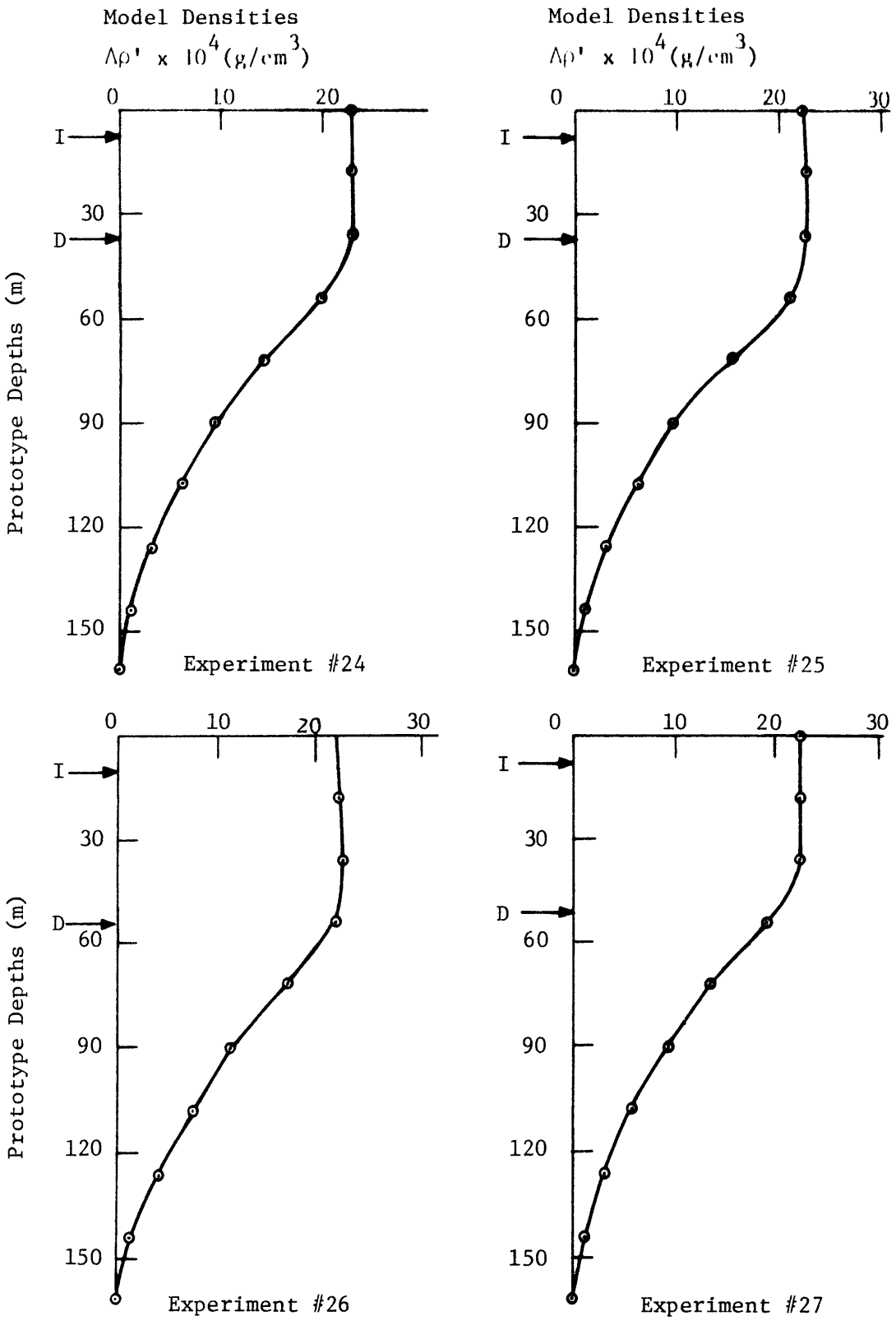
Model Densities
Δρ' x 10^4 (g/cm^3)
0
10
20
30
I
D
30
60
90
120
150
Prototype Depths (m)
Experiment #24
Experiment #25
Experiment #26
Experiment #27

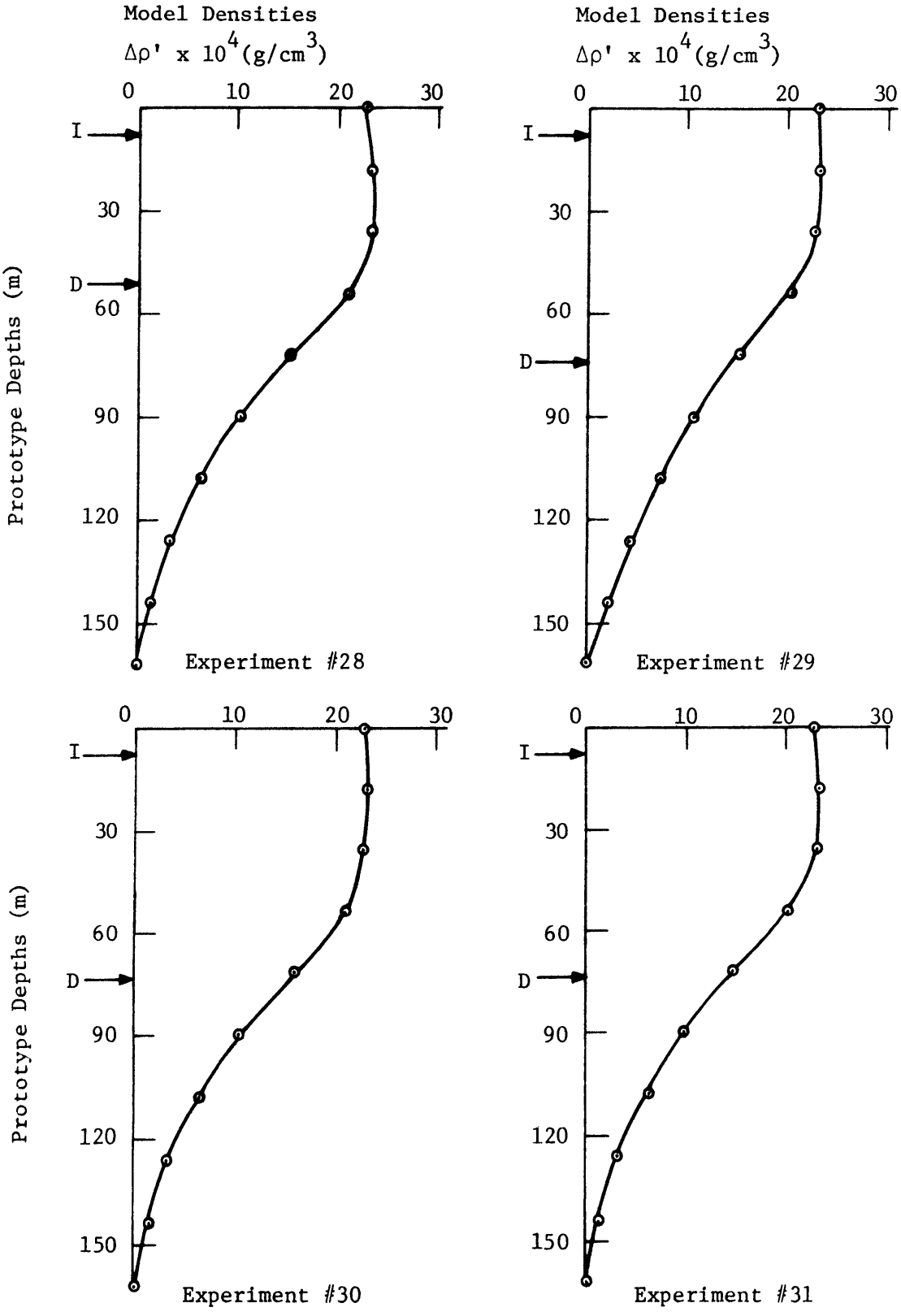
Model Densities
Δρ' x 10^4(g/cm^3)
0
10
20
30
I
D
30
60
90
120
150
Prototype Depths (m)
Experiment #28
Model Densities
Δρ' x 10^4(g/cm^3)
Experiment #29
Experiment #30
Experiment #31

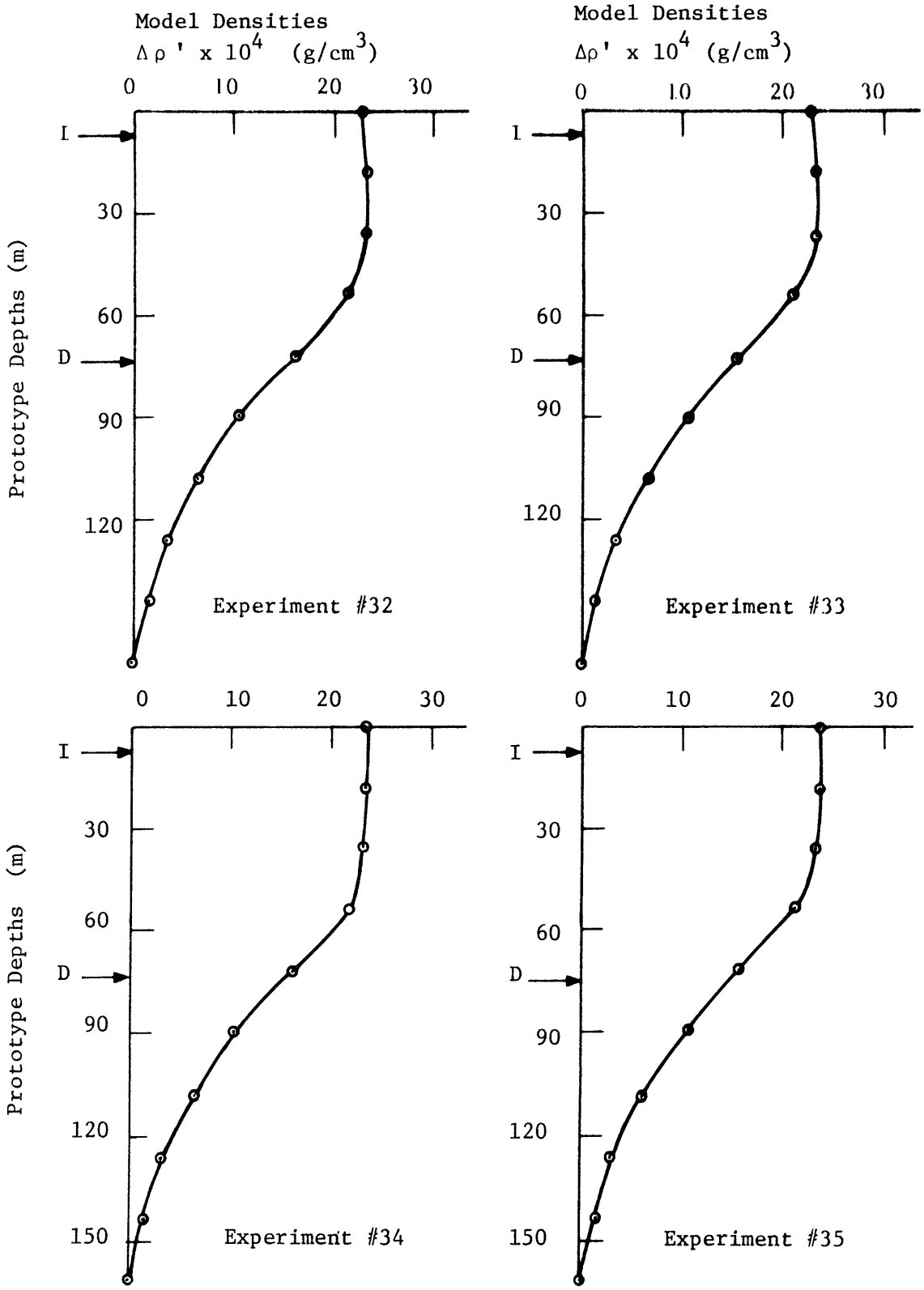
Model Densities
Δρ' x 10^4 (g/cm^3)
0
10
20
30
I
D
30
60
90
120
150
Prototype Depths (m)
Experiment #32
Experiment #33
Experiment #34
Experiment #35

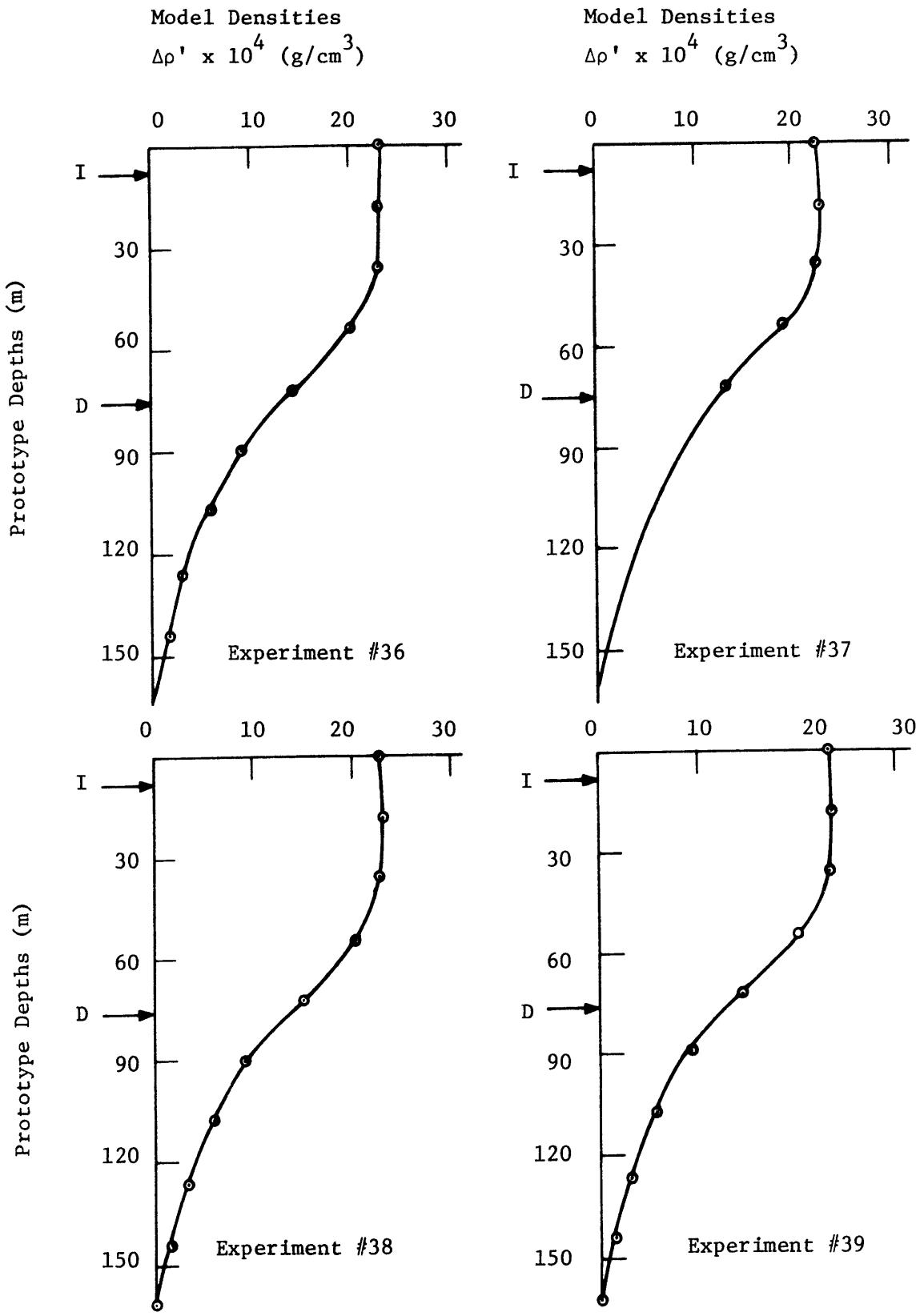
Model Densities
$\Delta\rho' \times 10^4$ (g/cm^3)
0
10
20
30
I
D
30
60
90
120
150
Prototype Depths (m)
Experiment #36
Experiment #37
Experiment #38
Experiment #39

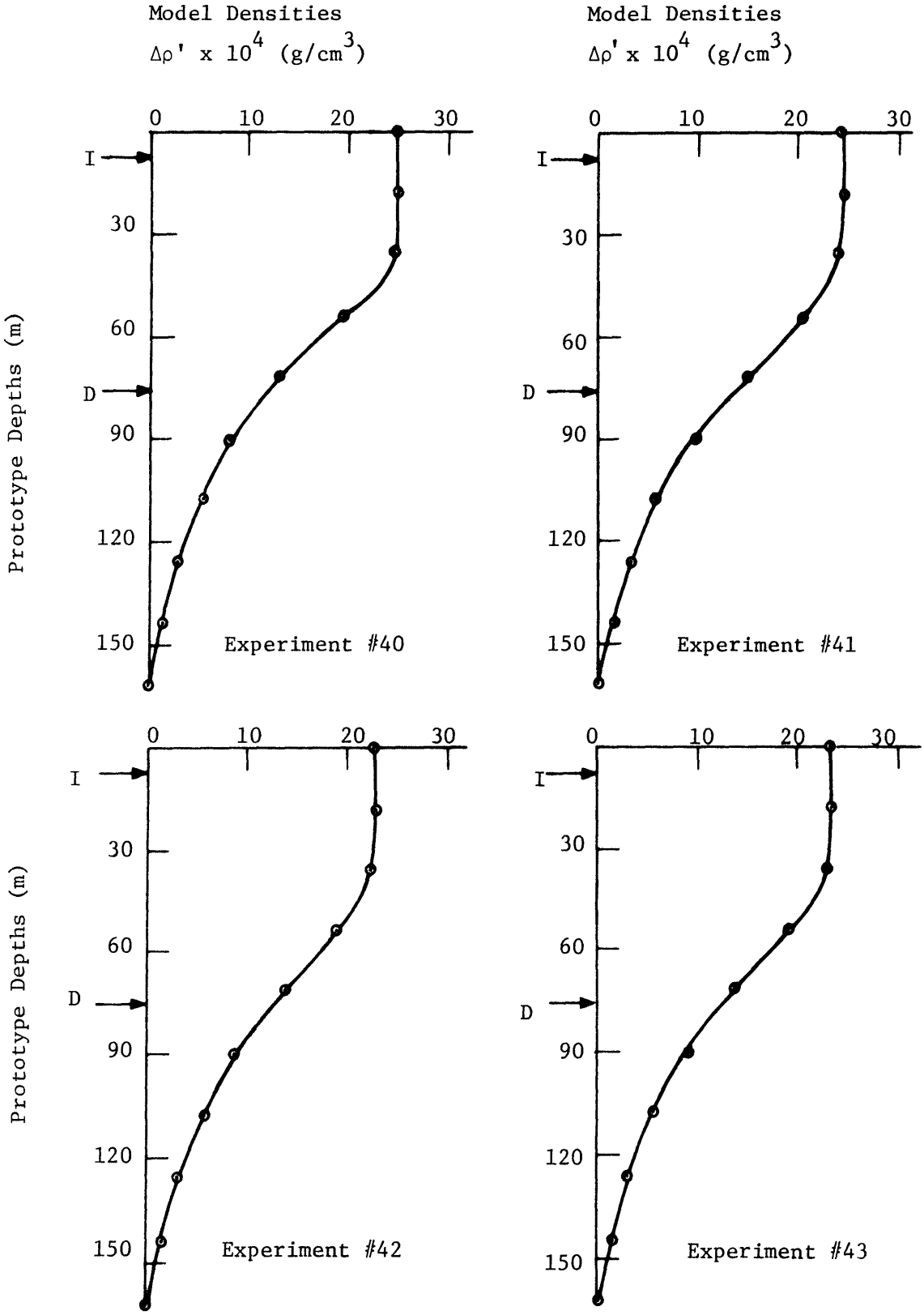
Model Densities
$\Delta\rho' \times 10^4$ (g/cm^3)
Model Densities
$\Delta\rho' \times 10^4$ (g/cm^3)
Prototype Depths (m)
Prototype Depths (m)
0
10
20
30
I
D
30
60
90
120
150
Experiment #40
Experiment #41
Experiment #42
Experiment #43

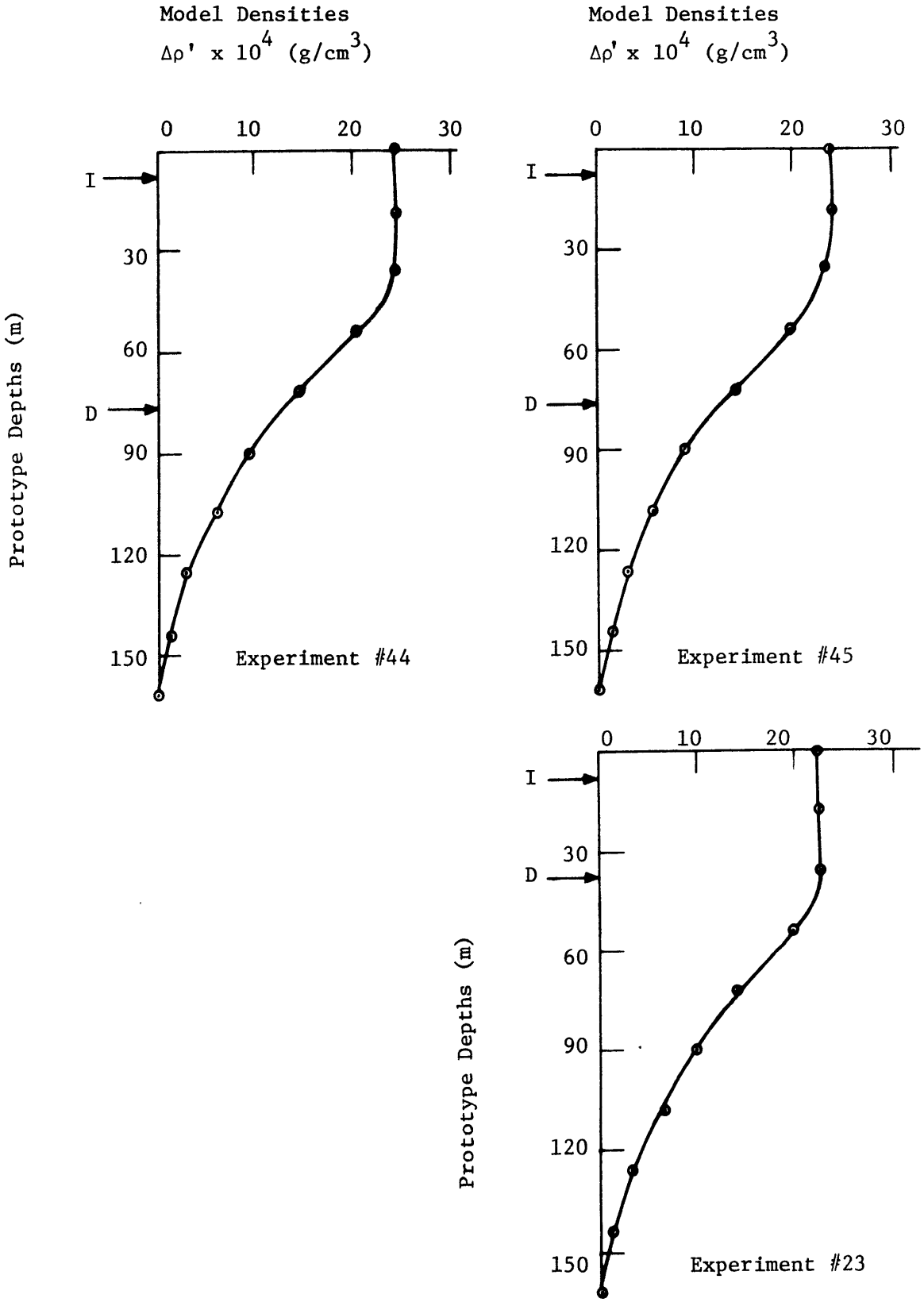
Model Densities
$\Delta\rho' \times 10^4$ (g/cm^3)
0
10
20
30
I
D
30
60
90
120
150
Prototype Depths (m)
Experiment #44
Model Densities
$\Delta\rho' \times 10^4$ (g/cm^3)
Experiment #45
Experiment #23